Design, processing and characterization of glass fibers and coatings for healthcare industries

Doctoral Dissertation
Doctoral Program in Materials Science and Technology (31st Cycle)

Design, processing and characterization of glass fibers and coatings for healthcare industries

Pablo López Iscoa
* * * * * *

Supervisors
Prof. Daniel Milanese. Politecnico di Torino, Italy.
Prof. Laeticia Petit. Tampere University, Finland.

Doctoral Examination Committee:
Dr. Wilfried Blanc, Institut de Physique de Nice (InPhyNi), Université Côte d'Azur, CNRS, Nice, France.
Dr. Pavel Peterka, Institute of Photonics and Electronics. The Czech Academy of Sciences, Prague, Czech Republic.
Prof. Ilaria Cacciotti, Università Niccolò Cusano, Roma, Italy.
Prof. Davide Janner, Politecnico di Torino, Turin, Italy.
Prof. Federico Smeacetto, Politecnico di Torino, Turin, Italy.

Politecnico di Torino
February 13th, 2019

Declaration

I hereby declare that, the contents and organization of this dissertation constitute my own original work and does not compromise in any way the rights of third parties, including those relating to the security of personal data.

Pablo López Iscoa
Turin, February 13th, 2019

To my grandfather José Ignacio Iscoa

Acknowledgments

First, I would like to express my deepest gratitude to my supervisors Prof. Daniel Milanese and Prof. Laeticia Petit for the constant support, responsiveness and guidance they have given me through the course of my PhD.

I am very grateful to have been part of the CoACH project (Advanced Glasses, Composites and Ceramics for High Growth Industries), a Marie Skłodowska-Curie Innovative Training Networks action (MSCA-ITNs) funded by the European Union's Horizon 2020 research and innovation program. It has provided me the opportunity to pursue my research interests and to develop my international career by collaborating with other research groups from academic and private institutions, and to participate in multiple international conferences and workshops.

I would also like to thank many researchers in the Department of Applied Science and Technology of Polytechnic University of Turin. Special thanks to Dr. Nadia Boetti, Dr. Diego Pugliese and Prof. Dr. Davide Janner for all the suggestions and help that they provided during this thesis. I also want to express my gratitude to all the people with whom I shared the laboratory.

I am very fortunate to have worked with people at the Faculty of Biomedical Sciences and Engineering and at Laboratory of Photonics of the Tampere University. I would like to thank Prof. Jonathan Massera, Nirajan Ojha and Ayush Mishra for all their support and help regarding both the experimental and theoretical parts of this thesis.

In addition, I also want to express my gratitude to the researchers at the Université de Rennes, in particular to Prof. Catherine Boussard-Plédel and Bruno Bureau for helping me with the fiber drawing activity. I am also very grateful to the staff of nLight and Colorobbia for providing a warm welcome and assistance during my research stays in the industry.

Finally, I wish to thank my family and friends for their endless support.

Summary

In this PhD, several bioactive phosphate glasses doped with erbium ions (Er^{3+}) were synthesized and characterized in order to develop new bioactive fiber sensors for medical diagnostics and therapeutics in healthcare applications.

Firstly, Er^{3+}-doped phosphate glasses within the glass system P_2O_5-SrO-Na_2O were fabricated using the melt-quenching technique. The glasses were prepared with different compositions and analyzed to understand the impact of the addition of Al_2O_3, TiO_2 or ZnO on the thermal, structural and luminescence properties of the glasses. The results showed that with the addition of Al_2O_3 and TiO_2 the phosphate network became more connected, whereas the addition of ZnO did not modify the optical, thermal and structural properties but it led to an enhanced fluorescence emission as compared to the other glasses.

Secondly, glass-ceramics (GCs) were processed by heat-treating the glasses to induce in-situ crystal growth. The effect of the crystallization on the properties of phosphate glasses containing Al_2O_3, TiO_2 or ZnO was investigated. The structural, optical, and spectroscopic characterization allowed assessing the occurrence and properties of the Er^{3+}-doped crystals in the glasses. Different crystal phases were obtained depending on the glass composition but $Sr(PO_3)_2$ was identified in all the glasses. Moreover, the surface crystallization of the GCs was increased along with the duration of the heat treatment. However, the site of the Er^{3+} ions was not strongly affected by the heat treatment except for the reference GC, where an increase of the luminescence properties was observed after the heat treatment probably due to the incorporation of Er^{3+} ions into the crystals.

Thirdly, particles-containing glasses were prepared using the direct doping method. A series of different Er^{3+}-doped Al_2O_3, TiO_2, ZnO and ZrO_2 nano- and microparticles were synthesized using soft chemistry and then were added to phosphate-based glass batches prior to and after the melting. The survival and dispersion of the particles were optimized in order to increase the luminescence properties of the glasses. As evidenced from the morphological and compositional analyses, the Er^{3+} ions diffused from the particles to the glass matrix and no improvement of the spectroscopic properties was observed. A large amount of Er^{3+}-doped particles were dissolved into the glasses probably due to the high temperatures achieved during the melting. As an alternative, glasses with different composition and lower melting temperatures were tested.

The last part of the project was the production and characterization of a multimode optical fiber made from phosphate-based glasses. The core composition was 0.25 Er_2O_3 – 97.25 (0.5 P_2O_5 – 0.4 SrO – 0.1 Na_2O) – 2.5 ZnO, while the

cladding composition was 98.25 (0.5 P_2O_5 – 0.4 SrO – 0.1 Na_2O) – 1.75 ZnO. The cladding component was processed using the rotational casting technique, and the preform was successfully drawn into an optical fiber. This novel optical fiber was found to be able to allow in-line monitoring of the fiber dissolution in H_3PO_4 and in simulated body fluid (SBF) solution. Bioactivity of the fiber was also assessed by the formation of an hydroxyl apatite layer at the surface of the fiber after 4 weeks of immersion in SBF solution at room temperature.

In this thesis, a bioactive fiber sensor able to monitor its optical properties and in vitro reactivity was reported. This research activity demonstrates as a proof of principle the idea of tracking the bio-response of a bioactive optical fiber “in vivo”.

Table of contents

List of figures

List of tables

Chapter 1

Introduction

Since the discovery of the first bioglass by Larry Hench in 1971 [1], several types of biomedical glasses, such as silicates, phosphates or chalcogenides, have attracted the attention of many researchers, especially for biomedical applications [2–5]. Above all, phosphate glasses with a P_2O_5 content of around 50 mol% have been shown to be biocompatible [6–10], and the addition of other elements such as Strontium has been demonstrated to increase the proliferation and growth of human cells [11], thus making the glasses bioactive. Moreover, the dissolution behavior of phosphate glasses can be adjusted from hours to years depending on its composition and its structure [12,13]. Thus, the phosphate glasses have been studied in many biomedical applications, especially for use in bone repair and reconstruction [14].

Apart from their biological properties, phosphate glasses are also known by their easy processing, excellent thermo-mechanical and chemical properties, homogeneity, good thermal stability and excellent optical properties, such as high transparency in the UV-Visible-Near Infrared (UV-Vis-NIR) region [15–19]. Besides, phosphate glasses allow high rare earth (RE) ions solubility. Thus, quenching phenomenon does only occur at very high concentrations of RE [19,20]. In addition, phosphate glasses with P_2O_5 higher than 45 mol % have been proven to be drawn easily into optical fibers [8,21–25]. Due to the optical properties, phosphate glasses have recently become appealing for the engineering of photonic devices for optical communications [26], laser sources and optical amplifiers [13,19,20,27,28]. However, to the best of our knowledge, up to now few studies focusing on glass compositions that combine both biocompatibility and suitable optical properties have been reported [23,29,30].

The RE ion dopant studied in this thesis is the Erbium (Er^{3+}), whose emissions at around 1540 nm and in the visible wavelength range are of great interest for optical and biomedical applications. The scope of this thesis is to demonstrate that the biological properties of phosphate glasses can be combined with the excellent luminescence properties of the Er^{3+} ions. In this research activity, innovative Er^{3+}-doped phosphate glasses with a composition of P_2O_5-SrO-Na_2O with good biological and optical properties have been synthesized. The glasses were synthesized by the conventional melting method and the changes in their thermal, structural and luminescence properties with the addition of Al_2O_3, TiO_2, or ZnO were reported. Moreover, the crystallization behavior of these glasses and the

influence on the luminescence properties were also investigated. Apart from glasses, different Er^{3+}-doped particles were synthesized by the sol-gel method: Al_2O_3, TiO_2, ZnO, and Zr_2O were successfully obtained and selected as crystalline hosts for the Er^{3+} ions. The crystalline particles were further incorporated into phosphate glasses fabricated by melt-quenching. These glasses were processed using different techniques such as the direct particle doping method or by the incorporation of particles prior to the melting. A full characterization of the morphological, structural and luminescence properties of the different Er^{3+}-doped materials was thoroughly investigated.

Lastly, an Er^{3+}-doped phosphate glass optical fiber was fabricated by preform drawing using the rod-in-tube technique. Properties such as the refractive index, emission, lifetime or CTE were characterized in order to process a fiber with good optical, thermal and mechanical properties. The optical fiber proposed in this thesis is intended to behave as a bioactive optical fiber sensor able to monitor "in situ" the optical and biological responses in aqueous media, in the prospect of developing an innovative biosensor for therapy monitoring.

This PhD thesis is divided into six chapters:

- ***Chapter 1: Introduction.***

- ***Chapter 2: Phosphate glasses for biophotonic applications.*** In this chapter, the definition of glass and several types of glasses are first introduced. Then, an overview of the structure and properties of phosphate-based glasses is reported. Additionally, the luminescence properties of the Er^{3+} ions and the different hosts used in this thesis are presented. In the last part of this chapter, the differences between conventional glasses, GCs and particles-containing glasses are discussed.

- ***Chapter 3: Materials and methods.*** This chapter outlines the experimental methods and procedures used to synthesize and characterize the several types of materials studied in this thesis.

- ***Chapter 4: Fabrication and characterization of erbium doped materials.*** This chapter presents the results of the Er^{3+}-doped phosphate glasses, GCs, particles-containing glasses, as well as Er^{3+}-doped Al_2O_3, TiO_2, ZnO, and Zr_2O crystalline particles.

- ***Chapter 5: Phosphate glass optical fibers for advanced bio-sensing.*** This chapter presents the results of the Er^{+3}-doped optical fiber. The aim of this section is to study the bioactivity and optical properties of the optical fiber with the further processing of an innovative biosensor.

- ***Chapter 6: Conclusions.*** The last chapter summarizes the results of the PhD thesis with emphasis on those goals outlined in the introduction of the thesis.

Finally, the references, list of acronyms and symbols, and the list of publications and conferences accomplished during this thesis are included at the end of the dissertation.

Chapter 2

Phosphate glasses for biophotonic applications

2.1 Introduction to glass science

The American Society for Testing and Materials (ASTM) defines a glass as a product obtained through cooling of a liquid which has no time to undergo crystallization [31]. According to this definition, a glass is a non-crystalline material obtained by a melt-quenching process. However, glasses can also be obtained by other techniques such as chemical vapor deposition or sol-gel process, just to cite a few.

Therefore, the glasses can also be defined as all non-crystalline solids that show a glass transition regardless of their preparation method [32]. The glass transition temperature (T_g) of a glass corresponds to the temperature where the bonds between the atoms start to break. Another main feature of glasses is their atomic structure, which lacks a long range order. Thus, glass is an amorphous (non-crystalline) solid, which has an atomic arrangement similar to that of a liquid (see Figure 2.1).

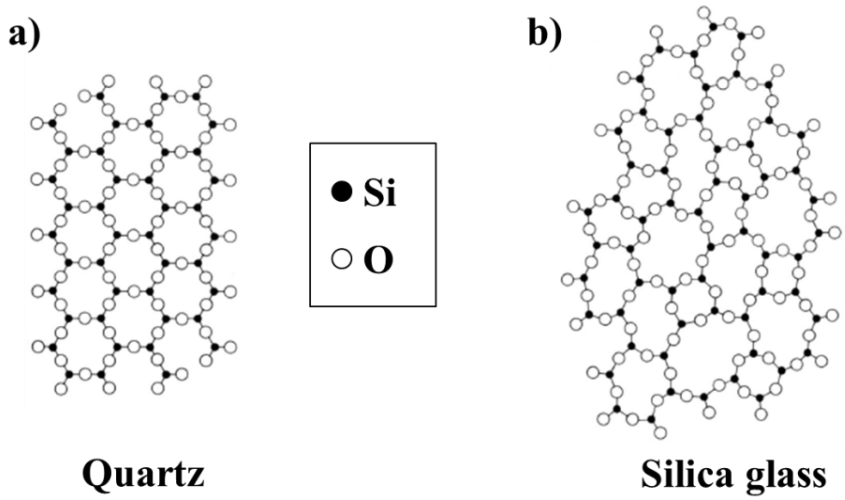

Figure 2.1 Atomic structure of SiO_2 in a quartz crystalline lattice (a) and in a random glass network (b). Picture modified from [32].

The transformation behavior of a melt forming a glass can be explained in Figure 2.2, where it is shown the specific volume or enthalpy of a material versus the temperature.

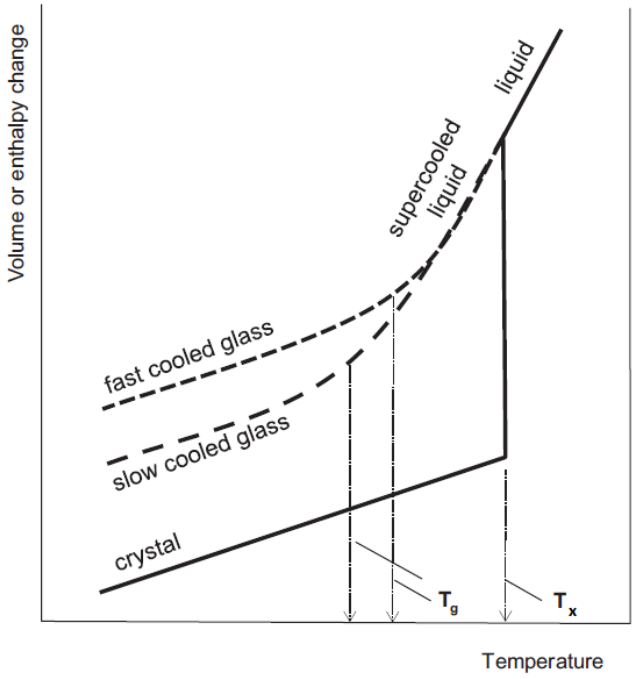

Figure 2.2 Diagram of the volume or the enthalpy versus the temperature for a liquid that forms either a glass or a crystalline solid. Image modified from [32].

If a liquid in high temperature starts to cool down, two different processes can occur at the crystallization temperature (T_x), either it crystallizes, or it becomes a glass:

- In the case that the liquid crystallizes, there is a noticeable change in the volume and the rate of cooling. This can be explained by the heat produced by the crystallization process.
- In the case that no crystallization occurs, the liquid appears to be supercooled and its volume decreases at about the same rate as it did above T_x.

One important characteristic about glasses is their dependence of T_g upon cooling rate. As opposed of T_x, T_g is not fixed [33]. Below T_g, all the glasses behave as amorphous materials, around T_g the glasses behave as viscoelastic solids, whereas above T_g the glasses start to act as liquids.

Another characteristic of the glasses is their thermal stability, which is an indicator of the resistance to crystallization during heating. The glass stability is often represented by ΔT, which corresponds to the difference between T_x and T_g. Typically, a ΔT value higher than 100 °C suggests a reasonable glass stability against crystallization [32].

In theory, every material cooled down at a fast rate could become a glass, and the more general definition includes also metallic glasses and organic materials. However, the formation of a glass is only possible using specific materials. Regarding the case of inorganic materials, depending on the presence of oxygen in the structure, the glasses can be divided into oxide and non-oxide glasses. Examples of non-oxide glasses are the halide glasses and chalcogenide glasses, which are formed from halides of various metals [34].

The reported research activity deals with oxide glasses, where specific metal oxides form random glass networks interconnected by bridging oxygens (BO). They are called ***network formers***, some examples of network formers are GeO_2, B_2O_3, TeO_2, SiO_2 and P_2O_5. Other components are the so-called ***network modifiers***. These components are weakly bonded to the network, and they are incorporated into the network by disrupting the strong bonds of the network formers. The incorporation of the modifiers changes the physical and chemical properties of the glasses by breaking the BOs and creating non-bridging oxygens (NBO). Examples of modifiers are Na_2O, K_2O, Li_2O, MgO, CaO, BaO and ZnO. Apart from the network formers and modifiers, the ***glass intermediates*** are substances that are strongly bonded to the glass network without causing any crystallization. They can be present in low amount in the glass, but they cannot form a glass alone. Some examples of intermediates are Al_2O_3, TiO_2 and ZrO_2 [32].

As a rule, the composition of a glass influences the glass structural network and so its properties (melting and glass transition temperatures, spectroscopic properties, solubility, bioactivity, etc.). Among the activities carried out in this thesis, a thorough understanding of the effect of the addition of determined intermediates (Al_2O_3, TiO_2) or modifiers (ZnO) on the thermal, structural and luminescence properties of Er^{3+}-doped phosphate glasses is investigated.

Most of the conventional glasses are made by the traditional melt quenching technique. However, another alternative route that has recently arisen is the sol-gel method.

- **Melt quenching method**

Generally, the glasses are manufactured by melt quenching method. The melt quenched glasses possess large flexibility of the composition, high flexibility of the geometry and excellent optical properties [32]. The melt quenching technique consists of mixing the glass precursors in a platinum, alumina or quartz crucible. After that, the crucible with the glass batch is melted in a furnace. After the melting, the glass is cast onto a graphite or metal mold already preheated at around its T_g. Finally, the glass is annealed by cooling it down slowly at room temperature in order to release the internal stress of the glass from the quench.

Usually, the chemical reagents used for melt-quenched glasses are metal oxides or carbonates [23]. Even if the weighing of the reagents is carried out in a dry box,

there is always a remaining presence of OH^- groups in the glasses, which can cause issues in the case of rare earth doped glasses e.g. through the decrease in the luminescence of Er^{3+}, for example. Various technique to control the water content have been reported in the literature. For example, instead of conventional melting with an open crucible [35], glasses can be manufactured using anhydrous glass precursors such as chlorides or fluorides, sealed ampoules [36], or by melting the glasses in vacuum [37]. In this thesis, a series of Er^{3+}-doped bioactive phosphate glasses were prepared by the melt quenching technique in air.

- **Sol-gel method**

Various studies have shown that the sol-gel glasses possess excellent mechanical strength [38], bioactivity [39], and lower processing temperatures [40] than the melt-quenched glasses. Besides, the sol-gel process produces glasses with a high surface area, which can be useful for functionalization with suitable biomolecules or for applications such as drug carriers [41]. Furthermore, due to the larger surface area, the dissolution rate of mesoporous sol-gel glasses is higher than that of melt-quenched glasses [42,43].

However, the major drawback of the sol-gel method is the long time needed for obtaining the glasses. The gel must be heated very slowly to the melting temperature to ensure that the residual organics are well removed. The obtained glasses are very fragile. Due to the shrinkage and cracking that the samples may experience during the drying step, they usually end up heavily cracked. Thus, additives such as the Dimethylformamide (DMF) are generally used to decrease the surface tension during the drying process [44].

Some of the precursors used for the sol-gel synthesis are TEOS for silica [45]; $(NH_4)_2HPO_4$ [46], $PO_4(C_2H_5)_3$ [47,48], phosphoric acid [46,49] or $P(OCH_2CH_3)_3$ [48] for P_2O_5; $Ca(NO_3)_2$ and $NaNO_3$ for CaO and Na_2O, respectively [47,49,50]; and $Sr(NO_3)_2$ for SrO [45].

In 2003, Knowles *et al.* [13] introduced the idea of using sol-gel phosphate glasses for biomedical applications. Later, Carta *et al.* [51] and Pickup *et al.* [52] successfully synthesized sol-gel phosphate glasses and demonstrated their potential drug delivery applications by incorporating a chemotherapy agent in a P_2O_5–CaO–Na_2O sol-gel glass [53]. However, contrary to the melt quenching technique, very little research has been carried out on the sol-gel phosphate glasses and the processing of functional luminescent phosphate sol-gel glasses still remains a major challenge.

2.1.1 Phosphate glasses

The interest for phosphate glasses started in the 1940s mainly due to their high transparency in the ultraviolet (UV) region [54,55]. At first, phosphate glasses were used for hard water treatments and as a dispersant for pigment manufacturing [56]. In 1960s, phosphate glasses started to become a material of interest for optical

communications [26], high-power laser sources and optical amplifiers [13,19,20,27,28] due to their high rare-earth (RE) solubility as compared to silicate glasses [57]. In the last decades, phosphate glasses have been found to be good candidates for other applications such as nuclear waste [58,59]. and biomedical applications [60]. However, few studies focusing on glass compositions that combine both biocompatibility and suitable optical properties have been reported [23,29,30].

Structure

The structural units of the phosphate glasses are the P-tetrahedral units. These tetrahedral phosphate anions are connected through bridging oxygens (BO) [55]. The tetrahedral unit is constituted by a sp^3 hybrid orbital from the outer electrons $3s^2 3p^3$ of the phosphorus (P). One of these five electrons is promoted to a 3d orbital creating another π-bonding molecular orbital with the electrons 2p of the oxygen [61,62]. These tetrahedral units are classified using the Q^n designation, being 'n' the number of BO per tetrahedron.

Figure 2.3 depicts the different types of glasses depending on the predominant tetrahedral structure present in the network [55].

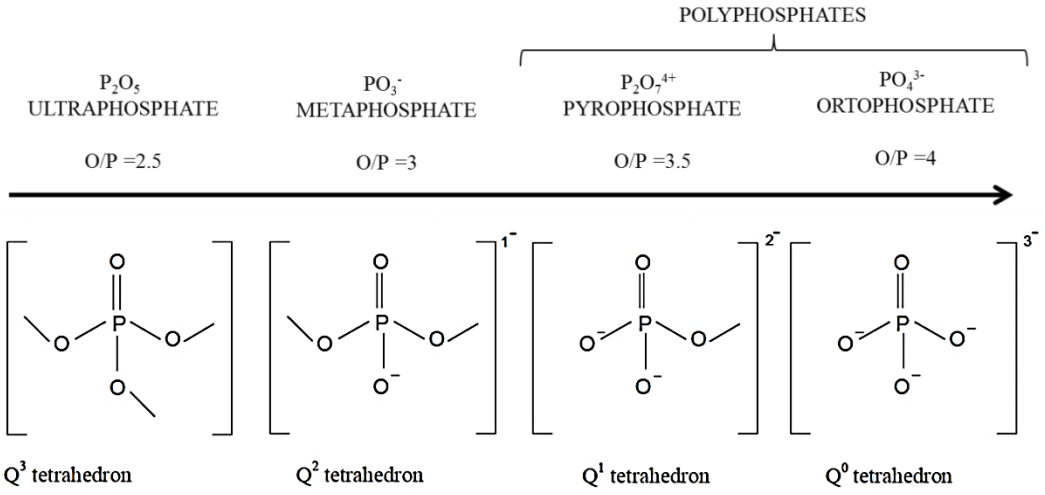

Figure 2.3 Tetrahedral structural units found in different phosphate glasses [63].

A vitreous P_2O_5 structure only consists of Q^3 units that form a three-dimensional network with three BOs and one double bonded oxygen for each tetrahedral unit. However, adding modifying alkali or alkaline earth cations results in the "depolymerization" of the network by breaking the P-O-P bonds and creating NBOs atoms at the expense of BOs. Thus, the Q^3 units are replaced with Q^2 units, and cross-linking bonds between the cations and the tetrahedral units are created. The polymerization of a glass and the connectivity are defined as the average number of BOs per P-tetrahedron.

The model of depolymerization was proposed by Kirkpatrick and Brow [64]. It predicts that the dominant tetrahedral structure changes according to $Q^3 \rightarrow Q^2 \rightarrow$

$Q^1 \rightarrow Q^0$ as the amount of modifying metal oxide increases resulting in an increase in the overall oxygen to phosphorus ratio (O/P). Consequently, the chain length of the phosphate anion decreases and the connectivity decreases. For example, when the content of P_2O_5 is around 50 mol%, the structure consists of mainly Q^2 units that form linear phosphate chains [65].

As it can be observed from Figure 2.3, different types of phosphate glasses can be classified depending on the O/P ratio, which determines the number of bridging oxygens to neighboring P-tetrahedra. There are three different groups of phosphate glasses: ultraphosphate, metaphosphate and polyphosphate glasses.

- The ultraphosphate glasses have an O/P ratio lower than 3, and their network is cross-linked by Q^3 tetrahedra.
- The metaphosphate glasses have an O/P ratio equal to 3, and their Q^2 units create chains of infinite length or rings within the network [64].
- The polyphosphate glasses have a O/P ratio higher than 3. They are characterized by a higher amount of more modifiers than phosphate. As a result, they are also called ***invert glasses***. The properties of polyphosphate glasses are more dependent on the bonds between the NBOs and the modifier cations, rather than on the P–O–P bonds [66]. The polyphosphate glasses can be subdivided into two groups: pyrophosphate glasses (O/P= 3.5) and orthophosphate glasses (O/P= 4). The pyrophosphate glasses have a chain-like structure and their Q^1 units terminate the chains. The orthophosphate glasses with Q^0 units have the shortest chain length and the lowest connectivity [64].

A pure ultraphosphate glass with a composition of 100% of P_2O_5 is very reactive and hygroscopic. Thus, such glass cannot be used for any practical application. However, by adding modifier oxides such as Al_2O_3, the glass network can be strengthened increasing the chemical durability and stability of the phosphate glasses. Indeed, this feature allows the phosphate glasses to be used as nuclear waste storage hosts for example [58,59,67].

Apart from metal oxides, H_2O in phosphate glasses can also act as network modifier by disrupting the P-O-P bonding and forming P-OH groups [68]. The water content is a critical factor in the case of the RE-doped glasses. The major problem with the hydroxyl groups (–OH) is that the RE energy levels couple with the energy of the –OH vibrations increasing the non-radiative transitions, and thus decreasing the luminescence properties. Therefore, for improving the luminescence properties of a RE-doped glass, the water content must be minimized [37].

Thermal and chemical properties

Changing the composition of a phosphate glass by adding metal oxides has also an enormous influence on the chemical and structural properties of the glass. The broad flexibility of the chemical composition of the phosphate glasses enables them

to have specific properties for the development of new technological applications. For example, the addition of metal oxides such as Al_2O_3 increases the chemical resistance of the glass, while Na_2O decreases the viscosity of the melt [58,67]. TiO_2 can also be introduced to reduce the degradation rate of the glass [13,69,70].

The phosphate glasses are characterized by their good thermal stability. They possess, if compared with pure silica glasses, low T_g (400-700°C) and T_p (800-1400°C) as well as a very large ΔT, which facilitates their processing and fabrication by melt-quenching [71,72]. Additionally, the phosphate glasses possess high thermal expansion coefficients ($13{,}4.10^{-6}$/K), if compared to other glasses such as silicate-glasses for example ($0{,}6.10^{-6}$/K) [73], which make them suitable to seal with other metals [74].

2.2 Glasses for biophotonics

Biophotonics is an emerging interdisciplinary science that studies the interaction of light with biological matter [75]. Specific inorganic glass families are suitable materials for biophotonics, since they can combine biocompatibility with good optical properties.

A necessary condition for a biophotonic glass is its biocompatibility. A material is biocompatible when it can be in contact with the human body without causing any damage or harm to the living tissues. Besides, apart from the biocompatibility, a biophotonic glass can also be bioactive or biodegradable.

An interesting subcategory of glasses for biophotonics is represented by degradable or resorbable glasses, which can be degraded in the human body once their functionality is finished. Thus, their removal by surgical operation is unnecessary. Devices based on these bioresorbable and optical glasses may be used in applications such as optical biosensing, deep tissue photo-therapy or optogenetics.

Another subcategory of biophotonic glasses is represented by bioactive glasses, which can repair damaged tissue by the formation of new soft tissues and bone structures. Generally, a calcium phosphate layer precipitates at the surface of the bioactive glass when it stays in contact with simulated body fluid solution or other buffer solution with a composition similar to the human blood.

A biophotonic glass, which is always characterized by its biocompatibility, can also be bioactive and/or biodegradable, depending on the glass composition. However, even though the biodegradability and bioactivity are interesting properties to be achieved for biophotonic applications, they are not required for biophotonic glasses [76][77].

In the next few paragraphs, the biological properties of bioactive glasses are first introduced. Then, the basics about the luminescence properties of Er^{3+}-doped glasses are reviewed. The scope of this section is to demonstrate that the biological

properties can be combined with the luminescence properties of the Er^{3+}-doped phosphate glasses.

2.2.1 Bioactive glasses

In 1971, Prof. Larry L. Hench discovered the first bioactive glass (45S5) with a composition in wt% of $45SiO_2$-24.5CaO-$24.5Na_2O$-$6P_2O_5$ [1]. Since then, interest in bioactive glasses with similar compositions for bone tissue regeneration has increased [2–5]. These bioactive glasses lead to the formation of a hydroxyapatite layer [78] which can be bonded to connective tissues.

Besides silicate glasses, phosphate glasses with a P_2O_5 content equal to 50 mol% have shown to be bioactive and biodegradable [7–10,21,23,24]. The phosphate glasses have been studied in many biomedical applications such as bone repair and reconstruction [14], dental ceramics [60] or nerve regeneration [24,25].

The novelty of the phosphate glasses in biomedical applications is related to their dissolution behavior, which can be tailored depending on its chemical composition and its structure [12,13]. Indeed, the time required for complete degradation of $CaO–Na_2O–P_2O_5$ glasses can be adjusted from hours to years depending on the glass composition [13]. By increasing the CaO content at the expense of Na_2O, the dissolution rate of a glass is decreased. Both cations, Ca^{2+} and Na^{+}, have similar radius, but the Ca^{2+} ion has a higher charge. The higher field strength of the Ca^{2+} as compared to that of Na^{+} causes a decrease in the dissolution of the glasses because the phosphate network connectivity is higher [8,66,79]. This is important because the degradation rate should be slow enough to allow the healing process while maintaining suitable mechanical properties [41].

Interestingly, the surface area influences the dissolution rate too [43]. Indeed, due to the higher surface area, the dissolution rate of a mesoporous sol-gel glass is usually higher than a melt-quenched glass [42,43]. For the same reason, an increase in the dissolution rate of the $P_2O_5–CaO–Na_2O$ fiber glasses as compared to their bulk counterparts has been reported [8,80].

Ions such as calcium [81], phosphorous [82], and silicon [83,84] are involved in bone mineralization, growth, metabolism and angiogenesis. In addition, trace elements in the human body, such as Sr^{2+} [85,86] and Zn^{2+} [87,88], have a stimulatory effect on bone formation and mineralization [89]. The release of these ions can regulate genes in the osteogenic cells and stimulate tissue regeneration [90,91]. Therefore, since the discovery of the bioglass 45S5, a lot of research has been developed in order to incorporate these ions into different types of bioactive glasses [92].

Zinc doping has been shown to enhance the bioactivity properties of bioactive glasses [93]. An extensive review of Zn-containing bioactive glasses can be found in [94]. This element plays a fundamental role in bone metabolism, cell division, angiogenesis, homeostasis and immune system [41,95,96]. Besides, when Zn is

present in phospho-silicate glasses, the pH of the SBF has been shown to be maintained within the physiological values due to the formation of insoluble $Zn(OH)_2$ [97,98]. Furthermore, Zn-phosphate glasses can be used for the treatment of chronic diseases such as Crohn's inflammatory disease or rheumatoid arthritis, which are both characterized by low blood levels of Zn^{2+} [99]. However, few studies on the bioactivity of Zn-phosphate glasses have been reported, and their bioactivity is still unclear. Thus, in vitro and in vivo studies of these glasses should be the object of future research.

Strontium doping also possesses excellent osteogenic properties [100]. For example, $50P_2O_5$-$10Na_2O$-(40-x)CaO-xSrO glasses showed an increase in the cell proliferation when increasing the SrO content, whereas the glasses without SrO did not show proper cell proliferation after 24 hours [11]. Studies reported that this effect is due to the slow initial dissolution rate when the SrO is incorporated in the glasses [101], which enhances the cell attachment [11,102].

The bioactivity of the glass system 50 P_2O_5-40SrO-$10Na_2O$ (in mol%) was previously assessed by J. Massera *et al.* [9]. However, the influence of the addition of Er_2O_3 and ZnO on the thermal, structural, biological and luminescence properties of these glasses has never been reported before. In this thesis, the bioactivity and optical properties of an optical glass fiber with a composition of 97.25 [50 P_2O_5 – 40 SrO – 10 Na_2O] - 2.5 ZnO - 0.25 Er_2O_3 in mol% are investigated.

2.2.2 Optically active glasses, Er^{3+}-doped glasses

The rare earth (RE) ions and their luminescent properties started to be studied at the beginning of the 20th century. Since then, the RE ions have been widely used as phosphor activators for color display optical devices. Later on, with the discovery of the solid-state laser of Nd:YAG in 1960, there has been an exponential growth for lasers, amplifiers, and other optical devices [103].

Among rare earth ions, Er^{3+} ions have been widely studied as dopants in different host matrices. Their emission around 1535 nm makes them suitable for applications such as fiber lasers and amplifiers for telecommunications [104]. Moreover, their up-conversion properties enable them to convert the infrared radiation into red and green emission, at around 550 and 660 nm respectively [105]. Thus, Er^{3+}-doped materials have many other applications such as photovoltaics [106], display technologies [107] and medical diagnostics [108].

The electron configuration of erbium is [Xe] $4f^{12}$ $6s^2$, and the number of electrons in each shell is 2, 8, 18, 30, 8, 2 [109]. The ions of erbium can exist in two oxidation states, Er^{3+} or Er^{2+}. Contrary to the Er^{2+} ion, which are found in some semiconductors, the Er^{3+} ions are the most common form and the ones of interest for photonic applications. The quantum numbers of the Er^{3+} ion are represented in Figure 2.4. It should be considered that the distribution of the electrons is crucial, as it affects the interaction of the atom with the light.

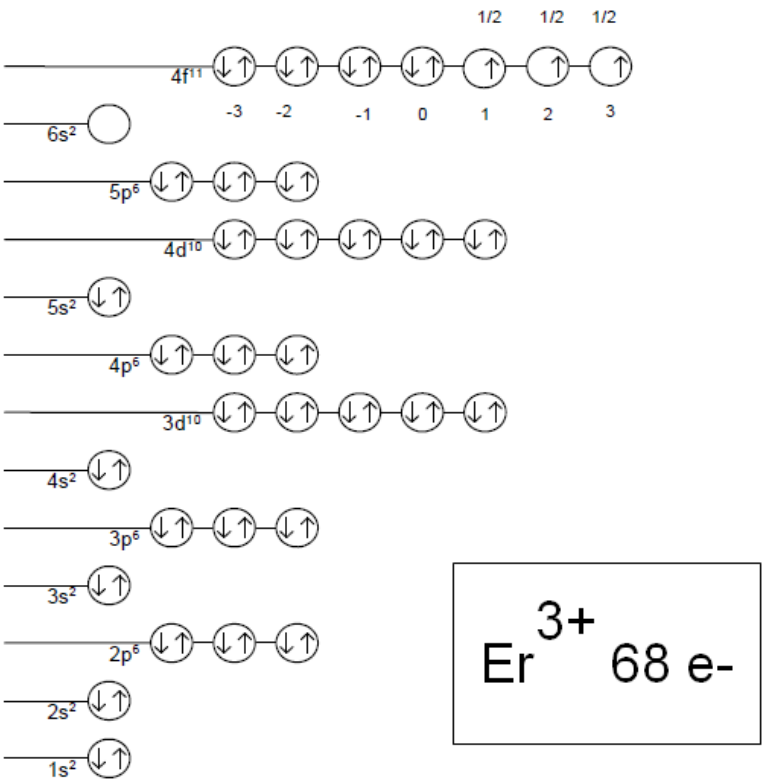

Figure 2.4 Energy distribution of the electron an Er^{3+} ion. Picture modified from [110].

As shown in Figure 2.4, the Er^{3+} ion is formed by the loss of one electron of the 4f energy level and two electrons of the 6s level. As a result, an external barrier of the 5s and 5p levels surrounds the incomplete shell of the 4f electrons, which are responsible for the intense and narrow emission bands in the spectra. Consequently, the luminescence of the Er^{3+} can be affected by the host. However, some variations of the emission spectra due to the Stark splitting or crystal field (CF) splitting may occur. For example, a host with low symmetry matrix gives higher Stark splitting with a higher number of sub-levels which broadens the levels, as compared to hosts with high symmetry matrix [111]. Indeed, full Stark splitting occurs in RE-doped glasses due to the low point symmetries of the RE sites [112].

As seen from Figure 2.5, each of the energy levels of the Er^{3+} ion is labeled with specific letters and numbers, such as $^4I_{15/2}$.

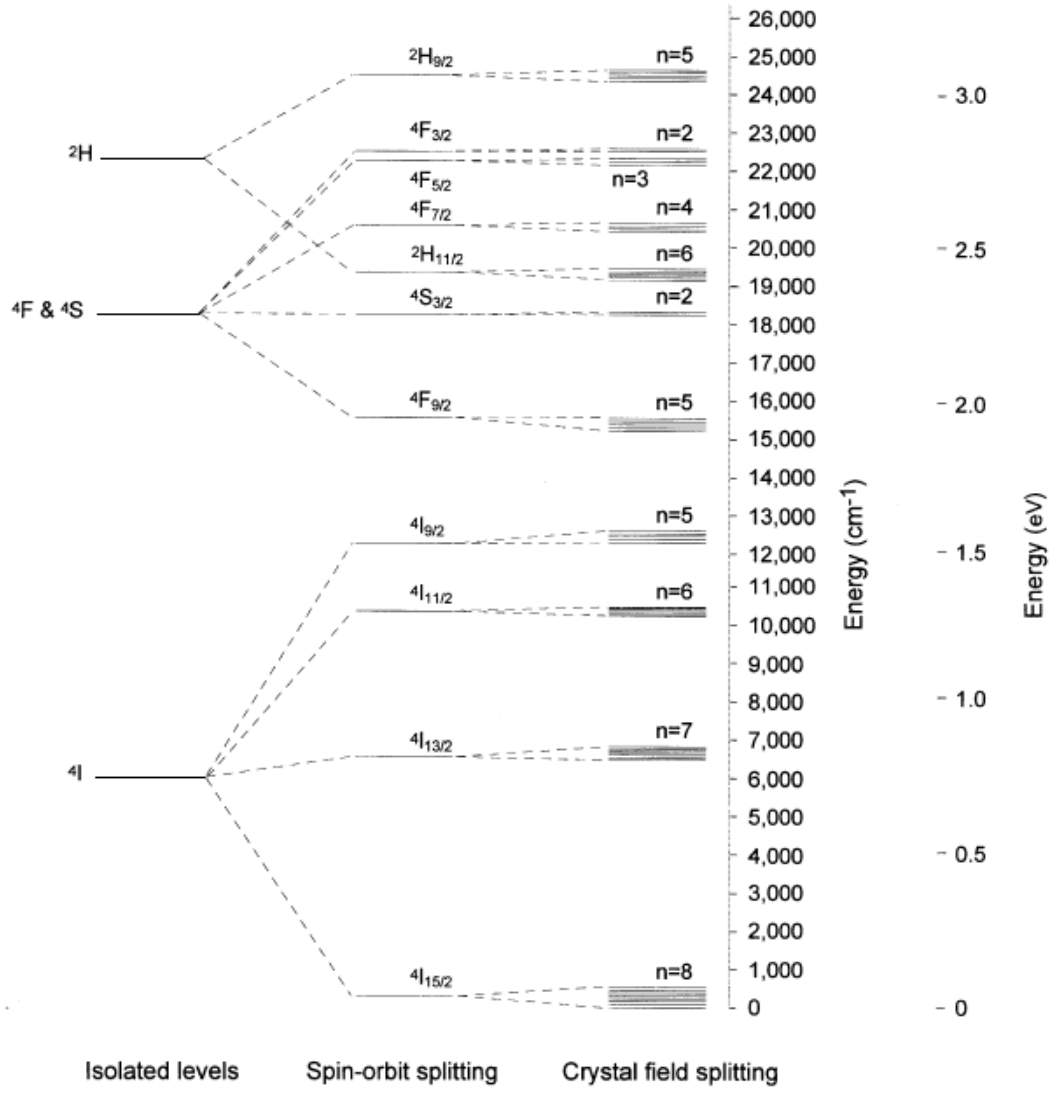

Figure 2.5 Splitting of the $4f^{11}$ electronic energy levels of an Er^{3+} ion [103].

The Russel-Saunder theory [113] describes the energy level with the label $^{2S+1}L_J$, where S is the total spin of the electrons, L is the total orbital angular momentum, and J is the total angular momentum.

- S: The total spin of electrons. From the Figure 2.4, S can be calculated as follows:

$$S = \frac{1}{2} + \frac{1}{2} + \frac{1}{2} = \frac{3}{2} \tag{2.1}$$

- L: The total orbital angular momentum, which defines the energy state for a system of electrons. These energy states or term letters are represented as follows:

S	P	D	F	G	H	I	J	K
0	1	2	3	4	5	6	7	8

Table 2.1 Total orbital momentum

From Figure 2.4 and Table 2.1, L = 6 and is thus labeled as “I”.

- J: The total angular momentum, which can be calculated as follows:

$$J = L + S, L + S - 1, L + S - 2, ..., L - S. \tag{2.2}$$

In the case of Er^{3+} ions, the interaction between the electron's spin and its orbital angular momentum produces a splitting of the ground state ^4I into four levels: 9/2, 11/2, 13/2 and 15/2. As an example, in the case of the ground state of Er^{3+} ions:

$$J = S+L = \frac{3}{2} + 6 = \frac{15}{2} \tag{2.3}$$

Therefore, the ground state of the Er^{3+} ion is $^4I_{15/2}$.

The energy states of the electrons can vary depending on the way the electromagnetic (EM) radiation interacts with the atoms. As seen from Figure 2.6, the photons can interact in three ways with a material with two energy levels, 1 (the ground level) and 2 (excited level): By absorption, spontaneous emission or stimulated emission.

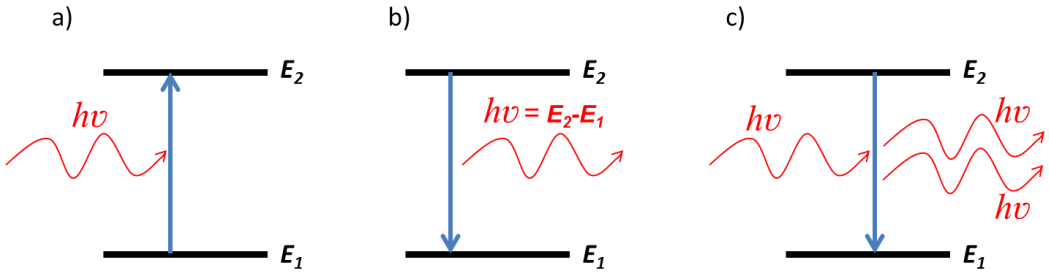

Figure 2.6 Schematic illustration of the interaction of radiation with matter: (a) absorption; (b) spontaneous emission; (c) stimulated emission. Picture modified from [114].

In the **absorption process**, when an EM radiation, hv, where v is the frequency and h is the Planck constant (6.6×10^{-34} Ws^2), hits the matter, its electrons are raised from a low energy level E_1 to a higher energy level E_2. This phenomenon can only occur if the energy of the photon equals the energy difference between the two levels:

$$hv = E_2 - E_1 \tag{2.4}$$

In the **spontaneous emission**, once an electron has been raised to the upper energy level, it can decay to the ground state and emits a photon with an energy equal to the energy difference between the two levels. This process is called radiative emission. However, a non-radiative emission can occur if the energy is released in the form of heat (e.g. through the emission of phonons) or other kinetic or internal energy.

In the **stimulated emission**, the emission process takes place spontaneously and by stimulation. The external radiation must have photon energy equal to the

energy difference between E_2 and E_1. Under stimulation with that EM radiation, the atomic system will produce spontaneous emission with photon having a phase independent from the one of the external radiation (different energy, direction, and polarization), and stimulated emission with photon in phase with the incoming one.

The atomic or molecular systems with two energy levels E_1 and E_2 have a population of electrons of N_1 and N_2, respectively. Under normal equilibrium conditions, the competition between absorption, spontaneous emission and stimulated emission processes usually ends up with a population of N_2 lower than N_1.

To have a **laser** (Light Amplification by Stimulated Emission Process of Radiation), a pumping excitation that causes a **population inversion** between N_2 and N_1 is required. Once the material receives the pumping energy by optical, thermal or other techniques depending on the laser gain medium, the lasing emission from E_2 to E_1 is released.

However, some other non-radiative phenomena can degrade the performance of the Er^{3+} ions luminescence. The non-radiative processes that can occur are: multiphonon relaxation, concentration quenching and non-radiative decay due to the water absorption or other quenching centers such as impurities.

A detrimental effect for the luminescence of RE-doped materials is the **multiphonon relaxation** (see Figure 2.7), which occurs when an excited state is rapidly depopulated by phonons [104]. However, this process requires enough phonons to bridge the energy gap (ΔE) between the upper and lower levels. Thus, the multiphonon quenching effect depends on the phonon energy of the matrix.

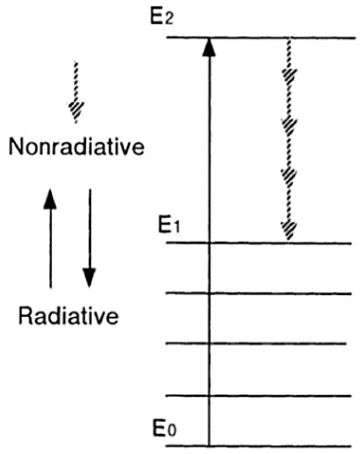

Figure 2.7 Multiphonon relaxation processes of RE ions [32].

As a rule, hosts with high phonon energies exhibit more multiphonon relaxation than a material that supports phonons with low energies. If the phonon energy of a material is higher than 25% of the ΔE, the luminescence is quenched. If the phonon energy is 10-25%, the quenching is temperature-dependent. Lastly, if the phonon energy is lower than 10%, the quenching by multiphonon processes is negligible

[115]. The ΔE of the $^4I_{13/2}$ to $^4I_{15/2}$ levels of Er^{3+} is about 6500 cm^{-1}. The phonon energy of phosphate is 1100-1200 cm^{-1}, so the quenching at 1535 nm can barely occur at room temperature.

Low phonon energy hosts, such as germanate, chalcogenide, tellurite or fluoride glasses, favors the radiative transitions of the RE ions [63,116] and allow certain radiative transitions at wavelengths that are generally quenched in silica or phosphate glasses (for example, the transition $^4I_{11/2} \rightarrow {}^4I_{13/2}$ results in emission at 2.8 μm) [117]. However, the physical and chemical properties of the low phonon energy hosts are not as good as those of the silicate or phosphate glasses. As it can be seen from Table 2.2, oxide glasses with strong covalent bonds possess higher phonon energy as compared to halide glasses with weaker ionic bonds.

Type of glass	Phonon energy (cm^{-1})
Borate	1400
Silicate	1100
Phosphate	1100-1200
Germanate	900
Tellurite	700
Fluorozirconate	500
Chalcogenide	350

Table 2.2 Phonon energies of different glasses [116].

The **concentration quenching** is produced due to the ion-ion interactions which reduce the fluorescence emission as the concentration of the RE ions increases. When the concentration of RE ions is high, the ions become closer one to another, and consequently, they can interact with each other. Three different concentration quenching processes can occur: cross relaxation, energy migration and cooperative up-conversion (See Figure 2.8) [103].

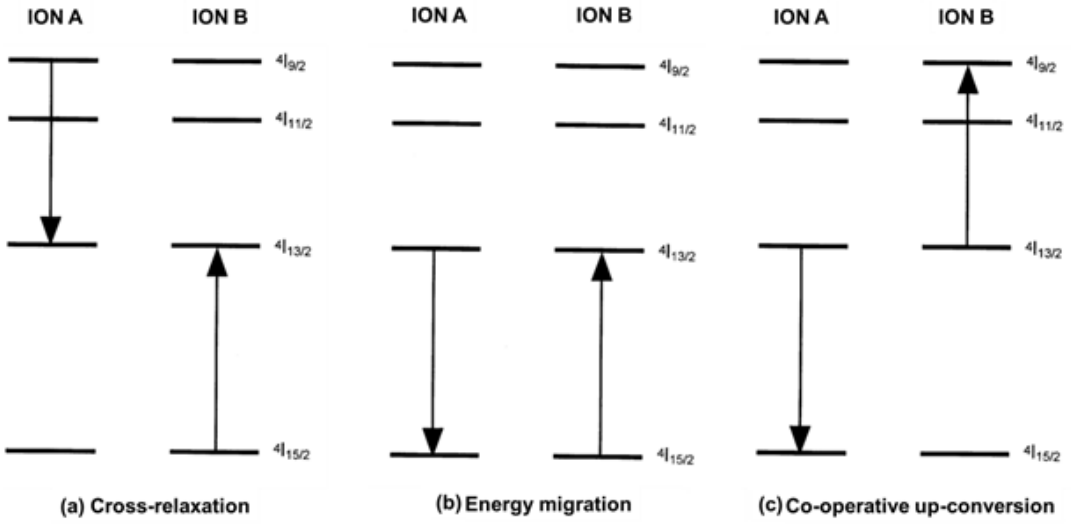

Figure 2.8 (a) Cross relaxation, (b) energy migration and (c) co-operative up-conversion processes between two neighboring Er^{3+} ions [103].

The **cross relaxation** process may take place between the ions of the same RE. Ion A, which is excited, gives half of its energy to the ion B, which is excited from the ground state to a metastable energy level. The transfer of energy is possible because the ΔE of $^4I_{9/2} \rightarrow {}^4I_{13/2}$ is similar to the $^4I_{13/2} \rightarrow {}^4I_{15/2}$ transition. As a result, both ions excited at the same intermediate level ($^4I_{13/2}$) leads to a non-radiative relaxation to the ground state [116].

Energy migration is a process where an ion in the metastable state gives its energy to a nearby ground state ion, promoting it to the $^4I_{13/2}$ level. The second ion may still release radiative emission. However, the non-radiative processes are increased for each successive transfer [116].

Co-operative up-conversion is a process with two ions, A and B, which are initially excited. Ion A gives its energy to ion B and promotes it to a higher energy level while A relaxes to the ground state. Ion B relaxes non-radiatively quickly to the ground state via phonon relaxation. Co-operative up-conversion is thought to be the dominant process in the concentration quenching of Er^{3+} ion in glass [104]. Besides, as seen from Figure 2.9, the co-operative up-conversion process can also lead to the emission in the UV-visible. The excitation of two or more low-energy photons (typically in the IR region), results in one high-energy photon, which typically emits in the UV-Vis regions. The excitation wavelength at 980 nm induces a first transition $^4I_{15/2} \rightarrow {}^4I_{11/2}$. Subsequently, another transition $^4I_{11/2} \rightarrow {}^4F_{7/2}$ occurs. The electron from the $^4F_{7/2}$ level decays non-radiatively to the $^2H_{11/2}$, $^4S_{3/2}$ and $^4F_{9/2}$ levels. Then, the green emission is emitted within the ranges 520-535 and 535-575 nm due to the radiative transitions from the $^2H_{11/2}$ and $^4S_{3/2}$ levels to the ground state, respectively. Additionally, the transition from the $^4F_{9/2}$ state produces red emission in the range 640-700 nm.

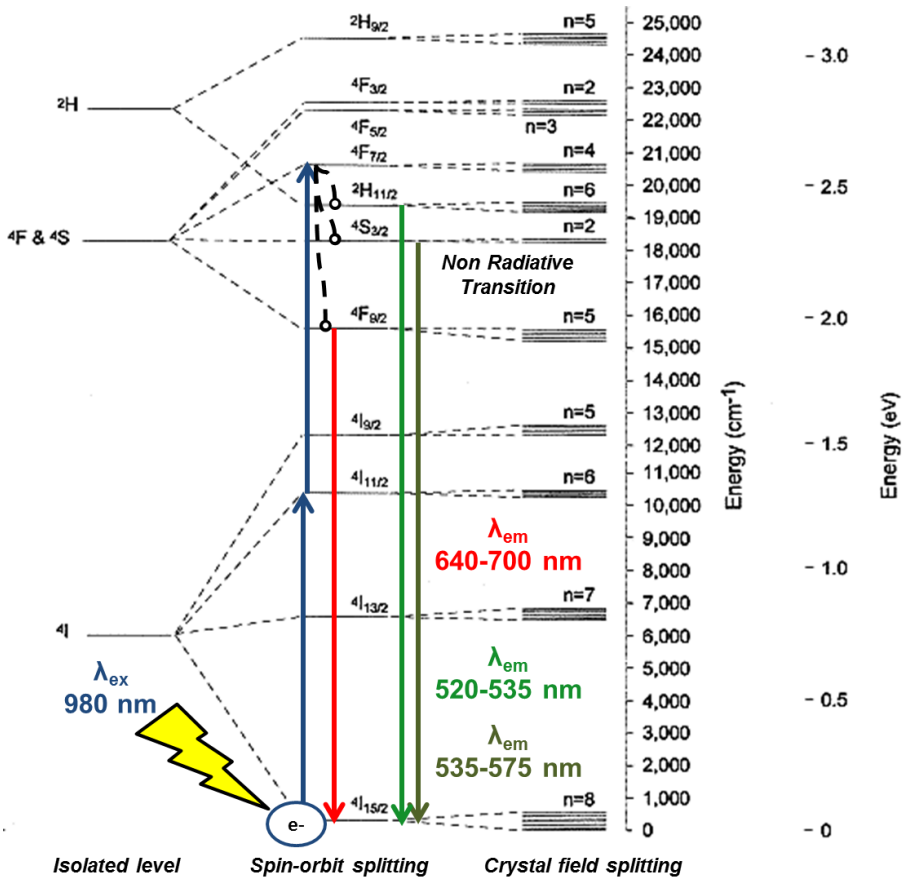

Figure 2.9 Up-conversion mechanisms in an Er^{3+}-doped material. Figure modified from [118] and [103].

Nowadays, one of the most significant applications of the Er^{3+}-doped glasses is as compact optical fiber devices such as high power lasers, which emit in the IR region, at 1535 nm [27,119]. Moreover, Er^{3+}-doped glasses that work in the visible region can also be used in other interesting applications such as temperature sensors, by measuring the differences in the intensity ratios of the $^2H_{11/2}$ and $^4S_{3/2}$ levels [120,121]. However, the up-conversion emission of Er^{3+}-doped phosphate glasses is very low, and lasing in the visible is not possible in phosphate glasses due to their high phonon energy [122,123].

A theoretical explanation of the concentration quenching effect was proposed by *Auzel et al.* in the early 2000s [124,125]. According to this theory, the quenching effect is described as follows:

$$\tau(N) = \frac{\tau_\omega}{1 + \frac{9}{2\pi}\frac{N}{N_0}} \tag{2.5}$$

Where τ is the lifetime of a RE ion, N is the concentration of RE, τ_ω is the theoretical lifetime at a concentration near to zero, and N_0 is the critical concentration at which the quenching effect starts to appear.

As an example, the Auzel's fitting of Er^{3+}-doped phosphate glasses at different concentrations is shown in Figure 2.10.

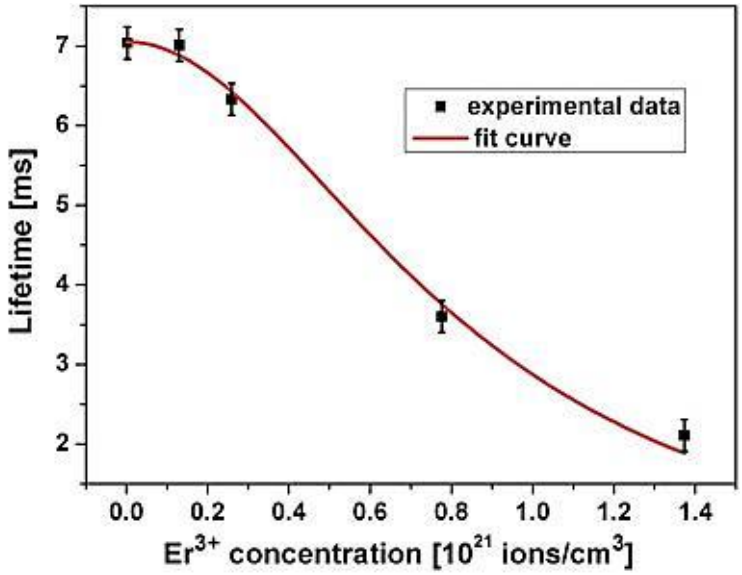

Figure 2.10 Lifetime decay as a consequence of the concentration quenching effect of the Er^{3+} doping. The red curve represents the Auzel's fitting equation [19].

Several studies of the concentration quenching effect on different RE-doped glasses have been performed. Interestingly, the N_0 values are always higher in the case of phosphate glasses than in silica glasses [19,126]. Thus, the amount of RE ions that the phosphate glasses can incorporate is about 50 times higher than in the silicate glasses, so the quenching effect appears at higher concentration [19,20,127].

Apart from the quenching effect due to the high concentration of RE ions, the presence of water in the structure of a glass matrix can have a detrimental effect on the luminescence properties. The **–OH groups** are very well-known to be quenched centers and to increase the non-radiative decay rates. The absorption bands of the –OH groups in the near IR, between 2500 and 3600 cm^{-1}, which correspond approximately to 2700 and 4000 nm, overlaps with the 1535 nm emission of the Er^{3+} ions (see Figure 2.11). This results in non-radiative decay processes due to the energy transfer from Er^{3+} ions to –OH groups [37]. The quenching effect of the water is significant for the phosphate glasses as they are very hygroscopic [128].

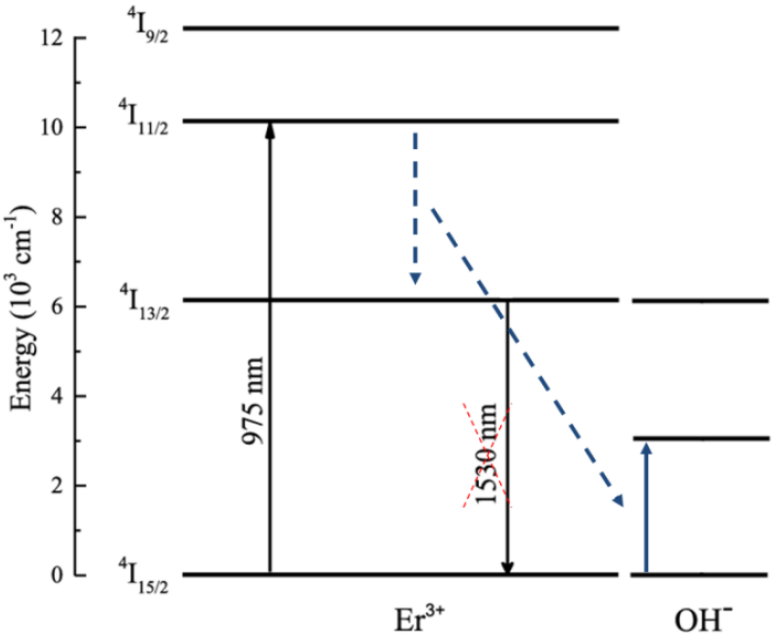

Figure 2.11 Influence of the OH absorption to the emission of Er^{3+} at 1530 nm. Picture modified from [129].

Phosphate glasses possess high transparency in the UV-Visible-Near Infrared (UV-Vis-NIR) region [15,17–19] and high absorption for RE elements which leads to high emission and long lifetime values. Moreover, phosphate glasses have demonstrated a higher photo-darkening threshold than silica glasses [130] which reduces the risk of power degradation in fiber lasers. These glasses also have a low nonlinear refractive index, which limits the detrimental effect of non-linear processes. Besides, the addition of heavy ions, such as Ti^{3+}, can increase the refractive index of the glasses [35].

In this thesis, we chose the phosphate glasses as hosts of Er^{3+} ions due to the following properties:

- Their processing is easy due to their excellent thermal stability [131]. They possess low glass transition temperature (400-700 °C) and softening temperature (500-800 °C).

- High RE solubility, which allows for high RE concentration (up to 10^{21} ions/cm^3) [19,20,131] and prevents the formation of Er-Er clusters, which cause non-radiative phenomena [132]. Thus, phosphate glasses usually possess high Er^{3+} ions emission and absorption cross sections compared to other glasses such as silica glasses, which have lower RE solubility [104].

- Wide optical transparency window, ranging from the ultraviolet (UV) to the near Infrared (NIR) region [23].

- Refractive index values suitable for optical fiber fabrication and integration with commercial silica fibers [131].

- They can become bioactive if the content of P_2O_5 is higher than 50% [6–10,21,23,24].

However, as mentioned in the previous section, the phosphate glasses have a hygroscopic nature. Thus, the water content must be as low as possible.

In the case of Er^{3+} ions, the absorption bands around 520, 800, 980 and 1480 nm correspond to transitions from the ground state to the levels $^4S_{3/2}$, $^4I_{9/2}$, $^4I_{11/2}$ and $^4I_{13/2}$, respectively [133]. Besides, the transition $^4I_{13/2} \rightarrow {}^4I_{15/2}$ produces a strong emission at 1535 nm, at which most common lasers based on Er^{3+}-doped phosphate glasses emit. The population inversion is achieved through a three-level system, which is usually excited with a high pump power at 980 nm ($^4I_{15/2} \rightarrow {}^4I_{11/2}$). The typical absorption and emission mechanisms of the Er^{3+}-doped phosphate glasses are represented in Figure 2.12.

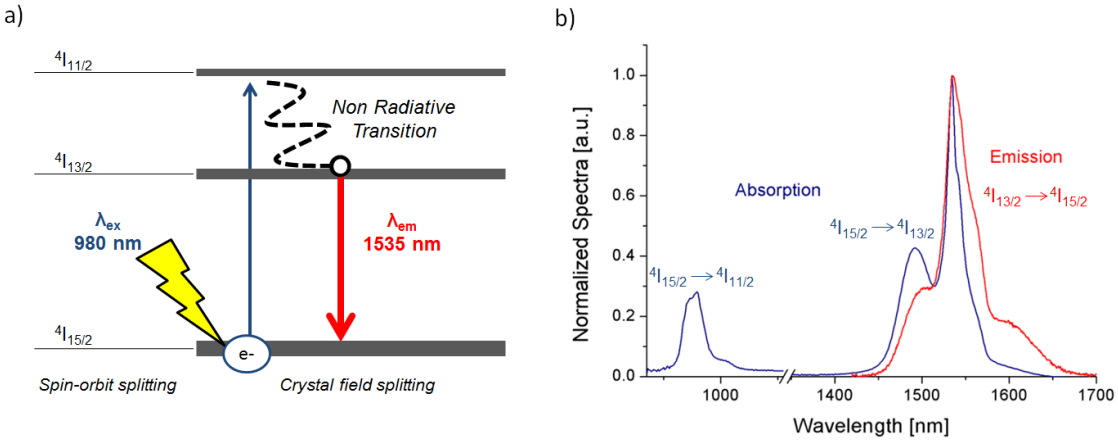

Figure 2.12 (a) Energy diagram of the Er^{3+} ions in a phosphate glasses. (b) Absorption and emission spectra from an Er^{3+}-doped phosphate glass excited at 980 nm [131].

2.3 Control of the Er^{3+} site

It is well known that the ions surrounding the Er^{3+} ions play a significant role in the luminescence properties. Specifically, parameters such as the mass, covalency or charge of the ligand atoms affect the luminescence properties as well as the solubility of RE ions in glassy hosts [134]. One of the goals of this thesis is to improve the luminescence properties of these glasses. Therefore, in this thesis, glasses with compositions in mol% of [0.25 Er_2O_3 – 100-x (0.5 P_2O_5 – 0.4 SrO – 0.1 Na_2O) – x (TiO_2/Al_2O_3/ZnO)], with x = 0 and x = 1.5 mol%, were prepared. These dopants were selected on the basis of their high covalency and their ability to change the structural network of the phosphate glasses: Al_2O_3 and TiO_2 are known to create cross-linking bonds such as Al-O-P [135] and Ti-O-P [136], respectively, whereas ZnO is considered a modifier and is responsible for the depolymerization of the glass matrix [137].

Apart from varying the composition around the Er^{3+} ions, a crystalline environment can also influence the luminescence properties. A heat treatment of

the glass can lead to the precipitation of the crystals. Crystals can also be added in the glass. In the case of RE-doped glasses, the RE ions are homogeneously distributed along the glass matrix, whereas in the case of RE-doped GCs and particles containing glasses, the RE ions can be incorporated in a crystalline structure separated from the glass matrix (see Figure 2.13).

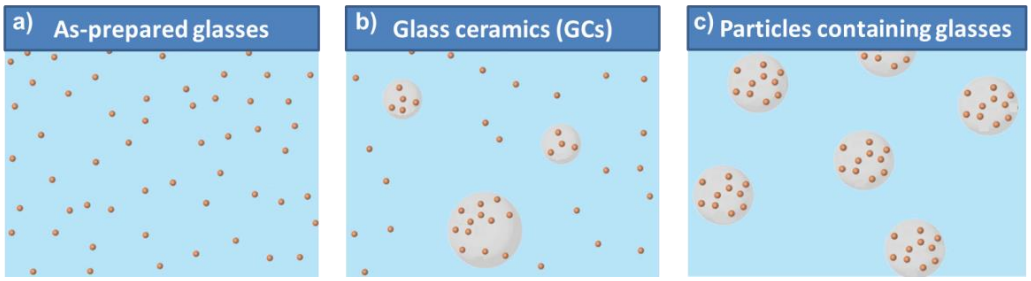

Figure 2.13 Representation of the RE ions distribution in different types of glasses: (a) RE-doped as-prepared glasses, (b) RE-doped GCs, and (c) RE-doped particles containing glasses. The red dots correspond to the RE ions, the grey area to the crystalline structure, and the blue area to the glass matrix. Image adapted from [138].

The shape of the IR and the up-conversion emission spectra of Er^{3+}-doped crystalline materials differ from the one shown by amorphous materials. Since the Er^{3+} ions in a crystal matrix can show long lifetimes and well-defined multi-peaks in the absorption and emission spectra, it is possible to distinguish between the Er^{3+} ions embedded into a suitable crystalline lattice and those diffused into the amorphous matrix. Hence, this can be useful to examine the survival and dissolution fraction of the particles in a glass [138].

2.3.1 Glass-ceramics by nucleation and growth

Glass-ceramics (GCs) are defined as a material that combines one or more glass and crystalline phases. They are usually fabricated from glasses by controlling the crystal nucleation and growth [139].

GCs were discovered by Stookey in 1953 [140]. Since then, they have been studied as promising materials in the construction, biomedical and electro-optical fields [141]. When doped with RE ions, the GCs combine the glass properties (large flexibility of composition and geometry) with some advantages of the RE-doped single crystals (higher absorption, emission and lifetimes) [142]. Moreover, these materials possess excellent mechanical properties such as compressive and bending strength [143] and high thermal durability [144].

The crystallization mechanisms have been studied on several families of GCs, such as tellurite [145], chalcogenide [146], silicate [147] or phosphate glasses [148]. The crystallization kinetics are described by using parameters such as the

activation energy and the Johnson–Mehl–Avrami (JMA) exponent *n*, which are obtained by differential scanning calorimetry (DSC) and differential thermal analysis (DTA). The activation energy gives information about the temperature dependence of the crystallization process, whereas the JMA exponent *n* defines the crystal growth morphology [148,149]. Depending on the crystallization kinetics and thermodynamics, bulk or surface crystallization may occur. Usually, bulk crystallization is often desirable to prepare GCs, but in the case of screen-printed, piezoelectric or pyroelectric GCs, a surface crystallization is more appropriate [150].

GCs can be obtained by a post heat treatment of melt-quenched or sol-gel glasses, which promotes the in-situ formation of crystals in the glass network. The crystallization process of GCs takes place in 2 different stages, the first step is the nucleation of small nuclei, and the second step is the growth of those nuclei into crystals. From Figure 2.14 it can be observed that the nucleation and crystal growth steps have a maximum value at different temperatures [151].

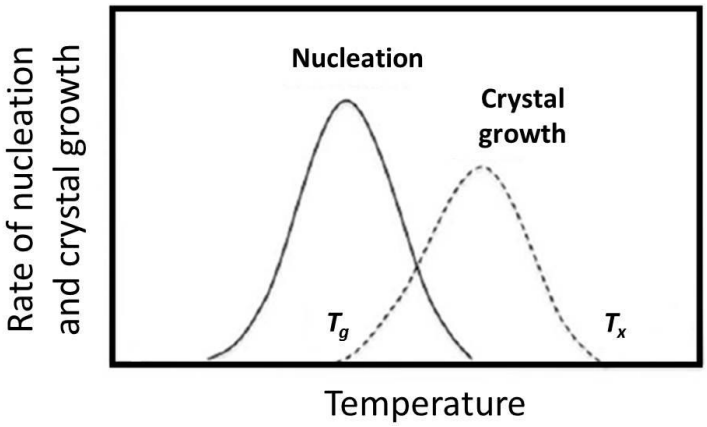

Figure 2.14 Graph showing the nucleation and crystal growth rates depending on the temperature. Picture modified from [152].

The minimum energy required to form nuclei with a stable radius or "critical radius" depends on various parameters such as the Gibbs free energy or the activation energy. Nuclei with smaller radii than the critical radius are unstable and tend to re-dissolve into the matrix, while nuclei with radius larger than the critical radius can lead to crystal growth. Once the thermodynamic and kinetic barriers are overcome, the critical radius can reach a size of a few tenths of a nanometer. Then, the stable nuclei could grow by the addition of atoms or molecules to the already formed nuclei and lead to crystallization of the glass [153].

The shape and size of the crystals inside the GCs depend on the growth mechanism occurred during the heat treatment and on the composition of the crystal. The temperature and time of the post heat treatments must be carefully selected because it will influence the transparency of the GCs [154].

Transparent GCs are achieved when the crystal size is smaller than the wavelength of the light, and when the refractive index of the crystal is similar to that of the surrounding glass matrix [155]. Instead, the opacity of the GCs is caused by the mismatch between the refractive index of the crystalline and glassy phases, which provide high scattering and an increase in opacity [156]. Apart from the crystals scattering, another major drawback of the GCs is their limitation to be drawn into fibers due to the possibility of a continuous growth of the crystals during fiber drawing. As an example, an increase of the light scattering and high optical losses of chalcogenide fibers occurred due to the growth of crystals while drawing [157].

Massera *et al.* [148] reported the crystallization mechanisms of phosphate bioactive GCs with the composition 50 P_2O_5 – (40-x) CaO – x SrO – 10 Na_2O in mol%. When x=0, $Ca(PO_3)_2$ and $NaCa(PO_3)_3$ crystals were formed, when x=20, crystalline solid solutions of $(Ca,Sr)(PO_3)_2$ and $Na(Ca,Sr)(PO_3)_3$ appeared, and when x=40, $Sr(PO_3)_2$ and $NaSr(PO_3)_3$ crystals were observed. Interestingly, all the glasses showed surface crystallization.

Furthermore, photonic RE-doped phosphate GCs have been further investigated due to the possibility to increase the luminescence of the RE ions by surrounding them with a crystalline environment [158–161]. Indeed, Yu *et al.* [162,163] reported an increase of the emission intensity of Er^{3+}/Yb^{3+} co-doped phosphate GCs as compared to the as prepared glasses with same composition. During the post heat treatment of Er^{3+}-doped phosphate GCs, the Er^{3+} ions may precipitate inside the crystals of the GCs and increase the optical properties. Therefore, one of the tasks of this research thesis aims to investigate the impact of the crystallization on the structural and luminescence properties of Er^{3+}-doped phosphate glasses.

2.3.2 Particles-containing glasses using direct doping method

2.3.2.1 Direct doping method

As mentioned before, the crystals shape and size of the GCs depend on the growth mechanism and the glass composition and so cannot be tailored. Hence, particles with a specific composition cannot be systematically grown in-situ in glasses. Particles-containing glasses can be prepared using the direct particles doping method. In this technique, particles are first prepared and then they are added in the glass batch during the melting process. With the direct particles doping method, particles with specific compositions and dopants can be incorporated into the glass. Thus, innovative particles-containing glasses with specific particle composition and nanostructures can be achieved.

Besides, similar to the conventional GCs, particles containing glasses, if successfully obtained, combine the advantages of the glasses (flexibility of composition and geometry) and of the crystals (higher absorption, emission and lifetimes) [142]. The advantage of the RE-doped particles-containing glasses is that the local environment of the RE ions is controlled by the crystal matrix of the particles independently of the glass composition [164]. Additionally, the particle matrix allows high RE content in a high dispersion state, thus avoiding the quenching effect [165].

Recently, Zhao *et al.* [138] developed nanoparticles-containing tellurite glasses by the direct doping method. The nanocrystals are added after the melting at lower temperature. Few minutes after (dwell time), the glass is cast. In order to balance the survival and dispersion of the particles in the glass, the doping parameters such as the doping temperature and the dwell time need to be optimized. Zhao *et al.* also demonstrated that optical fibers with low losses and up-conversion emission can be obtained using this technique.

One should remind that the presence of particles in the core of an optical fiber can cause Rayleigh scattering which can increase the optical losses [166,167]. In order to avoid this scattering, particles should have sizes lower than 100 nm. Thus, the losses would be lower than 0.1 dB/m, which is acceptable for optical fibers with lengths of few meters. Apart from the small size of the particles, nanoparticles (NPs) should also have a narrow size distribution, and the distances between the particles must be comparable to the particle size [168]. Another problem with the particles-containing optical fibers is that the particles can occupy a tiny fraction of the volume in the fiber core, so they are difficult to be quantified and characterized. For this reason, a full characterization of the particles-containing glass preform before the drawing into fibers should be performed.

2.3.2.2 Er^{3+}-doped particles

In this project, Er^{3+}-doped Al_2O_3, TiO_2, ZnO and ZrO_2 nano- and microparticles were synthesized using soft chemistry, with the further incorporation into Er^{3+}-doped phosphate glasses. These particles were chosen based on their high melting points and low phonon energies, which provide high thermal stability and high luminescence properties. Thus, the chances to survive the melting process and to enhance the luminescence of the particles-containing glasses are increased.

Although it is known that the size of the ions is affected by their local environment, it is very convenient to consider the ions as spheres with a fixed radius [169]. A table with the ionic radii sizes was proposed by Pauling in 1960, and completed by Shannon *et al.* in 1976 [170]. Based on that table, the following trends are considered:

- The radii of ions within a group in the periodic table increases along with the atomic number (Z)
- The radius of a cation is smaller than the corresponding atom.
- The radius of an anion is larger than the corresponding atom.

Therefore, it should be taken into account that the incorporation of Er^{3+} ions into different crystalline hosts, such as TiO_2 anatase or zirconia, is expected to modify the lattice. Indeed, the ionic radii size of Er^{3+} with a coordination number of 6 is 0.89 Å, while the Ti^{4+} with a coordination number of 6 is 0.61 Å or the Zr^{4+} with a coordination number of 8 is 0.84 Å [171]. Thus, these differences in the ionic radius will distort the crystalline host matrix and thus possibly alter the structural and spectroscopic properties of the particles.

Apart from selecting the right amount of dopant and a low phonon energy host, other parameters within the local environment around the RE, such as crystal field strength, the site symmetry or the electron-phonon interaction strength, influence the emission intensity. Moreover, the crystalline structure also affects the luminescence behaviors. A low symmetric crystal matrix usually improves the electronic coupling of the 4f energy levels and increases the emission intensity [172]. For example, the up-conversion efficiency of the monoclinic phase of ZrO_2 NPs is higher than the tetragonal phase [173].

There are several methods for obtaining crystalline particles:

- ***Mechanical methods:*** Based on the reduction of coarse-grained materials by milling, which produces particles with the desired size. This method offers low costs but also low purity of particles [174].
- ***Chemical methods:*** Methods such as co-precipitation and ***sol-gel***, offer several advantages over mechanical methods because they allow excellent control over the particle morphology and purity [174,175] .
- ***Vapor phase methods:*** They tend to be expensive but offer many advantages, such as the ability to produce non-oxides particles and to produce nanoparticles with a diameter of less than 10 nm [33,174,176].

The sol-gel method was proposed in this thesis because it offers an excellent control over the product purity. The sol-gel reaction starts from pure materials, requires low temperatures. It is an easy processing, and the obtained particles possess a homogeneous composition [41]. The sol-gel process consists in two steps. Firstly, a sol is formed by hydrolysis. Secondly, the sol is transformed into a gel by condensation. Lastly, the gel is dried [177]. As the name implies, a sol is a colloidal suspension of solid particles, whereas a gel is an interconnected network of solid particles throughout a secondary liquid phase [41]. The sols consist of solid colloidal particles, ranging from 1 to 1000 nm in diameter, which remain suspended in the liquid because the gravitational forces are negligible due to the Brownian forces [177]. The necessary steps in the sol-gel process are summarized in Figure 2.15.

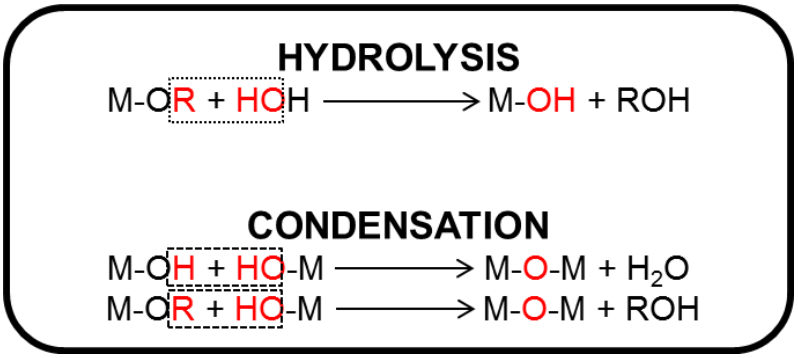

Figure 2.15 Main steps during the sol-gel process.

The precursors in the sol-gel synthesis are usually metal alkoxides $M(OR)_x$. These precursors react with water very quickly (hydrolysis step), creating metal hydroxides, water, and alcohol or organic by-products. After the hydrolysis step, the sol can react further, and the polymerization occurs (condensation step), where the metal hydroxides react to form the metal oxides. The sol and the gel formations occur at the same time. However, the gel is further strengthened by the Ostwald ripening process, and the nucleation and growth processes take place. The Ostwald ripening process is based on the growth and coarsening of big particles whereas the coexisting smaller particles are dissolved due to their higher solubility. Besides, during the gelation process, compounds such as alcohol and other organic by-products are evaporated. It can last from seconds to several weeks. When the gel is formed, it is usually amorphous, and a final calcination step is required to crystallize the sample [177].

The obtained particles depend on various parameters:

- Type(s) of alkoxide and their concentrations.
- Temperature (it affects the degree of polymerization of the gel).
- Amount of water added (It affects the degree of polymerization of the gel).
- The concentration of catalysts by altering the pH (it affects the rates of hydrolysis and condensation): a low pH favors the hydrolysis step, while a basic pH favors the condensation step. The pH also affects the isoelectric point and the stability of the sol, by changing the aggregation rate and the particle size.
- Surfactants or stabilizers: To maintain appropriate particle size and stability, surfactants are usually used for maintaining the surface tension between the particles, and thus, the particles aggregation is prevented. Examples of surfactants are Cetyltrimethylammonium bromide (CTAB), tween 80, span 80 or polyvinyl alcohol (PVA) [177].

Erbium-doped Al_2O_3 particles: Alumina (Al_2O_3) is a material frequently used as ceramic for structural applications in architecture and civil engineering, due to its excellent mechanical hardness [178]. Besides, this material has been used as a RE ions host, in particular of Er^{3+} ions, for waveguide applications [179]. Alumina has been chosen, in this study, as host of Er^{3+} ions due to the high solubilization of RE ions in a well-dispersed state. The high solubility of Er^{3+} ions in Al_2O_3 results from the valence match between the Er^{3+} and Al^{3+} ions. The Er^{3+} ions can substitute the Al^{3+} ions that occupy the octahedral sites of the lattice. Besides, as one-third of the matrix is unoccupied, various Er^{3+} ions can be easily incorporated without quenching the luminescence [180]. Besides, it has a phonon energy of 870 cm^{-1}, which makes the Er^{3+}-doped Al_2O_3 suitable for optical applications [181].

The only thermodynamically stable phase is the α-Al_2O_3 (corundum). The corundum unit cell is shown in Figure 2.16 [33]. Apart from the corundum phase, there also exist other metastable phases, denoted as χ, γ, η, θ, δ and κ. All these metastable phases have a partially deformed hexagonal oxygen sub-lattice with interstitial aluminum atoms. The crystalline structure of ***Al_2O_3 corundum*** is hexagonal. In this phase, the Al^{3+} ions occupy two thirds of the interstices to balance the charge of the structure.

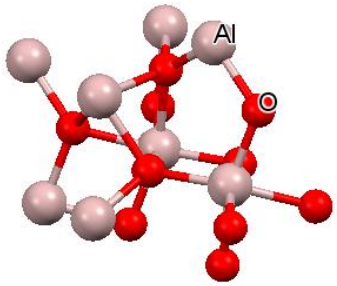

Figure 2.16 Corundum crystal phase of Al_2O_3. Picture generated by Mercury software [182].

Some properties of α-Al_2O_3 single crystal are the following:

- Melting point = 2053 °C
- Coefficient of Thermal Expansion (CTE) (25–1000 °C) = $8.8 \cdot 10^{-6}$ K^{-1} - $7.9 \cdot 10^{-6}$ K^{-1}
- Density = 3.98 g/cm^3

Sub-micrometer sized α-Al_2O_3 crystals have been shown to have higher mechanical strength [183,184] and hardness [185] than the coarser-grained Al_2O_3 crystals Thus, recent efforts have been aimed at reducing the particle size of α-Al_2O_3 [186]. Besides, with the incorporation of Er^{3+} ions, the phases in the Al_2O_3 structure may change to other crystalline phases such as erbium ***aluminum garnet ($Er_3Al_5O_{12}$)*** or ***perovskite ($ErAlO_3$)*** compounds [187,188]. Interestingly, the $Er_3Al_5O_{12}$ powder has been shown to emit strong up-conversion luminescence when pumped at 980 nm, and it seems to be an excellent up-converter phosphor

[189]. As it can be seen from Figure 2.17, it has a very complex and flexible crystalline structure.

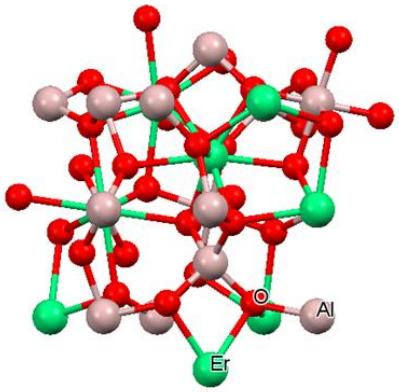

Figure 2.17 Er^{3+}-doped aluminum garnet ($Al_5Er_3O_{12}$) crystal phase. Picture generated by Mercury software [182].

The preparation of alumina particles is achieved by high-temperature flame synthesis, chemical synthesis (e.g., sol-gel), or mechanical processes (e.g., high-energy milling) [178]. The chemical methods require low or medium temperatures. The typical precursors include aluminum nitrate and aluminum hydroxides. Hydrothermal conditions are often applied [190], but colloidal methods, such as sol-gel, have been extensively studied over the past decades [191–193]. Lastly, in the case of Er^{3+}-doped Al_2O_3 synthesized by sol-gel, reported values of optimum concentration of Er^{3+} ions ranged from 0.5 and 1 mol% [194,195]. When annealed at 950°C (or at 1000°C in the case of sol-gel Er^{3+}-doped Al_2O_3 [195]), the Er^{3+} ions start to precipitate into colloids or another oxide phase such as Er_2O_3, which decreases the emission intensities [196].

In this thesis, Al_2O_3 particles doped with 1 and 7 mol% of Er_2O_3 were prepared by sol-gel with a further calcination step at 1300°C for 5 hours.

Erbium-doped TiO_2 particles: Nowadays, titania (TiO_2) is receiving great attention for its biomedical, photocatalytic and optical applications, due to its semiconductor behavior, biocompatibility, high chemical stability, and easy and low-cost production [197–199]. TiO_2 can acquire or improve its properties with the addition of dopants such as Er^{3+} ions. TiO_2 is an attractive host for the Er^{3+} ions due to its low phonon energy (< 700 cm^{-1}), which reduces the multiphonon relaxation [200]. Indeed, TiO_2 anatase phase has a phonon energy of 639 cm^{-1} [201]. The luminescence from the Er^{3+} ions at 1540 nm makes the Er^{3+}-doped TiO_2 a suitable material for optical devices such as optical planar waveguides [201,202]. Due to its up-conversion properties [203,204], the red/green up-conversion emissions enables the Er^{3+}-doped TiO_2 for an even broader range of applications such as display technologies, photovoltaics, medical diagnostics and solid-state lasers [106,205–207].

The titanium oxide can exist in three main phases: rutile, anatase, and brookite. The majority of the research of Er^{3+}-doped TiO_2 is based on the anatase and rutile phases, which are known to improve the luminescence properties and optical applications [201,202,208–210]. The phase stability depends on the particle size: rutile is the most thermodynamically stable phase when the particle size is larger than 14 nm, while anatase is the most stable phase when the particle size is smaller than 14 nm [211]. Besides, when the titania is obtained by sol-gel, anatase is usually the thermodynamically stable phase [212]. The rutile, anatase, and brookite crystalline structures consist of octahedral oxygens with Ti^{4+} cations located in the center.

- The ***rutile*** phase has a tetragonal symmetry with several octahedral units linked one with each other to give chains located along the z-axis. The cell unit consists of an octahedron with eight corners, which two of them are sharing an apex. As seen from Figure 2.18a, each O^{2-} is surrounded by three Ti^{4+}, and each Ti^{4+} is surrounded by six O^{2-}.

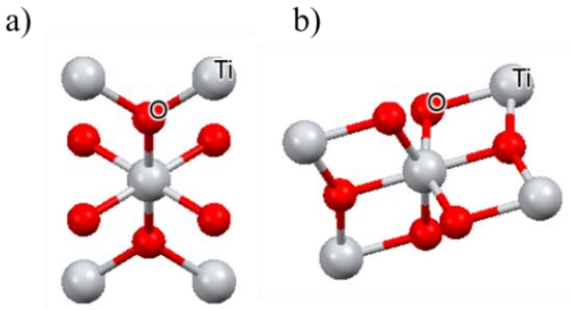

Figure 2.18 (a) Rutile and (b) anatase crystalline unit cells of TiO_2. Picture generated by Mercury software [182].

- The structure of the ***anatase*** phase is like the rutile phase, tetragonal. However, the octahedra are distorted by linking four of their corners with other octahedra (see Figure 2.18b).
- The structure of the ***brookite*** phase is even more distorted, due to the linking of the octahedra by all of their edges and corners. Therefore, the conversion rutile-anatase-brookite is expected to lower the symmetry of the crystalline environment [33].

Furthermore, by increasing the Er^{3+} doping concentration, other phases such as the ***pyrochlore*** ($Er_2Ti_2O_7$) may appear (see Figure 2.19) [213].

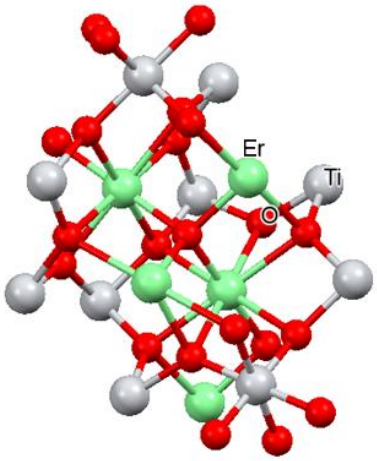

Figure 2.19 Er^{3+}-doped titanium pyrochlore ($Er_2Ti_2O_7$) crystal phase. Picture generated by Mercury software [182].

The pyrochlore or $Er_2Ti_2O_7$ presents a cubic crystalline structure formed by six Ti—O_2 and two Er—O bonds in a distorted octahedron. A more detailed study using X-ray and neutron diffraction can be found in [214].

Among the different synthesis methods employed for the production of TiO_2 particles, the sol-gel method has been demonstrated to control more accurately the particle size and the morphology [215,216]. The anatase to rutile transition may occur from 600 to 1100°C [217,218] while the presence of the compound $Er_2Ti_2O_7$ is predominant at very high temperatures (800-1000°C) [201,219]. This compound has been reported to possess very short lifetimes (<1 ms), which have been explained by the quenching concentration of Er^{3+} ions [220]. For samples heat treated at less than 600 °C, the luminescence is quenched by only water [212]. At a heat treatment of 800 °C or higher, the quenching can be explained by the different phases and concentration of Er^{3+} in the TiO_2 matrix [220].

In this thesis, we report on the synthesis by sol-gel of different TiO_2 particles doped with different concentrations of Er_2O_3 (0, 0.5, 2, 5, 14.3 mol%). To minimize the water quenching effect, the particles were calcined at temperatures higher than 700°C.

Erbium-doped ZnO particles: Zinc oxide (ZnO) is known for its use in applications such as photocatalysis, optoelectronics, piezoelectrics, gas sensing, solar cells and other luminescent devices [221]. Additionally, ZnO particles possess a therapeutic function, as they have shown to exhibit strong protein adhesion to cellular surface receptors, which can be exploited to modulate the cytotoxicity, metabolism or other cellular responses [95,96]. ZnO can also act as potential anticancer agent in the treatment of cancers [41]. The presence of chemical groups on the surface of the ZnO particles, such as $–ZnOH_2^+$, –ZnOH or $–ZnO^-$, is pH dependent [222], which allows the functionalization with antibodies, drugs, proteins or other biomolecules [223–226]. As an example, the addition of folate

groups to the ZnO particles enables the preferential localization toward cancerous cells with high amount of folate receptors [226].

Due to the large band gap and low phonon energy (550 cm^{-1}), RE-doped ZnO is also an excellent semiconductor material with good electromechanical and optical properties, which can be used in applications such as light emitting diodes (LEDs) and lasers [227][228]. Besides, when ZnO is doped with Er^{3+}, these materials can be used for the development of optical waveguide amplifiers, laser diodes and light emitting diodes (LEDs) [229,230].

The crystalline structures of the ZnO are *rocksalt*, *zinc blende*, and *wurtzite*, which are represented in Figure 2.20.

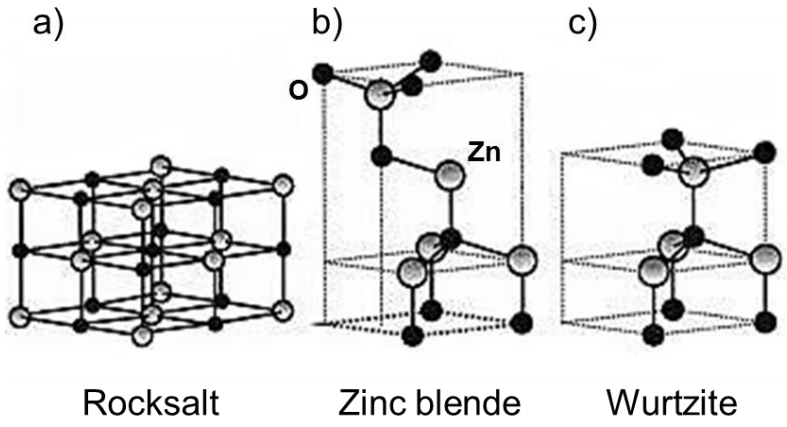

Figure 2.20 Representation of ZnO crystalline structures: (a) cubic rocksalt, (b) cubic zinc blende, and (c) hexagonal wurtzite. The white and black spheres denote Zn and O atoms, respectively. Figure modified from [221].

Zinc blende or ***hexagonal wurtzite*** phases have each anion surrounded by four cations at the corners of the tetrahedron, and vice versa. The ***rocksalt*** phase may be obtained at relatively high pressures. At room temperature, the thermodynamically stable phase is the ***wurtzite*** phase, whereas few reports on the zinc blende phase are reported [221]. Interestingly, the green up-conversion of Er^{3+}-doped ZnO particles with wurzite phase are enhanced by a calcination treatment due to the variation of the local structure around the Er^{3+} ions [231–233].

In this thesis, Er^{3+}-doped ZnO particles with 1 and 14.3 mol% of Er_2O_3 were synthesized by the sol-gel technique and were further calcined at 1000°C for 2 hours.

Erbium-doped ZnO_2 particles: Zirconia (ZrO_2) is a material with very high strength and toughness, low wear resistance, high elastic modulus, ionic conductivity, chemical inertness, low thermal conductivity, high coefficient of thermal expansion and high melting temperature (2706 °C) [234–236]. These properties make it an attractive material for applications such as sensors, catalysts,

thermal barrier material, corrosive coating and dental ceramics [237–239]. Besides, it has a phonon energy of 470 cm^{-1} [181].

ZrO_2 has three main phases: monoclinic, tetragonal and cubic. Usually, the ***monoclinic*** phase is present at room temperature, which transforms into the other phases by increasing the temperature. The monoclinic phase is present up to 1170°C, the ***tetragonal*** (metastable) phase is present up to 2370 °C and the ***cubic*** phase up to the melting temperature, at 2706 °C [181,240]. The crystalline structure of the three phases is represented in Figure 2.21.

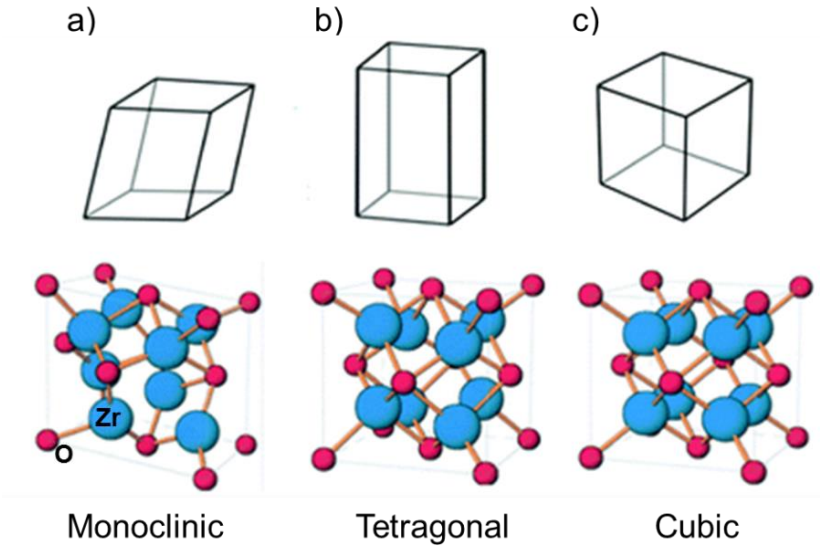

Figure 2.21 Crystalline phases of ZrO_2. Figure modified from [241].

In the monoclinic phase, the Zr^{4+} ions have a coordination number of seven, and the oxygen ions occupy the tetrahedral interstices. In the tetragonal phase, the Zr^{4+} ions have a coordination number of eight and the crystalline structure has a form of a straight prism, with rectangular sides. Lastly, the cubic ZrO_2 has a structure of a simple cubic lattice with eight oxygen ions, which occupy the tetrahedral interstices [241,242].

Although the monoclinic ZrO_2 is usually found at room temperature, the metastable tetragonal phase can also be stabilized at low temperatures by the surface energy of the small crystallites [240]. The crystallite size effect is present with a crystal size of particle lower than 30 nm, with bigger crystal sizes, the metastable tetragonal phase cannot appear at room temperature [243]. Additionally, this effect can be also observed with the addition of dopants such as Er^{3+}, Ca^{2+} or Y^{3+} cations [173,240,244,245].

RE-doped ZrO_2 particles can be exploited for phosphor devices or biological sensing [246]. Interestingly, it has been reported that Er^{3+}-doped ZrO_2 particles possess a strong green up-conversion emission, making them promising materials for solid-state illumination and optoelectronic devices [247–249]. However, it has been reported that the optimal doping concentration of Er^{3+} is at 1 mol%, since beyond that concentration the quenching effect was seen to occur [248].

In this thesis, Er^{3+}-doped ZrO_2 particles with 1 and 14.3 mol% of Er_2O_3 were synthesized by sol-gel and calcined at 1000°C for 2 hours.

2.4 Optical fibers

This section of the chapter starts with an introduction to the optical fibers, where the basics on the structure and the primary mechanisms of light transmission through the fibers are introduced. Subsequently, Er^{3+}-doped phosphate fibers, which are the subject of this thesis, are reviewed. Lastly, the different applications of optical fibers, especially in biomedicine, are discussed.

2.4.1 Introduction to optical fibers

The discovery of the laser in 1960 [250], the amplifier in 1964 [251], and the first silica-based optical fiber in 1966 [252], led to the rapid growth of reliable components for the telecommunication sector. Later, the development of Er^{3+}-doped fiber amplifier (EDFA) in 1987 [253,254], combined with the use of commercial silica fibers with low attenuation loss enabled the so-called "telecom revolution" [255].

These applications are based on the transmission of light along the optical fibers by the principle of total internal reflection (TIR). The typical structure of an optical fiber is shown in Figure 2.22. An optical fiber is a cylindrical optical waveguide made of cladding with a refractive index n_2 lower than the refractive index n_1 of the central core. Additionally, the cladding can be coated by a suitable polymeric thin film to protect the fiber from mechanical and chemical damage [256].

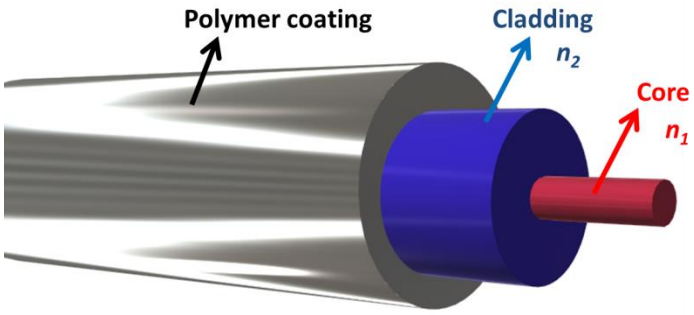

Figure 2.22 Structure of a core-cladding optical fiber.

When a light ray is transmitted along the axis of an optical fiber, the light at the interface between the core and the cladding is mainly reflected into the core by the TIR, and part of it may be refracted. The reflected light ray has an incident angle (θ_1) equal to the angle of reflection (θ_1), while the refracted angle (θ_2) is calculated by the **Snell's law**:

$$n_1 \sin\theta_1 = n_2 \sin\theta_2 \quad (2.6)$$

The optical fibers can be multimode or single-mode. In the single-mode fibers the light has only one path or mode of travelling inside the fiber core. A typical single-mode silica fiber used in telecommunication has a core diameter of ~8-10 μm and a cladding diameter of ~125 μm. Instead, the core diameter of a multimode fiber is higher, around ~25-60 μm, allowing the light to travel through several propagation ways or modes. The **number of propagating modes, *m,*** which a multimode fiber can propagate, can be estimated using the following equation:

$$m = \left(\frac{NA \cdot d}{\lambda}\right)^2 \quad (2.7)$$

Where *d* is the diameter of the core, λ is the wavelength of the transmitted light, and *NA* is the **numerical aperture**, which is calculated as follows:

$$NA = \sqrt{n_1^2 - n_2^2} \quad (2.8)$$

The **attenuation of a fiber** is the measurement of the optical loss of a fiber. It can be calculated by the following equation:

$$\alpha_{dB} = \frac{1}{L} \cdot 10 \cdot Log\left(\frac{P_{in}}{P_{out}}\right) \quad (2.9)$$

Where the length of the fiber is *L*, the input power is P_{in} and the output power P_{out}. The attenuation of a fiber is measured in dB/m and is the result of light absorption, Rayleigh scattering and bending losses [32].

Losses due to absorption: The absorption is the primary cause of attenuation loss in an optical fiber. The light can be absorbed by impurities such as OH groups, trace metals or imperfections and cause a reduction of the optical power due to the conversion in thermal energy [32]. In optical fibers, the water impurities should be lower than few ppb. The OH groups enter in the structure by thermal diffusion, contaminated reagents, or by the interaction of the melting glass batch with the environment [257]. The OH groups lead to significant losses at 1380 nm. Besides, the stretching vibration of OH can be located between 2.7 and 3 μm depending on the glass composition. For instance, in the silica glasses, water reacts with silica and produces Si-OH bonds, which absorb at 2.7 μm. The harmonics or overtones of the absorption at 2.7 μm are responsible for the losses at the operating region of the optical fibers (1383 nm, 1250 nm, and 950 nm) [258]. Similarly, trace metals can absorb at their own particular wavelengths and produce an attenuation loss of the fiber [32].

Losses due to scattering: The *Rayleigh scattering* is produced due to the small variations in the refractive index along the optical fiber. These changes are caused by particles or fluctuations of the density and composition of the glasses. The light

that travels interacts with these areas and is partially scattered [32]. The intensity of the Rayleigh scattering is given by the following equation:

$$\boldsymbol{I = I_0 \left(\frac{1 + \cos^2 \theta}{2R^2} \right) \left(\frac{2\pi}{\lambda} \right)^4 \left(\frac{n^2 - 1}{n^2 + 2} \right)^2 \left(\frac{d}{2} \right)^6} \quad (2.10)$$

Where θ is the scattering angle, R is the distance to the defect, n is the refractive index, and d is the diameter of the particle or fluctuation.

The Rayleigh scattering depends on the size of these compositional fluctuations. It occurs when the size of the fluctuations is lower than 1/10 of the wavelength (λ) of the propagated light. Besides, it is inversely proportional to the four power of λ, being the shortest λ the most influenced by the scattering [259]. Another Scattering effect is the so-called *Mie scattering*, which is produced when the size of the compositional fluctuations is similar to λ. This scattering is less λ dependent than the Rayleigh scattering. However, as opposed to the Rayleigh scattering which is an intrinsic property for all the fibers, the Mie scattering can be easily neglected by the high-quality fabrication of the commercial fibers [258].

Losses due to bending losses: The bending losses can be divided into *micro-bends* or *macro-bends* depending on the radius of curvature of the bending. Both can be produced by external mechanical forces.

Micro-bends are small microscopic bends due to imperfections or discontinuities along the fiber. They are commonly present when a fiber is coated or cabled. Instead, *macro-bends* appear when the bends have a considerable radius of curvature compared to the fiber diameter. Indeed, when the radius is less than few centimeters, the macro-bending losses can cause massive losses.

In a fiber bend, the light that propagates at the internal side of the bend travels a shorter distance than that on the external side. This creates additional modes or path of light, which are lost and radiated out of the fiber. The sensitivity to bending of fiber decreases with an increase of the refractive index of the core and also with an increase in the fiber diameter. However, an increase in the core diameter increases the sensitivity to bending, as a large core can propagate more modes which tend to lose more light [32].

The typical attenuation spectrum of a commercial silica fiber is shown in Figure 2.23.

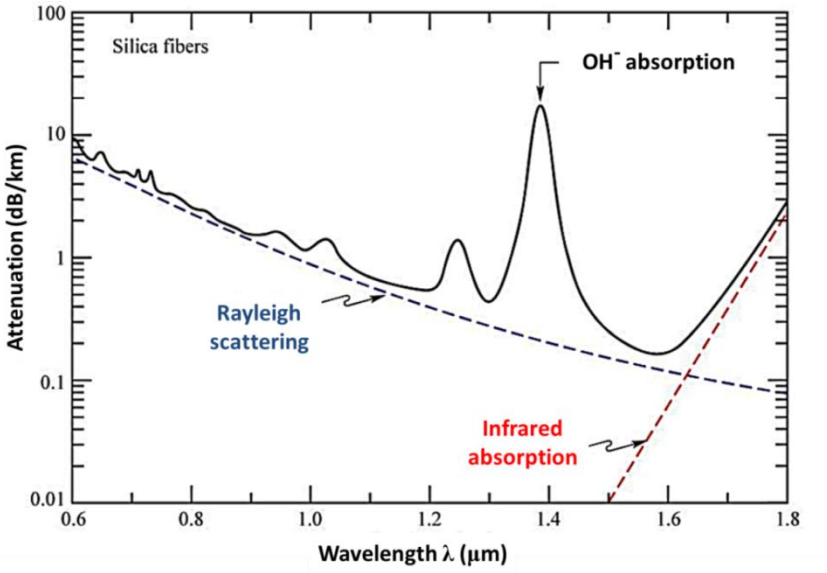

Figure 2.23 Attenuation spectrum of silica optical fiber (solid line), and theoretical limits (dashed lines) in the near IR region (Graph taken from [260]).

At wavelengths lower than 1550 nm the attenuation loss is mainly due to Rayleigh scattering, while at longer wavelengths the attenuation is due to the absorption of molecular vibrations of the silica glass network. The spectrum shows a peak at 1380 nm due to the absorption of the vibrational modes of OH groups. The transparency window of silica glasses is limited to ~ 2 μm, whereas it is shifted to longer wavelengths in chalcogenide or fluoride glasses.

Due to the combined effect of the Rayleigh scattering and the absorption losses, the attenuation loss spectrum of silica fiber has a low loss window at around 1500 nm, which coincides with the signal at 1535 nm of the Er^{3+} ions. Thus, the Er^{3+} ions are the main rare earth ions of choice for the optical fiber amplifiers and lasers for telecommunications [260].

2.4.2 Preform fabrication and drawing

There are several methods to produce optical fibers. They can be divided into direct fiber methods, which do not need a previous preform fabrication, and the methods based on preform drawing, which require and intermediate step of preform fabrication.

Direct drawing methods

The ***double crucible method*** (Figure 2.24) consists in simultaneously pulling down the molten core glass and molten cladding glass from a concentric reservoir. This method is rarely used, as many contaminants are usually generated from the crucible. This method is generally only used for soft optical fibers or for optical fibers that do not require a very high quality.

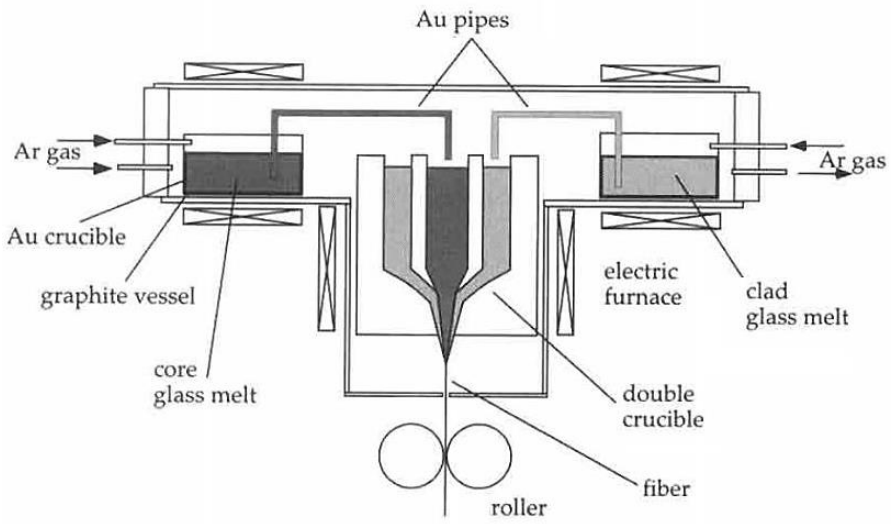

Figure 2.24 Double crucible method. Picture taken from [261].

A similar process is the ***extrusion method***, which is usually employed for making fibers made of plastic. Here, the core melt is pressed into the cladding melt while both are heated until the softening temperature is reached [262].

Preform drawing methods

Regarding the methods based on preform fabrication, different preform fabrication techniques with or without vapor deposition are employed:

- ***Modified Chemical Vapor Deposition (MCVD)*** (Figure 2.25): This method was developed in the 70s to produce telecom silica fibers. A hollow silica glass tube is placed horizontally and rotated slowly while a mixture of oxygen, $SiCl_4$, $GeCl_4$ or other reagents are injected inside the rotating tube. The temperature is increased by a hydrogen burner up to 1900°C. Chemical reactions between the tetrachloride and oxygen produce SiO_2 or GeO_2, which coat the inner surface of the glass tube. The torch is continuously moved along the tube to deposit the material. The process is repeated until a sufficient thick layer is achieved. Towards the end of the process, the composition of the layer is changed to form a layer with higher refractive index (the fiber core), resulting in a fiber with a controlled refractive index profile [263].

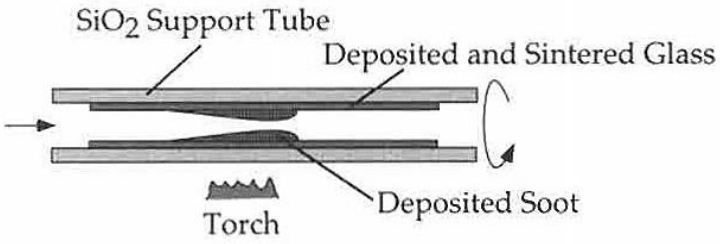

Figure 2.25 Modified Chemical Vapor Deposition method. Picture taken from [261].

- ***Outside Vapor Deposition (OVD) or vapor axial deposition*** (Figure 2.26): In this method, the silica soot is deposited onto the external surface of a solid rod made of a refractory material such as graphite or Al_2O_3. The glass is formed by flame hydrolysis of methane or hydrogen with the corresponding precursors, such as $GeCl_4$ or $SiCl_4$. At the end of the process, the solid rod is removed, and the fabricated preform is further processed in a furnace in Cl_2 and He gas flow at high temperature to remove the hydroxyl groups [261,264].

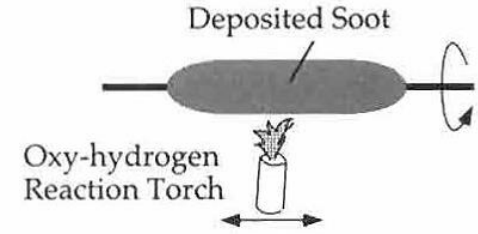

Figure 2.26 Outside Vapor Deposition method. Picture taken from [261].

- ***Vapor Phase Axial Deposition (VAD)*** (Figure 2.27): Contrary to the OVD and MCVD methods, the preform growth in the VAD is axial, and the preform is gradually extracted from the deposition chamber. Interestingly, this method allows the fabrication of very long preforms [261].

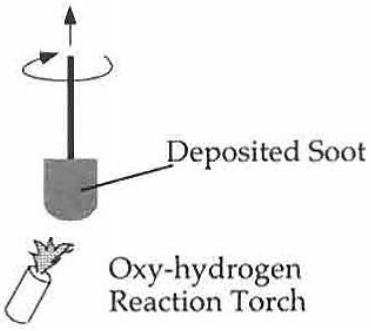

Figure 2.27 Vapor Phase Axial Deposition method. Picture taken from [261].

- ***Plasma Chemical Vapor Deposition (PCVD):*** The deposition is done in a similar way as in the MCVD. However, a microwave cavity resonator heats up the deposition region, and the deposition is done at a low speed but in a very controlled manner. Another analogous technique is the ***Plasma-Enhanced Chemical Vapor Deposition (PECVD)***, where the deposition rate is higher [265].

By using vapor deposition methods, the resulting propagation losses of the fibers are very low (<0.2 dB/km), and the contamination is almost null. The high quality is achieved due to the use of high purity precursors and the negligible water content in the fibers, as no hydrogen is present during the process. The incorporation of RE ions into the preforms by vapor deposition methods is challenging, as their precursors are not very volatile. Therefore, ***solution doping*** of RE chloride precursors in vapor deposition methods is usually proposed. Here, a porous silica frit is inserted into the hollow silica tube, and then it is soaked with the RE precursors solution [266].

- ***Rod in tube technique:*** In this technique, the cladding is a hollow tube and the core is a glass cylinder, both with similar chemical and physical properties. The core is stretched into a cane, inserted into the cladding tube and these are drawn inside a drawing tower. In order to obtain high quality fibers without bubbles or other defects, the core/clad interface must be carefully cleaned before the drawing process [26].

Once the preforms have been obtained, the drawing of the preforms is carried out. During the drawing, large diameter glass rod preforms are pulled down to form thin optical fibers. The reduction in the preform diameter down to that of the fiber is achieved by heating up the preform above its softening temperature. This method is usually employed for processing most of the optical fibers.

In this thesis, a multi-mode core/cladding Er^{3+}-doped optical fiber was fabricated by the rod-in-tube technique and by preform drawing. A detailed description of the rod-in-tube technique and the drawing equipment used in this thesis will be given in Chapter 3.

2.4.3 Er^{3+}-doped optical phosphate fibers and their applications

The discovery of lasers and their coupling with optical fibers attracted much interest in many fields e.g. new medical procedures of surgery, diagnostics, therapy, sensing and monitoring [267]. Er^{3+}-doped fiber lasers operate in an “eye-safe” wavelength region above 1.4 μm due to the absorption of the light by the eye's lens and cornea, so the light cannot reach and damage the more sensitive retina. Thus, the light scattered from the dust particles or the target itself cannot damage the

human eyes [268]. The Er^{3+}-doped fiber lasers can also interact with biological tissues. In this case, tissue components such as water, bone, veins, melanin or the epidermis have different absorption and refractive index, which causes absorption and scattering of the light, respectively. Therefore, the depth penetration tissue of light is usually in the range of a few millimeters [269,270].

Silica glasses are ideal materials for the development of fiber amplifiers as they have outstanding thermos mechanical properties, low propagation losses and transparency in the infrared region. However, due to the network structure of SiO_2, it is difficult to introduce a high concentration of Er^{3+} without clustering [271,272]. Moreover, silica glasses possess high melting temperatures, which make them difficult to draw into fibers using conventional heating systems, and specific equipment is required. As a solution, metal oxides such as Na_2O or CaO are usually added to lower the melting temperature. However, these components may increase the crystallization tendency decreasing their bioactivity [99]. In the field of telecommunications, despite the success of the EDFAs, a new generation of optical fibers is needed in order to overcome some of the limitations of the silica fiber such as gain bandwidth, luminescence efficiency, non-linearity, etc. For example, optical fibers containing nanoparticles in the core, or new optical fibers with different hosts and RE ions operating at around 1.4 μm have driven much of the research in the last decades [273–282].

Phosphate glasses with P_2O_5 concentrations higher than 45 mol % are easily drawn into fibers [8,21,22]. During the fiber drawing process, the PO_4 tetrahedra chains are parallel to the fiber axis, enabling the formation of continuous filaments as opposed to clusters [99]. Phosphate glass fibers are characterized by their good transparency in the UV-Visible/Near-infrared (UV-Vis/NIR) region, low intrinsic attenuation loss, refractive index suitable for splicing to commercial silica fibers and low-cost processing [17,19,23]. In addition, the phosphate glasses possess a high solubility of RE ions allowing high emission cross-sections and lifetime values, as well as high chemical stability and high optical damage threshold [131]. Moreover, phosphate fibers have shown excellent mechanical properties. For instance, phosphate fibers with a tensile modulus of 74 GPa [283] and tensile strength of 1.2 GPa [22] have been achieved. By adding different dopants such as silver, titanium, zinc, iron or strontium, the glasses can induce specific biological responses and enhance biocompatibility [8,77,284].

Phosphate glass fiber lasers demonstrated high output power and high-quality beam in a compact size devices [27,131]. For instance, Qui *et al.* reported an Er^{3+}-Yb^{3+} co-doped multimode high power fiber laser with an output power of 9.3W operating at 1535 μm [285]. Furthermore, as mentioned before, optical fibers containing RE-doped nanoparticles can enhance the luminescence efficiency [281,286]. The demand on glass fibers for biophotonics and biomedical applications has increased in the last two decades [267].

- *For hard and soft tissue regeneration*: Phosphate fibers can be used as "cargo" of cells, antimicrobial agents, proteins, enzymes or drugs. For example, they can deliver periodontal cells and heal the periodontitis [287]. Phosphate glass fibers can also be used as a template for the cells growth. For instance, C. Vitale-Brovarone *et al.* produced Ti-doped phosphate fibers which guided the neuronal cell growth along the nerves (See Figure 2.28a) [21,25]. Similarly, I. Ahmed *et al.* developed Fe-doped phosphate fibers that guided the formation of muscle precursor cells and myotubes (See Figure 2.28b) [8,80].

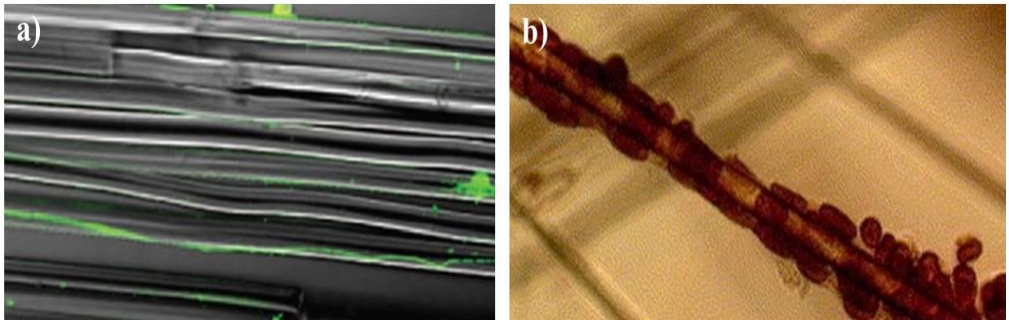

Figure 2.28 Ti-doped phosphate fibers with neuronal cell growth (a) and Fe-doped phosphate glass fibers with muscle cell growth (b). Adapted from [25] and [80], respectively.

The phosphate fibers are bonded together by thermal treatment and create scaffolds with porosity and mechanical properties similar to human bones [288–290]. A scaffold can be defined as a biomaterial that allows the cell attachment and tissue regeneration. The sintering step of these scaffolds generally causes glass crystallization, which makes them brittle, thus limiting their medical applications. However, phosphate glasses possess a large sintering window (range between T_g and T_x), preventing them from crystallization and making them suitable for scaffolds [291]. The possibility of these scaffolds to be used as "in situ" drug delivery system seems to be very promising and could be further exploited. Moreover, phosphate fibers can be doped with antimicrobial elements such as Ag^{+}, Cu^{2+} or Ga^{3+}, and be arranged in a mesh form to cover surgical wounds, burns or ulcers [292–294].

- *As imaging, photodynamic therapy (PDT), spectroscopy endoscopy, optogenetics and biosensing*, which require the delivery of light in specific deep tissue areas without damaging the surrounding organs [295]. The advantages of these lasers is that the light transmission is delivered directly at the skin or internal treatment area, such as the intestine, lungs, urinary bladder, esophagus, stomach, etc. For instance, the PDT consists of launching light to a light-sensitive drug previously incorporated in tumor cells or other targets. Thus, the light is absorbed by the tumor and results in the release of singlet oxygens, which causes the apoptosis of the malignant cells or bacteria. The PDT has usually been used for the cancer treatment, arteriosclerosis or age-related macular degeneration [296–298].

Additionally, optical fiber lasers can be used for photorejuvenation or resurfacing for the treatment of dermatological pathologies such as skin atrophy, acne, scars, vascular lesions, unwanted hair or wrinkle removal. The light pulses enable the removal of skin areas by controlling the wound formation while the creation of new cells is stimulated [299]. Examples of lasers typically used for this therapy are the CO_2 laser, which emits at 10.6 μm, or the Er:YAG laser, emitting at 2940 nm. Besides, the 1550 nm Er^{3+}-doped optical fiber lasers are also used for photorejuvenation or resurfacing therapy [267,300]. Another application of the optical fibers lasers is the optogenetic therapy, where light stimuli are launched at deep areas ofthe brain to activate specific neurons [301]. Similarly, time-domain diffuse optics is an alternative technique to study highly scattering tissues for applications such as functional brain imaging, mammography, oximetry or monitoring of neoadjuvant chemotherapy [302].

- *For Fiber Bragg Grating (FBG) fabrication* [303–305]: A FBG optical fiber has the ability to monitor the patient changes of pressure such as respiratory rates, articular joint pressure or pressure of the esophagus or intestines [306,307]. This technology has been implemented in smart-bed healthcare monitoring system [308,309]. Besides, FBG optical fibers are able to detect DNA [310] or to measure the mechanical strain in bones [311]. Interestingly, Pugliese *et al.* reported a biodegradable phosphate-based optical FBG fiber able to track the degradation of the fiber, as well as the pH and temperature of the medium [303]. Thus, it is foreseen an increase in the use of FBG optical fibers for diagnostic and monitoring in vivo applications.
- *For long-term monitoring and sensing, as well as continuous light delivery to deep tissues is possible*: The demand for biodegradable materials has led to the development of biodegradable fibers and waveguides made of glass, polymers and silk-based materials [312–314]. However, phosphate optical fibers offer better mechanical flexibility, controllable dissolution rate and low attenuation loss [23]. These fibers may be left inside the human body for short or long periods of time, enabling continuous sensing and imaging of deep areas, beyond the superficial skin. The idea of tracking the bio-response of a fiber "in vivo" was proposed by Massera *et al.* in 2014 [315].

In this work, a bioactive fiber sensor able to monitor its degradation and bio-response with a molar composition of $50P_2O_5$-40CaO-$10Na_2O$ (in mol%) was reported. Part of the fiber was immersed in SBF and tris(hydroxymethyl) aminomethane (TRIS) solutions and the in vitro reactivity and optical properties were measured as a function of immersion time. Based on the amount of optical transmission of light through the fiber, the different stages of formation of hydroxyapatite layer were monitored. Despite these attractive features, only few studies on the development of optical fibers that combine good optical and biological properties have been made [29,315].

To the best of our knowledge, the light transmission through an active Er^{3+}-doped fiber sensor has never been studied to monitor the glass bio-response in aqueous media. Therefore, the aim of this thesis is to produce a biodegradable or bioactive optical fiber which can be resorbed or lead to new soft tissue once the therapeutic or sensing utility has been accomplished. In this way, the surgical removal of the fiber sensor is not needed.

Chapter 3

Materials and methods

Part of the work described in this chapter has been previously published in [35, 105, 374]. This chapter focuses on the synthesis of Er^{3+}-doped phosphate glasses, glass-ceramics, and particles containing glasses. Additionally, the different methods used in this thesis to synthesize Er^{3+}-doped Al_2O_3, TiO_2, ZnO and ZrO_2 particles are presented. Moreover, the fabrication and processing of the optical fiber is discussed. Lastly, the characterization techniques used to assess the morphological, physical, structural and optical properties of the samples are described.

3.1 Materials fabrication and processing

3.1.1 Glasses

In this thesis, several Er^{3+}-doped phosphate glasses in the system P_2O_5–SrO–Na_2O were fabricated by the conventional melt-quenching technique. In order to optimize their luminescence properties, the addition of different metal oxides was studied. The composition of the investigated glasses is shown in Table 3.1.

Code	Al_2O_3 (mol%)	TiO_2 (mol%)	ZnO (mol%)	Er_2O_3 (mol%)	P_2O_5 (mol%)	SrO (mol%)	Na_2O (mol%)
RefG				0.25	49.88	39.90	9.98
AlG	1.50			0.25	49.25	39.40	9.85
TiG		1.50		0.25	49.25	39.40	9.85
ZnG			1.50	0.25	49.25	39.40	9.85

Table 3.1 Composition of the investigated glasses.

The glasses were synthesized using $Sr(PO_3)_2$, $NaPO_3$ (Alfa Aesar), Er_2O_3 (MV Laboratories Inc., 99.999%), Al_2O_3 (Sigma-Aldrich, ≥99.5% α-phase), TiO_2 (Sigma-Aldrich, 99.99% rutile) and ZnO (Sigma-Aldrich, ≥99%). The $Sr(PO_3)_2$ was independently prepared using $SrCO_3$ (Sigma-Aldrich, ≥99.9%) and $(NH_4)_2HPO_4$ (Sigma-Aldrich, ≥99.99%) as raw materials. For obtaining 30 grams of $Sr(PO_3)_2$, 18,04 g of $SrCO_3$ and 32.27 g of $(NH_4)_2HPO_4$ were mixed and ground in an alumina crucible. Subsequently, the crucible was heated up to 250 °C for 12 h, 650 °C for 12 h, and 850 °C for 12 h, with a heating rate of 1°C/min. Thus, the following reaction is optimized:

$$SrCO_3 + 2(NH_4)_2HPO_4 \rightarrow Sr(PO_3)_2 + 4NH_3 + 3H_2O + CO_2 \quad (3.1)$$

The reagents were ground and mixed to prepare 40 g batches, then placed into a quartz crucible and heated up to 1100 °C for 30 min with a heating rate of 10 °C/min. The quartz crucible was chosen due to its inertness and low reactivity behavior [316,317]. After melting, the melt was poured into a preheated brass mold and annealed at 400 °C for 5 h to release the residual internal stress. Finally, the glasses were cooled down to the ambient temperature. A representation of the procedure followed is shown in Figure 3.1.

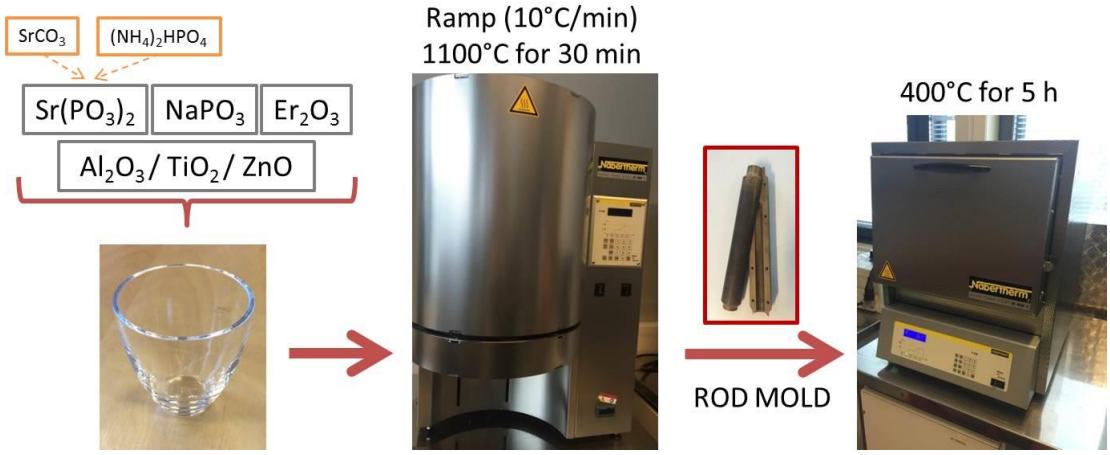

Figure 3.1 Glass fabrication carried out at Tampere University, Finland

After annealing, the glasses were cut and optically polished or ground, depending on the characterization technique. A precision cutter Brillant 220 (Germany) equipped with a diamond coated disc blade was used to prepare the disks. The polishing was made by using a LaboPol-2 machine and polyurethane plates with 1 μm diamond paste.

3.1.2 Glass-ceramics

The GCs were synthesized from the aforementioned glasses by growing in-situ the crystals in the glass matrix. The AlG, TiG and ZnG were cut into disks of 10 mm width and 5 mm thickness and were post heat treated with a heating ramp of 20 °C/min at T_g + 20 °C for 17 h to form nuclei and at T_p - 40 °C from 1 to 12 h to grow the nuclei into the crystals. A schematic representation of the process is shown in Figure 3.2.

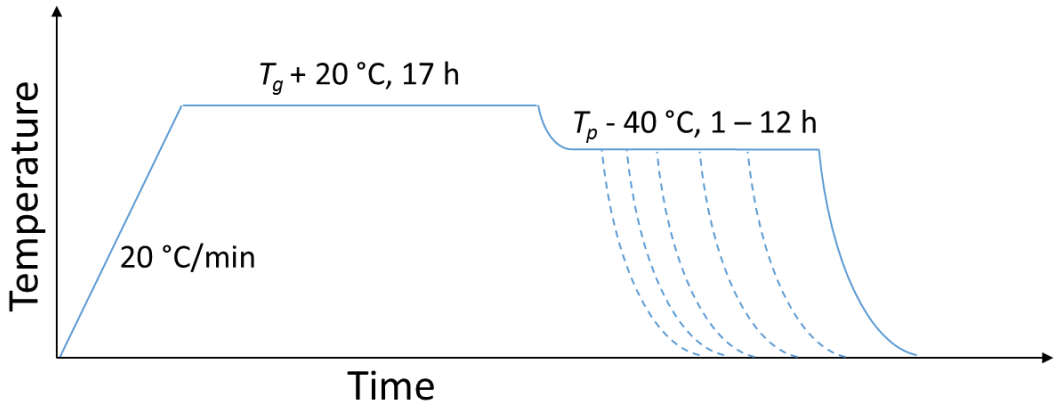

Figure 3.2 Schematic representation of the GCs heat treatment.

For the heat treatment, the glass disks were placed on a platinum foil to prevent any contamination from the sample holder and the heat treatments were performed in air. The temperature and duration of the heat treatments were selected on the basis of a previous study on the crystallization behavior of glasses with similar compositions [148]. Finally, the GCs specimens were either ground or their cross-sections of the GCs disks optically polished, depending on the characterization technique. The GCs with 1.5 mol% Al_2O_3, TiO_2 and ZnO are labeled as AlGC, TiGC and ZnGC, respectively, while the glass ceramic with x = 0 is labeled as RefGC.

3.1.3 Particles-containing glasses

Particles-containing glasses were synthesized using a standard melting in air. Firstly, the Er^{3+}-doped crystalline particles were prepared by sol-gel method. Afterwards, the particles were incorporated prior to and after the melting process. After quenching, the particles-containing glasses were annealed at 400 °C for 5 h.

3.1.3.1 Er^{3+}-doped particles fabrication

In this thesis, different Er^{3+}-doped TiO_2, Al_2O_3, ZnO and ZrO_2 particles were synthesized by the sol-gel route as illustrated in Figure 3.3. The laboratory equipment consists of:

1. Three-necked flask (where the sol-gel process takes place).
2. Mechanical stirrer.
3. Reflux condenser.
4. Constant temperature bath.

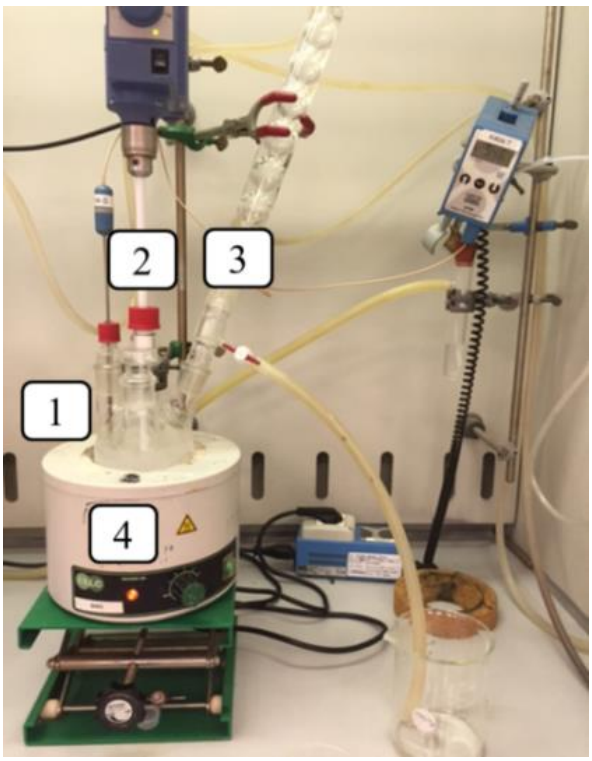

Figure 3.3 Equipment used for the sol-gel synthesis at Colorobbia S.p.A, Florence, Italy.

Synthesis of Er^{3+}-doped TiO_2 particles:

Homogeneous colloidal systems (sols) have been synthesized using titanium(IV) butoxide reagent grade (97% Sigma Aldrich) as TiO_2 precursor, erbium (III) acetate (>99.9% Sigma Aldrich) as precursors of Er^{3+} and ethanol (>99.8% Sigma Aldrich) and deionized water as reaction medium. For the synthesis of 5 grams of TiO_2 particles containing 14.3 mol.% of Er_2O_3, 21.28 g of Tetra (n-butyl) titanate were dissolved in ethanol (100 ml) and then added dropwise into a mixture of distilled water (2 ml), ethanol (100 ml), and 8.37 g of erbium (III) acetate. The process was carried out in a four-neck round-bottom flask equipped with thermometer, reflux refrigerator and stirrer. Once the addition was finished, the solution was heated at a reflux temperature of 90°C and left under reflux for 1 day. Finally, the precipitates were collected by centrifugation, washed with ethanol for several times and dried at 100 °C for 1 day. The as-prepared sample was further annealed in air at 800 °C for 2 h.

Similar fabrication process was used for the preparation of undoped and 0.5, 2, 5 and 10 mol% Er_2O_3-doped TiO_2 particles. The particles doped with 2 mol% of Er_2O_3 were heat treated in air for 2 h not only at 800 °C, but also at 700, 825, 837, 850, 900, and 1000 °C.

Synthesis of Er^{3+}-doped Al_2O_3 particles

For the synthesis of Al_2O_3 particles containing 7 mol% of Er_2O_3, 279 ml of deionized water, 9 ml of nitric acid (70% Fluka), 6.4 g of Triton™ X-100 laboratory grade (Sigma Aldrich) (1% mol) and 12.6 g of erbium nitrate pentahydrated (>99.9% Sigma Aldrich) were poured in a four-neck round-bottom flask equipped with thermometer, reflux refrigerator and stirrer. The solution was heated at 80°C, thereafter 94 g of Aluminum sec-butoxide (97% Alfa Aesar) were added leading to a white suspension. The mixture was left under reflux for 24 hours at 90°C. The obtained precipitate was dried at 100ºC for 24 hours and calcined at 1300ºC for 5 hours.

Apart from the previous composition, 1 mol% Er_2O_3-doped Al_2O_3 particles were also prepared.

Synthesis of Er^{3+}-doped ZnO particles

For the synthesis of 5 grams of ZnO particles containing 14.3 mol% of Er_2O_3, 13.5 g of Zinc acetate dihydrate (99.999% Sigma Aldrich) [$Zn(CH_3COO)_2{\cdot}2H_2O$)] and 7.8 g of erbium chloride hexahydrate ($ErCl_3{\cdot}6H_2O$) (Sigma Aldrich, 99.9% purity) were used as starting materials. The precursors were dissolved in ethanol-deionized water (50-50% in volume) with polyvinylpyrrolidone (PVP K 30, average Mw 40,000, Sigma Aldrich) as a surfactant and stirred for 30 min until a clear solution was formed. Then, the sodium hydroxide 0.1 M (Fluka) was added until reaching a pH of 9 for optimum for nucleation. The solution was heated up to 90 °C and stirred for 4 hours to get fine precipitation. The obtained precipitation was washed 4 times with deionized water and centrifuged. The precipitation was collected and dried at 80°C for 4 hours. After that, the sample was calcined at 1000°C for 2h.

Apart from the previous composition, 1 mol% Er_2O_3-doped ZnO particles were also prepared.

Synthesis of Er^{3+}-doped ZrO_2 particles

For the synthesis of 5 grams of ZrO_2 particles containing 14.3 mol% of Er_2O_3, 28 ml of aqueous solution of 0.1 M erbium chloride hexahydrate ($ErCl_3{\cdot}6H_2O$, 99.9%, Sigma Aldrich), and 1.83 ml of 0.1 M sodium bicarbonate (NaHCO3, 99.7%, Fluka) were added to 50 ml of absolute EtOH while stirring at 60°C. Then, 9.17 ml of Zirconium (IV) butoxide solution [($Zr(OBu)_4$) 80 wt. % in 1-butanol] (Sigma Aldrich) was added and kept under stirring for 2 h. The obtained colloidal solution was centrifuged and washed three times with EtOH (9000 rpm for 30 min). Lastly, the final product was calcined at 1000°C for 2h.

Apart from the previous composition, 1 mol% Er_2O_3-doped ZrO_2 particles were also prepared.

3.1.3.2 Direct particle doping method

The particles-containing glasses were prepared by incorporating the aforementioned particles in the glasses prior to and after the melting.

The particles-containing glasses obtained by the incorporation of particles prior to the melting were labeled as ***"in glass batch"*** glasses. These glasses were prepared by mixing the particles and the raw materials [$Sr(PO_3)_2$ and $NaPO_3$] in a quartz crucible and melting at 1050 °C for 20 min with a heating rate of 20°C/min. Glasses with the same composition as AlG and TiG were prepared with the incorporation of Er^{3+}-doped Al_2O_3 and TiO_2 particles in the glass batch prior to the melting.

In the case of the direct particle doping method (see Figure 3.4), the particles were incorporated at 1000°C after the melting of the glasses with the composition of $50P_2O_5$-40SrO-$10Na_2O$ (mol%) at 1050°C for 20 min and a heating ramp of 20°C/min. After adding the particles, the glasses were manually stirred to improve the dispersion of the particles within the glass melts, and were put back into the furnace for another 5 min (dwell time). Lastly, the melts were poured onto a brass mold. The particles-containing glasses fabricated by this method were labeled as ***"direct particle doping"*** glasses. The optimization of the direct doping process for this glass composition can be found in [318].

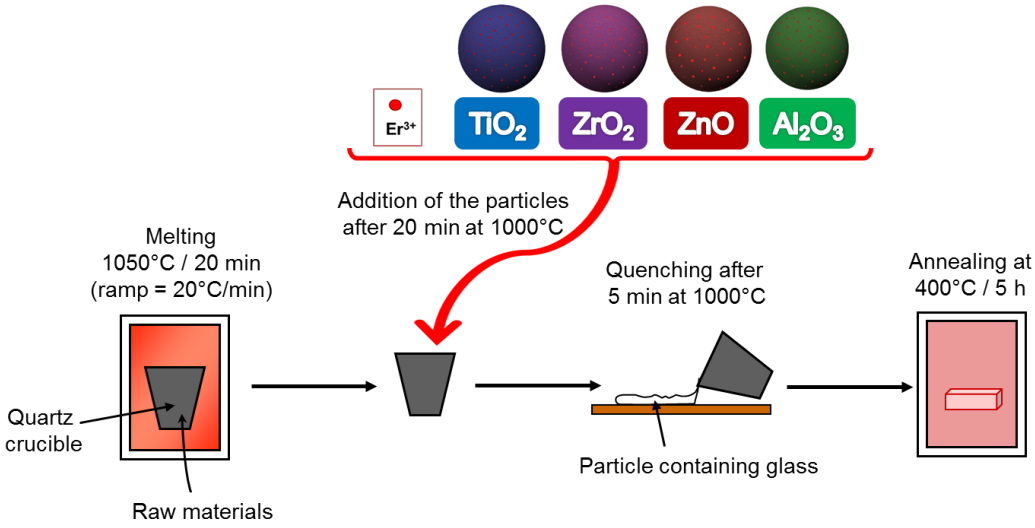

Figure 3.4 Direct particle doping method.

3.1.4 Optical fiber

A multi-mode optical fiber was obtained by preform drawing. Similar fabrication procedures and compositions to the ZnG were chosen for the fabrication of the core and cladding preforms based on the promising biological and optical

properties. The core composition was 0.25 Er_2O_3 – 97.25 (0.5 P_2O_5 – 0.4 SrO – 0.1 Na_2O) – 2.5 ZnO, while the cladding composition was 98.25 (0.5 P_2O_5 – 0.4 SrO – 0.1 Na_2O) – 1.75 ZnO.

First, the core and cladding preforms were fabricated in batches of 80 g. In order to minimize the water content, the precursors were weighed and mixed in a glove box with a humidity < 0.1% and under flux of N_2. The core was prepared by the conventional casting method while the cladding preform was obtained by rotational casting. Both preforms were melted at 1200 °C for 1 h, with a heating ramp of 5 °C/min and with the further annealing at 430 °C for 5 h. Once the glasses were cooled down to room temperature, their external surfaces were optically polished.

In the case of the cladding tube, the rotational casting was performed by casting the cladding melt into a preheated cylindrical mold at 350 °C for 5 h which was spun at a speed around 3000 rpm for few seconds (see Figure 3.1).

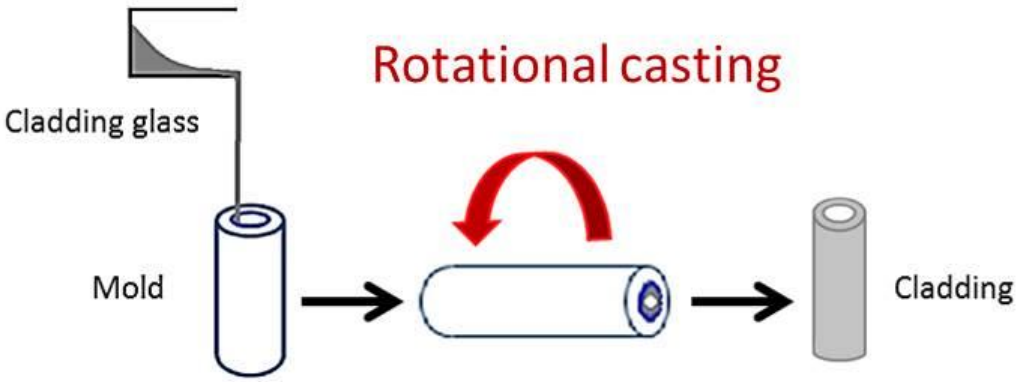

Figure 3.5 Rotational casting technique.

In order to obtain homogeneous and bubble- and crack-free preforms, parameters such as the annealing and mold preheating temperature, and rotational speed must be carefully controlled. After processing the preforms, the two glass components were combined by the rod-in-tube technique. The resulting core-clad preform was drawn into an optical fiber at the Université de Rennes, France. A schematic picture of the rod-in-tube technique and the drawing tower is shown in Figure 3.6.

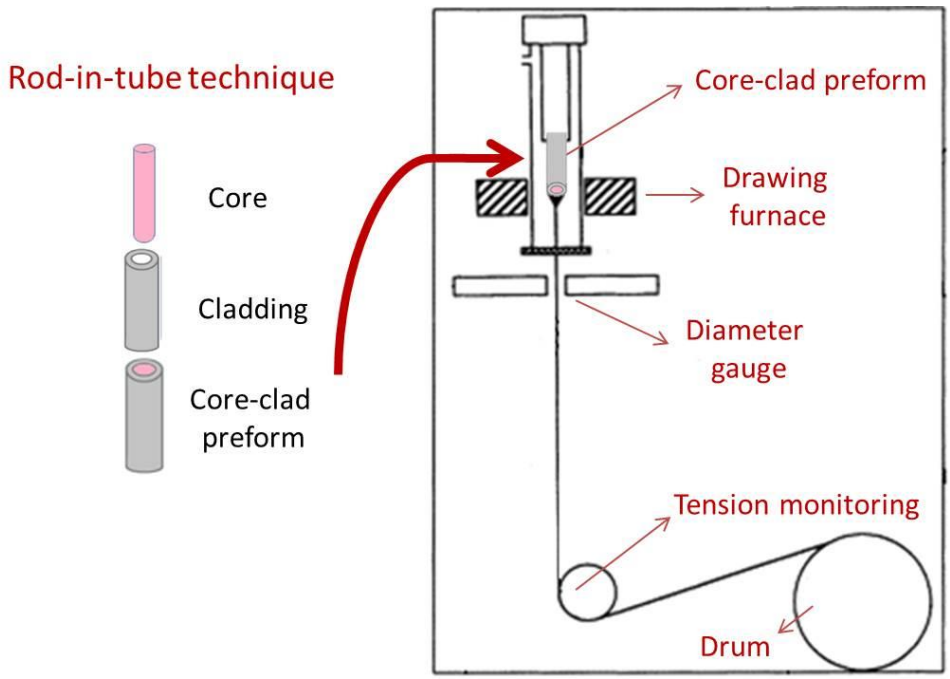

Figure 3.6 Schematic representation of the rod-in-tube technique and the drawing tower at the Université de Rennes, France

A 2 meters high drawing tower in a basic configuration was used. Before the drawing, the core preform was purged with argon for 30 minutes. A furnace at the top part of the drawing tower was used to heat the core preform and stretch it to a proper size (4.3 mm diameter). Then, a cane preform was drawn from the core preform and inserted into the hollow clad preform. The spaces between the core and the cladding were reduced by applying a vacuum of -50 mbars. Afterwards, the lower extremity of the core-clad preform was softened until a glass drop fell down. The resulting fiber was pulled down by a rotating drum, which spun at a known velocity. The drawing process was carried out under a helium-controlled atmosphere. The feed speed at which the core and core-cladding preforms were gradually inserted into the furnace and the drum speed at which the respective fibers were collected, as well as the drawing temperatures, are reported in Table 3.2.

Parameters	Core stick	Multimode fiber
Preform speed (mm/min)	7	0.4
Drawing speed (m/min)	0.04	3
Temperature (°C)	630	575

Table 3.2 Drawing parameters of the core stick and the multi-mode fiber.

At the end of the process, 40 meters of multi-mode core/cladding fiber with inner/outer diameters of around 50/120 µm were obtained.

3.2 Characterization techniques

The glasses and particles investigated in this thesis were submitted to physical, thermal, structural, morphological and optical characterizations. Several techniques such as differential thermal analysis (DTA), dilatometry, field-emission scanning electron microscopy (FE-SEM), infrared spectroscopy (IR), X-ray diffraction (XRD), micro-Raman, UV-Vis-IR spectroscopy, fluorescence emission, lifetime and other characterization techniques were used. The optical fibers were characterized using optical microscopy, near-field imaging, and the cut-back method. Moreover, experiments used for the assessment of the sensing properties of the optical fiber in-vitro and other media are presented.

3.2.1 Physical and thermal properties

Density: The density of the glasses was measured using Archimedes method with an accuracy of ±0.02 g/cm^3, using distilled water as the immersion liquid. The Archimedes principle states that the upward buoyant force experienced by a sample immersed in a liquid is equivalent to the weight of the fluid displaced by the sample. Thus, the density can be calculated as follows:

$$\rho = \frac{W_{dry}}{W_{dry} - W_{wet}} \tag{3.2}$$

Where ρ is the density, W_{dry} is the weight of the sample in air and W_{wet} is the weight of the sample immersed in water.

The density set-up is shown in Figure 3.7.

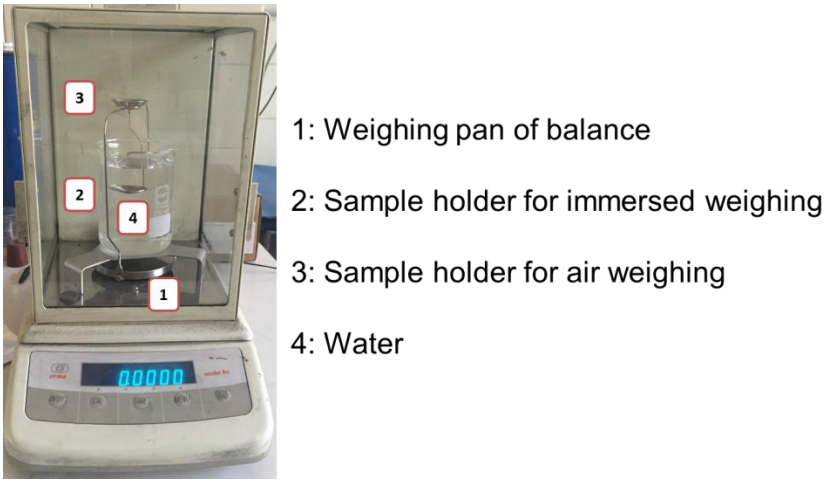

Figure 3.7 Density set-up used at Polytechnic University of Turin.

In order to obtain the true density of a non-porous material, glass samples without defects such as crystals, bubbles or cracks that may increase the measured density were used for all measurements.

Differential Thermal Analysis (DTA): The glass transition temperature (T_g) and crystallization temperature (T_p) were measured by differential thermal analysis (DTA) using a Netszch JUPITER F1 instrument (Figure 3.1a). The set-up consists of 2 holders equipped with one thermocouple each. The DTA runs a program which records the difference in temperature between the holder with the sample and the holder without the sample. 30 mg of glass or particles samples were broken into small pieces to have a better thermal conductivity with the holder's bottom. The measurement was carried out in Pt holders at a heating rate of 10 °C/min.

Figure 3.1b shows an example of a thermogram. T_g was determined as the inflection point of the endotherm obtained by taking the first derivative of the DTA curve, while T_p was taken as the maximum of the exothermic peak. All measurements were performed with an error of ±3 °C.

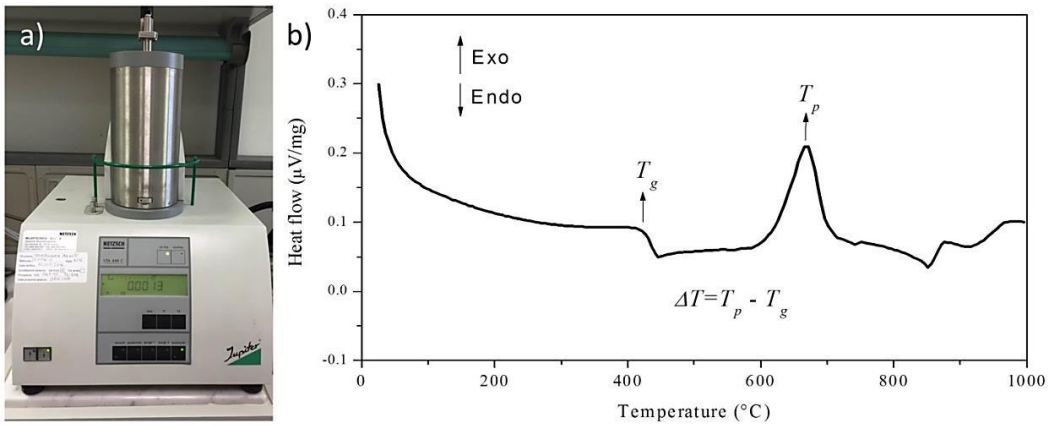

Figure 3.8 (a) Netszch JUPITER F1 DTA at Polytechnic University of Turin. (b) Typical DTA thermogram of a phosphate glass.

Thermogravimetric Analysis (TGA): In this technique, the mass of the sample is recorded upon a specific heating program in a controlled atmosphere (N_2 flow). The TGA machine (Perkin Elmer TGS-2), consists of a sample holder equipped with a precision balance (see Figure 3.9).

Figure 3.9 Perkin Elmer TGS-2 facility used for the TGA Polytechnic University of Turin.

TGA measurements give valuable information that can be used to determine the thermal and compositional properties. It can give us information about the mass loss or gain due to decomposition, oxidation or loss of volatiles (such as H_2O), as well as the possible crystalline phase transitions. All the measurements were carried out in a Pt crucible at a heating rate of 10 °C/min with an error of ± 3 °C. The samples were approximately 10 mg of grounded particles.

Dilatometry: The coefficient of thermal expansion (CTE or α), the glass transition temperature (T_g) and the softening temperature (T_d) of the glasses were measured using a Netzsch thermal dilatometer (DIL 402 PC, Germany) by heating the samples at 5 °C/min up to 650 °C. After a calibration with an Al_2O_3 cylinder, the error of the measurement is ± 0.1×10^{-6} K^{-1}. The machine consists of an inert probe applying force on a cylindrical bulk glass sample with a length of 5 mm. The set-up output is a graph of the elongation of the sample as a function of the temperature. The expansion behavior of a glass is supposed to be linear. Thus, the shape of the thermal expansion curve assesses the presence of the internal residual stress in the glass, and thus, the quality of the annealing [319]. As seen from Figure 3.10, the slope of the dilatometric line between 200 °C and 400 °C was measured as the CTE of the glass, whereas the T_g corresponded to the onset of the peak, and the T_d to the maximum point of the peak. An increase of the CTE can be observed after the T_g, whereas after T_d the glass is shrunk as a consequence of the applied force of the probe.

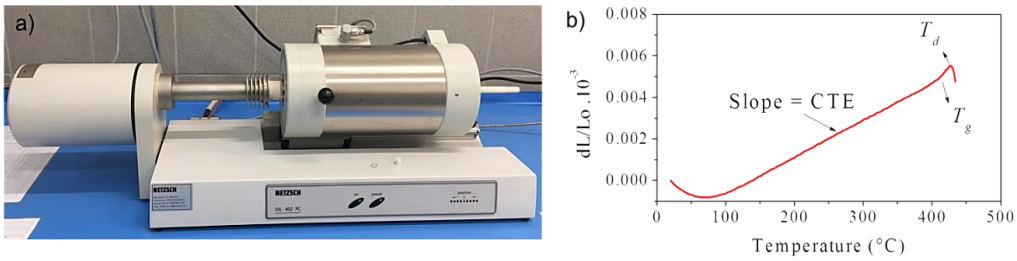

Figure 3.10 (a) Netzsch thermal dilatometer DIL 402 PC at Polytechnic University of Turin. (b) Typical diagram obtained from dilatometric analysis of a phosphate glass.

3.2.2 Morphological properties

Optical microscopy: In this thesis, an optical microscope (Nikon Eclipse 50i) connected to a PC with a picture acquisition system was used. The optical microscopy allowed the measurement of the fiber dimensions and the complete adhesion of the core-cladding interface. Besides, it is an easy way to observe the presence and size of defects such as crystals or particles.

Elemental Dispersive Spectroscopy / Field-Emission Scanning Electron Microscopy (EDS/FE-SEM): The composition and the morphological analyses of the samples were performed using a Field Emission-Scanning Electron Microscope (FE-SEM, Zeiss Merlin 4248, Oberkochen, Germany) operating at 5 keV, equipped with an Oxford Instruments X-ACT detector and Energy Dispersive X-Ray Spectroscopy Systems (EDS/EDX). The samples were coated with a thin chromium layer before the measurements. The semi-quantitative elemental analysis of the composition of the samples was performed by using the EDS within the accuracy of the measurement (±1.5 mol%), whereas the visual observation was performed by the FE-SEM.

The SEM technique is based on the stimulation of the samples by incident electron beams. Once the electrons hit the samples, many secondary and backscattered electrons, as well as X-rays are generated. Consequently, these signals allow the visual image or the elemental composition analysis.

As shown in Figure 3.11, the EDS is displayed as a histogram of electronic counts as a function of X-Ray energy.

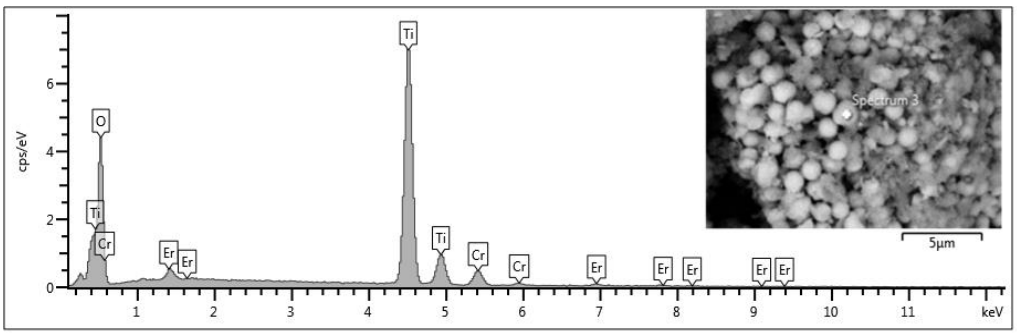

Figure 3.11 Example of an EDS analysis with its respective SEM image of Er_2O_3-doped TiO_2 particles.

3.2.3 Structural properties

X-Ray Diffraction (XRD): The crystalline phases of the particles and the glass-ceramics were identified using an X-ray Diffraction (XRD) analyzer (Philips X'pert) with CuK_α X-ray radiation (λ= 1.5418 Å). The data were collected from 2θ = 0 up to 60° with a step size of 0.003° (See Figure 3.12). This technique is based on the diffraction of an X-Ray beam, which hits the sample with an angle θ. By measuring the diffracted beams, crystallographic information can be determined. The peaks of the spectrum, which correspond to the d-spacing of the crystalline structure, were identified by using the International Center Diffraction Database (ICDD), also known as the Joint Committee on Powder Diffraction Standards (JCPDS).

Figure 3.12 XRD analyzer (Philips X'pert) used at Polytechnic University of Turin.

The GC samples were optically polished, whereas the particles were crushed into powder. All samples were mounted on holder in a flat position for the measurement.

Fourier Transformed Infrared spectroscopy (FTIR): The structural properties of the glasses were assessed using the Fourier Transform Infrared (FTIR) spectroscopy, both in Transmission mode and Attenuated Total Reflection mode (FTIR-ATR).

The FTIR-ATR spectra were acquired on glass powders with a Bruker Tensor 27 spectrometer equipped with a liquid nitrogen-cooled mercury–cadmium–telluride (MCT) detector, operating at 2 cm^{-1} resolution, equipped with an ATR cell (see Figure 3.13a). The spectra were recorded in the range from 600 to 1400 cm^{-1} and were normalized to the band with maximum intensity (~880 cm^{-1}).

The absorption spectra in the range from 2500 to 4000 cm^{-1} were recorded by means of a Bruker Equinox 55 FTIR spectrometer (Alpha, Bruker Optics, Ettlingen, Germany) working in transmission mode with a deuterated triglycine sulphate (DTGS) detector and liquid nitrogen cooled (see Figure 3.13b). The measurements were performed at room temperature and corrected for Fresnel losses and glass thickness. The glass samples were optically polished disks of approximately 1 mm of thickness.

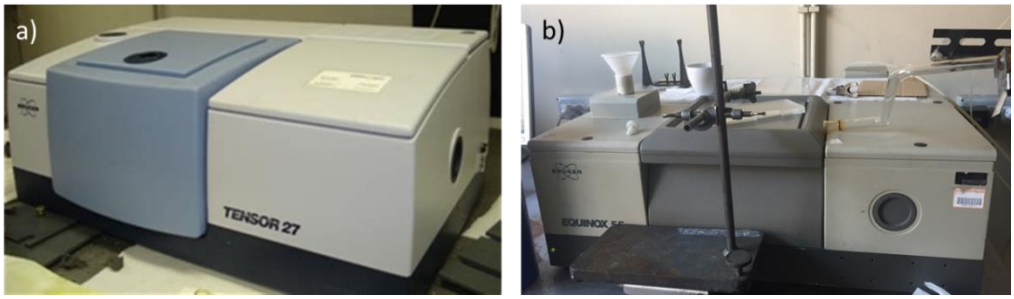

Figure 3.13 (a) Bruker Tensor 27 and (b) Bruker Equinox 55 FTIR spectrophotometers at Polytechnic University of Turin.

The FTIR spectroscopy collects the absorption spectrum in the near IR region from 1 to 12μm. Each one of the bands of the spectrum corresponds to the vibration of atoms, ions, and molecular groups [319]. The FTIR in transmission mode allows a quantitative analysis of the −OH content, by measuring the absorption peak located at 3300 cm^{-1} [320] and the FTIR-ATR gives information about the amount of structural units present in the glasses, such as Q^1, Q^2 or Q^3 units [319].

Micro-Raman spectroscopy: The Raman spectra were acquired with a Renishaw inVia Reflex micro-Raman spectrophotometer (Renishaw plc, Wotton-under-Edge, UK) equipped with a cooled CCD camera using a 785 nm excitation line (Figure 3.14). The spectra were recorded in the range 600–1400 cm^{-1} and were normalized at the maximum point (~1170 cm^{-1}).

The Raman spectroscopy provides structural information by determining the vibrational, rotational and other low-frequency modes in the sample. The technique relies on the Raman scattering of light via the interaction with optical and molecular vibrational modes [319].

Figure 3.14 Renishaw inVia Reflex micro-Raman spectrophotometer at Polytechnic University of Turin.

3.2.4 Optical properties

Refractive index: The refractive index (n) of the glasses was measured at 5 different wavelengths (633, 825, 1061, 1312 and 1533 nm) by the prism coupling technique (Metricon, model 2010) (see Figure 3.15a). Ten scans were performed for each wavelength. Estimated error of the measurement was ±0.001. All of the glass samples were optically polished disks of 5 mm of thickness.

As seen from Figure 3.15b, the prism coupling technique consists of the measurement of the critical angle obtained when a laser is launched through the prism and reflected at the prism-sample interface. The critical angle can be detected when the angle of incidence is lower than the critical angle. Thus, the laser is not reflected and the detector intensity drops.

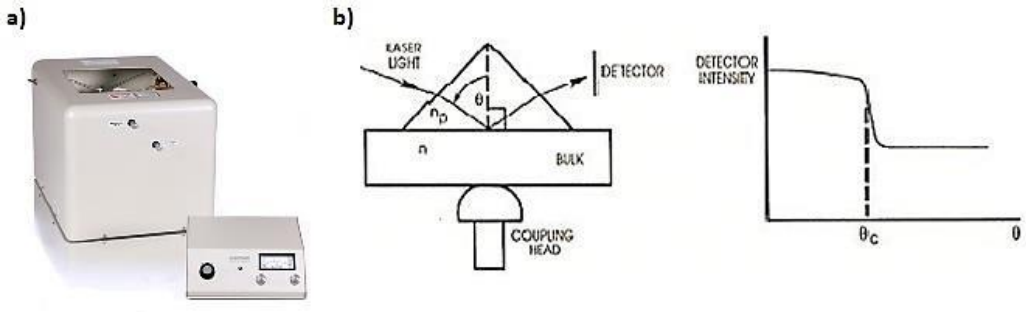

Figure 3.15 (a) Metricon, model 2010 Prism Coupler apparatus used at Polytechnic University of Turin. (b) Schematic representation of the measurement of the refractive index by the prism coupling technique. Picture taken from the Metricon2010 user's manual.

Consequently, the refractive index can be calculated with the following equation:

$$\theta_c = \arcsin\left(\frac{n}{n_p}\right) \tag{3.3}$$

Where θ_c is the critical angle, which is easily measured using the detector, n is the refractive index of the bulk glass sample and n_p is the known refractive index of the prism.
Since np is known, n can then be readily determined by the formula.

The experimental data of the refractive indexes were fitted using Sellmeier's equation:

$$n^2(\lambda) = 1 + \frac{B_1 \cdot \lambda^2}{\lambda^2 - C_1} + \frac{B_2 \cdot \lambda^2}{\lambda^2 - C_2} + \frac{B_3 \cdot \lambda^2}{\lambda^2 - C_3} \tag{3.4}$$

Where λ is the wavelength and $B_{1,2,3}$ and $C_{1,2,3}$ are the experimentally determined Sellmeier's coefficients.

Fluorescence emission spectra: For the emission measurements, an optical bench in clean room environment was used. The emission spectra in the 1400–1700 nm range were measured with a Jobin Yvon iHR320 spectrophotometer equipped with a Hamamatsu P4631-02 detector and a filter (Thorlabs FEL 1400). Emission spectra were obtained at room temperature using a monochromatic excitation source at 976 nm, emitted by a single-mode fiber pigtailed laser diode (CM962UF76P-10R, Oclaro).

The glass samples used were optically polished disks of 1 mm of thickness. Instead, the particles samples were pressed to form flat disks and placed between two transparent pure silica glasses.

A schematic representation of the equipment used is shown in Figure 3.16.

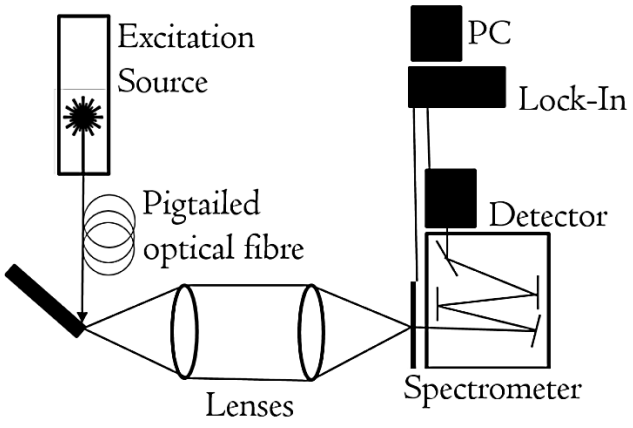

Figure 3.16 Schematic representation of the set-up used for the emission measurements.

In the case of GCs and particles-containing glasses, a Micro-photoluminescence (PL) set-up was used. The measurements were taken at the surface of the polished samples at room temperature using a continuous wave 976 nm diode laser for excitation. The excitation laser beam was focused on the glasses with a 40X magnifying high-NA objective. This technique offers a spatial resolution of 1 μm. The signal was recorded with the same objective and detected with a thermoelectric cooled InGaAs array camera attached to a 750 mm spectrometer.

Fluorescence lifetime: The fluorescence lifetime of Er^{3+}:$^4I_{13/2}$ energy level was obtained by exciting the samples with light pulses of a fiber pigtailed laser diode operating at the wavelength of 976 nm, recording the signal using a digital oscilloscope (Tektronix TDS350) and fitting the decay traces by single exponential. The detector used for this measurement was a Thorlabs PDA10CS-EC.

The lifetime value was calculated by collecting the fluorescence decay curve excited by a fiber coupled diode with pulses that are usually in the range from 5 to 20 Hz. A schematic representation of the set-up used is shown in Figure 3.17.

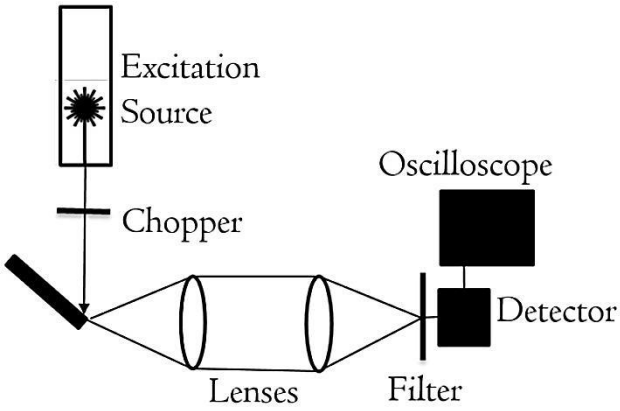

Figure 3.17 Schematic representation of the set-up used for the lifetime values measurements.

The emitted light from the sample is collected by the oscilloscope, which displays a decay curve that is fitted by single exponential between 10% and 90% of the measured signal, in order avoid the possible noise and residual pump effect. Deviations from single exponential decay were not observed. For all samples, the fluorescence lifetime (τ) was obtained using the following single exponential fitting:

$$y = A \cdot \exp(-t/\tau) \tag{3.5}$$

Where *y* is the signal intensity, *t* is the time, and *A* is a constant.

The glass samples were optically polished disks of 1 mm of thickness, while the particles samples were pressed to form flat disks and placed between two transparent pure silica glasses. The laser beam was launched at the edge of the samples to minimize re-absorption processes. Usually, 3 to 5 measurements are performed on each sample. For the glass samples, the estimated error of the measurement was ±0.20 ms, while for the particles, the error was calculated as the standard deviation of the individual lifetimes.

Absorption spectroscopy: The UV-Vis-NIR absorption spectra of the glasses were measured at room temperature from 190 to 3300 nm using a dual beam UV-Vis-NIR Agilent Cary 5000 spectrophotometer (Agilent, Santa Clara, CA, USA) (See Figure 3.18). The measurements were performed in single beam configuration.

Figure 3.18 UV-Vis-NIR Agilent Cary 5000 spectrophotometer used at Polytechnic University of Turin.

The absorption spectroscopy collects the fraction of incident light absorbed by the sample as a function of the wavelength. Indeed, the technique consists of launching a broadband light source with a known power to the sample. Afterwards, the amount of transmitted light which passes through the sample is recorded by the detector of the spectrophotometer. Thus, the absorbance (*Abs*) can be defined by the following equations:

$$Abs = log_{10}\left(\frac{I_0}{I}\right) = log_{10}\left(\frac{1}{T}\right) \tag{3.6}$$

Where I_o is the intensity of the incident light, I is the intensity of the transmitted light and T is the transmittance.

The attenuation of a light beam of intensity I_o passing through a sample can also be expressed as:

$$I = I_o \cdot e^{(-\alpha L)} \tag{3.7}$$

Where α is the absorption coefficient and L is the sample thickness.

Thus, substituting from the two abovementioned equations, the absorption coefficient, expressed in cm^{-1}, can be calculated by the following equation:

$$\alpha = \frac{1}{L} ln\left(\frac{I_0}{I}\right) = \frac{2.303 \cdot Abs}{L} \tag{3.8}$$

The absorption cross-section (σ_{Abs}) of a material, which is expressed in cm^2, is defined as:

$$\sigma_{Abs}(\lambda) = \frac{\alpha}{N} = \frac{2.303 \cdot Abs}{NL} \tag{3.9}$$

Where α is the absorption coefficient, N is the Er^{3+} ions concentration (ions/cm^3), *Abs* is the absorbance and L is the thickness of the sample (in cm).

The estimated error is $\pm 0.02 \times 10^{-20}$ cm^2. The Er^{3+} ions concentration (N) was calculated from the measured glasses density and the initial composition by the following equation:

$$N = \frac{Wt\%\ (Er_2O_3)}{Mr(Er_2O_3)} \cdot 2\,N_A \cdot \rho \qquad (3.10)$$

Where Wt% is the weight percentage, and Mr is the molecular mass of dopant, N_A is the Avogadro number ($6.022 \cdot 10^{23}$ mol^{-1}), and ρ the glass density.
The glass samples were optically polished disks of 1 mm of thickness.

McCumber emission cross-section: The McCumber equation was used to predict the emission cross-section spectrum of the 1.5 μm transition of Er^{3+}-doped glasses. The exact McCumber relation [321] is barely used because it requires the knowledge of the $^4I_{15/2}$ and $^4I_{13/2}$ stark sublevel energies of the RE ions, which are host dependent and difficult to measure. However, an approximate method of the McCumber relation without the need for these energies was proposed by Miniscalco et al. [322]. This method is known for its easiness and has been shown to be reasonably accurate for laser crystals, low-fluorine fluorophosphate fibers and RE-doped glasses [322,323]. Yet, some authors have shown that the McCumber procedure overestimates the peak emission cross-section (by up to 75%) and predicts a cross-section spectral shape that is distorted [324].

The McCumber theory relates the absorption cross-section (σ_{Abs}) and the emission cross-section (σ_e) spectra by the following equation:

$$\sigma_e = \sigma_{Abs} \cdot exp\frac{(\varepsilon - E)}{kT} \qquad (3.11)$$

Where σ_{Abs} is calculated by the abovementioned equation, ε is the photon energy at which the two spectra cross at temperature *T*, i.e. the values of the maximum of the Absorption peak in e.V and the maximum of the Emission peak in e.V divided by two, E is the energy of the radiation in e.V., k is the Boltzmann constant (8.617×10^{-5} $eV \cdot K^{-1}$), and ε is the temperature-dependent excitation energy, i.e. the net free energy required to excite one Er^{3+} ion from the $^4I_{15/2}$ to the $^4I_{13/2}$ state at temperature *T* (in our case at 298 K).
Lastly, the relationship between the energy (E) and wavelength (λ) is given by:

$$E = h \cdot \upsilon = h \cdot \frac{c}{\lambda} = \frac{1240}{\lambda} \qquad (3.12)$$

Where *h* is the speed of light and *c* is the Planck's constant.

3.2.5 Optical fiber characterization

Near-field imaging: The near-field imaging was used to evaluate the guiding properties of the optical fiber. In this thesis, a laser light at 1300 nm with no interaction with the Er^{3+} ions was chosen as the lighting source. The investigated optical fiber was coupled to the laser diode source at 1300 nm and the output facet was observed with a charge-coupled device (CCD) camera with magnifying lens. A schematic representation of the set-up used for the measurement is shown in Figure 3.19.

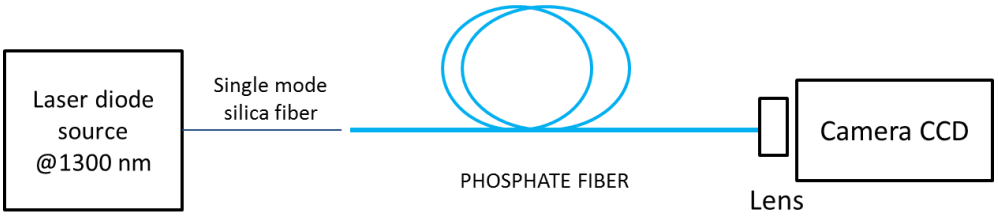

Figure 3.19 Set-up used for the measurement of the near-field imaging at 1300 nm.

Optical loss by cut-back method: The cut-back method was employed to assess the optical fiber losses, as performed by Kaminow *et al.* [325]. The optical losses are usually due to the attenuation of the fiber, which can be produced by imperfections in the core-cladding interface or by bending losses. The cut-back method consists of recording the optical losses by measuring the output power transmitted through the optical fiber after being launched with a laser light with a known power (see Figure 3.20).

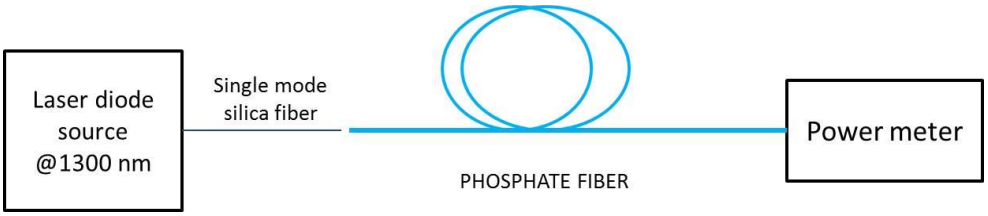

Figure 3.20 Optical losses measured obtained by exciting at 1300 nm.

The optical loss can be calculated using the following equation:

$$\frac{\mathrm{Log}\left(\frac{P_{out}}{P_{out2}}\right)}{L-l} = \frac{dB}{m} \tag{3.13}$$

Where P_{out} is the power output of a fiber with length L, and P_{out2} is the output power of the fiber with length l.

The measurements were taken before and after several sections of the fiber were removed. A graph plotting the output power as a function of the fiber length is obtained. The experimental data was fitted with a linear least square fitting. The slope of the graph gives the loss of the optical fiber, usually expressed in dB/m. An estimated error of the measurement is expected to be around 10%.

The optical loss of the fiber was performed using a length of 115 cm butt-coupled with a single mode silica fiber pigtailed laser diode source at 1300 nm (Infineon SBM 52414x). A Thorlabs PM100 equipped with S144A InGaAs power meter was used as a detector.

Optical fiber sensor, principle and design: The optical fiber is intended to behave as a bioactive optical fiber sensor able to monitor "in situ" the optical and biological responses in aqueous media. The aim of the study is to test the biological

and optical response of an Er^{3+}-doped fiber with the further processing of an innovative biosensor for therapy monitoring.

At first, the cladding was etched so the core of the fiber was in contact with the media. For the etching, the optical fiber was immersed in phosphoric acid (H_3PO_4) 1M solutions. Fibers of 5 cm length were placed sideways through a mold of 2 cm length filled up with a 3 ml diluted solution of H_3PO_4 1M (see Figure 3.21).

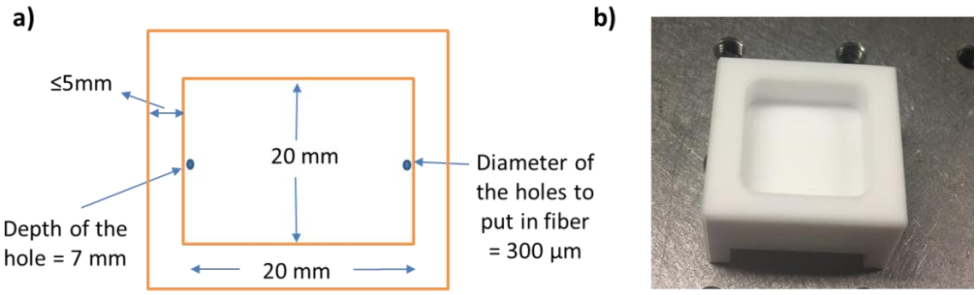

Figure 3.21 (a) Schematic picture with the dimensions of the mold. (b) Mold used in the dissolution test with H_3PO_4 1M solution.

The samples were etched at different times, from 1 to 8 hours. At each time data point, the diameter of the fiber was measured using an optical microscope. The optical fibers were rinsed with acetone twice and dried before the optical imaging. The estimated error of the diameter measurements was 2 µm.

The SBF solution was prepared by following the methodology of the standard ISO/FDIS 23317 [326]. The samples were immersed in eppendorfs of 3 ml capacity with 2 ml of SBF solution. The medium was refreshed following the ISO protocol twice per week to simulate the physiological conditions. The samples were immersed in SBF solution for up to 4 weeks at room temperature in an incubating shaker (INFORS Multitron II) with an orbital speed of 100 rpm.

After selective etching of the cladding of the optical fibers, the changes in absorption and in the intensity of the emission were measured as a function of immersion time in H_3PO_4 1M solution and also in Simulated body fluid. A schematic representation of the set-up is shown in Figure 3.22.

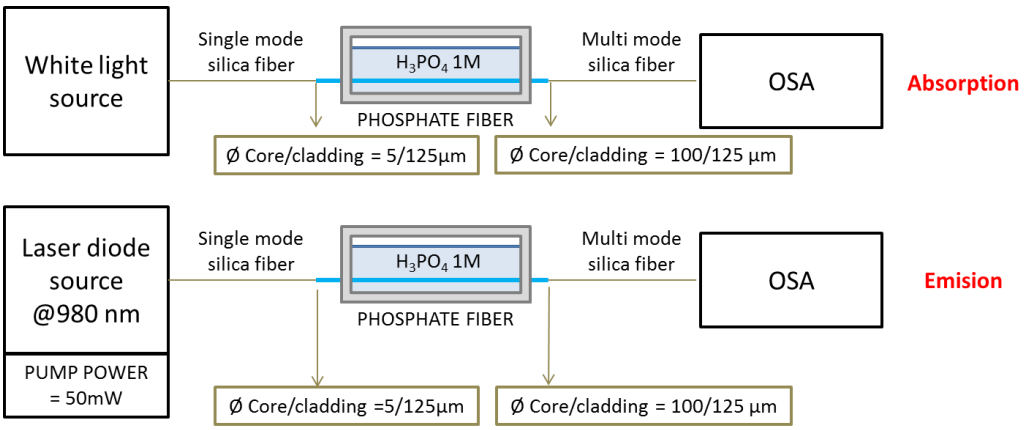

Figure 3.22 Schematic representation of the set-up used for the emission and absorption measurements of the fiber immersed in H_3PO_4 1M solution

The light transmitted through the optical fiber was measured in continuous mode using a white light source (Thorlabs SLS201L(/M)) with a wavelength range from 400 to 1700 nm. The light at the fiber output was measured using a light power meter (PM100D from Thorlabs) and an Optical Spectrum Analyzer (OSA, Ando AQ6315A). The optical fiber was immersed into a 1M H_3PO_4 solution (3 ml) and butt-coupled to the light source and the power meter using two silica fibers. Additionally, the emission spectra of the Er^{3+}:$^4I_{13/2}$ energy level in the range from 1400 to 1700 nm was collected at room temperature by exciting the optical fiber with a fiber pigtailed laser diode operating at 976 nm (CM962UF76P-10R, Oclaro). The optical fiber was coupled to the pigtailed laser diode and a multi-mode silica fiber. The signal was recorded using the same power meter.

Apart from the "proof of concept" of the optical fiber sensor in H_3PO_4 solution, an experiment at room temperature in SBF for up to 4 weeks was performed. The emission spectrum of the fiber immersed in SBF was measured every 3 - 4 days.

The set up used for the absorption and emission measurements is shown in Figure 3.23.

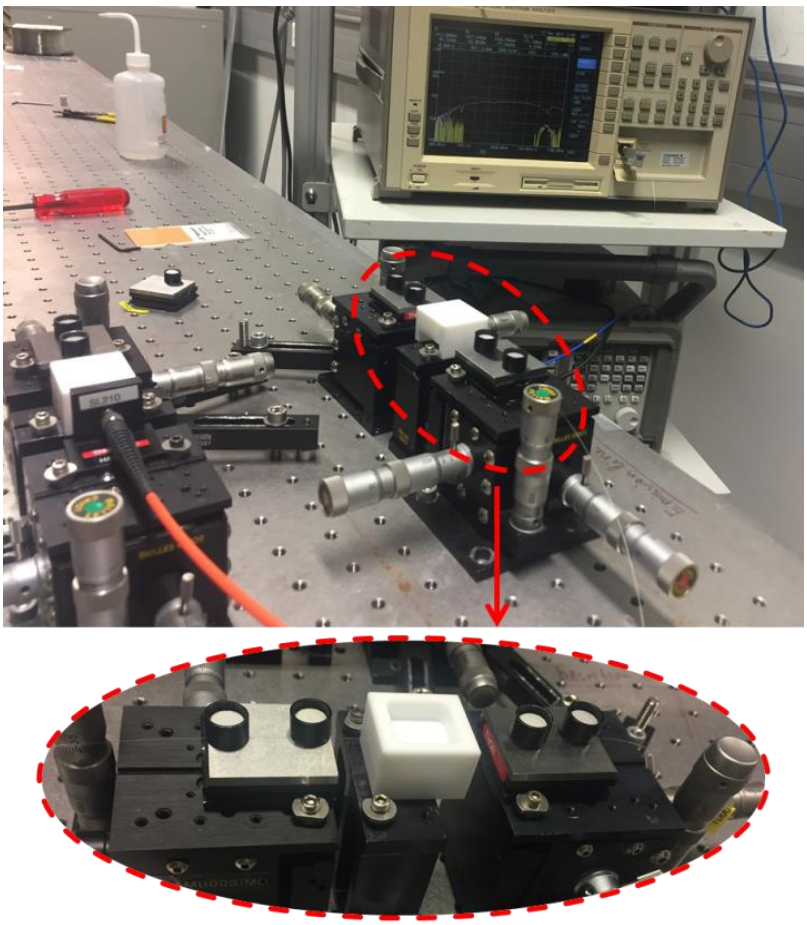

Figure 3.23 Set-up used for phosphate optical fiber sensors at Laboratory of Photonics, Tampere University.

Splicing and insertion losses: The phosphate optical fibers were cleaved and spliced using the cleaver Fujikura CT-106 and the splicer Fujikura FSM-100P+, respectively (See Figure 3.24).

Fiber splicing consists of joining two fibers together permanently by heating above the melting temperature while pushing the fiber ends together in an axial direction. Before the splicing, the fiber polymer coating is removed, and the fibers are cleaned with ethanol. Then, the fibers are carefully cleaved, and the two fiber ends aligned. Multi-mode phosphate optical fibers (50-120 μm) were spliced with commercial silica single-mode fibers (7-125 μm). It should be taken into account that fibers with different geometries and compositions are challenging to splice due to the differences in their thermal and mechanical properties. Nevertheless, splicing phosphate optical fibers with commercial silica optical fibers is essential in order to integrate the investigated fibers with commercial systems.

Figure 3.24 (a) Cleaver equipment (Fujikura CT-106) and (b) the splicer equipment (Fujikura FSM-100P+) used at Polytechnic University of Turin.

To conclude this chapter, a table summarizing the different materials prepared during this thesis and their concentrations is shown in Table 3.3.

Code	Al_2O_3 (mol%)	TiO_2 (mol%)	ZnO (mol%)	Er_2O_3 (mol%)	P_2O_5 (mol%)	SrO (mol%)	Na_2O (mol%)
RefG				0.25	49.88	39.90	9.98
AlG	1.50			0.25	49.25	39.40	9.85
TiG		1.50		0.25	49.25	39.40	9.85
ZnG			1.50	0.25	49.25	39.40	9.85
RefGC				0.25	49.88	39.90	9.98
AlGC	1.50			0.25	49.25	39.40	9.85
TiGC		1.50		0.25	49.25	39.40	9.85
ZnGC			1.50	0.25	49.25	39.40	9.85
Ti particles		99.50		0.50			
Ti particles		98		2			
Ti particles		95		5			
Ti particles		90		10			
Ti particles		85.70		14.30			
Al particles		99		1			
Al particles		93		7			
Zn particles		99		1			
Zn particles		85.70		14.30			
Zr particles		99		1			
Zr particles		85.70		14.30			
Core			2.50	0.25	48.63	38.90	9.72
Cladding			1.75		49.13	39.3	9.82

Table 3.3 Composition of the materials manufactured in this thesis.

Chapter 4

Fabrication and characterization of erbium doped materials

Part of the work described in this chapter has been previously published in [35, 105, 374]. This chapter deals with the fabrication and characterization of Er^{3+}-doped phosphate glasses, glass-ceramics, and particles-containing glasses. The first part of the chapter is devoted to the study of the addition of different metal oxides such as Al_2O_3, TiO_2 and ZnO on the properties of Er^{3+}-doped phosphate glasses fabricated by melt-quenching. The second part of this chapter is dedicated to the study of the crystallization behavior and the structural, optical and luminescence properties of Er^{3+}-doped phosphate glass-ceramics. The third part of the chapter describes the synthesis of particles containing glasses using the direct doping method.

4.1 Er^{3+}-doped glasses

Glasses with the compositions in mol% [0.25 Er_2O_3 – 100-x (0.5 P_2O_5 – 0.4 SrO – 0.1 Na_2O) – x (TiO_2/Al_2O_3/ZnO/ZrO_2)], with x = 0 and x = 1.5 mol%, were prepared. The glasses with 1.5 mol% Al_2O_3, TiO_2, ZnO and ZrO_2 were labeled as AlG, TiG, ZnG and ZrG, respectively, while the glass with x = 0 was labeled as RefG. All of the glasses were fully characterized except the ZrG, which was crystallized after the quenching (see Figure 4.1).

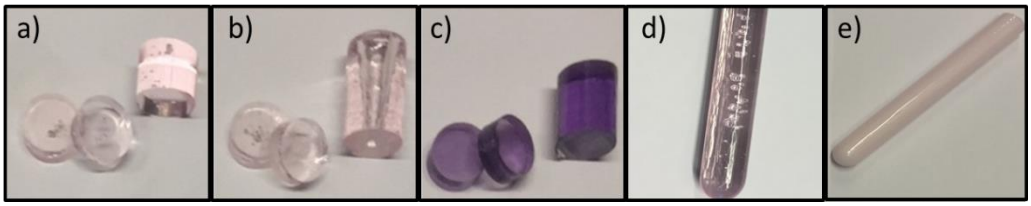

Figure 4.1 (a) RefG, (b) AlG, (c) TiG, (d) ZnG, (e) ZrG glasses obtained by melt-quenching.

After the glass fabrication, the composition of the glasses was determined by semi-quantitative analyses carried out by an EDS/FE-SEM. The composition of all the glasses was found to be in agreement with the nominal one, within the accuracy of the EDS measurement (± 1.5 mol%). Despite the use of quartz crucibles, no Si

was found in the EDS analysis of the investigated glasses. It should be pointed out that the sensitivity of the EDS is approximately 0.1 wt% for all elements. The physical and thermal properties of the investigated glasses are reported in Table 4.1.

Glass label	$\rho \pm 0.02$ g/cm^3	$T_g \pm 3$°C	$T_p \pm 3$°C	$\Delta T \pm 6$°C	[Er^{3+}] ($\cdot 10^{19}$) (ions/cm^3) ± 5%
RefG	3.08	440	555	115	7.775
AlG	3.10	447	583	136	7.843
TiG	3.09	448	563	115	7.840
ZnG	3.08	439	538	99	7.813

Table 4.1 Physical and thermal properties of the glasses.

As seen from Table 4.1, the addition of Al_2O_3, TiO_2 or ZnO has no impact on the density. The addition of ZnO decreases slightly T_p and ΔT, whereas the addition of TiO_2 and Al_2O_3 increases T_g, T_p and ΔT ($\Delta T = T_p - T_g$). In addition, ΔT is larger than 100 °C in all the glasses, suggesting their reasonable thermal stability. The increase in T_g could indicate that the addition of Ti and Al improves the strength of the network, whereas Zn is suspected to act as a network modifier, in agreement with Schwarz *et al.*[327]. It is worthwhile noting that the AlG exhibits the highest T_g, T_p and ΔT, thus suggesting that Al_2O_3 has the highest impact on the bond strength [328].

The structural properties of the glasses were investigated using Raman and infrared spectroscopies. The FTIR-ATR and Raman spectra of the glasses are shown in Figure 4.2 and Figure 4.3, respectively. All spectra were normalized to the band with maximum intensity, thus all the discussed intensity changes are expressed relatively to the main peak.

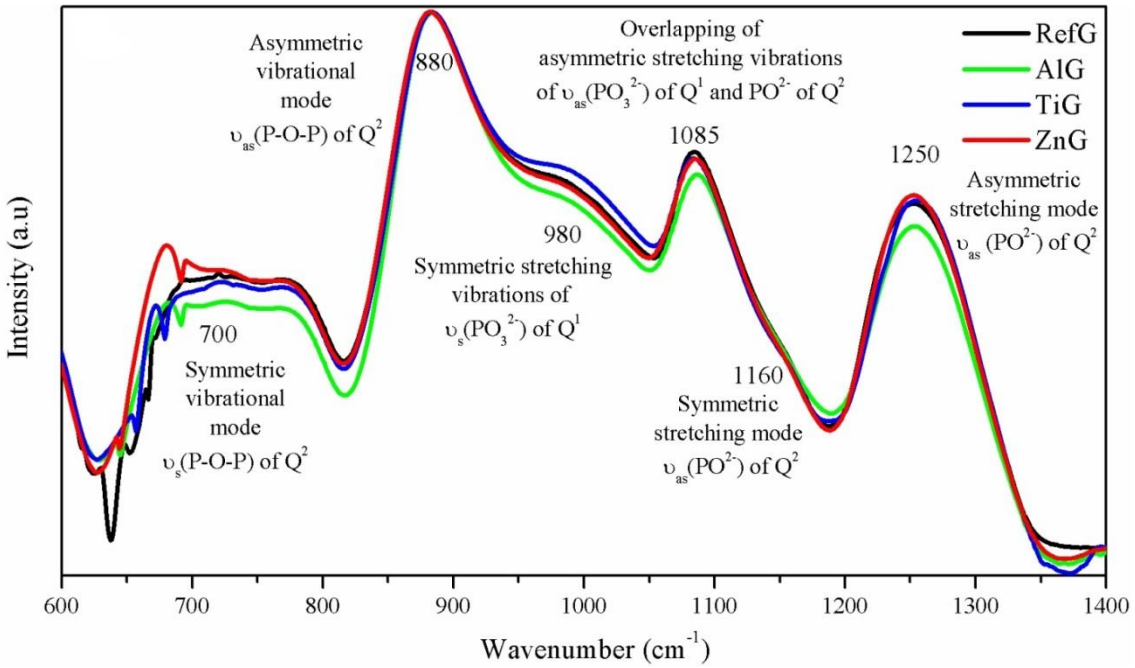

Figure 4.2 FTIR-ATR spectra of the investigated glasses.

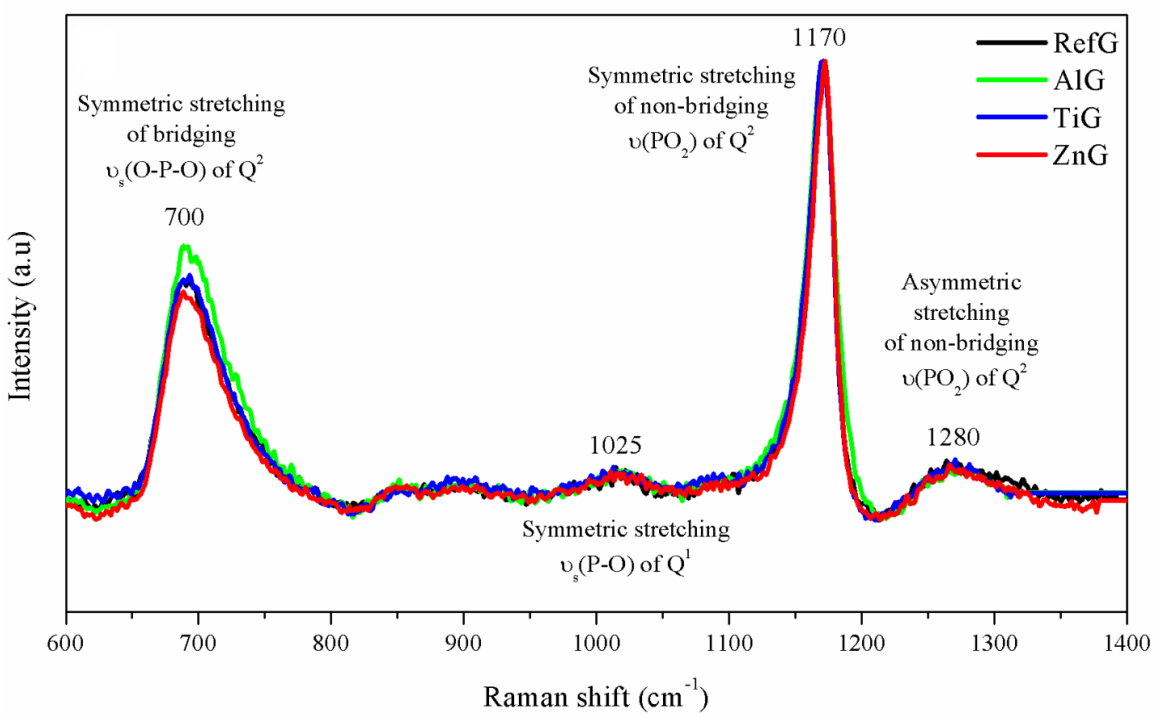

Figure 4.3 Raman spectra of the investigated glasses.

The IR spectra shown in Figure 4.2 displays a broad band between 650 and 800 cm^{-1} corresponding to symmetric vibrational modes ν_{sym} (P-O-P) of Q^2 units [329]. The main band at ~ 880 cm^{-1} is attributed to the asymmetric vibrational mode ν_{as} (P-O-P) in Q^2 units in chains [329–332]. The several bands between 930 and 1010 cm^{-1} are often related to rings-type formation in the glass network [333]. The shoulder centered at ~ 980 cm^{-1} and the band peaked at 1085 cm^{-1} correspond to the symmetric and asymmetric stretching vibration of PO_3^{-2} in Q^1 units, respectively [331,332,334,335]. Additionally, the band at 1085 cm^{-1} can be attributed to an overlap between PO_3^{2-} of Q^1 units and PO_2 of Q^2 groups in metaphosphate [336]. The shoulder at 1160 cm^{-1} and the absorption band at 1250 cm^{-1} correspond to the symmetric and asymmetric vibrations of PO_2^- in Q^2 units, respectively [329,331,332,334,337]. No bands are revealed at wavenumbers higher than 1300 cm^{-1}, where the ν(P=O) of Q^3 groups typically locate.

These IR spectra clearly indicate the presence of a metaphosphate structure [338], which is confirmed from the Raman spectra presented in Figure 4.3. A metaphosphate glass typically has a composition of 50 mol% of P_2O_5 and an O/P ratio of 3, with a structure consisting of rings and/or long chains of Q^2 units [339]. Interestingly, it has been reported that the properties of metaphosphate glasses are less dependent on the structure of the P-O-P bonds rather than on the P-O-Metal bonds. Thus, the field strength of the modifying cation has a great influence on the rigidity of the glass network [63,99].

The Raman band at around 700 cm^{-1} corresponds to the symmetric stretching of bridging ν_{sym}(O-P-O) of Q^2 groups and the band at 1025 cm^{-1} to the symmetric stretching ν(P-O) of terminal groups (Q^1) [329]. The bands at 1170 and 1280 cm^{-1}

can be ascribed to the symmetric and asymmetric stretching of non-bridging $\nu(PO_2)$ of Q^2 groups, respectively [340–342]. The incorporation of TiO_2 has a small influence on the broadening and shifting of the Q^2 units. The increase in intensity of the IR shoulder at 980 cm^{-1} might be related to the decrease of bridging oxygens due to the formation of P-O-Ti bonds, as suggested by Kiani *et al.* [69]. The addition of TiO_2 leads to an increase in T_g, which may be ascribable to the distortion of the glass network due to the formation of three-dimensional networks of P-O-Ti linkages, as suggested in Segawa *et al.* [343].
The addition of Al_2O_3 has the highest impact on the glass structure. The decrease in the intensity of all IR bands, as compared to the main band, indicates that Al^{3+} ions are expected to enter gradually the network, as reported by Saddeek *et al.* [344]. The non-bridging oxygens of P=O bonds may be converted into bridging oxygens upon formation of P-O-Al bonds [344]. These P-O-Al cross-linking bonds between phosphate chains increase the network connectivity, as suspected from the increase in intensity of the Raman band at 700 cm^{-1} and the broadening of the main band at 1170 cm^{-1}. This is also in agreement with the increase of T_g.
The addition of ZnO barely affects the IR and Raman spectra, in agreement with the analysis of the density and of the thermal properties of this glass. Thus, the Zn seems to act as a modifier, leading to a depolymerization of the phosphate network and to a less cross-linked network. However, its concentration is probably too low to induce noticeable changes in its physical, thermal and structural properties.

The water content in the glasses was assessed by the IR absorption spectra shown in Figure 4.4. The spectra exhibit a broad absorption band between 2700 and 3500 cm^{-1}, which corresponds to the stretching vibration mode of OH^- groups in several oxide glasses [345].

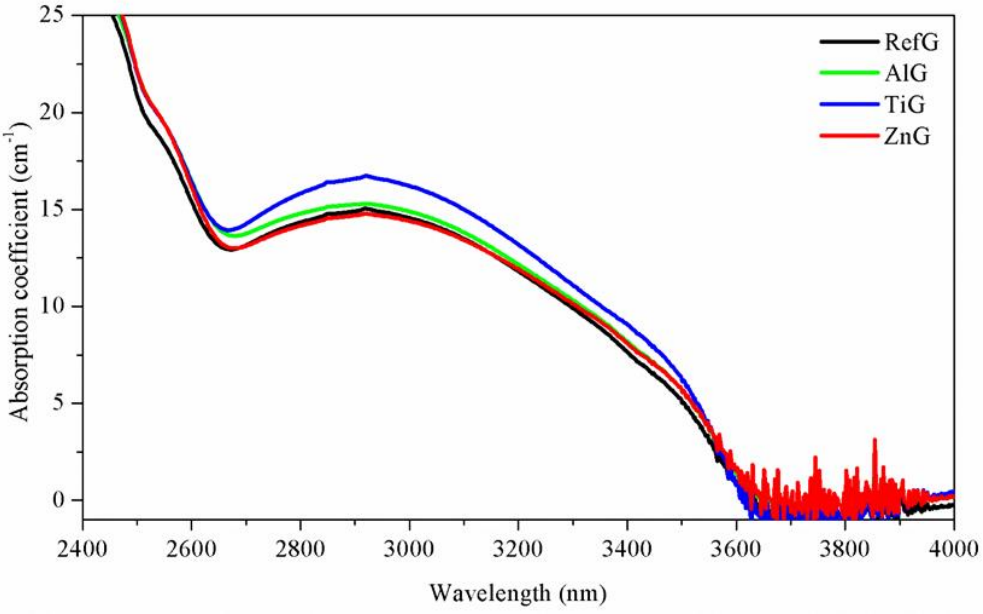

Figure 4.4 IR absorption spectra of the glasses.

The TiG glass exhibits the highest absorption band intensity, suggesting a larger OH^- population as compared to the other glasses. This may indicate that the formation of P-O-Ti bonds distorts the phosphate network, increasing the free volume in the glass network and so the OH^- content.

The UV-Vis absorption spectra of all the glasses are reported in Figure 4.5.

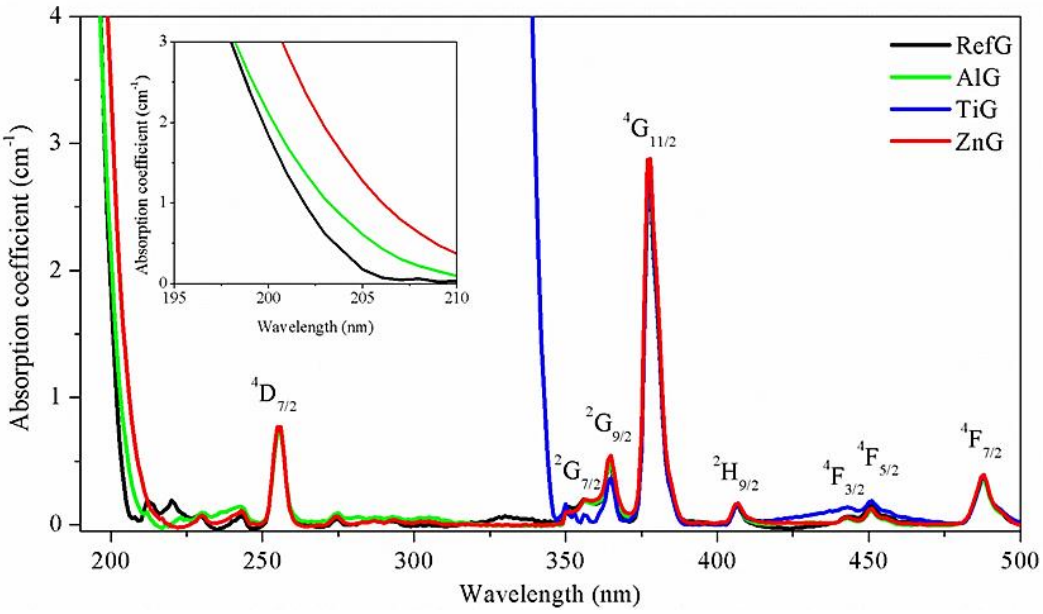

Figure 4.5 UV-Vis absorption spectra of the investigated glasses. The inset shows the UV edge of RefG, AlG and ZnG in the range between 195 and 210 nm.

The spectra exhibit several bands characteristics of the Er^{3+} ion 4f-4f transitions from the ground state to various excited levels [346,347]. The UV absorption edge was not significantly affected by the addition of Al_2O_3 or ZnO. However, with the addition of TiO_2, the band-gap shifted to longer wavelengths due to the presence of Ti^{3+}, as explained in Zikmund *et al.* [348]. In the inset of Figure 4.5, the absorption edge at the UV end of the UV-Vis spectra can be seen in more detail. As stated in [101,349], an increase in the polymerization of the phosphate network leads to a shift of the band-gap to lower wavelength values. Due to the formation of Al-P-O bond, the polymerization in the AlG is more significant than in TiG and ZnG, thus leading to a more pronounced shift of the band-gap to lower wavelengths with respect to the Zn and Ti glasses.

The absorption cross-section spectra at around 980 are represented in Figure 4.6.

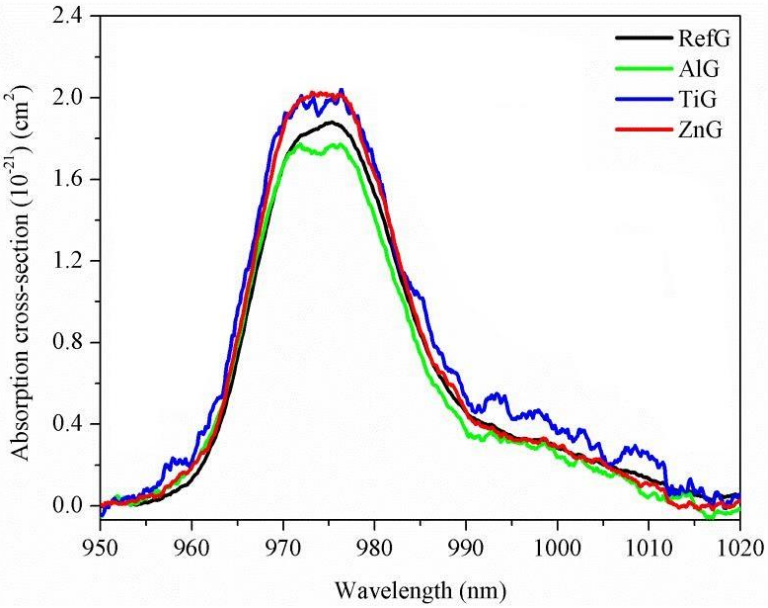

Figure 4.6 Absorption cross-section of the investigated glasses centered at 980 nm.

The absorption cross-section remains similar with the addition of Al_2O_3, TiO_2 and ZnO, thus indicating that the site of the Er^{3+} ions is not strongly influenced by the changes in the glass composition. The typical error on the measurement is ± 10 %.

Luminescence decay curves from the $^4I_{13/2}$ to the $^4I_{15/2}$ emission upon 976 nm excitation are reported in Figure 4.7.

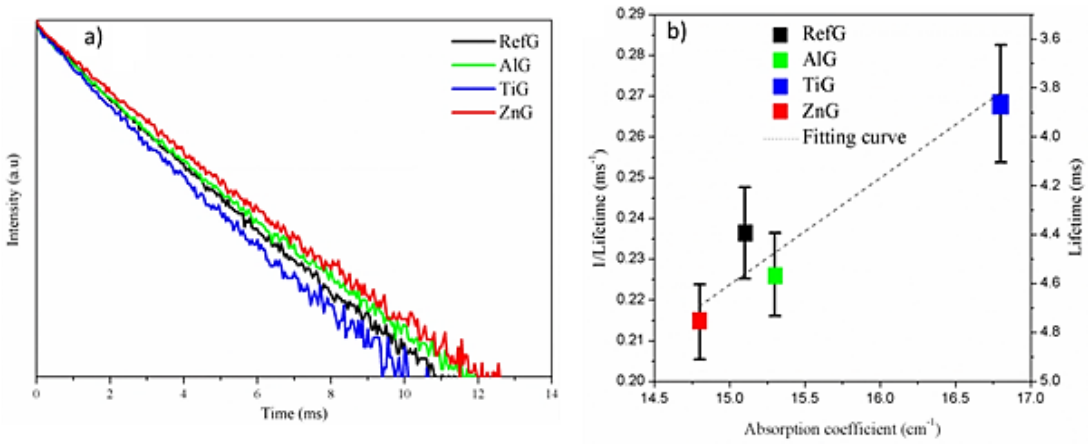

Figure 4.7 (a) Room temperature decay curves of the $^4I_{13/2}$ level of Er^{3+} ions in the glasses obtained under excitation at 980 nm. The intensity data are reported on a Log scale. (b) Decay rate, defined as the inverse of the Er^{3+}:$^4I_{13/2}$ level lifetime, as a function of the absorption coefficient of OH- vibration band at 2900 cm^{-1} of all the glasses. The experimental data were fitted through the formula reported in [350].

The AlG shows similar lifetime value as compared to the reference glass, whereas the TiG exhibits the shortest lifetime and the ZnG the longest one. The low lifetime

of TiG could be related to the slightly higher OH^- content in this glass as compared to the other ones.

The emission and normalized emission spectra, measured in the wavelength range 1400-1700 nm under excitation at the wavelength of 976 nm, are illustrated in Figure 4.8a and Figure 4.8b, respectively. Besides, the McCumber's emission cross-section spectra are also shown in Figure 4.8c.

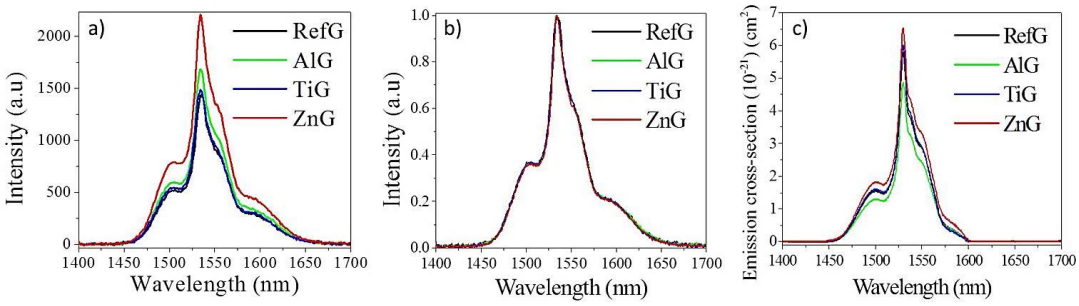

Figure 4.8 (a) Emission, (b) normalized emission and (c) emission cross-section spectra of the investigated glasses.

All spectra exhibit the typical emission band assigned to the Er^{3+} transition from $^4I_{13/2}$ to $^4I_{15/2}$. The ZnG exhibits the highest intensity of the relative emission and also the highest emission cross-sections at 1550 nm, whereas the TiG and AlG show the lowest intensity of relative emission at 1540 nm as compared to the RefG. The higher emission of the ZnG as compared to the other glasses cannot be related to the absorption properties of the glasses at 976 nm, as all the investigated glasses possess similar absorption cross-sections at this pump wavelength. It is not possible either to relate it to the OH^- groups, which are known to diminish the emission intensity by non-radiative phenomena [345], as the glasses have also similar OH^- content except for the TiG. Therefore, we believe that the different emission properties of the glasses could be related to the different Er^{3+} ions solubility in the glasses and so to the different network connectivity: the larger relative emission intensity and emission cross-section of the ZnG could be associated to a better solubility of the Er^{3+} ions in the ZnG due to the depolymerization of the network induced by the addition of ZnO. On the contrary, the addition of Al_2O_3 and TiO_2, which are suspected to increase the network connectivity, most probably reduces the Er-Er distance and so the Er^{3+} ions solubility. Finally, the shape of the emission band (see Figure 4.8b) is unaffected by the changes in glass composition, thus confirming that Al, Ti and Zn have no significant impact on the site of the Er^{3+} ions.

In summary, the phosphate network becomes more connected with the addition of Al_2O_3 and TiO_2 through the formation of P-O-Ti and P-O-Al linkages increasing the T_g. However, the addition of Al_2O_3 and TiO_2 had a slight impact on the spectroscopic (absorption and emission) properties. ZnO acted as a modifier depolymerizing the phosphate network. Due to its low concentration, the addition of ZnO did not show significant changes in the thermal and structural properties but

it increased the intensity of the emission at 1540 nm. As all the investigated glasses had similar absorption cross-section at the pump wavelength, the modification in the glass connectivity is thought to affect the Er^{3+} ions solubility and thus the emission properties of the glasses. Moreover, the investigated glasses possessed good thermal stability and are therefore promising for the fabrication of rare earth doped optical fibers.

4.2 Er^{3+}-doped glass-ceramics

This section aims to investigate the impact of the glass composition on the crystallization tendency of the glass and the effect of nucleation and growth of crystals on the structural and luminescence properties of Er^{3+}-doped phosphate glasses. The glass ceramics (GCs) had the same composition as the aforementioned glasses. Figure 4.9 shows the RefGCs, AlGCs, TiGCs and ZnGCs heat treated at T_g + 20 °C for 17 h and at T_p - 40 °C from 1 to 12 h.

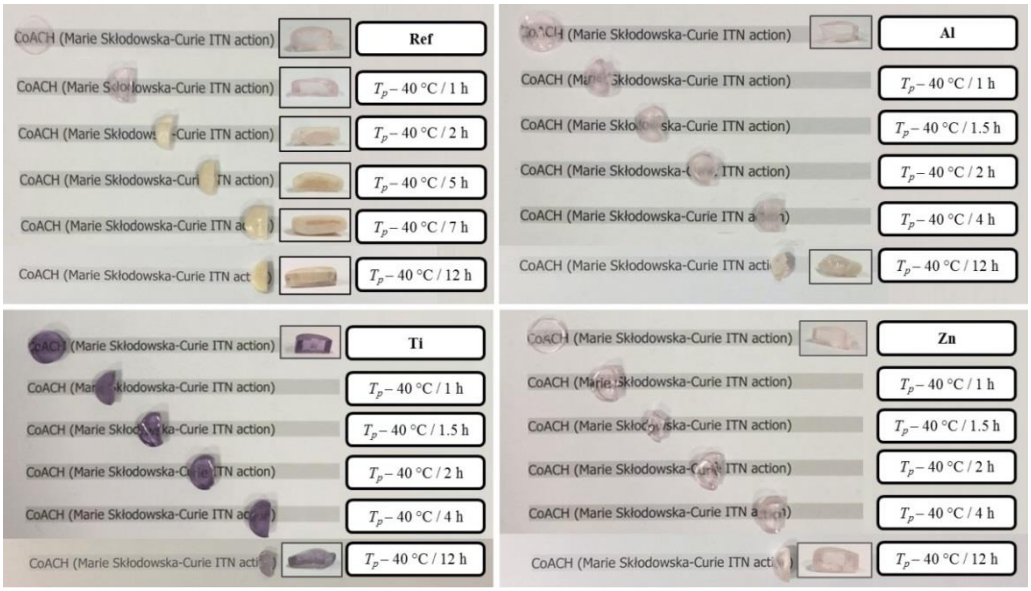

Figure 4.9 Picture of the GCs prior to and after different post heat treatments at T_g + 20 °C for 17 h and at T_p - 40 °C from 1 to 12 h.

As depicted in Figure 4.9, no noticeable signs of crystallization are observed by visual inspection in any investigated glasses when heat treated at their respective T_p - 40 °C for 1 h. After 5 h of post heat treatment, the RefGC starts to be opaque, which is a clear indication of full crystallization whereas the other GCs appear to be translucent, indicating that partial crystallization is present. When heat treated at T_p - 40 °C for 12 h, only the RefGC is fully crystallized, while all the other sample disks exhibit a ceramic appearance at the surface due to surface crystallization and a glassy appearance in the inner part. Besides, the thickness of the crystallized layer increases with the duration of the post heat treatment, in agreement with the results reported in [148].

Interestingly, the RefGC exhibits the highest crystallization rate, while the ZnGC is the least prone to crystallization. The difference in the crystallization tendency of the glasses can be related to their different structure. As explained in section 4.1, Zn ions act as modifiers leading to a depolymerization of the network, which most likely reduces the amount of nucleation sites and therefore decreases the crystallization tendency of the glass. The increase in the glass connectivity induced by the formation of P-O-Al/Ti links also seems to delay the crystallization in the AlGC and TiGC. Therefore, the addition of the metal oxides such as Al_2O_3, TiO_2 and ZnO in low concentration (~1.5 mol%) is responsible for the decrease of the glass crystallization tendency.

The crystals of the GCs were analyzed by EDS/FE-SEM. Figure 4.10 shows the EDS mapping and FE-SEM micrographs of the cross-section of the GCs after a heat treatment at T_g + 20 °C for 17 h and T_p - 40 °C for 12 h.

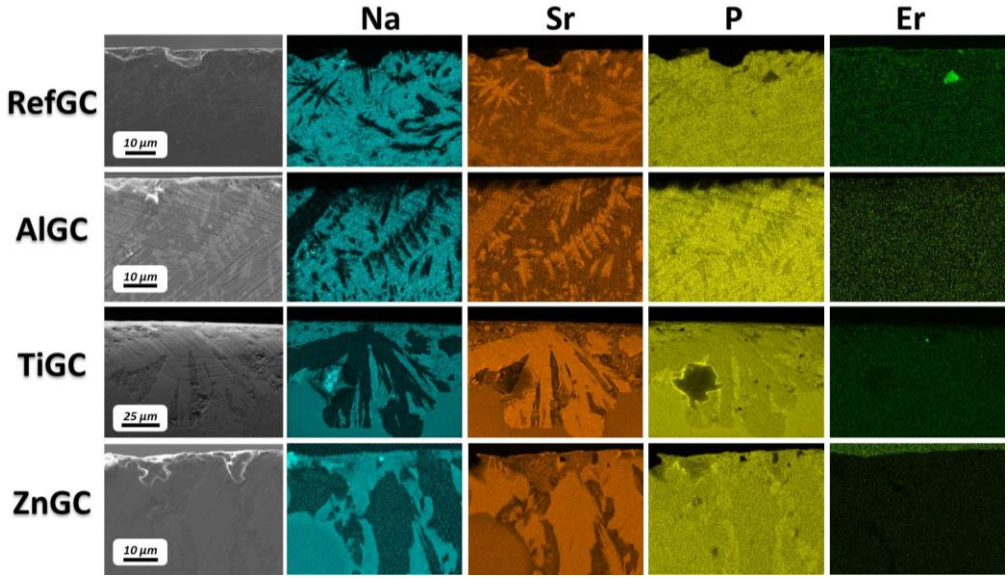

Figure 4.10 FE-SEM images and EDS mapping of the cross-section of the GCs after the heat treatment at T_g + 20 °C for 17 h and T_p - 40 °C for 12 h (brighter areas indicate higher element content).

The external surface of the samples, displayed at the top of the images, highlights evident signs of surface crystallization. The crystals precipitating in the RefGC and AlGC seem to grow dendritically with split ends, whereas in the case of TiGC and ZnGC the crystals show rounded borders. Additionally, the EDS mapping clearly shows Sr-rich crystals surrounded by Na-rich crystals. The Sr-rich crystals seem to have a lower P content than the Na-rich ones. The Er^{3+} ions seem to be homogeneously distributed in all the GCs but their concentration is probably too small to show clear variations.

The crystalline phases were identified by XRD. The XRD patterns (see Figure 4.11) of the GCs after different heat treatments at T_p - 40 °C.

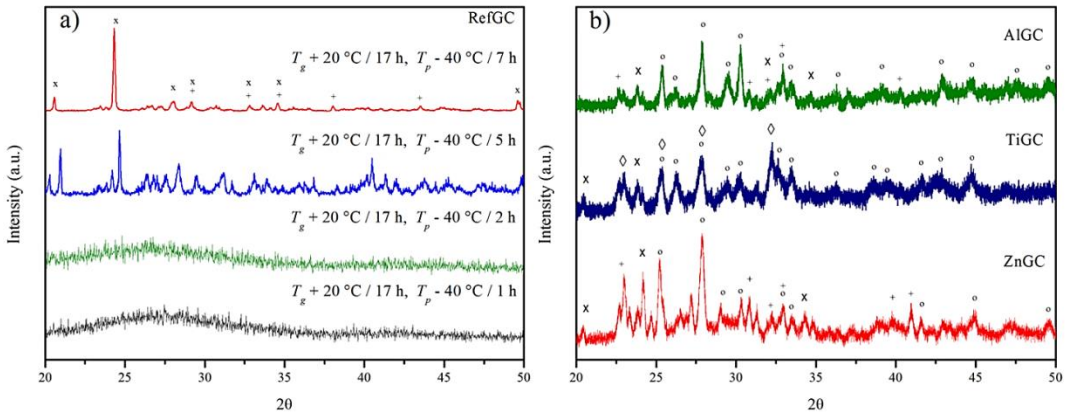

Figure 4.11 (a) XRD patterns of the RefGC after different post heat treatments and (b) of AlGC, TiGC and ZnGC after the heat treatments at T_g + 20 °C for 17 h and T_p - 40 °C for 12 h (b). The following crystal phases were identified: x $Sr(PO_3)_2$ [00-044-0323], + $NaSrPO_4$ [00-033-1282], o $Sr_3P_4O_{13}$ [04-015-2023] and ◊ $Ti(P_2O_7)$ [04-012-4504].

As it can be observed from Figure 4.11a, the intensity of the peaks rises when the duration of the heat treatment at T_p - 40 °C increases from 1 to 7 h confirming that a longer heat treatment induces the crystal growth. The XRD peaks of the RefGC are primarily related to $Sr(PO_3)_2$ [00-044-0323], while the other ones refer to the crystalline phase $NaSrPO_4$ [00-033-1282]. Similar crystals were found to precipitate in glasses with similar compositions [148].
The XRD patterns of the AlGC, TiGC and ZnGC heat treated at T_p - 40 °C for 12 h are presented in Figure 4.11b. The patterns exhibit the same sharp peaks related to $Sr(PO_3)_2$ [00-044-0323] and $NaSrPO_4$ [00-033-1282] and also additional peaks attributed to $Sr_3P_4O_{13}$ [04-015-2023]. A new phase identified as $Ti(P_2O_7)$ [04-012-4504] was detected in the TiGC. It is interesting to point out that none of the crystalline phases contain Er^{3+} ions in their structure.

The micro-Raman spectra of the edge crystalline (close to the surface) and inner glassy parts of the RefGC sample heat treated at T_p - 40 °C for 5 h are shown in Figure 4.12. The spectra were normalized at the maximum point at 1170 cm^{-1}.

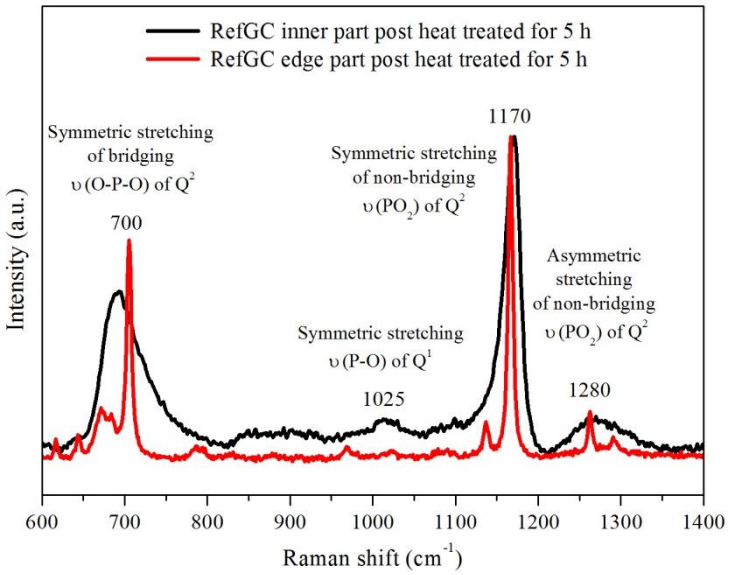

Figure 4.12 Micro-Raman spectra of the inner and edge parts of the RefGC post heat treated at T_p - 40 °C for 5 h.

The spectrum of the glassy part of the RefGC exhibits defined bands at ~ 700, 1170 and 1280 cm^{-1} and smaller bands between 800 and 1110 cm^{-1}. A complete analysis of the Raman spectrum of the glass can be found in section 4.1. The Raman spectrum measured in the crystal part exhibits a reduction between 25 and 15% of the full width at half maximum (FWHM) of the bands attributed to the Q^2 groups, confirming the crystallization. Interestingly, the ratio Iv_{sym}(P-O-P) / Iv_{sym} (PO_2) between the intensities of the peaks at 700 and 1170 cm^{-1} increases from 0.5 to 0.7 after the heat treatment. At the same time, a depletion of the peak at 1025 cm^{-1} associated with the terminal Q^1 groups is observed. Thus, the decrease of the Q^1 groups and the narrowing of the bands related to Q^2 groups might be an evidence of an increase in the polymerization of the phosphate network after the heat treatment.

The absorption spectra of the RefGCs prior to and after the heat treatments at T_p - 40 °C for 5 an 7 h are reported in Figure 4.13a. A magnification of the absorption spectra and normalized absorption spectra in the range between 1450 and 1600 nm is shown in Figure 4.13b and Figure 4.13c.

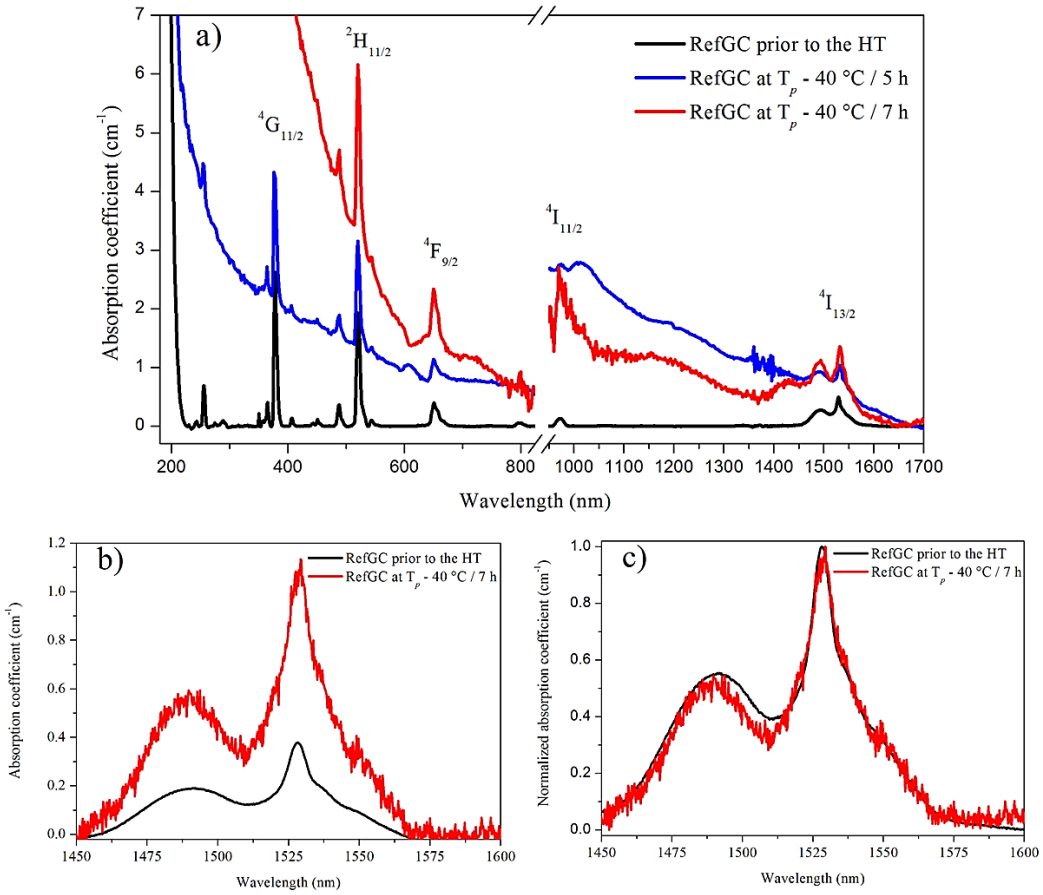

Figure 4.13 Absorption spectra of the RefGC prior to and after the heat treatments at T_g + 20 °C for 17 h and T_p - 40 °C for 5 and 7 h (a). Absorption band (b) and normalized absorption band (c) in the range between 1450 and 1600 nm of the RefGC prior to and after the heat treatment at T_g + 20 °C for 17 h and T_p - 40 °C for 7 h.

The heat treatments induce a shift of the absorption edge towards longer wavelengths and an increase in the absorption coefficient at 1530 nm. Similar results were obtained for the other GCs. According to the scattering theory [156], crystals with a large size produce differences between the refractive index of the crystal and of the glassy parts, which provide high scattering. Thus, the opacity of the GCs as well as their absorption coefficient increase along with the crystal size. No significant variations in the shape of the normalized absorption band were observed, indicating that the formation of crystals does not influence the site of the Er^{3+} ions.

The emission spectra of the glasses prior to and after the heat treatment were measured under excitation at 976 nm. Figure 4.14 depicts the normalized emission spectrum of the GCs prior to and after the heat treatment at T_g + 20 °C for 17 h and T_p - 40 °C for 12 h.

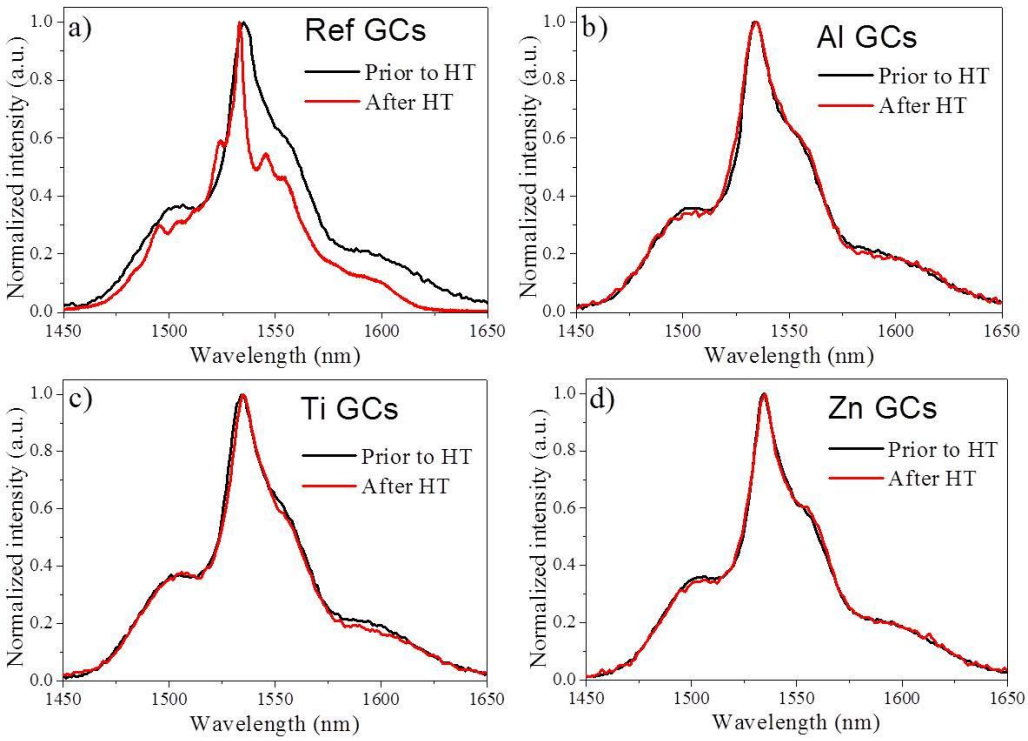

Figure 4.14 Normalized emission spectra of the RefGC (a), AlGC (b), TiGC (c) and ZnGC (d) prior to and after the heat treatment at T_g + 20 °C for 17 h and T_p - 40 °C for 12 h.

The spectra exhibit the typical emission band assigned to the Er^{3+} ion transition from $^4I_{13/2}$ to $^4I_{15/2}$. The heat treatment was responsible for a noticeable change in the shape of the emission band only for the RefGC (see Figure 4.14a). The emission peak at 1530 nm became narrower and was found to slightly shift to lower wavelengths. Moreover, the intensity of the shoulder at ~ 1500 nm and ~ 1550 nm slightly decreased after the heat treatment. Therefore, the Er^{3+} ions are supposed to be located in the crystals precipitating in the RefGC. However, the other GCs show negligible changes in their emission spectra after heat treatment. As no sharp peaks can be observed in the emission spectra of the AlGC, TiGC and ZnGC, the crystals precipitating in these GCs seem to be Er^{3+} ions free. As a consequence, the Er^{3+} ions are expected to remain in the amorphous glassy part.

The fluorescence lifetime values of the Er^{3+}:$^4I_{13/2}$ level upon 976 nm excitation for all the GCs are listed in Table 4.2.

Heat treatment	τ [ms] ± 0.20 ms RefGC	τ [ms] ± 0.20 ms AlGC	τ [ms] ± 0.20 ms TiGC	τ [ms] ± 0.20 ms ZnGC
T_p - 40 °C / 1 h	4.23	4.57	3.73	4.72
T_p - 40 °C / 2 h	4.35	4.54	3.74	4.70
T_p - 40 °C / 5 h	4.43	----	----	----
T_p - 40 °C / 7 h	4.80	----	----	----
T_p - 40 °C / 12 h	6.16	4.46	3.70	4.62

Table 4.2 Excited state $^4I_{13/2}$ lifetime values of the GCs under laser excitation at 976 nm.

An increase in the duration of the heat treatment at T_p - 40 °C leads to an increase of the Er^{3+}:$^4I_{13/2}$ lifetime in the RefGC, while no changes in the lifetime values were observed for the AlGC, TiGC and ZnGC, in agreement with the emission measurements. The increase in the lifetime values of the RefGC sample is attributed to a change in the local environment surrounding the Er^{3+} ions. This could be associated to the incorporation of Er^{3+} ions inside the crystalline phases or to an increase in the interionic distance within the amorphous matrix.

In summary, GCs were successfully fabricated by the standard melt-quenching technique followed by a heat treatment. The RefGCs showed the highest crystallization rate as compared to the other glasses. Based on the XRD and EDS mapping, $Sr(PO_3)_2$ appeared to be the main phase of the crystals in the Er^{3+}-doped GCs. Additionally, the micro-Raman spectra displayed an increase of the polymerization of the phosphate network due to the crystal growth. The fully crystallized RefGC heat treated at T_g + 20 °C for 17 h and T_p - 40 °C for 12 h showed the longest lifetime. Moreover, the changes in the absorption and in the emission bands after the heat treatment indicate that the site of the Er^{3+} ions in the RefGC is strongly modified by the heat treatment. However, no change in the lifetime values and in the shape of the emission band located at around 1550 nm was observed after the heat treatment for all the other GCs indicating that the Er^{3+} remain in the amorphous part. GCs constitute an attractive approach towards the development of new materials for photonic applications.

4.3 Er^{3+}-doped particles containing glasses

These glasses were processed by adding Er^{3+}-doped particles in the glass batch or melt.

4.3.1 Er^{3+}-doped particles

Different particles were prepared with various Er^{3+} concentrations. The purpose of varying the concentration of Er_2O_3 is to study possible changes in the structural and spectroscopic properties of the particles. Besides, the study explored particles having high concentration of Er_2O_3 to allow the detection of the Er^{3+} luminescence when the particles are added in the glasses. Thus, the assessment of the particles survival after the melting can be achieved by comparing the properties of the particles-containing glasses with the corresponding particles. The compositions of the Er^{3+}-doped particles synthesized during this thesis are listed in Table 4.3.

	[Al_2O_3] $_{100-x}$	[TiO_2] $_{100-x}$	[ZnO] $_{100-x}$	[ZrO_2] $_{100-x}$
x = Er_2O_3 mol%	1	0.5	1	1
	7	2	14.3	14.3
		5		
		10		
		14.3		

Table 4.3 Composition of the Er^{3+}-doped Al_2O_3, TiO_2, ZnO and ZrO_2 particles.

4.3.1.1 Er^{3+}-doped Al_2O_3 particles

Al_2O_3 particles doped with 1 and 7 mol% of Er_2O_3 were prepared by the sol-gel method. A calcination step at 1300 °C for 5 h was used after the sol-gel synthesis.

The morphology and composition of the samples was assessed by EDS/FE-SEM. FE-SEM images of the Er^{3+}-doped Al_2O_3 as-prepared particles are shown in Figure 4.15.

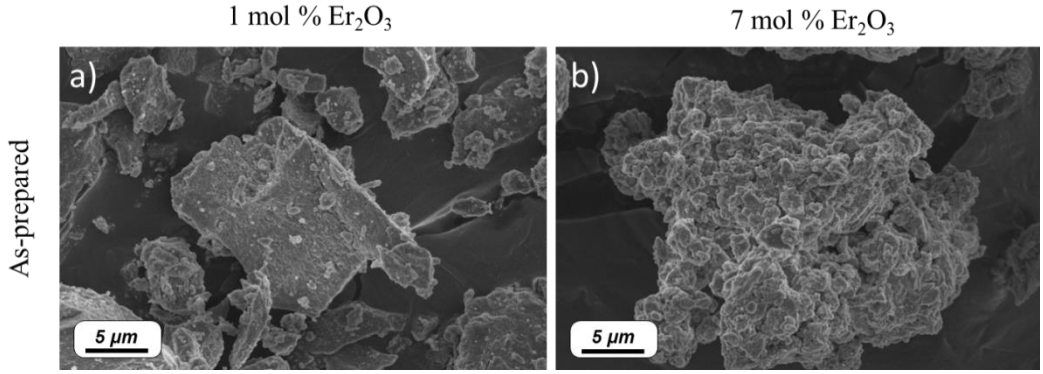

Figure 4.15 FE-SEM pictures of 1 mol% Er^{3+}-doped Al_2O_3 (a) and 7 mol% (b) Er^{3+}-doped Al_2O_3 particles as-prepared.

The as-prepared Er^{3+}-doped Al_2O_3 samples show agglomerates and microparticles with a size bigger than 5 µm (see Figure 4.15a and Figure 4.15b). After the calcination at 1300°C for 5 h, the microparticles showed similar sizes as the as-prepared particles, ranging from 5 to 100 µm. Additionally, based on the EDS analyses, the composition the particles was in agreement with the nominal one.

The crystalline phases of the calcined particles were identified using XRD. The XRD patterns of 1 and 7 mol% Er_2O_3-doped Al_2O_3 samples calcined at 1300 °C for 5 h are shown in Figure 4.16.

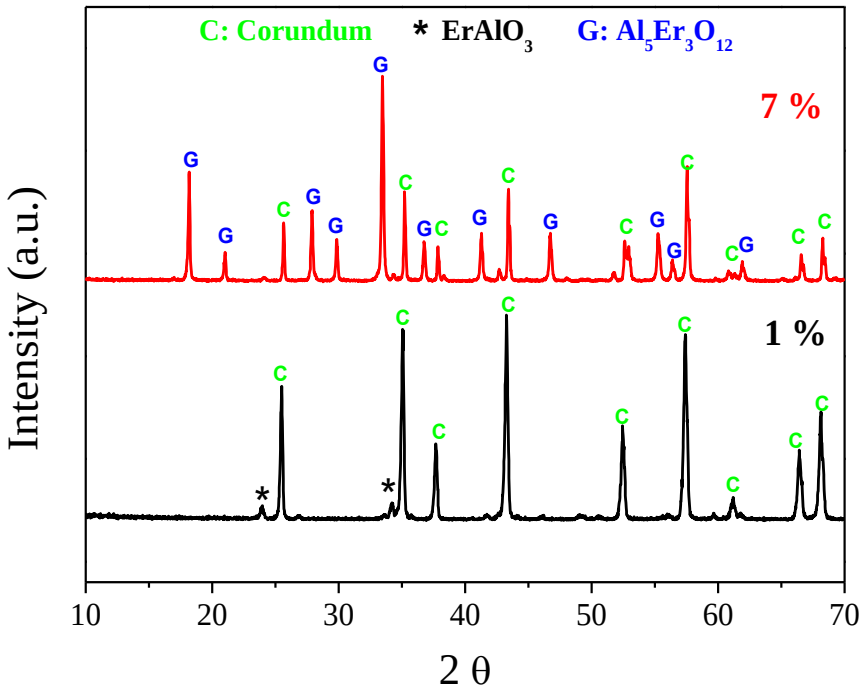

Figure 4.16 XRD patterns of Er^{3+}-doped Al_2O_3 calcined particles with the reference pattern of $Al_5Er_3O_{12}$ [ICSD 170147] and corundum [98-001-1621] crystalline phases.

Corundum is the predominant phase when adding 1 mol% of Er_2O_3. A small amount of the crystalline phase perovskite ($ErAlO_3$) (JCPDS No. 24-0396) [187] is also part of the particles. When increasing the concentration of Er_2O_3 to 7 mol%, a new phase corresponding to the erbium aluminum garnet ($Er_3Al_5O_{12}$) appears [188].

The IR emission spectra of the Al_2O_3 particles ranging from 1450 nm to 1700 nm were measured under excitation at 976 nm (see Figure 4.17).

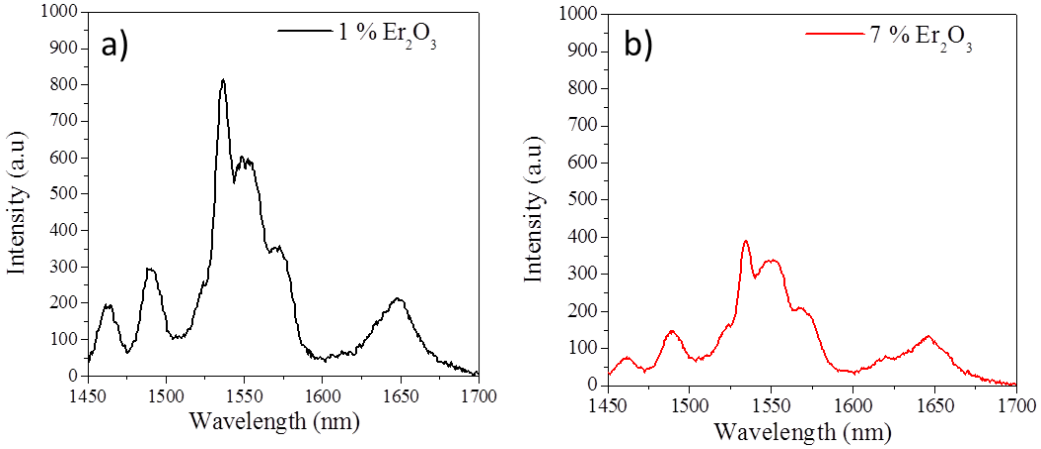

Figure 4.17 Emission spectra of (a) 1 and (b) 7 mol% Er^{3+}-doped Al_2O_3 particles calcined at 1300°C for 5h.

Both spectra show similar band shape, corresponding to the emission band assigned to the Er^{3+} transition from $^4I_{13/2}$ to $^4I_{15/2}$. The sharp peaks correspond to the stark splitting produced due to the crystalline environment [351]. It should be pointed out that the intensity of the emission spectra cannot be compared due to the different morphology of the samples, although their shape gives valuable information on the particles properties.

Additionally, the fluorescence lifetime values of the Er^{3+}:$^4I_{13/2}$ level upon 976 nm excitation were measured. The lifetime values of the 1 and 7 mol% Er^{3+}-doped Al_2O_3 particles were 4.43 and 3.32 ms, respectively. The estimated error was calculated as the standard deviation of the measurements of the individual lifetimes (~ ± 0.2 ms).. The lower lifetime of the 7 mol% Er^{3+}-doped Al_2O_3 particles is expected due to the quenching effect at high concentration of Er_2O_3 [352].

Lastly, the normalized up-conversion fluorescence spectra of the Er^{3+}-doped Al_2O_3 particles calcined are presented in Figure 4.18.

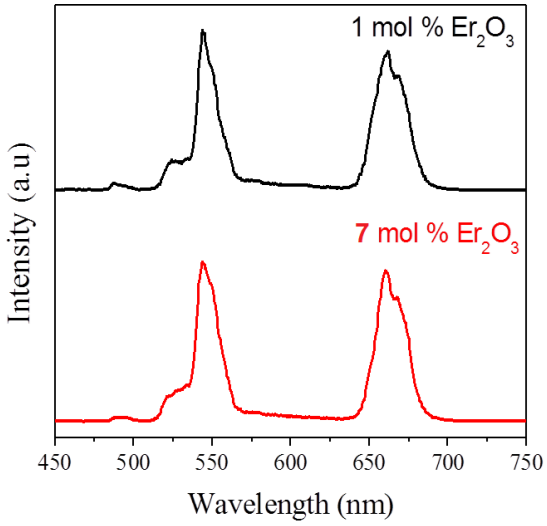

Figure 4.18 Normalized up-conversion emission spectra of the Al_2O_3 particles doped with 1 and 7 mol% of Er_2O_3 and calcined at 1300 °C for 5 h. Both spectra were normalized to 1 at 550 nm.

As shown from the spectra, both Al_2O_3 particles show a similar shape with a green emission band at 550 nm and a red emission band at 660 nm. The process of the up-conversion can be found in section 2.2.1. It should be pointed out that during the measurement of the up-conversion, both samples exhibited a strong green emission in the visible, due to the high sensitivity of the green light to the human eyes.

In summary, the Er^{3+}-doped Al_2O_3 particles formed big microparticles with a size dimensions between 5 and 100 μm. The samples with 1 mol% of Er_2O_3 presented the corundum crystalline phase, while the sample with 14.3 mol% of Er_2O_3 presented a mixture of corundum and erbium aluminum garnet ($Er_3Al_5O_{12}$) phases. Both samples showed strong emission intensity in the IR and in the visible

region. Thus, these Al_2O_3 particles seem to be good candidates for the incorporation into phosphate glasses.

4.3.1.2 Er^{3+}-doped TiO_2 particles

TiO_2 particles were synthesized by sol-gel method with 0.5, 2, 5, 10 and 14.3 mol% of Er_2O_3.

FE-SEM micrographs of the 0.5, 2 and 14.3 mol% Er_2O_3–doped TiO_2 particles both as-prepared and calcined at 800 °C for 2 h are shown in Figure 4.19.

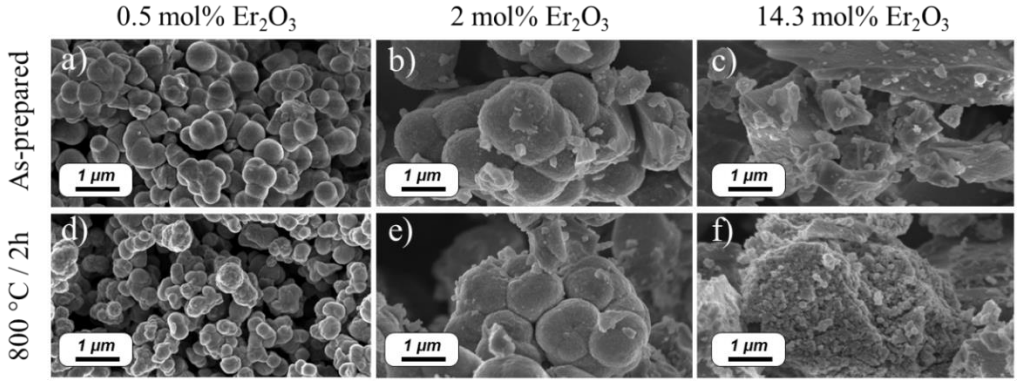

Figure 4.19 FE-SEM micrographs of 0.5, 2 and 14.3 mol% Er_2O_3–doped TiO_2 particles as-prepared (a, b, c) and calcined at 800 °C for 2 h (d, e, f), respectively.

The morphology of the particles changed when increasing the amount of Er^{3+} ions. The 0.5 and 2 mol% Er_2O_3-doped particles resulted to be spherical, whereas at higher Er_2O_3 concentration the particles formed agglomerates with irregular shape. At the same time, the diameter of the spherical particles increased from 400 nm to 1.5 µm as the Er_2O_3 concentration raised from 0.5 to 2 mol%. This might be caused by the difference in ionic radii of Er^{3+} and Ti^{4+} ions. Indeed, the ionic radius of the Er^{3+} ions for coordination numbers equal to 6 and 8 are 0.89 and 1 Å, respectively, whereas the one of Ti^{4+} is 0.61 Å [171]. Thus, the Er^{3+} doping affects the crystalline lattice of the particles, modifying their morphology [212,353,354].

In addition, the FE-SEM pictures of the particles doped with 2 mol% of Er_2O_3 prior to and after the calcination at different temperatures are shown in Figure 4.20.

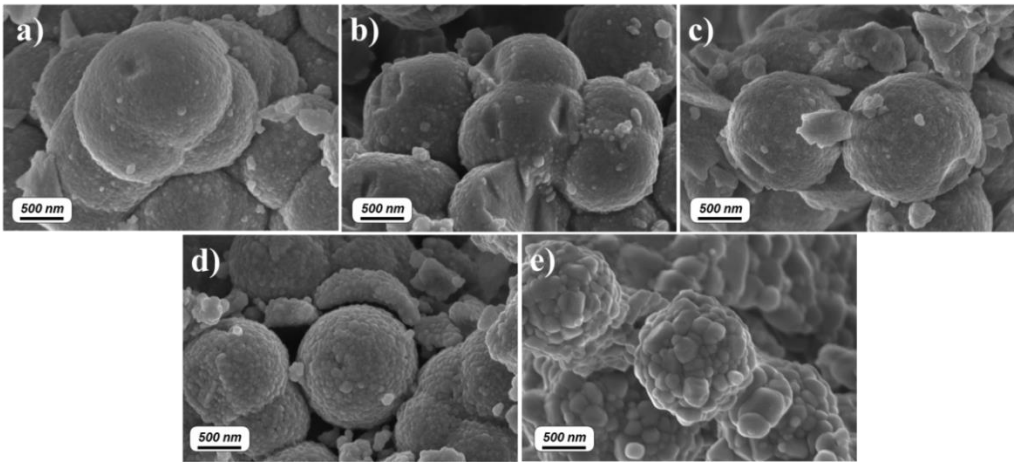

Figure 4.20 FE-SEM micrographs of the 2 mol% Er_2O_3–doped TiO_2 particles as-prepared (a) and calcined at 700 (b), 800 (c), 900 (d) and 1000 °C (e) for 2 h.

All the particles exhibited similar spherical shape, ranging from 1.2 to 1.7 μm, independently of the heat treatment. Interestingly, the increase in the calcination temperature led to the growth of the crystallite size. These crystal grains possess a dimension of around 30, 40 and 50 nm for samples calcined at 700, 800 and 900 °C, respectively, while a diameter of 250 nm is reached when using a calcination temperature of 1000 °C.

The crystalline phases of the TiO_2 particles are shown in Figure 4.21a.

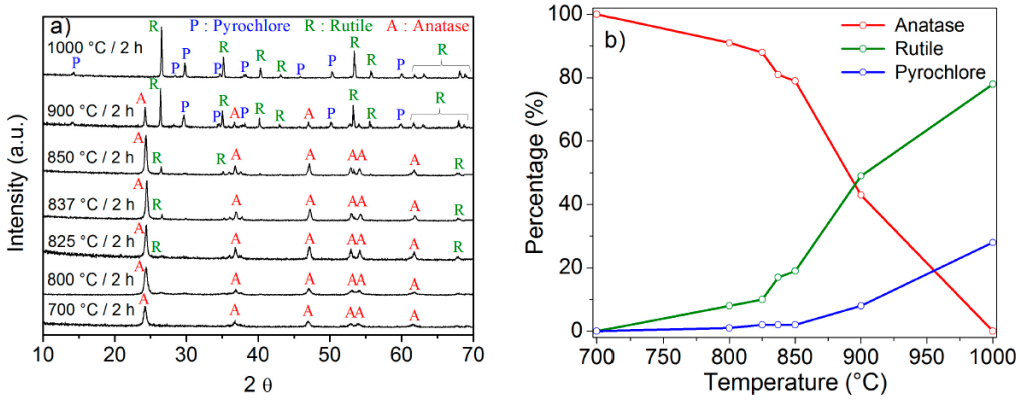

Figure 4.21 (a) XRD patterns of the 2 mol% Er_2O_3–doped TiO_2 particles calcined at different temperatures. The diffraction peaks of anatase, rutile and pyrochlore ($Er_2Ti_2O_7$) are indexed in the figure as A, R and P, respectively. (b) Phase composition of the TiO_2 samples calcined at different temperatures.

The diffraction patterns correspond to the following crystalline phases: anatase (ICSD file No. 00-021-1272), rutile (ICSD file No. 00-021-1276) and pyrochlore (ICSD file No. 01-073-1647). The decrease of the Full Width at Half Maximum (FWHM) values along with an increase in the calcination temperature clearly shows that the crystallinity of the samples is greatly enhanced when increasing the temperature [355]. The XRD pattern of the sample calcined at 700 °C shows only the anatase phase. The anatase to rutile phase transformation and pyrochlore phase

started to appear at 800 °C. In the case of the particles calcined at 900 °C, the three phases are simultaneously present, being the rutile the major one (the main). Lastly, at 1000 °C, the pyrochlore and rutile phases are the prominent ones.
The phase composition of the samples was semi-quantitatively assessed using the Reference Intensity Ratio (RIR) method [356]. The percentages of the anatase, rutile, and pyrochlore phases present in the TiO_2 samples are shown in Figure 4.21b.

Figure 4.22a shows the XRD patterns of the TiO_2 particles calcined at 800 °C for 2 h doped with different concentration of Er_2O_3.

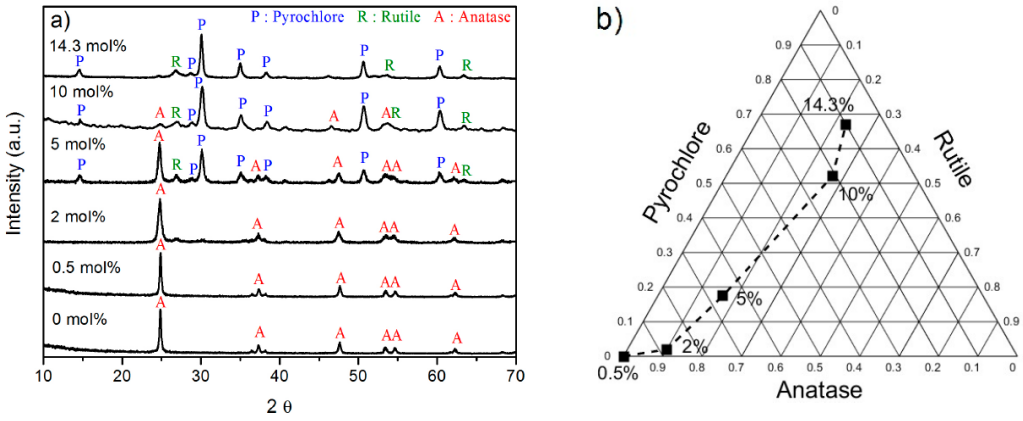

Figure 4.22 (a) XRD patterns of the 0.5, 2, 5, 10 and 14.3 mol% Er_2O_3–doped TiO_2 particles calcined at 800 °C for 2 h. The diffraction peaks of anatase, rutile and pyrochlore are indexed in the figure. (b) Ternary diagram showing the proportion of the crystalline phases present in the Er-doped particles calcined at 800 °C for 2 h.

The 0.5 mol% Er_2O_3-doped samples show the typical XRD pattern of anatase. At higher concentrations of Er_2O_3, anatase, rutile and pyrochlore phases are simultaneously present: at a concentration of 2 mol% the anatase phase is predominant, whereas at 5 mol% the anatase and pyrochlore phases are the prominent ones. At 10 and 14.3 mol%, the major phase seems to be the pyrochlore. Therefore, the addition of Er^{3+} ions into the TiO_2 matrix seems to retard the anatase to rutile phase transformation. Besides, as reported in [357], the limited solubility of the Er^{3+} ions in the TiO_2 matrix led to the formation of the pyrochlore phase, which tends to coexist with the rutile phase. It should be pointed out that no peaks related to the Er_2O_3 were observed in the XRD measurements of all the samples.
The phase composition of the samples was semi-quantitatively calculated using the RIR method. The ternary diagram showing the proportion of the crystalline phases present in the TiO_2 samples doped with different concentrations of Er_2O_3 is shown in Figure 4.22b.

Figure 4.23a and b show, respectively, the normalized emission spectra centered at around 1550 nm and the lifetime values corresponding to the Er^{3+}:$^4I_{13/2} \rightarrow {}^4I_{15/2}$ of the Er-doped TiO_2 particles calcined at 800 °C for 2 h doped with different concentrations of Er_2O_3.

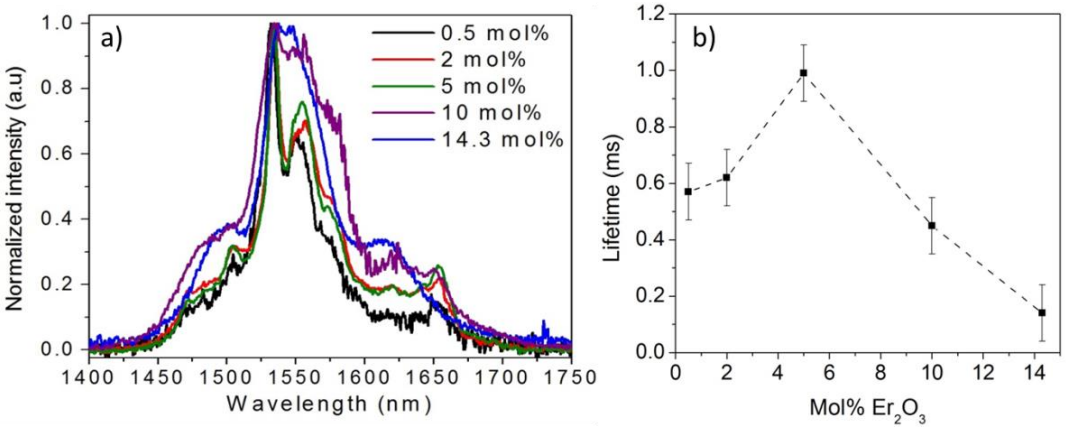

Figure 4.23 (a) Normalized emission spectra and (b) lifetime values of the TiO_2 particles doped with different concentrations of Er_2O_3 and calcined at 800 °C for 2 h.

The shape of the emission spectrum is maintained for all the samples except for the ones doped with 10 and 14.3 mol% of Er_2O_3, where the $^4I_{13/2}$ to $^4I_{15/2}$ transition peak becomes broader most probably due to the presence of the pyrochlore phase, in agreement with [201].

The lifetimes of the TiO_2 particles doped with 0.5, 2, 5, 10 and 14.3 mol% of Er_2O_3 and calcined at 800 °C for 2 h were 0.57, 0.62, 0.99, 0.45 and 0.14 ms. The estimated error was calculated as the standard deviation of the measurements of the individual lifetimes (~ ± 0.10 ms). The 5 mol% Er_2O_3-doped TiO_2 particles exhibited the highest lifetime. For this concentration, both the rutile and pyrochlore phases are present, together with the anatase phase. The presence of rutile and pyrochlore phases is thought to decrease the amount of Er^{3+} ions in the anatase phase, thus causing an increase in the radiative emission from the anatase phase as a consequence of the reduction of the quenching.

The emission spectra and lifetime values under an excitation wavelength of 976 nm of the sample doped with 2 mol% of Er_2O_3 calcined at different temperatures are presented in Figure 4.24. In this case the emission intensities were compared due to the similar particle shape and composition.

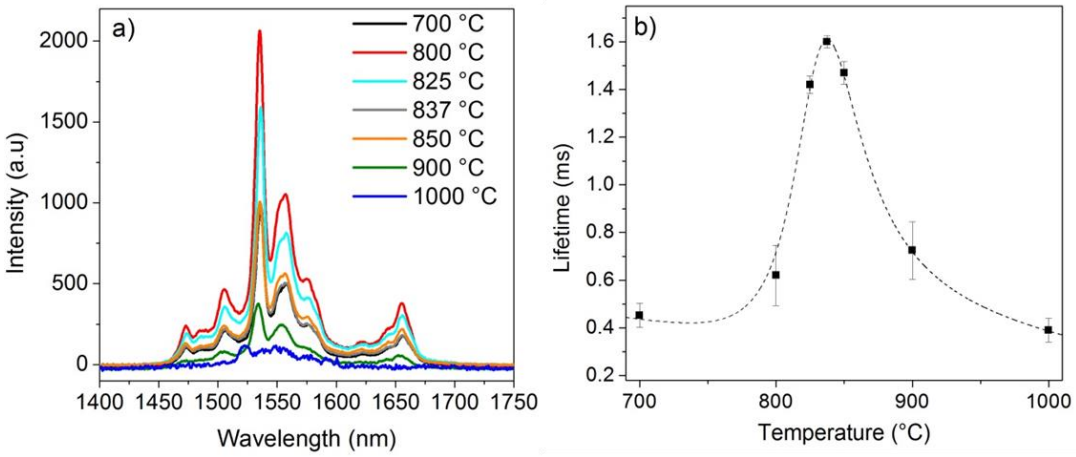

Figure 4.24 (a) Emission spectra and (b) lifetime values of the 2 mol% Er_2O_3-doped TiO_2 particles calcined at 700, 800, 825, 837.5, 850, 900 and 1000 °C for 2 h.

An intense emission was observed from the sample calcined at 800 °C, whereas the samples heat treated at 900 and 1000 °C displayed lower emission intensity. The lifetime values of the Er^{3+}:$^4I_{13/2}$ level in the TiO_2 particles calcined at 700, 800, 825, 837 ,850, 900 and 1000 °C for 2 h were 0.45, 0.62, 1.42, 1.60, 1.47, 0.73 and 0.39 ms, respectively. The estimated error was calculated as the standard deviation of the measurements of the individual lifetimes. The dependence of the lifetime on the calcination temperature could be explained by the presence of the pyrochlore phase and the reduction of the anatase phase in the particles. Surprisingly, the sample calcined at 825, 837 and 850 °C are characterized by the highest lifetime value, even though the pyrochlore phase is present in their structure. Nonetheless, the emission intensities of the samples heat treated at 825, 837 and 850 °C are clearly weaker than the one exhibited by the sample calcined at 800 °C. Unlike the anatase phase, the rutile phase is known to reduce the luminescence of Er^{3+} ions [358,359]. The occurrence of the rutile and pyrochlore phases together in the samples calcined at 825, 837 and 850 °C might thus cause a decrease in the emission intensity.

The normalized up-conversion spectra of the Er_2O_3-doped TiO_2 particles excited at 976 nm is shown in Figure 4.25a. The spectra were normalized to 1 at 550 nm ($^4S_{3/2}$ to $^4I_{15/2}$ transition). Besides, the integral area ratio of the red/green emissions bands is shown in Figure 4.25b.

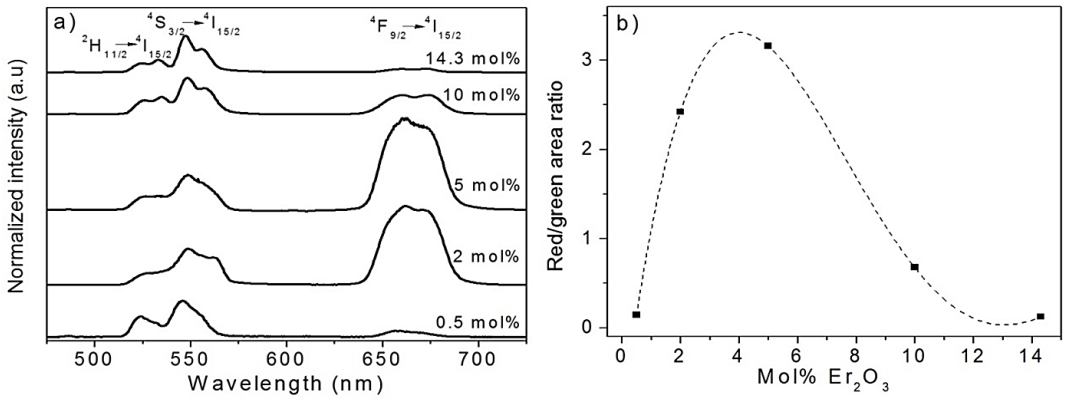

Figure 4.25 (a) Normalized up-conversion emission spectra of the TiO_2 particles doped with different concentrations of Er_2O_3 and calcined at 800 °C for 2 h. (b) Integral area ratio of the red/green emissions bands.

At very low dopant concentration (0.5 mol%), the green emission is stronger than the red emission. However, at 2 and 5 mol% of Er_2O_3, strong red emission resulting from the $^4F_{9/2}$ to the $^4I_{15/2}$ transition is observed. However, for larger Er_2O_3 content, the green emission is favored again. Previous studies [360,361] have reported the increase of the ratio of the red/green emission intensities with the increasing of the Er^{3+} concentration from 0 to 10 % of Er^{3+} in TiO_2 particles. However, most of the studies were performed at low concentrations of Er^{3+} ions, where no presence of the pyrocholore phase was evidenced. In this study, at 10 and 14.3 mol% of Er_2O_3, the green emission at 550 nm was predominant. This strong green emission at high Er^{3+} ion levels is thought to be associated with the huge amount of the pyrochlore phase, which enhances the up-conversion in the green.

As for the 2 mol% Er_2O_3-doped TiO_2 particles calcined at different temperatures, their normalized up-conversion fluorescence spectra and the integral area ratio of the red/green emissions bands are shown in Figure 4.26.

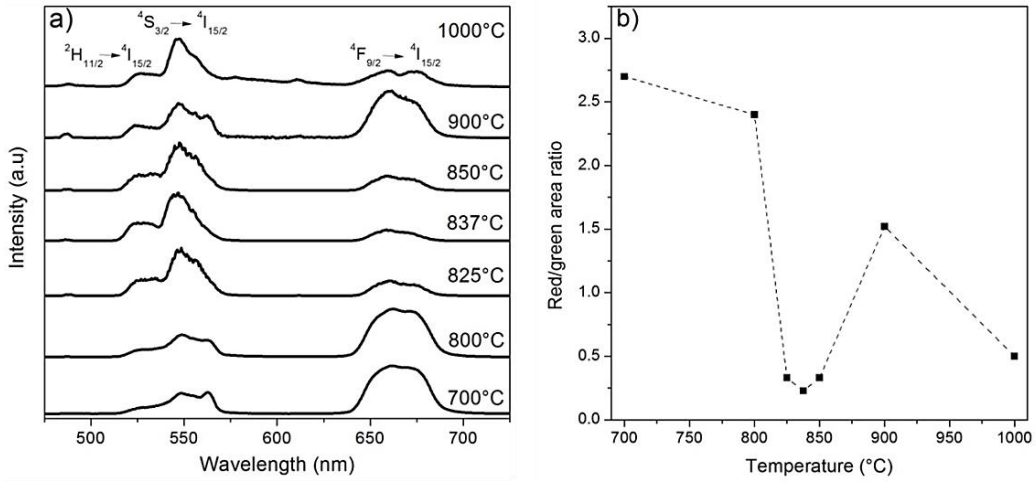

Figure 4.26 (a) Normalized up-conversion emission spectra of the 2 mol% Er_2O_3-doped TiO_2 particles calcined at 700, 800, 825, 837, 850, 900 and 1000 °C for 2 h. (b) Integral area ratio of the red/green emissions bands.

The spectra of the TiO_2 particles calcined at 700 and 800 °C show similar shape, and both exhibit a high intensity ratio of the red/green emissions. This ratio decreases at higher calcination temperatures, being the samples calcined at 825, 837 and 850 °C the ones with the lowest red emission. Interestingly, Patra *et al.* [360] obtained the maximum up-conversion emission intensity with Er^{3+}-doped TiO_2 particles calcined at 800 °C, when both the anatase and the rutile phases were present. In our case, the samples calcined at 700 and 800 °C possess the highest intensity ratio of the red/green emissions, whereas at higher temperatures the ratio considerably diminishes, probably due to the presence of the pyrochlore phase.

In conclusion, the surface roughness and the grain size of the particles were found to increase with the rise in the calcination temperature, while a change in the particles shape from spherical to irregular was observed upon increasing the Er_2O_3 content. Strong fluorescence in the IR region was displayed by the particles calcined at around 837 °C, while the ones heat treated at 1000 °C showed poor fluorescence properties, probably due to the formation of the pyrochlore ($Er_2Ti_2O_7$) phase. This crystalline phase also seems to be the reason for the decrease in the lifetime values of the particles doped with 10 and 14.3 mol% of Er_2O_3. Interestingly, the 5 mol% Er_2O_3-doped TiO_2 particles calcined at 800 °C for 2 h exhibited the highest lifetime value in the IR, while strong up-conversion luminescence was observed in all the synthesized samples. The intensity ratio of the red/green emissions was found to change as a function of the Er^{3+} ions concentration and the calcination temperature.

Overall, the crystalline phases of the particles can be tuned by varying the calcination temperature and the concentration of Er_2O_3, and thus, their luminescence properties. A clear correlation between the occurrence of one crystalline phase and the corresponding lifetime values is still to be demonstrated and further investigations will possibly allow optimizing the Er-doped particles parameters (e.g. rare earth ion concentration, calcination time and temperature) in order to maximize their performance for the envisaged applications.

4.3.1.3 Er^{3+}-doped ZnO particles

In this thesis, 1 and 14.3 mol% Er_2O_3-doped ZnO particles were prepared by the sol-gel technique with a calcination step at 1000°C for 2h.

The FE-SEM micrographs of the 1 and 14.3 mol% Er_2O_3–doped ZnO particles calcined at 1000 °C for 2 h are shown in Figure 4.27.

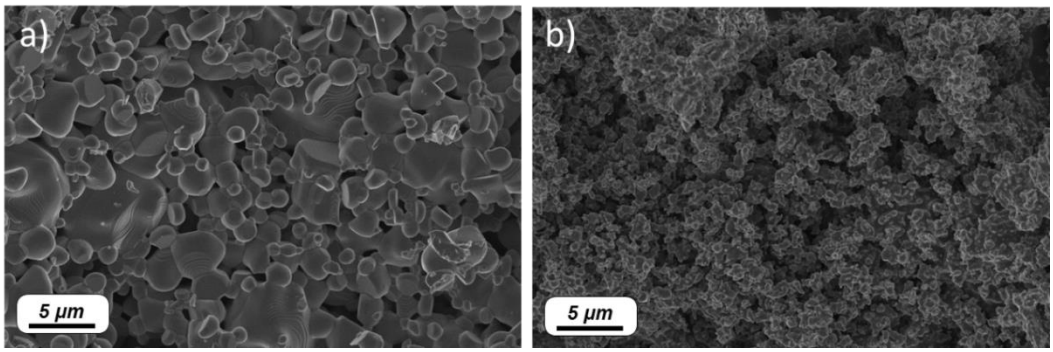

Figure 4.27 FE-SEM micrographs of (a) 1 and (b) 14.3 mol% Er_2O_3–doped ZnO particles calcined at 1000 °C for 2 h.

The FESEM images of the calcined samples revealed big agglomerates with a size of around 50 µm, which were not able to be captured in an image due to their big dimensions for the FESEM magnifications. As can be seen from Figure 4.27, at the surface of these agglomerates, smaller particles are close together to form the agglomerates.

The XRD patterns of the ZnO particles calcined at 1000 °C for 2 h doped with 1 and 14.3 mol% Er_2O_3 are presented in Figure 4.28.

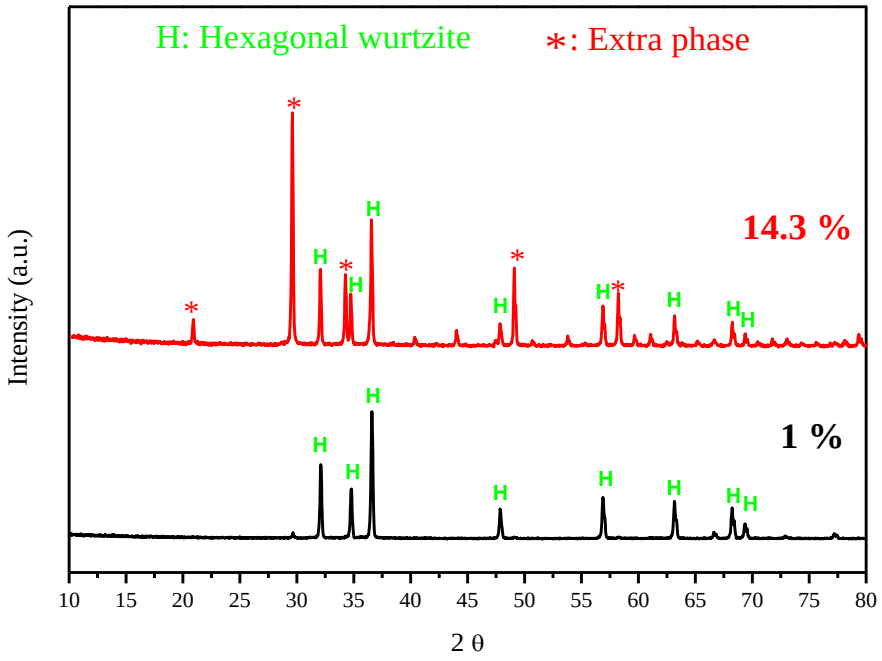

Figure 4.28 XRD patterns of 14.3 and 1 mol% Er_2O_3–doped TiO_2 particles calcined at 1000 °C for 2 h. The diffraction peaks of the corresponding crystalline phases are indexed in the figure.

The XRD pattern of 1% Er_2O_3 doped ZnO revealed the presence of hexagonal wurtzite structure of ZnO. Diffraction peaks correspond to the JCPDS data of the ZnO hexagonal wurtzite phase (Card No. 89-1397). Instead, in the XRD pattern of the 14.3 mol% Er_2O_3-doped ZnO particles, apart from the wurzite phase, a presence

of an extra phase related to the high content of Er_2O_3 is present. Similar results were reported by Rita John *et al.* [228], where the same unidentified phase was found in the XRD analysis of highly Er_2O_3 doped ZnO particles.

The emission spectra under an excitation wavelength of 976 nm of the samples doped with 1 and 14.3 mol% of Er_2O_3 calcined at 1000 °C for 2 h are represented in Figure 4.29a and b, respectively.

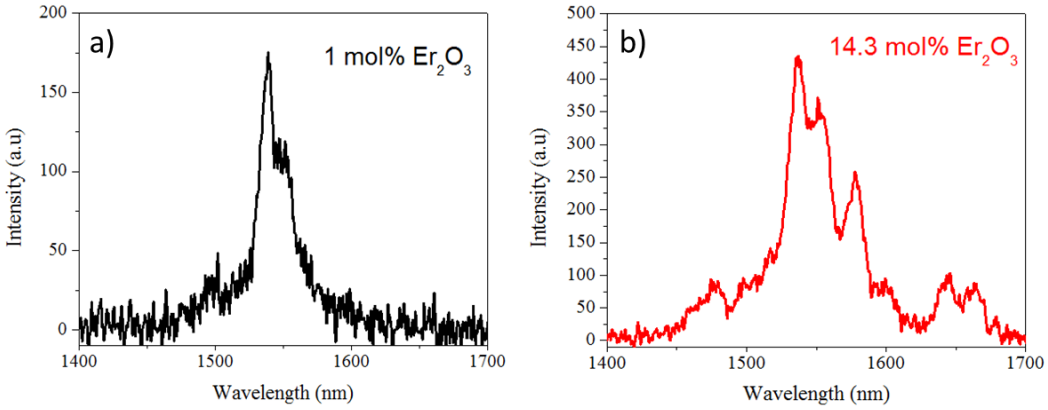

Figure 4.29 Emission spectra of the (a) 1 and (b) 14.3 mol% Er_2O_3-doped ZnO particles calcined at 1000 °C for 2 h.

Both spectra show the band at 1550 nm of the Er^{3+}:$^4I_{13/2} \rightarrow {}^4I_{15/2}$ transition. The emission spectra were not compared due to the difference in morphology and composition of the particles that can lead to difference in scattering and emission. As seen from Figure 4.29a, the sample with 1 mol% of Er_2O_3 presents a low intensity luminescence. However, the emission spectrum of the 14.3 mol% Er^{3+}-doped ZnO showed stronger emission with sharp peaks, corresponding to the stark splitting produced due to the crystalline environment [351]. However, the fluorescence lifetime values of the Er^{3+}:$^4I_{13/2}$ level upon 976 nm excitation were not able to be measured.

Lastly, the up-conversion emission spectra of the Er_2O_3-doped ZnO particles excited at 976 nm is shown in Figure 4.30.

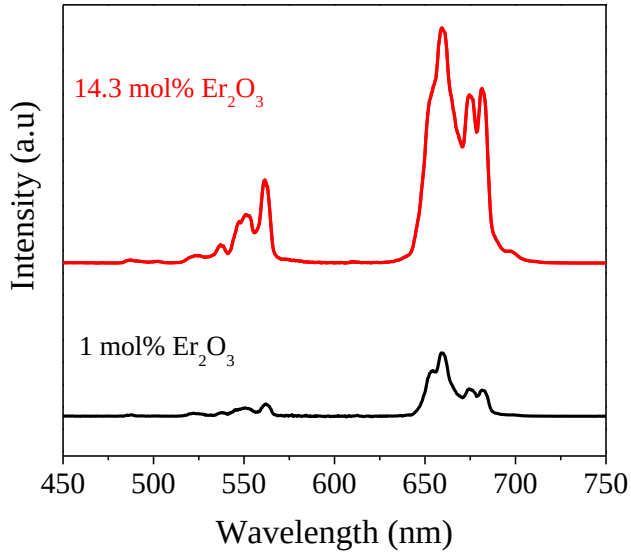

Figure 4.30 Up-conversion emission spectra of the 1 and 14.3 mol% Er_2O_3-doped ZnO particles calcined at 1000 °C for 2 h.

In agreement with the IR emission and lifetime values of the sample with 1 mol% of Er_2O_3, the emission in the visible was hardly detected. For the sample with 14.3 mol% of Er_2O_3, the emission was very strong in the red region at 660 nm, resulting from the $^4F_{9/2}$ to the $^4I_{15/2}$ transition of the Er^{3+} ions.

In summary, microparticles of 1 and 14.3 mol% of Er_2O_3-doped ZnO with a diameter larger than 50 μm were synthesized. The main crystalline phase present in the samples was the hexagonal wurzite phase, while an extra phase was detected for the highest concentration of Er^{3+}. The IR and visible emission of the sample with 1 mol% of Er_2O_3 was almost negligible, while the sample with 14.3 mol% had a strong emission in the IR and in the red region. Therefore, these results suggest that the ZnO particles doped with 14.3 mol% of Er_2O_3 are good candidates for the fabrication of particles-containing glasses.

4.3.1.3 Er^{3+}-doped ZrO_2 particles

ZrO_2 particles were prepared with 1 and 14.3 mol% of Er_2O_3. Both were prepared by the sol-gel technique with a calcination step at 1000 °C for 2 h.

The FE-SEM micrographs of the 1 and 14.3 mol% Er_2O_3–doped ZrO_2 particles calcined at 1000 °C for 2 h are shown in Figure 4.31a and b, respectively.

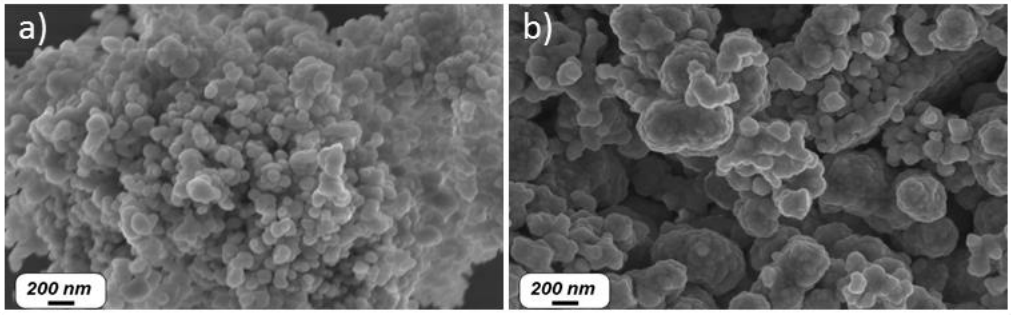

Figure 4.31 FE-SEM micrographs of (a) 1 and (b) 14.3 mol% Er_2O_3–doped ZrO_2 particles calcined at 1000 °C for 2 h.

Both samples present a similar morphology with agglomerates with sizes larger than 50 μm (not shown here). The surface roughness of these agglomerates consists of smaller particles with a size of 100 to 400 nm.

Figure 4.32 shows the XRD patterns of the ZrO_2 particles calcined at 1000 °C for 2 h doped with 1 and 14.3 mol% Er_2O_3.

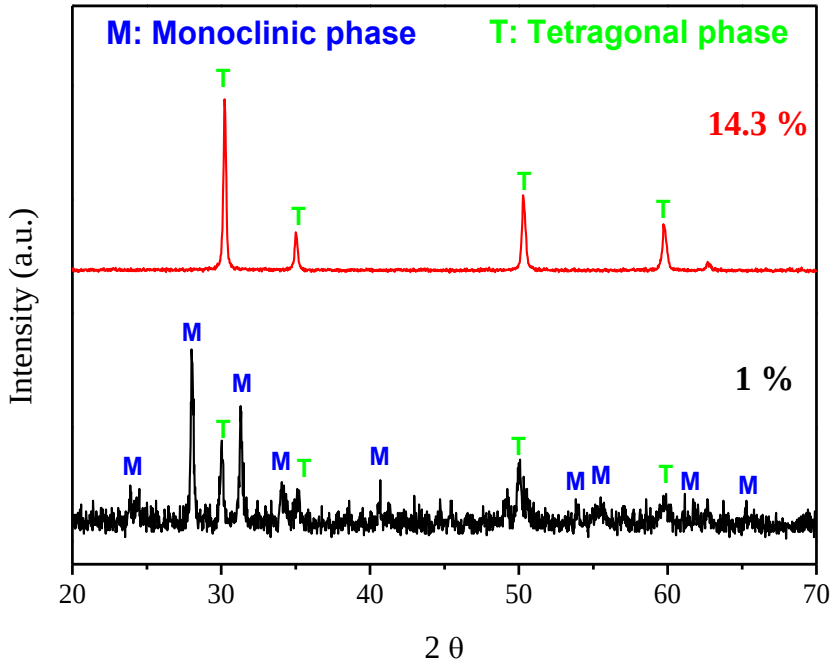

Figure 4.32 XRD patterns of 1 and 14.3 mol% Er_2O_3–doped ZrO_2 particles calcined at 1000 °C for 2 h, with the reference pattern of the monoclinic and tetragonal crystalline phases.

As seen from Figure 4.32, the monoclinic and tetragonal crystalline phases are simultaneously present in the sample with 1 mol% of Er_2O_3, whereas in the sample with 14.3 mol% only the tetragonal phase is present. As explained in Chapter 2, the transition from monoclinic to tetragonal phases is due to the addition of the addition of dopants such as Er^{3+} [173,244].

The emission spectra under an excitation wavelength of 976 nm of the samples doped with 1 and 14.3 mol% of Er_2O_3 calcined at 1000 °C for 2 h are presented in Figure 4.33a and b, respectively.

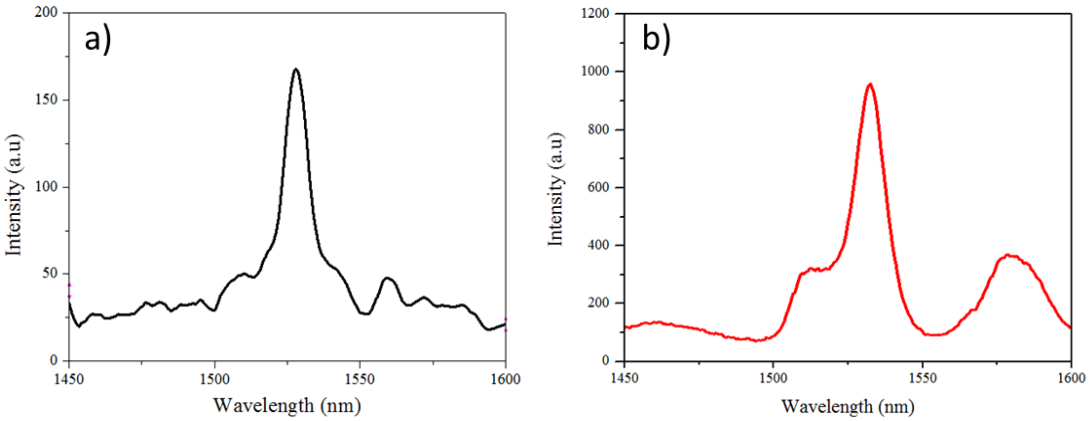

Figure 4.33 Emission spectra of the (a) 1 and (b) 14.3 mol% Er_2O_3-doped ZrO_2 particles calcined at 1000 °C for 2 h.

The emission spectra of the samples were not compared due to the difference of shape and composition of the particles. Both spectra show slightly different shape, probably due to the difference in the composition of crystalline phases. Indeed, the absence of the monoclinic phase may originate the broad peak located at around 1580 nm. Additionally, the fluorescence lifetime values of the Er^{3+}:$^4I_{13/2}$ level upon 976 nm excitation were measured. The lifetime values of the 1 and 14.3 mol% Er^{3+}-doped ZrO_2 particles were 1.25 and 1.02 ms, respectively. The estimated error was calculated as the standard deviation of the measurements of the individual lifetimes (~ ± 0.20 ms). The diminishment of the lifetime values is due to the quenching effect, which has been reported to occur at Er^{3+} concentrations higher than 1 mol% [248].

Lastly, the up-conversion spectra of the Er_2O_3-doped ZnO particles excited at 976 nm is shown in Figure 4.34.

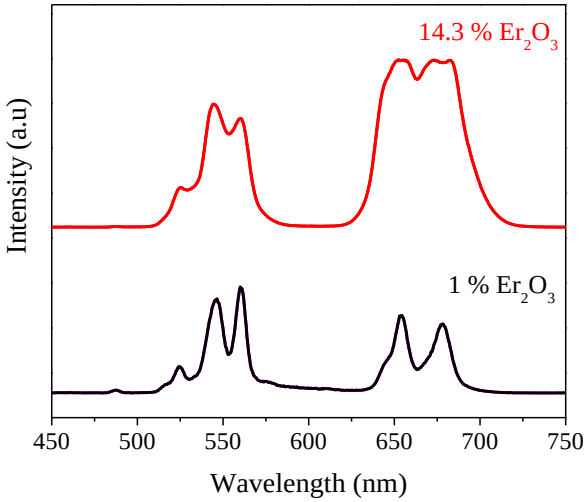

Figure 4.34 Up-conversion spectra of the Er_2O_3-doped ZrO_2 particles calcined at 1000°C for 2h.

Interestingly, the ZrO_2 particles doped with 1 mol% of Er_2O_3 has the highest intensity in the green region, whereas the ZrO_2 doped with 14.3 mol% exhibits the highest intensity in the red region at 660 nm.

In summary, Er^{3+}-doped ZrO_2 particles form big agglomerates with strong IR and up-conversion emission. The monoclinic and tetragonal crystalline phases co-exist in the sample with 1 mol% of Er_2O_3, whereas the sample with 14.3 mol% only shows the tetragonal phase. The particles show different shapes of the IR and visible spectra due to the changes in the crystalline phases. The properties of the Er^{3+}-doped ZrO_2 particles seem to be hardly dependent on the surrounding environment of the Er^{3+} ions. Thus, these particles seem to be promising materials for the fabrication of particles-containing glasses.

4.3.2 Particles containing glasses

In this section, the development of Er^{3+}-doped particles-containing phosphate glasses using two different techniques is reported. The characterization of the ***"direct particle doping"*** glasses and the ***"in glass batch"*** glasses is discussed.

Before the incorporation of the particles into the glasses, the thermal stability of the 7% Er_2O_3-doped Al_2O_3, as well as 14.3% Er_2O_3-doped TiO_2, ZnO and ZrO_2 calcined particles were assessed by TGA (see Figure 4.35).

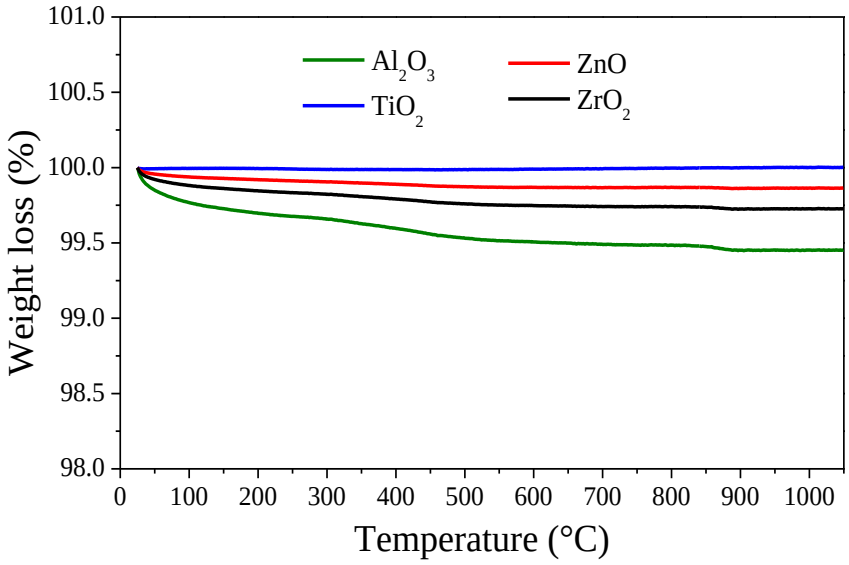

Figure 4.35 TGA analyses of the calcined Al_2O_3, TiO_2, ZnO and ZrO_2 particles.

The calcined particles are stable up to 1050°C. Indeed, only weight losses lower than 1 % were observed. As the maximum melting temperature reached during the fabrication of particles-containing glasses was 1050°C, the particles should not suffer any further degradation when added in the glass melt.

10 g of ***"direct particle doping"*** glasses were prepared with 0.1, 0.4, 0.8 and 1.25 wt% of Er_2O_3-doped Al_2O_3, TiO_2, ZnO and ZrO_2 particles. The glasses were melted at 1000 °C with a composition of $50P_2O_5$-40SrO-$10Na_2O$ (mol%). In order to balance the survival and dispersion of the particles, the particles were added at 1000°C and a 5 min dwell time was used before casting the glasses. The optimization of the direct doping process for this glass composition can be found in [318]. Figure 4.36 shows a picture of some of the particles-containing glasses prepared during this thesis.

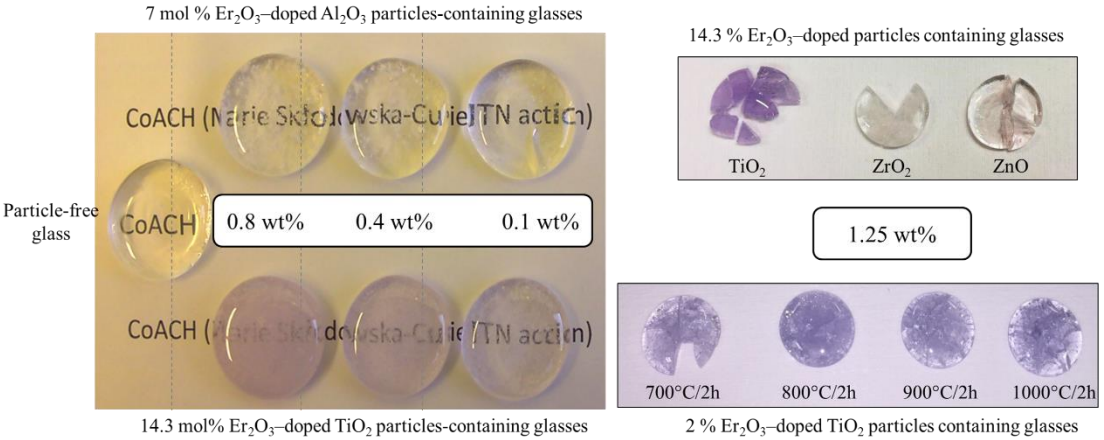

Figure 4.36 Pictures of "direct particles doping" glasses with different amounts and types of particles.

Remaining particles can be observed from all the samples by visual inspection except for the glass without particles, which appeared to be transparent. Besides, a slight pink coloration was observed in all the glasses, becoming purple with the incorporation of TiO_2 particles.

The morphology and the composition of the particles incorporated in the glasses were analyzed using EDS/SEM. As an example, the elemental mapping and the SEM pictures of particles found in the glasses with 14.3 mol% of Er_2O_3-doped ZnO and TiO_2 are shown in Figure 4.37a and Figure 4.37b, respectively.

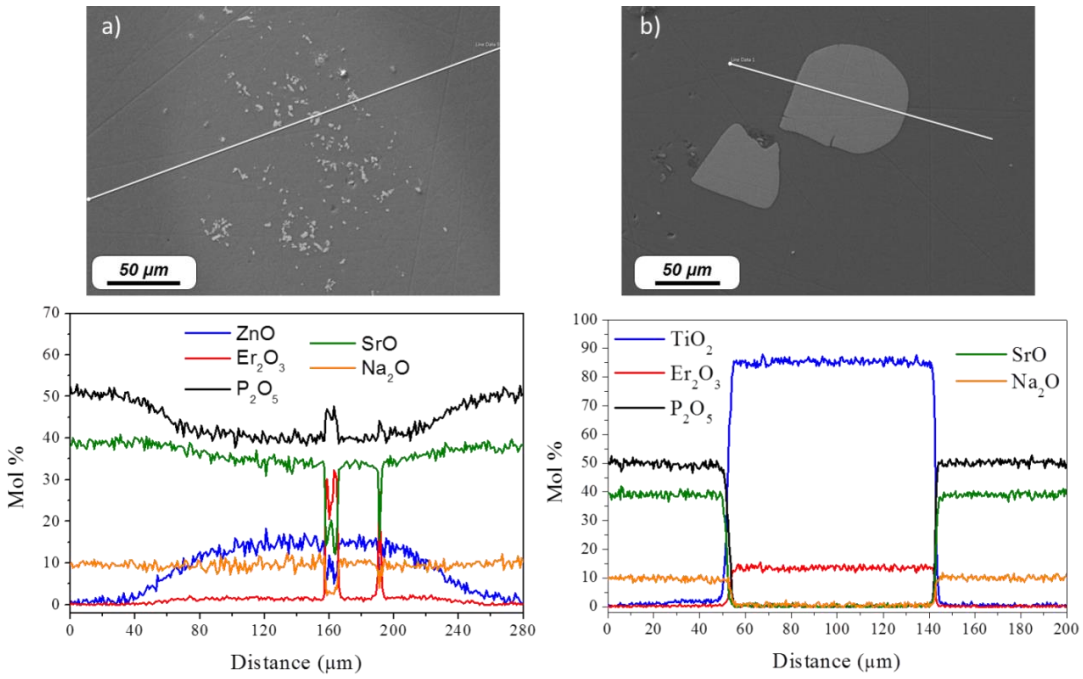

Figure 4.37 SEM pictures with their corresponding elemental mapping of Er_2O_3-doped ZnO (a) and TiO_2 (b) particles-containing glasses.

As it can be seen from Figure 4.37a, a bright cloudy area of Zn surrounds smaller particles with a composition of mostly Er and P. This might indicate that the ZnO particles are degraded after the melting conditions. Thus, the Zn^{3+} ions seem to diffuse into the glass matrix and the remained particles may be converted into $ErPO_4$ crystals.

The mapping of the TiO_2 particles containing glasses is shown in Figure 4.37b. In these glasses, big microparticles with a size of ~100 µm were found in the glass matrix. The composition of the glass matrix and the particles was in accordance with the theoretical one, in the case of TiO_2 particles, 85.7 TiO_2 and 14.3 Er_2O_3 (mol%). Thus, some of the remaining particles seem to maintain their compositional integrity and so survive the melting process. In order to clarify the particles degradation, the EDS elemental mapping and SEM pictures of the spherical 2 mol% Er_2O_3-doped TiO_2 particles found inside the glass were analyzed more in detail in Figure 4.38.

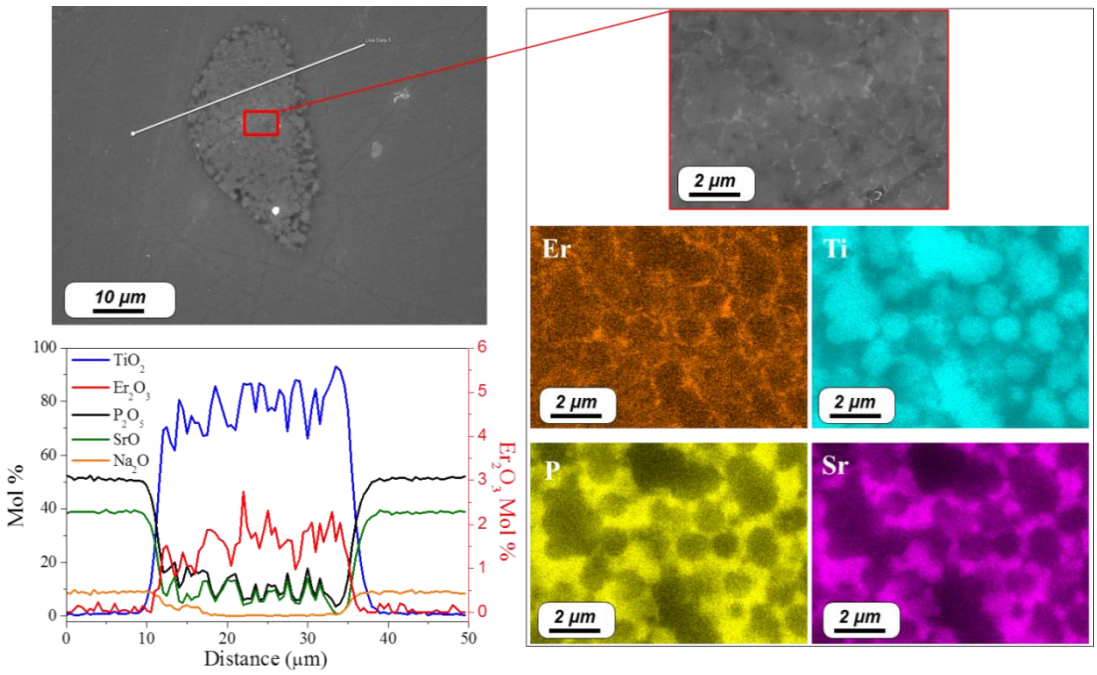

Figure 4.38 SEM-EDS line scanning and EDS elemental mapping images of the 2 mol% Er_2O_3-doped TiO_2 particles-containing glasses.

Interestingly, the spherical shape of the 2% Er_2O_3-doped TiO_2 particles is well retained.

Concerning the XRD analyses, the spectra of the 14.3 mol% Er_2O_3-doped TiO_2 particles-containing glasses and the corresponding particles is shown in Figure 4.39.

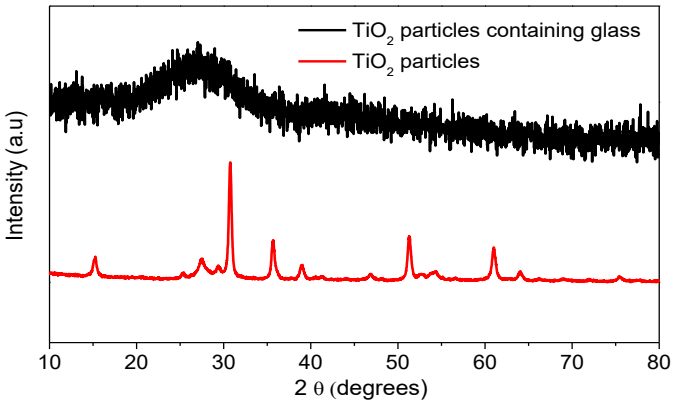

Figure 4.39 XRD spectra of 14.3 mol% Er_2O_3-doped TiO_2 particles-containing glasses and 14.3 mol% Er_2O_3-doped TiO_2 particles.

As seen from Figure 4.39, no diffraction peaks of any crystalline phase were found in the particles-containing glass. Indeed, the typical curve of an amorphous material at 28 degrees is observed. This might indicate that the amount of particles in the glasses is not enough to be detected. Nevertheless, all the glasses show similar XRD spectra, indicating that the crystalline phases were not possible to be detected under XRD.

The spectroscopic properties of the "direct particle doping" glasses and of the Er^{3+}-doped Al_2O_3 and TiO_2 particles alone are presented in Figure 4.40a and b respectively.

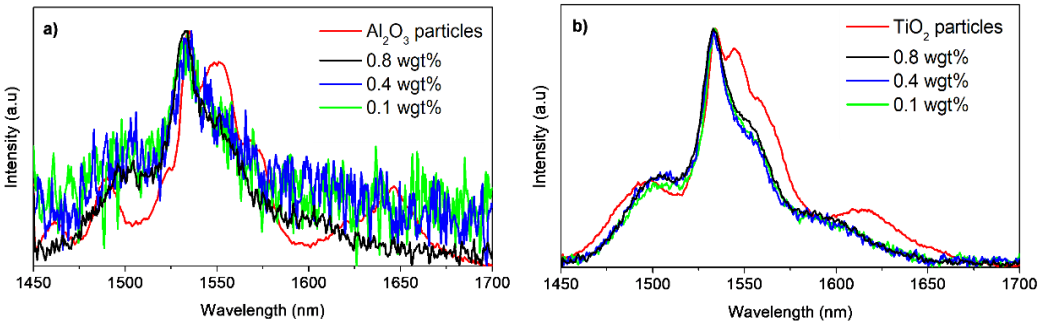

Figure 4.40 Emission spectra of Er_2O_3-doped Al_2O_3 (a) and TiO_2 (b) particles-containing glasses with different concentration of particles and their corresponding particles.

As seen from Figure 4.40a and b, the spectra of the glasses showed the same shape after varying the amount of particles incorporated into the glasses. The absence of the stark splitting peaks in the IR emission of the particles containing glasses indicate that the Er^{3+} ions are not embedded in a crystalline field.

Besides, the micro-luminescence spectra of the 2 mol% Er_2O_3-doped TiO_2 particles-containing glasses and the respective optical microscopy image are presented in Figure 4.41.

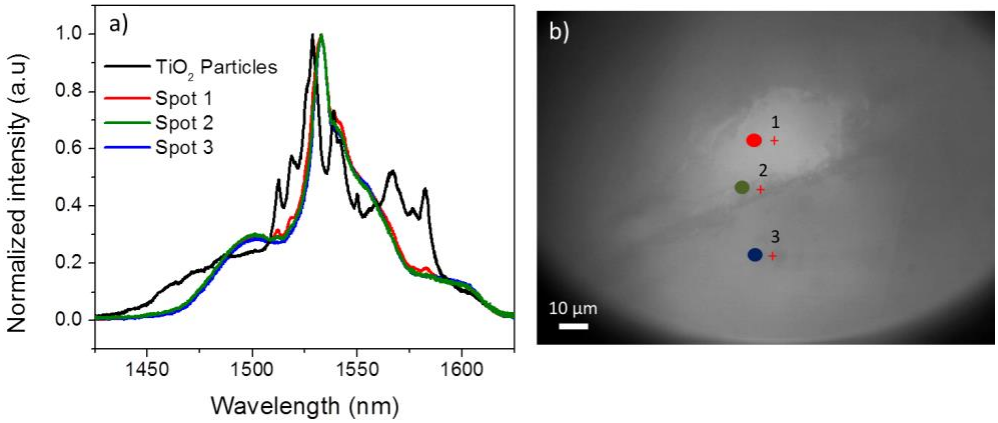

Figure 4.41 (a) Micro-photoluminescence spectra at different positions in the Er_2O_3-doped TiO_2 particles-containing glass. (b) Optical image of the sample with the spots where the PL spectra were measured.

From Figure 4.40 and Figure 4.41, it can be observed that all of the spectra of the particles containing glasses exhibit a very different shape compared to the particles alone. This might indicate that the crystalline environment around the Er^{3+} ions is lost and that the Er^{3+} ions are diffused from the particles to the glass matrix. The absence of sharp peaks in the emission spectra together with the absence of up-conversion, clearly suggest that the spectroscopic properties of the particles change

when they are added into the glass. Similar results were obtained for the ***"in glass batch"*** glasses, where no improvement of the spectroscopic properties was observed. Besides, all of the particles-containing glasses exhibited similar Er^{3+}:$^4I_{13/2}$ lifetime values (4.0 ± 0.2) ms, independently on the wt% of the particles.

In summary, the absence of XRD peaks and up-conversion, together with the pink coloration, similar lifetime values and lack of well-defined peaks in the IR emission suggest that a large number of particles suffer an important degradation after the melting process. As the Er^{3+} ions environment in the particles-containing glasses differs from the one in the particles, most of the Er^{3+} ions are suspected to diffuse from the particle into the glass matrix during the melting. The Er^{3+} ions environment of the particles seems to change from crystalline to glassy when the particles are incorporated into the glasses. Therefore, the melting conditions are detrimental for the integrity of the particles. Boivin *et al.* [362] suggested the incorporation of core-shell particles with a layer of Si or Al [363,364]. Hence, the shell may prevent the degradation of the core particles during the melting [365]. In this thesis, core-shell particles covered by a SiO_2 layer were fabricated. The SiO_2 layer did not improve the stabilization of the particles in the glass, and the luminescence properties of the particles-containing glasses were not increased. However, those results are not shown in this thesis as the SiO_2 layer surrounding the particles was not confirmed.

Finally, apart from the phosphate glasses, another glass system with a composition of 90 $NaPO_3$-(10-x)Na_2O-xNaF with x=0 and 10 is being studied as an alternative host for the Er^{3+}-doped particles. The study of their spectroscopic properties is on-going and will be published separately. Interestingly, promising results are being obtained due to the lower melting temperature required for the fabrication of these oxyfluoride glasses.

Chapter 5

Phosphate glass optical fibers for advanced bio-sensing

5.1 Preliminary results on the optical fiber

In this chapter, the preparation and characterization of the core and clad preforms in the Na_2O-P_2O_5-SrO system are first presented. Then, the thermal, morphological, structural and optical properties of the multimode core/clad optical fiber are discussed. Lastly, the dissolution kinetics of the optical fiber are reported both in strong acid environment and in simulated body fluid in the prospect of developing novel types of sensors for biomedical applications.

5.1.1 Preform characterization

Based on the thermal properties of the conventional glasses (see Chapter section 4.1), AlG glass was the best candidate and less prone to crystallization during the drawing process. However, the ZnG glass showed the highest luminescence properties, allowing for a higher sensitivity of the signal and better sensing properties of the optical fiber. Therefore, core and cladding components based on the composition of the ZnG glass were designed. The core composition was 0.25 Er_2O_3 – 97.25 (0.5 P_2O_5 – 0.4 SrO – 0.1 Na_2O) – 2.5 ZnO, while the cladding composition was 98.25 (0.5 P_2O_5 – 0.4 SrO – 0.1 Na_2O) – 1.75 ZnO.

The core component was obtained in the form of a rod by casting the molten glass into a cylindrical mold. The cladding component was processed into a tubular shape using the rotational casting technique described in Chapter 3. After annealing, the external surfaces of the rod and the tube were polished and visually inspected. The optimized processing allowed the fabrication of a preform with good homogeneity. No defects such as bubbles or crystals were observed. The diameter and the length of the core/cladding preform were 1 and 10 cm, respectively (see Figure 5.1).

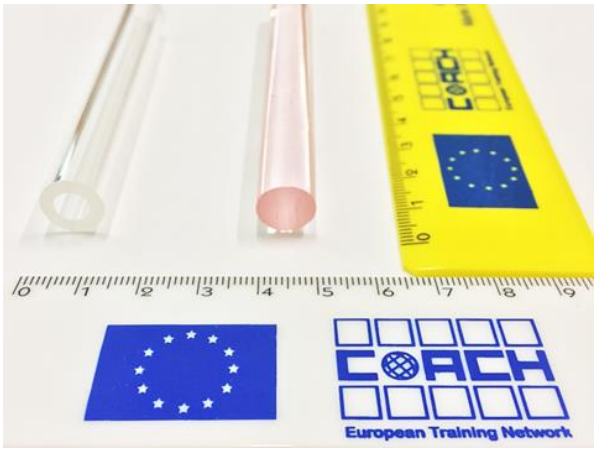

Figure 5.1 The core rod and the cladding tube developed for this thesis.

The pink coloration of the core rod is due to the Er_2O_3 doping. Once fabricated, both core and cladding components were characterized to check their suitability for drawing into optical fiber.

In order to prepare a good quality optical fiber, the glass preforms must withstand the drawing process without crystallization. Typically, during the fiber drawing, temperatures above T_g are reached and a suitable glass viscosity is obtained [71]. Generally, a glass preform with a ΔT higher than 100°C is appropriate for a correct fiber drawing without crystallization [23,366]. Another necessary step to be checked is the mechanical and thermal properties of the core and clad preforms, which should have similar values for T_g and *CTE* so the simultaneous drawing of the core and the cladding preforms can be performed without causing stress forces at the core/cladding interface [367,368].

The thermal properties and the CTE were measured using a dilatometer and DTA (see Figure 5.2a and Figure 5.2b, respectively). Table 5.1 lists the corresponding glass transition temperature (T_g), glass crystallization temperature (T_x), glass softening temperature ($T_{softening}$), and coefficient of thermal expansion (*CTE*) of the preforms. The dilatometric diagram shows a CTE of 17.773×10^{-6} °C for the core preform. However, due to the geometry of the sample, the CTE value of the cladding was not possible to measure. Nevertheless, as the cladding and core preforms had analogous compositions, similar CTE values for the glass used as the cladding are expected. The analyses indicate similar values of T_g and T_p, and a ΔT above 100 °C for the core and clad preforms, confirming that the preforms have similar thermal properties (including drawing temperature) and also are stable against crystallization and suitable for fiber drawing.

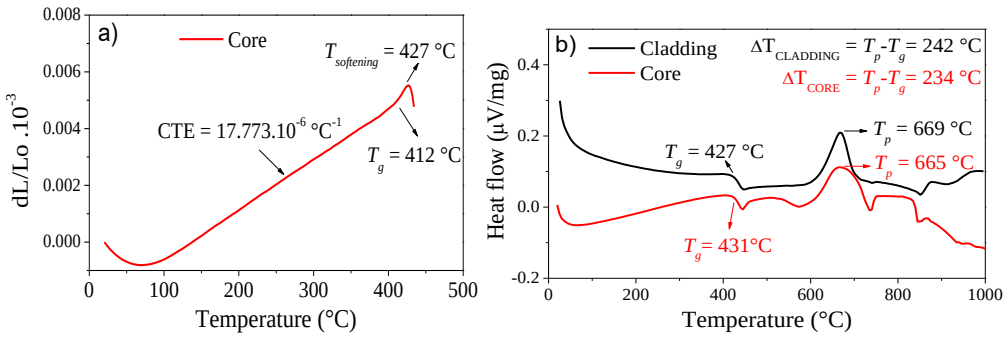

Figure 5.2 Dilatometry curve and DTA curve of the core and clad preforms.

Preform	***CTE*** **(×10^{-6} °C^{-1})**	***$T_{softening}$*** **± 3 °C**	***T_g*** **± 3 °C** **(by Dilatometer)**	***T_g*** **± 3 °C** **(by DTA)**	***T_x*** **± 3 °C**	***T_p*** **± 3 °C**	***ΔT*** **± 6 °C**
Core	1.8	427	412	431	611	665	234
Cladding				427	615	669	242

Table 5.1 Thermal properties of the core and clad preforms obtained by Dilatometry and DTA.

Another very important feature of an optical fiber is its numerical aperture (*NA*), which is defined by the refractive index difference between the core and the cladding (see section 2.4.1). Figure 5.3 shows the refractive index values of the preforms measured at 5 different wavelengths fitted with the Sellmeier's formula. The estimated error of the measurement was ±0.001. The core displays higher refractive index values at all the wavelengths, probably due to an increase in the electron density induced by the Er^{3+} ions [369,370]. The refractive index difference between the core and the cladding at 1550 nm results in a *NA* value of 0.0945, which is suitable for the proper propagation of light along the optical fiber.

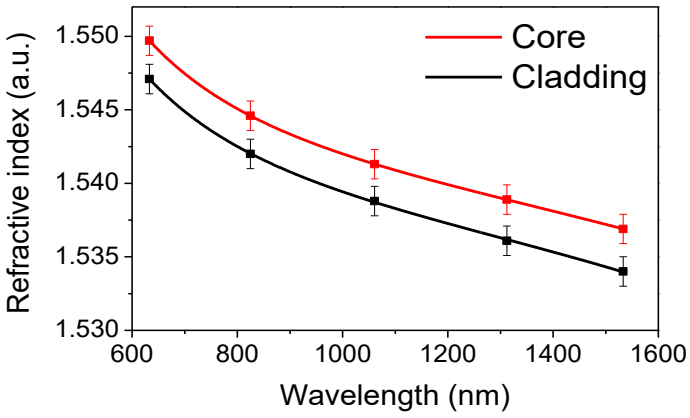

Figure 5.3 Refractive index values of the preforms at 5 different wavelengths fitted with the Sellmeier's formula. The filled squares represent the experimental data, while the continuous lines are the fitting curves.

The absorption and emission spectra of the Er_2O_3-doped active core preform is shown in Figure 5.4.

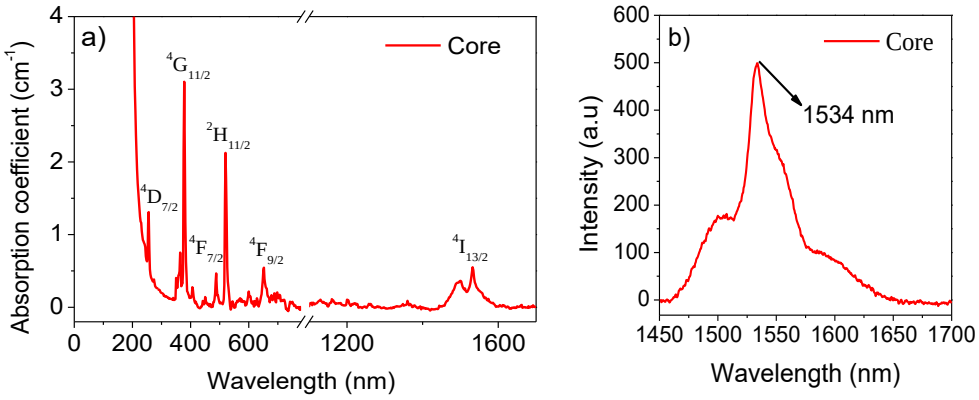

Figure 5.4 (a) Absorption and (b) emission spectra of the core preform.

The core preform absorption spectrum exhibits the typical absorption peaks of the Er^{3+} ions (see Figure 5.4a) with a UV absorption edge located at 200 cm^{-1} whereas the spectrum of the undoped clad preform showed no absorption peaks in the visible range as expected (data not shown). The emission spectrum measured in the wavelength range 1450–1700 nm upon excitation at 976 nm is reported in Figure 5.4b. It exhibits the typical emission band assigned to the Er^{3+} transition $^4I_{13/2} \rightarrow {}^4I_{15/2}$ with the peak centered at 1534 nm. Additionally, the lifetime value of the Er^{3+}:$^4I_{13/2}$ level of the core preform was 2.3 (± 0.2 ms).

5.1.2 Optical fiber drawing and characterization

The stability against crystallization, compatible thermo-mechanical and optical properties, as well as suitable *NA* between the core and cladding components allow the processing of a high quality optical fiber. An optical fiber in multi-mode regime was fabricated by preform drawing, with the preform obtained using the rod-in-tube technique (see Figure 5.5), as explained in Chapter 3.

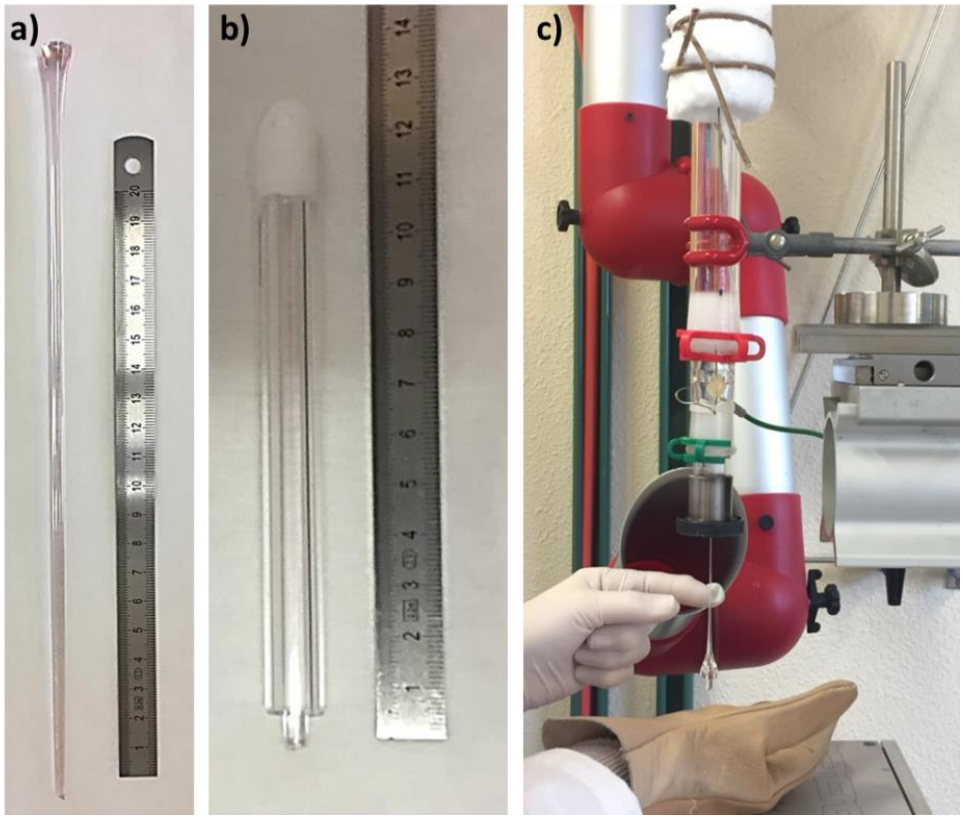

Figure 5.5 (a) Cane preform stretched from the core preform. (b) Core-clad preform made by the rod in tube technique. (c) Drawing of the core-clad preform into the multimode optical fiber.

Half of the core-clad preform was drawn into 40 meters of multimode optical fiber. Figure 5.6 shows a picture of the fiber cross-section of the fiber.

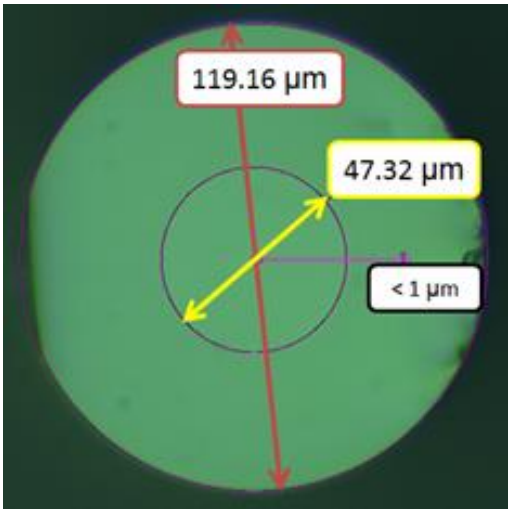

Figure 5.6 Optical image of the fiber cross-section with the core and clad dimensions illuminated with a white light source and captured at 50X magnification.

A multi-mode optical fiber with core/cladding diameters of around 47/119 µm was successfully drawn at 575 °C and at a drawing speed of 3 m/min. No significant

defects in the core/cladding interface can be observed. The distance between the center of the circumference of the core and the cladding (eccentricity) was less than 1 μm, assessing the good control during the fabrication process.

The near-field imaging of the optical fiber was analyzed with a light source at 1300 nm. As it can be seen from Figure 5.7, the light is properly confined inside the core of the fiber, assessing the light guiding properties of the optical fiber.

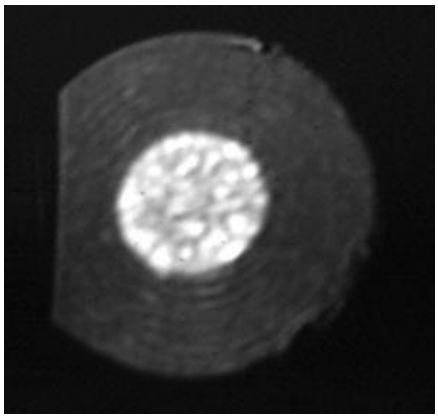

Figure 5.7 Near-field image of the optical fiber at the wavelength of 1300 nm.

The optical loss of the fiber at the wavelength of 1300 nm was measured by the cut-back method. The fiber loss value was calculated through linear least square fitting of the experimental data. As shown in Figure 5.8, the slope of the graph revealed an attenuation loss value of 2 dB/m. The error of the measurement is expected to be around 10%.

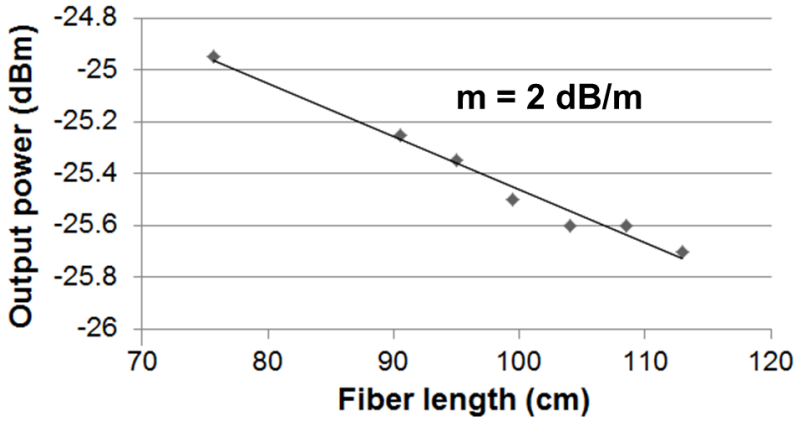

Figure 5.8 Attenuation loss measurements of the fiber at the wavelength of 1300 nm.

An attenuation value of 2 dB/m is lower than those reported in the literature for bioresorbable waveguides made of polymer materials [371–373], and similar to the ones reported for phosphate optical glass fibers [23]. Thus, based on the low attenuation losses together with the proper light propagation, the optical fiber seems to be a promising material for the development of bioactive optical fiber sensors.

5.2 Proof of concept of an optical fiber sensor

The luminescence studies on the fiber were carried out after etching the cladding. Then, the changes of the fiber diameter and the spectroscopic properties as a function of immersion time in different solutions were reported.

The etching of the core-clad optical fibers with a length of 5 cm was performed in 3 ml of phosphoric acid (H_3PO_4) 1M solution to reveal the core. The samples were etched in H_3PO_4 for up to 8 hours. In order to estimate the etching rate, the fiber diameter was measured using an optical microscope at different time point (Figure 5.9). The estimated error of the diameter measurements was 2 μm. An etching rate of 8.4 μm/h is expected for this fiber when immersed in phosphoric acid.

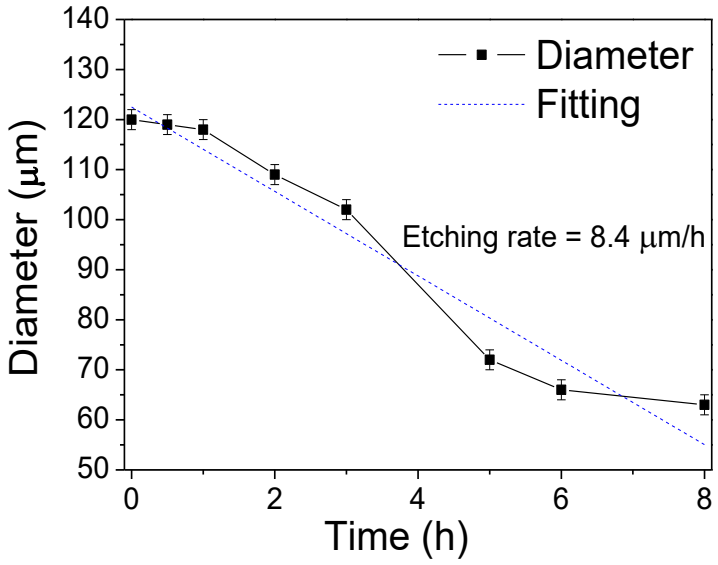

Figure 5.9 Etching of the optical fiber in H_3PO_4 1M solution.

Based on these results, the core-clad fiber was etched for 5 h in H_3PO_4 to reveal the core. After that, the fiber was again immersed in 3 ml of H_3PO_4 solution, and the absorption and emission spectra were measured every 10 minutes until the signal reached the noise floor (see Figure 5.10).

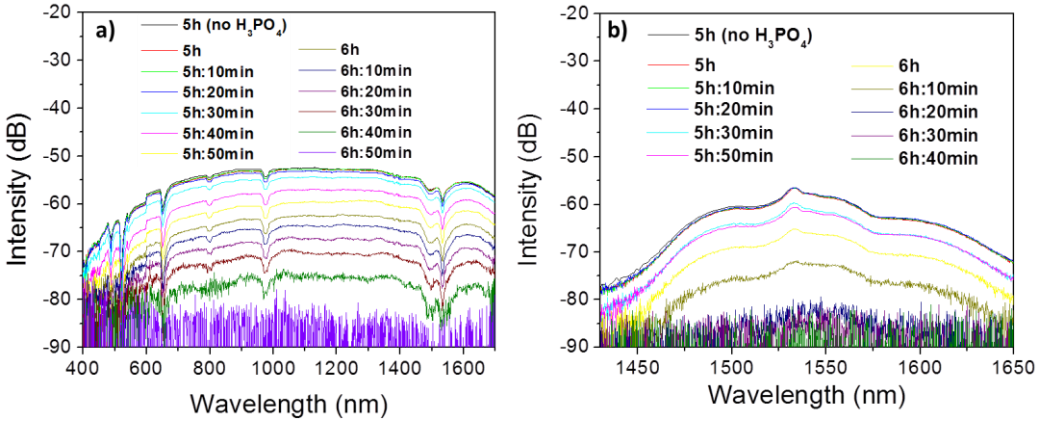

Figure 5.10 (a) Absorption and (b) emission spectra of the optical fiber as a function of the immersion time in H_3PO_4 solution. The absorption was collected under an excitation with a white light source, while the emission was recorded under an excitation of 976 nm.

From the absorption and emission spectra, it can be observed that immersion times longer than 6 h causes a loss of signal. Specifically, the emission and absorption spectra were completely noisy at 6h:30min and 6h:50min, respectively. Thus, the emission signal is lost 20 min before the absorption signal probably due to the poor light transmission properties. Overall, the loss of absorption and emission signals in H_3PO_4 can be ascribed to the acid, which acts as a quencher of the emission and transmission of the fiber.

Apart from the sensing properties in H_3PO_4, another investigation was performed using a SBF solution. Once the core was revealed after immersing the fiber for 5 h in H_3PO_4, the fiber was then immersed in 3ml of SBF for up to 4 weeks, and the emission spectrum was measured every 3 – 4 days.

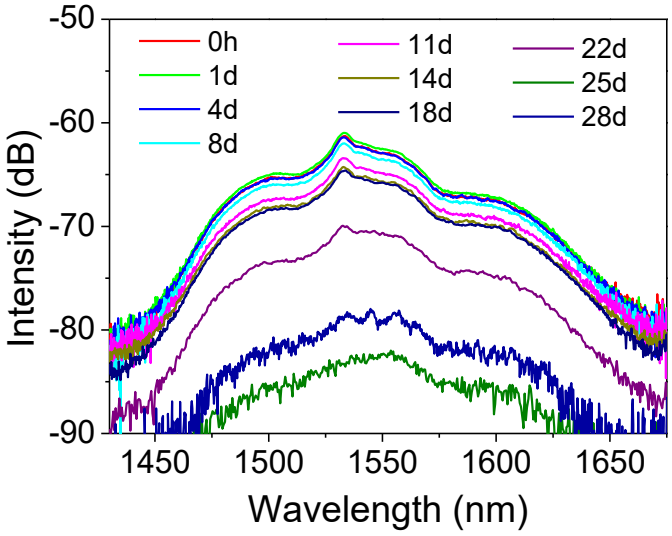

Figure 5.11 Emission spectra of the optical fiber under an excitation at 976 nm, as a function of immersion time in SBF solution at room temperature.

A progressive decrease of the emission intensity upon immersion is observed. The emission spectra of the fiber immersed in SBF at room temperature shows a noisy signal after 25 days, probably related to the loss of luminescence properties of the optical fiber.

The structure of the fiber before and after several etching times was analyzed by micro-Raman spectra by using an excitation wavelength of 785 nm. Normalized Raman Spectra at 1170 cm^{-1} of the fibers can be seen in Figure 5.12.

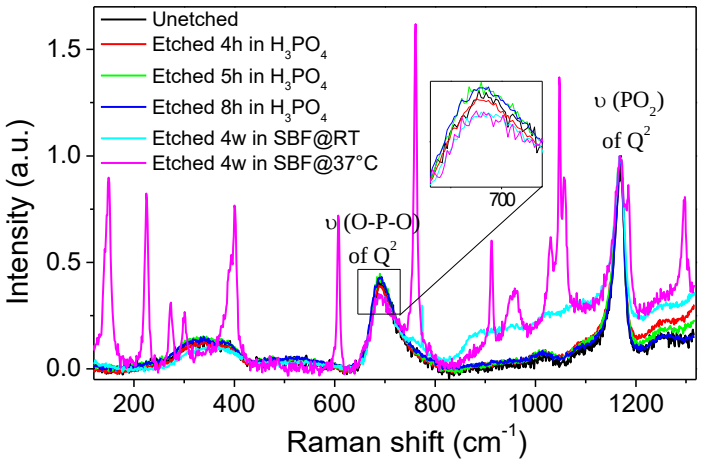

Figure 5.12 Normalized Raman spectra of fibers prior to and after etching in H_3PO_4 and after immersion in SBF solutions.

All the Raman spectra showed the typical bands corresponding to the structure of a metaphosphate glass [35,374]. A broad band from 200 to 400 cm^{-1} corresponds to the P–O bond bending mode of the Q^2 groups [375]. The rest of the bands were previously discussed in section 4.1.

As observed from Figure 5.12, the etching in H_3PO_4 does not have an impact on the Raman spectra and glass structure, whereas after immersion in SBF the Raman spectra were changed. The Raman spectrum of the fiber immersed in SBF solution after 4 weeks at room temperature showed a slight decrease in the intensity of the band at 700 cm^{-1} and an increase in intensity of the bands in the 800 – 1100 cm^{-1} region. Besides, the fiber immersed in SBF solution for 4 weeks at 37 °C showed sharp peaks corresponding to the formation of the hydroxyl apatite layer, which consists mainly of calcium and phosphate [376,377] confirming the bioactivity of the fiber.

Apart from the structural analyses, the changes of morphology and composition of the etched fibers were analyzed by SEM/EDS. Figure 5.13 shows the SEM images of the as-drawn fibers and after etching in H_3PO_4 and after immersion in SBF.

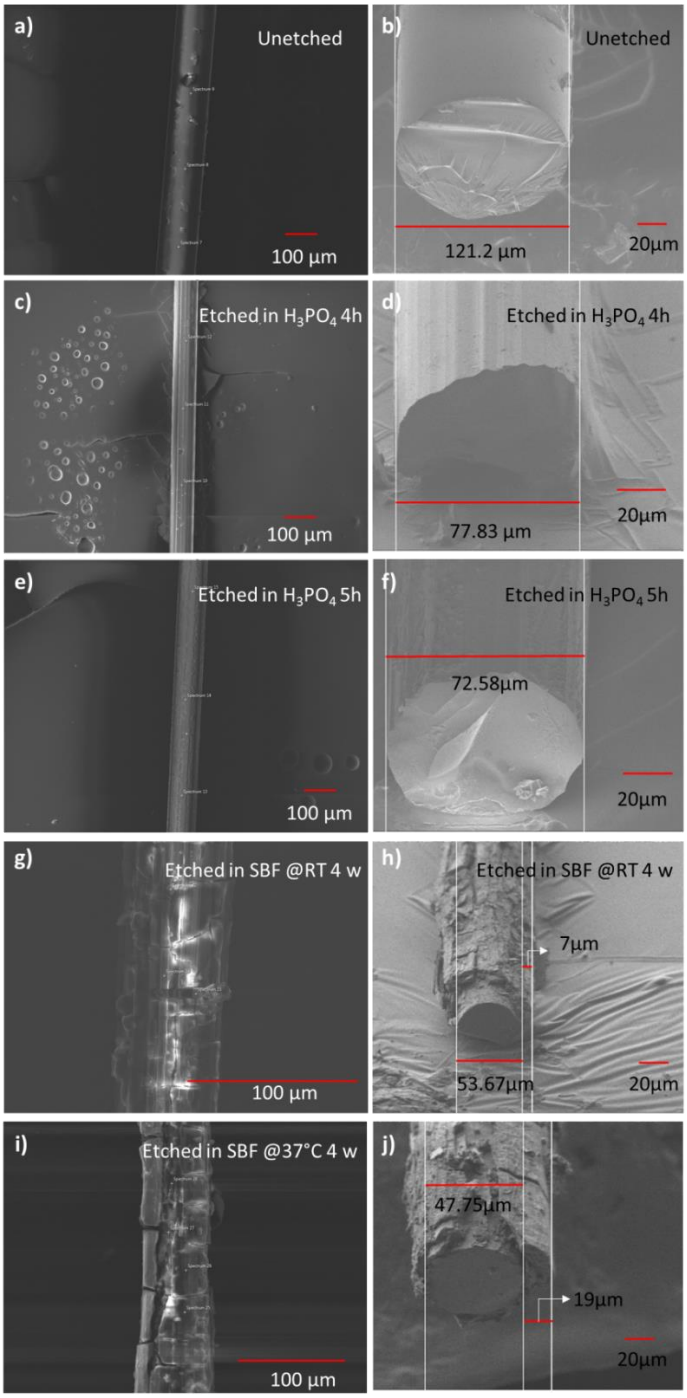

Figure 5.13 SEM images taken at the surface and at the cross-section of the optical fiber unetched (a, b), etched in H_3PO_4 for 4 h (c, d), etched in H_3PO_4 for 5 h (e, f), etched in SBF solution for 4 weeks at room temperature (g, h) and etched in SBF solution for 4 weeks at 37 °C (i, j).

The fibers immersed in H_3PO_4 solution showed a smooth surface, similar to the unetched fiber. However, clear signs of the formation of a layer are observed at the surface of the fibers immersed in SBF solution. The roughness of the surface after 4 weeks in SBF is increased when treated at 37 °C. Indeed, the layer's thickness increased from ~7 to ~19µm when immersed in SBF at room temperature and at 37°C, respectively. Besides, a strong reduction in the fiber diameter after 4 weeks in SBF was observed.

The composition analyses at the surface of the fibers were performed by EDS and are summarized in Table 5.2. Within the accuracy of the measurements (±1.5 mol%), the composition of the fibers etched in H_3PO_4 remained unchanged. Thus, the dissolution of the glass fibers is congruent.

Element (At%)	O	Na	Mg	P	Cl	K	Ca	Zn	Sr	Er
Unetched fiber	64.21	3.19	0	23.93	0	0	0	0.26	8.35	0
SBF@RT/4w	61.4	5.25	1.83	11.54	9.8	0.73	8.93	0.04	0.3	0.02
SBF@37°C/4w	62.37	2.53	1.77	15.43	4.62	0.42	11.51	0.17	1.01	0.07

Table 5.2 Composition analyses of the optical fibers after 4 weeks of immersion in SBF solution.

Elements from the SBF solution such as Ca, Mg, K and Cl were detected at the surface of fiber. Additionally, a high amount of Ca and traces of Zn and Sr were found at the surface of the glass, confirming the formation of the hydroxyl apatite layer in the fibers etched in SBF solution. Furthermore, erbium was detected confirming the dissolution of the cladding.

Interestingly, higher Ca concentration was found at the surface of the fiber immersed in SBF at 37 °C as compared to the fiber etched at room temperature. This, together with the SEM images indicates that the formation of the hydroxyl apatite layer seems to be accelerated when the temperature is increased to 37 °C.

The integration of the phosphate optical fibers with commercial optical fibers was also investigated. Sections of the fabricated multi-mode fiber with core/clad dimensions of around 50/120 µm were cleaved and then spliced with commercial silica single-mode fiber samples with core/clad dimensions of 7-125 µm. The insertion losses after splicing were measured. A picture of one of the splicing experiments is shown in Figure 5.14.

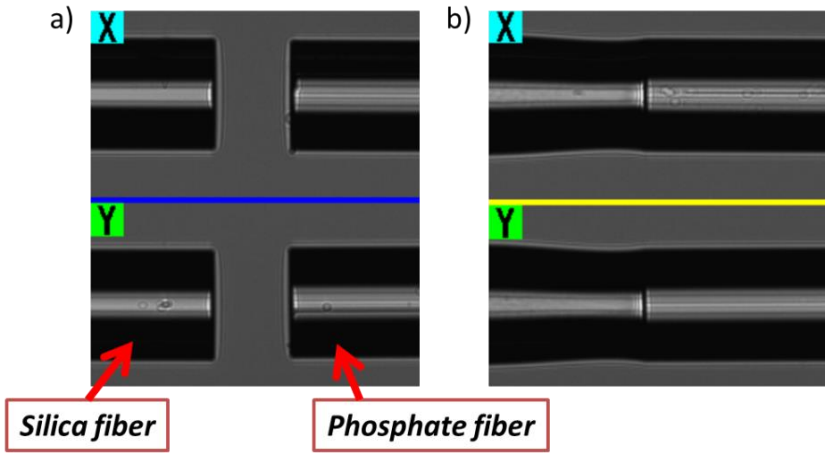

Figure 5.14 Pictures taken at the end faces of silica and phosphate optical fibers (a) before and (b) after the splicing.

Due to the different geometry and composition of the silica and phosphate fibers, the splicing was particularly challenging due to differences in thermal and

mechanical properties. Nonetheless, as seen in Figure 5.15, successful spliced fibers with good mechanical robustness was obtained. A radius of curvature of 2.5 cm before breaking the fiber was achieved.

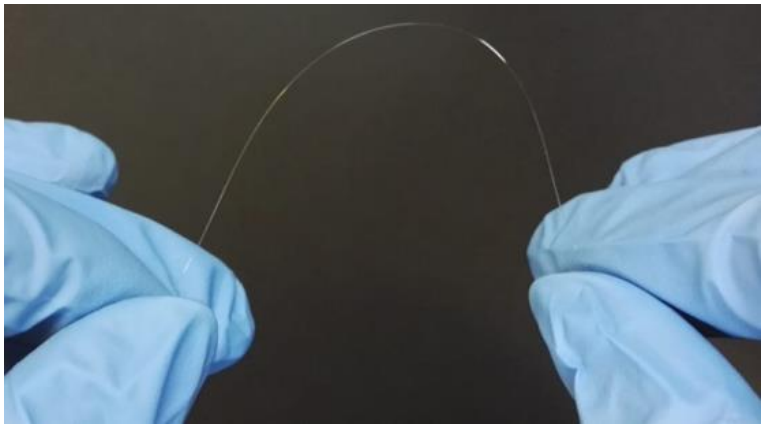

Figure 5.15 Spliced fiber with good mechanical properties.

In order to create a continuous path of light along the spliced optical fibers, the light should not be scattered or reflected back by the splice region, and the insertion losses should be kept as minimum. In this thesis, various trials with segments of around 10 cm of phosphate and silica fibers were spliced. Their insertion losses were obtained by measuring the difference in voltage between the input and the output power.

Power in (dBm)	Power out (dBm)	Insertion loss (±0.1 dB)
-20.4	-20.6	0.2
-20.4	-20.7	0.3
-20.4	-20.7	0.3
-20.5	-20.8	0.3
-20.5	-20.7	0.2
-20.5	-20.8	0.3

Table 5.3 Insertion losses trials with the respective input and output voltage applied.

An average insertion loss of 0.3 ± 0.1 dB was obtained confirming that the phosphate optical fiber sensor can be spliced with commercial silica fibers, broadening the field of applications.

In summary, new core-clad phosphate fibers were successfully drawn. The changes in the optical fiber diameter followed a linear etching rate of 8 µm/h when using H_3PO_4. A decrease in the absorption and emission spectrum intensity upon immersion in H_3PO_4 solution was reported and was related to the changes in the fiber diameter. A similar decrease in the emission at 1.5 µm was reported upon immersion in SBF. Based on the SEM/EDS analyses, a hydroxyl apatite layer was detected after 4 weeks of immersion in SBF solution confirming the bioactivity of

the fiber. A faster dissolution rate was observed when the temperature was increased to 37°C.

These results show that the optical fiber developed in this thesis combines good optical properties with a suitable bioactive behavior, making it a promising material for the development of biomedical devices for biophotonics and photomedicine applications.

Chapter 6

Conclusions and further work

In this thesis, several types of innovative bioactive phosphate glasses and particles have been studied, from their fabrication and characterization to the development of optical fiber sensors for biomedical applications.

The first type of materials that were manufactured in this thesis were Er^{3+}-doped phosphate glasses within the system of P_2O_5–SrO–Na_2O by using the conventional melt-quenching technique. The effect of the addition of Al_2O_3, TiO_2 and ZnO on the physical, structural and luminescence properties of the Er^{3+}-doped glasses was studied. The Al and Ti glasses showed an increase in T_g compared to other glasses, indicating that their phosphate glass network is more connected. The Zn glass showed an increase of the emission intensity at 1540 nm, although this glass exhibited similar absorption cross-section at the pump wavelength compared to the other glasses. Based on these results, the modification in the glass connectivity seems to affect the Er^{3+} ions solubility and therefore the emission properties of the glasses. Overall, the investigated melt-quenched glasses possessed good optical properties, as well as an excellent thermal stability with a ΔT larger than 100 ºC and are therefore promising materials for the fabrication of optical fiber lasers and amplifiers.

In order to improve the spectroscopic properties of the glasses, different GCs were successfully synthesized by processing the aforementioned glasses with a specific post-heat treatment. This method allowed the formation of nuclei and their growth into crystals. The structural, optical, and spectroscopic characterization allowed assessing the occurrence and properties of the Er^{3+}-doped crystals in the glasses and the effect of the addition of Al_2O_3, TiO_2 and ZnO on the crystallization behavior. The surface crystallization rate changed depending on the glass composition, depending on the network connectivity. After the post-heat treatment, the ZnGC was the least crystallized, while the RefGC was fully crystallized. Based on the structural analyses, $Sr(PO_3)_2$ was identified as the main phase of the crystals grown in all the GCs. Concerning the luminescence properties, the RefGC displayed the longest lifetime indicating that the crystals are doped with Er^{3+}. No changes in the lifetime values and in the shape of the emission band at 1540 nm were observed after the heat treatment for all the other GCs indicating that the Er^{3+} ions remained in the amorphous part of the glass-ceramics.

In summary, the research activity of this thesis has shown that the local environment of the Er^{3+} ions might have been influenced by changing the composition or the crystallization behavior of glasses. Therefore, this experimental evidence should be the subject for future investigations involving advanced characterization techniques, since it is crucial to assess the relationships between the rearrangement of the glass network and the solid-state diffusion in influencing the changes in the spectroscopic properties.

As the processing of GCs did not lead to the inclusion of Er^{3+} ions into the in-situ grown crystals, the work was focused on the fabrication of particles-containing glasses as an innovative approach where Er^{3+}-doped particles were incorporated into the glasses. Er^{3+}-doped Al_2O_3, TiO_2, ZnO and ZrO_2 particles were synthesized using soft chemistry with different concentrations of Er_2O_3 and at different calcination temperatures. Their morphological, structural, and luminescence properties were thoroughly investigated. The crystalline phases were found to have an important role on the luminescence properties. The so-obtained particles were added in the glasses prior to and after the melting. The survival and dispersion of the particles in the particles-containing glasses were assessed and based on the experimental results, the Er^{3+} ions seemed to diffuse from the particles to the glass matrix and no improvement of the spectroscopic properties was observed.

Further research is ongoing towards the development of particles-containing glasses with different host glass compositions, such as oxyfluoride glasses, that require low melting temperature for their fabrication. Indeed, the low melting temperature is expected to improve the survival and dispersion of the particles, and thus the spectroscopic properties. However, finding a suitable balance of the survival and dispersion of RE-doped particles in the glass melt is a major challenge. Another possibility to increase the chances of survival might be the incorporation of core-shell particles with a shell of SiO_2 or Al_2O_3. Nevertheless, the results obtained in this thesis pave the way towards the development of new particles-containing glasses.

Based on the studies carried out during this PhD, the addition of Zn was found to enhance the optical properties of the Er^{3+}-doped phosphate glasses. Therefore, a Zn-doped phosphate glass was processed as the active core of a multi-mode fiber. The cladding tube was processed by the rotational casting technique.The so obtained preform was drawn into an optical fiber with a core with a molar composition of 97.25 [50 P_2O_5 – 40 SrO – 10 Na_2O] - 2.5 ZnO - 0.25 Er_2O_3, and a cladding of 98.25 [50 P_2O_5 – 40 SrO – 10 Na_2O] - 1.75 ZnO. An optical fiber with a numerical aperture of 0.0945 and good thermal and optical properties was successfully drawn. The reaction and dissolution behavior of the optical fiber were studied in SBF solution and H_3PO_4. The optical fiber was found to be bioactive due to the formation of a hydroxyapatite layer when immersed after 4 weeks in SBF. The impact of the degradation and bioactivity behavior on the optical properties was assessed by measuring the changes in the emission and absorption spectra of

the developed optical fiber. After 6 h in H_3PO_4, the emission and absorption spectra exhibited a noisy signal, probably related to the high scattering effect produced along the degraded optical fiber. In the case of SBF, the fiber exhibited a noisy signal when it was immersed for 25 days, probably due to the formation of the hydroxyapatite layer at the surface of the fiber. Moreover, the optical fibers were successfully spliced with commercial silica fiber, exhibiting good mechanical and optical properties. To the best of the author's knowledge, this is the first bioactive and optically active optical fiber able to measure the light propagation as a function of immersion time in aqueous media.

Overall, this proof of principle clearly shows that it is possible to track the degradation and bioactivity reaction of a fiber when immersed in aqueous media through the measurement of the fiber's optical properties. These investigations pave the way toward the use of optical fibers for the development of bioactive and biodegradable photonic sensing probes, which could monitor "in situ" the chemical, mechanical, optical and biological parameters of the fiber inside the human body. Furthermore, recent medical procedures such as PDT, which require the delivery of light in deep tissue areas of the body, will benefit from biocompatible devices such as bioactive optical fibers, which can lead to soft tissue regeneration and thus, their surgical removal would not be needed.

In summary, the results accomplished in this thesis have led to new prospects toward developing new bioactive fiber sensors and lasers for medical diagnostics and therapeutics in healthcare applications.

This research has received funding from: the European Union's Horizon 2020 research and innovation program under the Marie Sklodowska-Curie grant agreement No. 642557.

References

1. Hench, L. L.; Splinter, R. J.; Allen, W. C.; Greenlee, T. K. Bonding mechanisms at the interface of ceramic prosthetic materials. *J. Biomed. Mater. Res.* **1971**, *5*, 117–141, doi:10.1002/jbm.820050611.
2. Fagerlund, S.; Massera, J.; Hupa, M.; Hupa, L. T-T-T behaviour of bioactive glasses 1-98 and 13-93. *J. Eur. Ceram. Soc.* **2012**, *32*, 2731–2738, doi:10.1016/j.jeurceramsoc.2011.10.040.
3. Pirhonen, E.; Niiranen, H.; Niemelä, T.; Brink, M.; Törmälä, P. Manufacturing, mechanical characterization, and in vitro performance of bioactive glass 13-93 fibers. *J. Biomed. Mater. Res. - Part B Appl. Biomater.* **2006**, *77*, 227–233, doi:10.1002/jbm.b.30429.
4. Groh, D.; Döhler, F.; Brauer, D. S. Bioactive glasses with improved processing. Part 1. Thermal properties, ion release and apatite formation. *Acta Biomater.* **2014**, *10*, 4465–4473, doi:10.1016/j.actbio.2014.05.019.
5. Baino, F.; Vitale-Brovarone, C. Three-dimensional glass-derived scaffolds for bone tissue engineering: current trends and forecasts for the future. *J. Biomed. Mater. Res - Part A* **2011**, *97*, 514–535, doi: 10.1002/jbm.a.33072.
6. Uo, M.; Mizuno, M.; Kuboki, Y.; Makishima, A.; Watari, F. Properties and cytotoxicity of water soluble Na_2O–CaO–P_2O_5 glasses. *Biomaterials* **1998**, *19*, 2277–2284, doi:10.1016/S0142-9612(98)00136-7.
7. Suzuya, K.; Price, D. L.; Loong, C. K.; Kohara, S. Structure of magnesium phosphate glasses. *J. Phys. Chem. Solids* **1999**, *60*, 1457–1460, doi:10.1016/S0022-3697(99)00140-7.
8. Ahmed, I.; Lewis, M.; Olsen, I.; Knowles, J. C. Phosphate glasses for tissue engineering: part 1. Processing and characterisation of a ternary-based P2O5–CaO–Na2O glass system. *Biomaterials* **2004**, *25*, 491–499, doi:10.1016/S0142-9612(03)00546-5.
9. Massera, J.; Petit, L.; Cardinal, T.; Videau, J. J.; Hupa, M.; Hupa, L. Thermal properties and surface reactivity in simulated body fluid of new strontium ion-containing phosphate glasses. *J. Mater. Sci. Mater. Med.* **2013**, *24*, 1407–1416, doi:10.1007/s10856-013-4910-9.
10. Sharmin, N.; Hasan, M. S.; Parsons, A. J.; Furniss, D.; Scotchford, C. A.; Ahmed, I.; Rudd, C. D. Effect of boron addition on the thermal, degradation, and cytocompatibility properties of phosphate-based glasses. *BioMed. Res. Int.* **2013**, *2013*, doi:10.1155/2013/902427.
11. Massera J, Kokkari A, Narhi T, H. L. The influence of SrO and CaO in silicate and phosphate bioactive glasses on human gingival fibroblasts. *J Mater Sci Mater Med* **2015**, *26*, 196, doi: DOI: 10.1007/s10856-015-5528-x.
12. Bunker, B. C.; Arnold, G. W.; Wilder, J. A. Phosphate glass dissolution in aqueous solutions. *J. Non. Cryst. Solids* **1984**, *64*, 291–316, doi:10.1016/0022-3093(84)90184-4.
13. Knowles, J. C. Phosphate based glasses for biomedical applications. *J. Mater. Chem.* **2003**, *13*, 2395–2401, doi:10.1039/b307119g.
14. Clement, J.; Manero, J. M.; Planell, J. A.; Avila, G.; Martinez, S. Analysis of the structural changes of a phosphate glass during its dissolution in simulated body fluid. *J Mater Sci Mater Med* **1999**, *10*, 729–732, doi:

10.1023/A:1008927222081.
15. Campbell, J. H.; Suratwala, T. I. Nd-doped phosphate glasses for high-energy/high-peak-power lasers. *J. Non. Cryst. Solids* **2000**, *263*, 318–341, doi:10.1016/S0022-3093(99)00645-6.
16. Jiang, S.; Myers, M. J.; Rhonehouse, D. L.; Hamlin, S. J.; Myers, J. D.; Griebner, U.; Koch, R.; Schonnagel, H. Ytterbium-doped phosphate laser glasses. *Proc. SPIE* 1997, *2986*, 10–15, doi: 10.1117/12.269990.
17. Gapontsev, V. P.; Matitsin, S. M.; Isineev, A. A.; Kravchenko, V. B. Erbium glass lasers and their applications. *Opt. Laser Technol.* **1982**, *14*, 189–196, doi:10.1016/0030-3992(82)90095-0.
18. Jiang, S.; Myers, M.; Peyghambarian, N. Er^{3+} doped phosphate glasses and lasers. *J. Non. Cryst. Solids* **1998**, *239*, 143–148, doi:10.1016/S0022-3093(98)00757-1.
19. Pugliese, D.; Boetti, N. G.; Lousteau, J.; Ceci-Ginistrelli, E.; Bertone, E.; Geobaldo, F.; Milanese, D. Concentration quenching in an Er-doped phosphate glass for compact optical lasers and amplifiers. *J. Alloys Compd.* **2016**, *657*, 678–683, doi:10.1016/j.jallcom.2015.10.126.
20. Boetti, N. G.; Scarpignato, G. C.; Lousteau, J.; Pugliese, D.; Bastard, L.; Broquin, J.-E.; Milanese, D. High concentration Yb-Er co-doped phosphate glass for optical fiber amplification. *J. Opt.* **2015**, *17*, 065705, doi:10.1088/2040-8978/17/6/065705.
21. Vitale-Brovarone, C.; Novajra, G.; Milanese, D.; Lousteau, J.; Knowles, J. C. Novel phosphate glasses with different amounts of TiO_2 for biomedical applications: dissolution tests and proof of concept of fibre drawing. *Mater. Sci. Eng. C* **2011**, *31*, 434–442, doi:10.1016/j.msec.2010.11.001.
22. Sharmin, N.; Parsons, A. J.; Rudd, C. D.; Ahmed, I. Effect of boron oxide addition on fibre drawing, mechanical properties and dissolution behaviour of phosphate-based glass fibres with fixed 40, 45 and 50 mol% P_2O_5. *J. Biomater. Appl.* **2014**, *29*, 639–653, doi:10.1177/0885328214539824.
23. Ceci-Ginistrelli, E.; Pugliese, D.; Boetti, N. G.; Novajra, G.; Ambrosone, A.; Lousteau, J.; Vitale-Brovarone, C.; Abrate, S.; Milanese, D. Novel biocompatible and resorbable UV-transparent phosphate glass based optical fiber. *Opt. Mater. Express* **2016**, *6*, 2040–2051, doi:10.1364/OME.6.002040.
24. Novajra, G.; Lousteau, J.; Milanese, D.; Vitale-Brovarone, C. Resorbable hollow phosphate glass fibres as controlled release systems for biomedical applications. *Mater. Lett.* **2013**, *99*, 125–127, doi:10.1016/j.matlet.2013.02.076.
25. Vitale-Brovarone, C.; Novajra, G.; Lousteau, J.; Milanese, D.; Raimondo, S.; Fornaro, M. Phosphate glass fibres and their role in neuronal polarization and axonal growth direction. *Acta Biomater.* **2012**, *8*, 1125–1136, doi:10.1016/j.actbio.2011.11.018.
26. Jiang, S.; Luo, T.; Hwang, B. C.; Smekatala, F.; Seneschal, K.; Lucas, J.; Peyghambarian, N. Er^{3+}-doped phosphate glasses for fiber amplifiers with high gain per unit length. *J. Non. Cryst. Solids* **2000**, *263*, 364–368, doi:10.1016/S0022-3093(99)00646-8.
27. Hofmann, P.; Voigtlander, C.; Nolte, S.; Peyghambarian, N.; Schulzgen, A. 550-mW output power from a narrow linewidth all-phosphate fiber laser. *J. Light. Technol.* **2013**, *31*, 756–760, doi:10.1109/JLT.2012.2233392.
28. Hwang, B. C.; Jiang, S.; Luo, T.; Seneschal, K.; Sorbello, G.; Morrell, M.; Smektala, F.; Honkanen, S.; Lucas, J.; Peyghambarian, N. Performance of high-concentration Er^{3+}-doped phosphate fiber amplifiers. *IEEE Photonics*

Technol. Lett. **2001**, *13*, 197–199, doi:10.1109/68.914319.
29. Massera, J.; Shpotyuk, Y.; Sabatier, F.; Jouan, T.; Boussard-Plédel, C.; Roiland, C.; Bureau, B.; Petit, L.; Boetti, N. G.; Milanese, D.; Hupa, L. Processing and characterization of novel borophosphate glasses and fibers for medical applications. *J. Non. Cryst. Solids* **2015**, *425*, 52–60, doi:10.1016/j.jnoncrysol.2015.05.028.
30. Soltani, I.; Hraiech, S.; Horchani-Naifer, K.; Massera, J.; Petit, L.; Férid, M. Thermal, structural and optical properties of Er^{3+} doped phosphate glasses containing silver nanoparticles. *J. Non. Cryst. Solids* **2016**, *438*, 67–73, doi:10.1016/j.jnoncrysol.2015.12.022.
31. ASTM Committee C14 Standards on Glass and Glass Products. *Am. Soc. Test. Mater.* **1955**.
32. Yamane, M.; Asahara, Y. *Glasses for photonics*; Cambridge University Press: Cambridge, **2000**, ISBN: 978-0521018616.
33. Carter, C. B.; Norton, M. G. *Ceramic Materials: Science and Engineering*; Springer Science & Business Media, **2013**; Vol. 56; ISBN 9781461435228.
34. Adam, J. Lanthanides in Non-Oxide Glasses. *Chem. Rev.* **2002**, *102*, 2461–2476, doi:10.1021/cr010305b.
35. Lopez-Iscoa, P.; Petit, L.; Massera, J.; Janner, D.; Boetti, N. G.; Pugliese, D.; Fiorilli, S.; Novara, C.; Giorgis, F.; Milanese, D. Effect of the addition of Al_2O_3, TiO_2 and ZnO on the thermal, structural and luminescence properties of Er^{3+}-doped phosphate glasses. *J. Non. Cryst. Solids* **2017**, *460*, 161–168, doi:10.1016/j.jnoncrysol.2017.01.030.
36. J. J. Hudgens *The structure and properties of anhydrous, alkali ultra-phosphate glasses*, Iowa State University, **1994**.
37. Yan, Y.; Faber, A. J.; de Waal, H. Luminescence quenching by OH groups in highly Er-doped phosphate glasses. *J. Non. Cryst. Solids* **1995**, *181*, 283–290, doi:10.1016/S0022-3093(94)00528-1.
38. Eqtesadi, S.; Motealleh, A.; Miranda, P.; Pajares, A.; Lemos, A.; Ferreira, J. M. F. Robocasting of 45S5 bioactive glass scaffolds for bone tissue engineering. *J. Eur. Ceram. Soc.* **2014**, *34*, 107–118, doi:10.1016/j.jeurceramsoc.2013.08.003.
39. Fan, J. P.; Kalia, P.; Di Silvio, L.; Huang, J. In vitro response of human osteoblasts to multi-step sol-gel derived bioactive glass nanoparticles for bone tissue engineering. *Mater. Sci. Eng. C* **2014**, *36*, 206–214, doi:10.1016/j.msec.2013.12.009.
40. Rau, J. V.; Teghil, R.; Fosca, M.; De Bonis, A.; Cacciotti, I.; Bianco, A.; Albertini, V. R.; Caminiti, R.; Ravaglioli, A. Bioactive glass-ceramic coatings prepared by pulsed laser deposition from RKKP targets (sol-gel vs melt-processing route). *Mater. Res. Bull.* **2012**, *47*, 1130–1137, doi:10.1016/j.materresbull.2012.02.011.
41. Owens, G. J.; Singh, R. K.; Foroutan, F.; Alqaysi, M.; Han, C. M.; Mahapatra, C.; Kim, H. W.; Knowles, J. C. Sol-gel based materials for biomedical applications. *Prog. Mater. Sci.* **2016**, *77*, 1–79, doi:10.1016/j.pmatsci.2015.12.001.
42. Sepulveda, P.; Jones, J. R.; Hench, L. L. In vitro dissolution of melt-derived 45S5 and sol-gel derived 58S bioactive glasses. *J. Biomed. Mater. Res.* **2002**, *61*, 301–311, doi:10.1002/jbm.10207.
43. Pereira, M. M.; Hench, L. L. Mechanisms of hydroxyapatite formation on porous gel-silica substrates. *J. Sol-Gel Sci. Technol.* **1996**, *7*, 59–68, doi:10.1007/BF00401884.

44. Foroutan, F. Sol-Gel Synthesis of Phosphate-Based Glasses for Biomedical Applications. **2015**.
45. Taherkhani, S.; Moztarzadeh, F. Influence of strontium on the structure and biological properties of sol–gel-derived mesoporous bioactive glass (MBG) powder. *J. Sol-Gel Sci. Technol.* **2016**, *78*, 539–549, doi:10.1007/s10971-016-3995-2.
46. Shankhwar, N.; Kothiyal, G. P.; Srinivasan, A. Influence of phosphate precursors on the structure, crystallization behaviour and bioactivity of sol–gel derived 45S5 bioglass. *RSC Adv.* **2015**, *5*, 100762–100768, doi:10.1039/C5RA19184J.
47. Catteaux, R.; Grattepanche-Lebecq, I.; Désanglois, F.; Chai, F.; Hornez, J. C.; Hampshire, S.; Follet-Houttemane, C. Synthesis, characterization and bioactivity of bioglasses in the Na_2O-CaO-P_2O_5-SiO_2 system prepared via sol gel processing. *Chem. Eng. Res. Des.* **2013**, *91*, 2420–2426, doi:10.1016/j.cherd.2013.05.017.
48. Cacciotti, I.; Lombardi, M.; Bianco, A.; Ravaglioli, A.; Montanaro, L. Sol-gel derived 45S5 bioglass: Synthesis, microstructural evolution and thermal behaviour. *J. Mater. Sci. Mater. Med.* **2012**, *23*, 1849–1866, doi:10.1007/s10856-012-4667-6.
49. Siqueira, R. L.; Zanotto, E. D. The influence of phosphorus precursors on the synthesis and bioactivity of SiO_2-CaO-P_2O_5 sol-gel glasses and glass-ceramics. *J. Mater. Sci. Mater. Med.* **2013**, *24*, 365–379, doi:10.1007/s10856-012-4797-x.
50. Padilla, S.; Román, J.; Carenas, A.; Vallet-Regí, M. The influence of the phosphorus content on the bioactivity of sol-gel glass ceramics. *Biomaterials* **2005**, *26*, 475–483, doi:10.1016/j.biomaterials.2004.02.054.
51. Carta, D.; Knowles, J. C.; Smith, M. E.; Newport, R. J. Synthesis and structural characterization of P_2O_5-CaO-Na_2O sol-gel materials. *J. Non. Cryst. Solids* **2007**, *353*, 1141–1149, doi:10.1016/j.jnoncrysol.2006.12.093.
52. Pickup, D. M.; Guerry, P.; Moss, R. M.; Knowles, J. C.; Smith, M. E.; Newport, R. J. New sol–gel synthesis of a $(CaO)_{0.3}(Na_2O)_{0.2}(P_2O_5)_{0.5}$ bioresorbable glass and its structural characterisation. *J. Mater. Chem.* **2007**, *17*, 4777, doi:10.1039/b709955j.
53. Pickup, D. M.; Newport, R. J.; Knowles, J. C. Sol-gel phosphate-based glass for drug delivery applications. *J. Biomater. Appl.* **2012**, *26*, 613–22, doi:10.1177/0885328210380761.
54. Kreidl, N. J.; Weyl, W. A. Phosphates in ceramic ware: phosphate glasses. *J. Am. Ceram. Soc.* **1941**, *24*, 372–378, doi:10.1111/j.1151-2916.1941.tb15444.x.
55. Brow, R. Review: the structure of simple phosphate glasses. *J. Non. Cryst. Solids* **2000**, *263–264*, 1–28, doi:10.1016/S0022-3093(99)00620-1.
56. Wazer, J. R. *Phosphorus and its Compounds, Vol. 1*. Interscience, New York, USA; 1958.
57. Weber, M. J. Science and technology of laser glass. *J. Non. Cryst. Solids* **1990**, *123*, 208–222, doi:10.1016/0022-3093(90)90786-L.
58. Ropp, R. C. *Inorganic polymeric glasses*; Elsevier, New York, USA; 1992.
59. Day, D. E.; Wu, Z.; Ray, C. S.; Hrma, P. Chemically durable iron phosphate glass wasteforms. *J. Non. Cryst. Solids* **1998**, *241*, 1–12, doi:10.1016/S0022-3093(98)00759-5.
60. Loong, C.-K.; Suzuya, K.; Price, D. L.; Sales, B. C.; Boatner, L. A. Structure and dynamics of phosphate glasses: from ultra- to orthophosphate

composition. *Phys. B Condens. Matter* **1997**, *241–243*, 890–896, doi:10.1016/S0921-4526(97)00747-3.
61. Cruickshank, D. W. J. The role of 3d-orbitals in pi-bonds between (a) silicon, phosphorus, sulphur, or chlorine and (b) oxygen or nitrogen. *J. Chem. Soc.* **1961**, 5486–5504, doi:10.1039/JR9610005486.
62. Mitchell, K. A. R. Use of outer d orbitals in bonding. *Chem. Rev.* **1969**, *69*, 157–178, doi:10.1021/cr60258a001.
63. Richard K, B. Review: the structure of simple phosphate glasses. *J. Non. Cryst. Solids* **2000**, *263–264*, 1–28.
64. Brow, R. K.; Click, C. A.; Alam, T. M. Modifier coordination and phosphate glass networks. *J. Non. Cryst. Solids* **2000**, *274*, 9–16, doi:https://doi.org/10.1016/S0022-3093(00)00178-2.
65. Ojovan, M. I.; Lee, W. E. *An Introduction to Nuclear Waste Immobilisation*; **2014**; ISBN 9780080993928.
66. Hoppe, U.; Walter, G.; Kranold, R.; Stachel, D. Structural specifics of phosphate glasses probed by diffraction methods: a review. *J. Non. Cryst. Solids* **2000**, *263–264*, 29–47, doi:10.1016/S0022-3093(99)00621-3.
67. Sales, B. C.; Boatner, L. A. Physical and chemical characteristics of lead-iron phosphate nuclear waste glasses. *J. Non. Cryst. Solids* **1986**, *79*, 83–116, doi:10.1016/0022-3093(86)90040-2.
68. Uhlmann, D. R.; Kreidl, N. J. *Optical properties of glass*; American Ceramic Society, Westerville, OH, **1991**; ISBN 0944904351 9780944904350.
69. Kiani, A.; Hanna, J. V.; King, S. P.; Rees, G. J.; Smith, M. E.; Roohpour, N.; Salih, V.; Knowles, J. C. Structural characterization and physical properties of P_2O_5–CaO–Na_2O–TiO_2 glasses by Fourier transform infrared, Raman and solid-state magic angle spinning nuclear magnetic resonance spectroscopies. *Acta Biomater.* **2012**, *8*, 333–340, doi:10.1016/j.actbio.2011.08.025.
70. Kiani, a.; Lakhkar, N. J.; Salih, V.; Smith, M. E.; Hanna, J. V.; Newport, R. J.; Pickup, D. M.; Knowles, J. C. Titanium-containing bioactive phosphate glasses. *Philos. Trans. R. Soc. A Math. Phys. Eng. Sci.* **2012**, 1352–1375, doi:10.1098/rsta.2011.0276.
71. Seneschal, K.; Smektala, F.; Bureau, B.; Floch, M. Le; Jiang, S.; Luo, T.; Lucas, J.; Peyghambarian, N. Properties and structure of high erbium doped phosphate glass for short optical fibers amplifiers. *Mater. Res. Bull.* **2005**, *40*, 1433–1442, doi:10.1016/J.MATERRESBULL.2005.05.004.
72. Campbell, J. H.; Hayden, J. S.; Marker, A. High-Power Solid-State Lasers: a Laser Glass Perspective. *Int. J. Appl. Glas. Sci.* **2011**, 3–29, doi:10.1111/j.2041-1294.2011.00044.x.
73. Boetti, N. G.; Negro, D.; Scarpignato, G. C.; Perrone, G.; Abrate, S.; Lousteau, J.; Mura, E.; Milanese, D. Photonic glasses for IR and mid-IR spectral range. *International Conference on Space Optics — ICSO*. **2012**, SPIE, 2017; Vol. 10564, p. 74.
74. Wilder, J. A. Glasses and glass ceramics for sealing to aluminum alloys. *J. Non. Cryst. Solids* **1980**, *38–39*, 879–884, doi:10.1016/0022-3093(80)90548-7.
75. Popp, J.; Tuchin, V. V.; Chiou, A.; Heinemann, S. H. *Handbook of biophotonics*; Wiley-VCH, **2011**; ISBN 9783527410477.
76. Kaur, G. *Bioactive Glasses: Potential Biomaterials for Future Therapy*; **2017**, Springer, New York, USA, ISBN 978-3-319-45716-1.
77. Hoppe, A.; Güldal, N. S.; Boccaccini, A. R. A review of the biological response to ionic dissolution products from bioactive glasses and glass-

ceramics. *Biomaterials* **2011**, *32*, 2757–2774, doi: 10.1016/j.biomaterials.2011.01.004.
78. Hill, R. An alternative view of the degradation of bioglass. *J. Mater. Sci. Lett.* **1996**, *15*, 1122–1125, doi:10.1007/BF00539955.
79. Christie, J. K.; Ainsworth, R. I.; Di Tommaso, D.; De Leeuw, N. H. Nanoscale chains control the solubility of phosphate glasses for biomedical applications. *J. Phys. Chem. B* **2013**, *117*, 10652–10657, doi:10.1021/jp4058115.
80. Ahmed, I.; Collins, C. A.; Lewis, M. P.; Olsen, I.; Knowles, J. C. Processing, characterisation and biocompatibility of iron-phosphate glass fibres for tissue engineering. *Biomaterials* **2004**, *25*, 3223–3232, doi:10.1016/J.BIOMATERIALS.2003.10.013.
81. Valerio, P.; Pereira, M. M.; Goes, a M.; Leite, M. F. Effects of extracellular calcium concentration on the glutamate release by bioactive glass (BG60S) preincubated osteoblasts. *Biomed. Mater.* **2009**, *4*, 045011, doi:10.1088/1748-6041/4/4/045011.
82. Julien, M.; Khoshniat, S.; Lacreusette, A.; Gatius, M.; Bozec, A.; Wagner, E. F.; Wittrant, Y.; Masson, M.; Weiss, P.; Beck, L.; Magne, D.; Guicheux, J. Phosphate-dependent regulation of MGP in osteoblasts: role of ERK1/2 and Fra-1. *J. Bone Miner. Res.* **2009**, *24*, 1856–1868, doi:10.1359/jbmr.090508.
83. Carlisle, E. M. E. Silicon: a possible factor in bone calcification. *Science.* **1970**, *1363*, 4–5, doi:10.1126/science.167.3916.279.
84. Reffitt, D. M.; Ogston, N.; Jugdaohsingh, R.; Cheung, H. F. J.; Evans, B. A. J.; Thompson, R. P. H.; Powell, J. J.; Hampson, G. N. Orthosilicic acid stimulates collagen type 1 synthesis and osteoblastic differentiation in human osteoblast-like cells in vitro. *Bone* **2003**, *32*, 127–135, doi:10.1016/S8756-3282(02)00950-X.
85. Delannoy, P.; Bazot, D.; Marie, P. J. Long-term treatment with strontium ranelate increases vertebral bone mass without deleterious effect in mice. *Metabolism.* **2002**, *51*, 906–911, doi:10.1053/meta.2002.33360.
86. Grynpas, M. D.; Marie, P. J. Effects of low doses of strontium on bone quality and quantity in rats. *Bone* **1990**, *11*, 313–319, doi:10.1016/8756-3282(90)90086-E.
87. Brandão-Neto, J.; Stefan, V.; Mendonça, B. B.; Bloise, W.; Castro, A. V. B. The essential role of zinc in growth. *Nutr. Res.* **1995**, *15*, 335–358, doi:10.1016/0271-5317(95)00003-8.
88. Yamaguchi, M. Role of zinc in bone formation and bone resorption. *J. Trace Elem. Exp. Med.* **1998**, *11*, 119–135, doi:10.1002/(SICI)1520-670X(1998)11:2/3<119::AID-JTRA5>3.0.CO;2-3.
89. Saltman, P. D.; Strause, L. G. The role of trace minerals in osteoporosis. *J. Am. Coll. Nutr.* **1993**, *12*, 384–389, doi:10.1080/07315724.1993.10718327.
90. Murphy, S.; Wren, A. W.; Towler, M. R.; Boyd, D. The effect of ionic dissolution products of Ca-Sr-Na-Zn-Si bioactive glass on in vitro cytocompatibility. *J. Mater. Sci. Mater. Med.* **2010**, *21*, 2827–2834, doi:10.1007/s10856-010-4139-9.
91. Xynos, I. D.; Edgar, a J.; Buttery, L. D.; Hench, L. L.; Polak, J. M. Ionic products of bioactive glass dissolution increase proliferation of human osteoblasts and induce insulin-like growth factor II mRNA expression and protein synthesis. *Biochem. Biophys. Res. Commun.* **2000**, *276*, 461–465, doi:10.1006/bbrc.2000.3503.

92. Hench, L. L. The story of Bioglass®. *J. Mater. Sci. Mater. Med.* **2006**, *17*, 967–978, doi:10.1007/s10856-006-0432-z.
93. Saino, E.; Grandi, S.; Quartarone, E.; Maliardi, V.; Galli, D.; Bloise, N.; Fassina, L.; de Angelis, M. G. C.; Mustarelli, P.; Imbriani, M.; Visai, L. In vitro calcified matrix deposition by human osteoblasts onto a zinc-containing bioactive glass. *Eur. Cells Mater.* **2011**, *21*, 59–72, doi:10.22203/eCM.v021a05.
94. Balasubramanian, P.; Strobel, L. A.; Kneser, U.; Boccaccini, A. R. Zinc-containing bioactive glasses for bone regeneration, dental and orthopedic applications. *Biomed. Glas.* **2015**, *1*, doi:10.1515/bglass-2015-0006.
95. Tanaka, S.; Akaishi, E.; Hosaka, K.; Okamura, S.; Kubohara, Y. Zinc ions suppress mitogen-activated interleukin-2 production in Jurkat cells. *Biochem. Biophys. Res. Commun.* **2005**, *335*, 162–167, doi:10.1016/j.bbrc.2005.07.059.
96. Sutherland, L. C.; Anderson, C. L.; Williams, G. T. Zinc has no effect on IL-3-mediated apoptosis of BAF-3 cells but enhances CD95-mediated apoptosis of Jurkat cells. *J. Immunol. Methods* **2000**, *234*, 43–50, doi:10.1016/S0022-1759(99)00202-1.
97. Oki, A.; Parveen, B.; Hossain, S.; Adeniji, S.; Donahue, H. Preparation andin vitro bioactivity of zinc containing sol-gel-derived bioglass materials. *J. Biomed. Mater. Res.* **2004**, *69A*, 216–221, doi:10.1002/jbm.a.20070.
98. Balamurugan, A.; Balossier, G.; Kannan, S.; Michel, J.; Rebelo, A. H. S.; Ferreira, J. M. F. Development and in vitro characterization of sol-gel derived CaO-P_2O_5-SiO_2-ZnO bioglass. *Acta Biomater.* **2007**, *3*, 255–262, doi:10.1016/j.actbio.2006.09.005.
99. Abou Neel, E. A.; Pickup, D. M.; Valappil, S. P.; Newport, R. J.; Knowles, J. C. Bioactive functional materials: a perspective on phosphate-based glasses. *J. Mater. Chem.* **2009**, *19*, 690–701, doi:10.1039/B810675D.
100. Jones, J. R. Review of bioactive glass: From Hench to hybrids. *Acta Biomater.* **2013**, *9*, 4457–4486, doi:10.1016/J.ACTBIO.2012.08.023.
101. Mishra A., R. J. and M. J. Ag-doped phosphate bioactive glasses: thermal, structural and in-vitro dissolution properties. *Biomed. Glas.* **2016**, *2*, 38–48.
102. Salih, V.; Franks, K.; James, M.; Hastings, G. W.; Knowles, J. C.; Olsen, I. Development of soluble glasses for biomedical use part II: The biological response of human osteoblast cell lines to phosphate-based soluble glasses. *J. Mater. Sci. Mater. Med.* **2000**, *11*, 615–620, doi:10.1023/A:1008901612674.
103. Kenyon, A. J. *Recent developments in rare-earth doped materials for optoelectronics*; **2002**, Vol. 26, ISBN 0079-6727.
104. Miniscalco, W. J. Erbium-Doped Glasses for Fiber Amplifiers at 1500 nm. *J. Light. Technol.* **1991**, *9*, 234–250, doi:10.1109/50.65882.
105. Lopez-Iscoa, P.; Pugliese, D.; Boetti, N. G.; Janner, D.; Baldi, G.; Petit, L.; Milanese, D. Design, synthesis, and structure-property relationships of Er^{3+}-doped TiO_2 luminescent particles synthesized by sol-gel. *Nanomaterials* **2018**, *8*, doi:10.3390/nano8010020.
106. De Wild, J.; Meijerink, A.; Rath, J. K.; van Sark, W. G. J. H. M.; Schropp, R. E. I. Upconverter solar cells: materials and applications. *Energy Environ. Sci.* **2011**, *4*, 4835, doi:10.1039/c1ee01659h.
107. Rapaport, A.; Milliez, J.; Bass, M.; Cassanho, A.; Jenssen, H. Review of the properties of Up-conversion phosphors for new emissive displays. *IEEE/OSA J. Disp. Technol.* **2006**, *2*, 68–78, doi:10.1109/JDT.2005.863781.

108. Wang, M.; Mi, C.-C.; Wang, W.-X.; Liu, C.-H.; Wu, Y.-F.; Xu, Z.-R.; Mao, C.-B.; Xu, S.-K. Immunolabeling and NIR-Excited Fluorescent Imaging of HeLa Cells by Using NaYF4:Yb,Er Upconversion Nanoparticles. *ACS Nano* **2009**, *3*, 1580–1586, doi: 10.1021/Nn900491j.
109. Elements, A. Erbium Available online: www.americanelements.com/er
110. Bouzid, B. Theoretical analysis of erbium doped fiber amplifier. *2011 Saudi Int. Electron. Commun. Photonics Conf.* **2011**, 1–5, doi:10.1109/SIECPC.2011.5876989.
111. Johannsen, S. R.; Roesgaard, S.; Julsgaard, B.; Ferreira, R. A. S.; Chevallier, J.; Balling, P.; Ram, S. K.; Larsen, A. N. Influence of TiO_2 host crystallinity on Er^{3+} light emission. *Opt. Mater. Express* **2016**, *6*, 1664, doi:10.1364/OME.6.001664.
112. Brecher, C.; Riseberg, L. A. Laser-induced fluorescence line narrowing in Eu glass: A spectroscopic analysis of coordination structure. *Phys. Rev. B* **1976**, *13*, 81–93, doi:10.1103/PhysRevB.13.81.
113. Atkins, P.; Paula, J. De *Atkins' physical chemistry*; Springer, New York, USA; **2009**; ISBN 9780199543373.
114. Svelto, O. *Principles of lasers*; **2010**; Springer, New York, USA; ISBN 9781441913012.
115. Shinn, M. D.; Sibley, W. a.; Drexhage, M. G.; Brown, R. N. Optical transitions of Er^{3+} ions in fluorozirconate glass. *Phys. Rev. B* **1983**, *27*, 6635–6648, doi: 10.1103/PhysRevB.30.2429.
116. Reisfeld, R.; Jørgensen, C. K. Excited state phenomena in vitreous materials. *Handb. Phys. Chem. Rare Earths*, **1987**, *9*, 1–90, ISBN 0-444-87045-8.
117. Schweizer, T.; Brady, D.; Hewak, D. W. Fabrication and spectroscopy of erbium doped gallium lanthanum sulphide glass fibres for mid-infrared laser applications. *Opt. Express* **1997**, *1*, 102, doi:10.1364/OE.1.000102.
118. Tamrakar, R.; Bisen, D. P.; Brahme, N. Influence of Er^{3+} concentration on the photoluminescence characteristics and excitation mechanism of Gd_2O_3:Er^{3+} phosphor synthesized via a solid-state reaction method. *Luminescence* **2014**, *30*, doi: 10.1002/bio.2803.
119. Yang, F.; Ye, Q.; Pan, Z.; Chen, D.; Cai, H.; Qu, R.; Yang, Z.; Zhang, Q. 100-mW linear polarization single-frequency all-fiber seed laser for coherent Doppler lidar application. *Opt. Commun.* **2012**, *285*, 149–152, doi:10.1016/j.optcom.2011.09.030.
120. Dos Santos, P. V.; De Araujo, M. T.; Gouveia-Neto, A. S.; Medeiros Neto, J. A.; Sombra, A. S. B. Optical temperature sensing using upconversion fluorescence emission in Er^{3+}/Yb^{3+}-codoped chalcogenide glass. *Appl. Phys. Lett.* **1998**, *73*, 578–580, doi:10.1063/1.121861.
121. Maurice, E.; Monnom, G.; Dussardier, B.; Saïssy, A.; Ostrowsky, D. B.; Baxter, G. W. Erbium-doped silica fibers for intrinsic fiber-optic temperature sensors. *Appl. Opt.* **1995**, *34*, 8019, doi:10.1364/AO.34.008019.
122. Digonnet, M. J. F. *Rare-earth-doped fiber lasers and amplifiers*; Springer, New York, USA; 2001; ISBN 0824704584.
123. Ming, C.; Song, F.; Liu, H. Intense blue up-conversion emission in Tm^{3+}/Yb^{3+} co-doped phosphate glass. *J. Non. Cryst. Solids* **2013**, *360*, 1–3, doi:10.1016/J.JNONCRYSOL.2012.10.014.
124. Auzel, F.; Baldacchini, G.; Laversenne, L.; Boulon, G. Radiation trapping and self-quenching analysis in Yb^{3+}, Er^{3+}, and Ho^{3+} doped Y_2O_3. In *Opt. Mat.*; 2003; Vol. 24, pp. 103–109, doi: 10.1016/S0925-3467(03)00112-5.
125. Auzel, F.; Bonfigli, F.; Gagliari, S.; Baldacchini, G. The interplay of self-

trapping and self-quenching for resonant transitions in solids; role of a cavity. *J. Lumin.* **2001**, *94*, 293–297, doi:10.1016/S0022-2313(01)00308-8.
126. Rivera-López, F.; Babu, P.; Jyothi, L.; Rodríguez-Mendoza, U. R.; Martín, I. R.; Jayasankar, C. K.; Lavín, V. Er^{3+}-Yb^{3+} codoped phosphate glasses used for an efficient 1.5 μm broadband gain medium. *Opt. Mater. (Amst).* **2012**, *34*, 1235–1240, doi:10.1016/j.optmat.2012.01.017.
127. Hwang, B.-C.; Jiang, S.; Luo, T.; Watson, J.; Sorbello, G.; Peyghambarian, N. Cooperative upconversion and energy transfer of new high Er and Yb-Er-doped phosphate glasses. *J. Opt. Soc. Am. B* **2000**, *17*, 833–839, doi:10.1364/JOSAB.17.000833.
128. Speghini, A.; Francini, R.; Martinez, A.; Tavernese, M.; Bettinelli, M. Spectroscopic properties of Er^{3+}, Yb^{3+} and Er^{3+}/Yb^{3+} doped metaphosphate glasses. *Spectrochim. Acta - Part A Mol. Biomol. Spectrosc.* **2001**, *57*, 2001–2008, doi:Doi 10.1016/S1386-1425(01)00473-5.
129. Cai, M.; Wei, T.; Zhou, B.; Tian, Y.; Zhou, J.; Xu, S.; Zhang, J. Analysis of energy transfer process based emission spectra of erbium doped germanate glasses for mid-infrared laser materials. *J. Alloys Compd.* **2015**, *626*, 165–172, doi:10.1016/j.jallcom.2014.11.077.
130. Lee, Y. W.; Sinha, S.; Digonnet, M. J. F.; Byer, R. L.; Jiang, S. Measurement of high photodarkening resistance in heavily Yb31-doped phosphate fibres. *Electron. Lett.* **2008**, *44*, 14–16, doi:10.1049/el:20082698.
131. Boetti, N.; Pugliese, D.; Ceci-Ginistrelli, E.; Lousteau, J.; Janner, D.; Milanese, D. Highly Doped Phosphate Glass Fibers for Compact Lasers and Amplifiers: A Review. *Appl. Sci.* **2017**, *7*, 1295, doi:10.3390/app7121295.
132. Bourhis, K.; Shpotyuk, Y.; Massera, J.; Aallos, V.; Jouan, T.; Boussard-Plèdel, C.; Bureau, B.; Petit, L.; Koponen, J.; Hupa, L.; Hupa, M.; Ferraris, M. Thermal and structural characterization of erbium-doped borosilicate fibers with low silica content containing various amounts of P_2O_5 and Al_2O_3. *Opt. Mater.* **2014**, *37*, 87–92, doi:10.1016/j.optmat.2014.05.004.
133. Kenyon, A. J. Erbium in silicon. *Semicond. Sci. Technol.* **2005**, *20*, doi: 10.1088/0268-1242/20/12/R02.
134. Tikhomirov, V. K.; Naftaly, M.; Jha, A. Effects of the site symmetry and host polarizability on the hypersensitive transition $^3P_0 \rightarrow {}^3F_2$ of Pr^{3+} in fluoride glasses. *J. Appl. Phys.* **1999**, *86*, 351–354, doi:10.1063/1.370737.
135. Brow, R. K. Nature of alumina in phosphate glass: I, properties of sodium aluminophosphate glass. *J. Am. Ceram. Soc.* **1993**, *76*, 913–918, doi:10.1111/j.1151-2916.1993.tb05315.x.
136. Shaharuddin, S.; Ahmed, I.; Furniss, D.; Parsons, A.; Rudd, C. Investigation on the thermal properties, density and degradation of quaternary iron and titanium phosphate based glasses. *IOP Conf. Ser. Mater. Sci. Eng.* **2016**, *114*, 012124, doi:10.1088/1757-899X/114/1/012124.
137. Zaid, M. H. M.; Matori, K. A.; Abdul Aziz, S. H.; Zakaria, A.; Ghazali, M. S. M. Effect of ZnO on the physical properties and optical band gap of soda lime silicate glass. *Int. J. Mol. Sci.* **2012**, *13*, 7550–7558, doi:10.3390/ijms13067550.
138. Zhao, J.; Zheng, X.; Schartner, E. P.; Ionescu, P.; Zhang, R.; Nguyen, T. L.; Jin, D.; Ebendorff-Heidepriem, H. Upconversion Nanocrystal-Doped Glass: A New Paradigm for Photonic Materials. *Adv. Opt. Mater.* **2016**, *4*, 1507–1517, doi:10.1002/adom.201600296.
139. Strnad, Z. Role of the glass phase in bioactive glass-ceramics. *Biomaterials* **1992**, doi:10.1016/0142-9612(92)90056-T.

140. Stookey, S. D. Chemical Machining of Photosensitive Glass. *Ind. Eng. Chem.* **1953**, *45*, 115–118, doi:10.1021/ie50517a039.
141. Zanotto, E. D. A bright future for glass-ceramics. *Am. Ceram. Soc. Bull.* **2010**, *89*, 19–27, doi:10.2217/fmb.11.55.
142. Dantelle, G.; Mortier, M.; Vivien, D.; Patriarche, G. Influence of Ce^{3+} doping on the structure and luminescence of Er^{3+}-doped transparent glass-ceramics. *Optical Materials*; **2006**; Vol. 28, pp. 638–642, doi: 10.1016/j.optmat.2005.09.008.
143. Nakamura, T.; Yamamuro, T.; Higashi, S.; Kokubo, T.; Itoo, S. A new glass-ceramic for bone replacement: Evaluation of its bonding to bone tissue. *J. Biomed. Mater. Res.* **1985**, *19*, 685–698, doi:10.1002/jbm.820190608.
144. Yu, X.; Song, F.; Zou, C.; Luo, L.; Ming, C.; Wang, W.; Cheng, Z.; Han, L.; Sun, T.; Tian, J. Temperature dependence of luminescence behavior in Er^{3+}/Yb^{3+} co-doped transparent phosphate glass ceramics. *Opt. Mater.* **2009**, *31*, 1645–1649, doi:10.1016/j.optmat.2009.03.017.
145. Massera, J.; Remond, J.; Musgraves, J.; Davis, M. J.; Misture, S.; Petit, L.; Richardson, K. Nucleation and growth behavior of glasses in the TeO_2–Bi_2O_3–ZnO glass system. *J. Non. Cryst. Solids* **2010**, *356*, 2947–2955, doi:10.1016/J.JNONCRYSOL.2010.03.045.
146. Ziani, N.; Belhadji, M.; Heireche, L.; Bouchaour, Z.; Belbachir, M. Crystallization kinetics of $Ge_{20}Te_{80}$ chalcogenide glasses doped with Sb. *Phys. B Condens. Matter* **2005**, *358*, 132–137, doi:10.1016/J.PHYSB.2004.12.068.
147. Zanotto, E. D.; Fokin, V. M. Recent studies of internal and surface nucleation in silicate glasses. *Philos. Trans. R. Soc. London A Math. Phys. Eng. Sci.* **2003**, *361*, 591–613, doi:10.1098/rsta.2002.1150.
148. Massera, J.; Mayran, M.; Rocherullé, J.; Hupa, L. Crystallization behavior of phosphate glasses and its impact on the glasses' bioactivity. *J. Mater. Sci.* **2015**, *50*, 3091–3102, doi:10.1007/s10853-015-8869-4.
149. Joraid, A. A. Limitation of the Johnson–Mehl–Avrami (JMA) formula for kinetic analysis of the crystallization of a chalcogenide glass. *Thermochim. Acta* **2005**, *436*, 78–82, doi:10.1016/J.TCA.2005.07.005.
150. Ray, C. S.; Day, D. E. Identifying internal and surface crystallization by differential thermal analysis for the glass-to-crystal transformations. *Thermochim. Acta* **1996**, *280–281*, 163–174, doi:10.1016/0040-6031(95)02640-1.
151. Dejneka, M. J. Transparent Oxyfluoride Glass Ceramics. *MRS Bull.* **1998**, *23*, 57–62, doi:10.1557/S0883769400031018.
152. Karpukhina, N.; Hill, R.; Law, R. *Crystallisation in oxide glasses - A tutorial review*; **2014**, 43, 2174-2186, doi: 10.1039/c3cs60305a.
153. Turnbull, D. Phase changes. *Solid State Phys.* **1956**, *3*, 225–306, doi:10.1016/S0081-1947(08)60134-4.
154. Shelby, J. E. *Introduction to Glass Science and Technology: Edition 2*; **2005**, Royal Society of Chemistry, Cambridge, UK, ISBN: 978-0854046393.
155. Beall, G. H.; Pinckney, L. R. Nanophase glass-ceramics. *J. Am. Ceram. Soc.* **1999**, *82*, 5–16, doi: 10.1111/j.1151-2916.1999.tb01716.x.
156. Morimoto, S. Phase separation and crystallization in the system SiO_2–Al_2O_3–P_2O_5–B_2O_3–Na_2O glasses. *J. Non. Cryst. Solids* **2006**, *352*, 756–760, doi:10.1016/j.jnoncrysol.2006.02.007.
157. Liu, C.; Heo, J. Lead Chalcogenide Quantum Dot-Doped Glasses for Photonic Devices. *Int. J. Appl. Glas. Sci.* **2013**, 4, 163–173,

doi:10.1111/ijag.12032.
158. Massera, J.; Sevrette, B.; Petit, L.; Koponen, J.; Trngren, B.; Glorieux, B.; Hupa, L.; Hupa, M. Effect of partial crystallization on the thermal, optical, structural and Er^{3+} luminescence properties of silicate glasses. *Mater. Chem. Phys.* **2014**, *147*, 1099–1109, doi:10.1016/j.matchemphys.2014.06.064.
159. Peretti, R.; Jurdyc, A. M.; Jacquier, B.; Blanc, W.; Dussardier, B. Spectroscopic signature of phosphate crystallization in erbium-doped optical fibre preforms. *Opt. Mater.* **2011**, *33*, 835–838, doi:10.1016/j.optmat.2011.01.005.
160. Kukkonen, L. L.; Reaney, I. M.; Furniss, D.; Seddon, A. B. Nucleation and crystallisation behaviour of transparent, erbium doped, oxyfluoride glass ceramics for active photonic devices. *Phys. Chem. Glas.* **2001**, *42*, 265–273.
161. Lou, K.; Song, Z.; Shang, J.; Yang, Z.; Qiu, J. Nano-crystals precipitation and upconversion luminescence properties in Er^{3+}/Yb^{3+} co-doped fluoride phosphate glass-ceramics. *J. Non. Cryst. Solids* **2011**, *357*, 2251–2254, doi:10.1016/j.jnoncrysol.2010.11.117.
162. Yu, X.; Duan, L.; Ni, L.; Wang, Z. Fabrication and luminescence behavior of phosphate glass ceramics co-doped with Er^{3+} and Yb^{3+}. *Opt. Commun.* **2012**, *285*, 3805–3808, doi:10.1016/j.optcom.2012.04.042.
163. Yu, X.; Song, F.; Wang, W.; Luo, L.; Han, L.; Cheng, Z.; Sun, T.; Tian, J.; Pun, E. Y. B. Comparison of optical parameters and luminescence between Er^{3+}/Yb^{3+} codoped phosphate glass ceramics and precursor glasses. *J. Appl. Phys.* **2008**, *104*, 113105, doi:10.1063/1.3028268.
164. Liu, G.; Jacquier, B. *Spectroscopic Properties of Rare Earths in Optical Materials*; Springer, New York, USA; **2005**; ISBN 7302074097.
165. Boivin, D.; Föhn, T.; Burov, E.; Pastouret, A.; Gonnet, C.; Cavani, O.; Collet, C.; Lempereur, S. Quenching investigation on new erbium doped fibers using MCVD nanoparticle doping process. *Proceedings Fiber Lasers VII: Technology, Systems, and Applications*. **2010**, 7580, 7580–9, https://doi.org/10.1117/12.841369
166. Bohren, C. F.; Huffman, D. R. *Absorption and scattering of light by small particles.* Wiley Interscience; New York, USA; **1983**. ISBN: 978-0-471-29340-8
167. Chýlek, P.; Zhan, J. Absorption and scattering of light by small particles: the interference structure. *Appl. Opt.* **1990**, *29*, 3984, doi:10.1364/AO.29.003984.
168. Tick, P. A. Are low-loss glass-ceramic optical waveguides possible? *Opt. Lett.* **1998**, *23*, 1904–1905, doi:10.1364/OL.23.001904.
169. Pauling, L. *The Nature of the Chemical Bond and the Structure of Molecules and Crystals: An Introduction to Modern Structural Chemistry.*; Cornell University Press, California, USA; **1960**; ISBN 0801403332.
170. Shannon, R. D. Revised effective ionic radii and systematic studies of interatomic distances in halides and chalcogenides. *Acta Crystallogr. Sect. A* **1976**, *32*, 751–767, doi:10.1107/S0567739476001551.
171. Lide, D. R. *CRC Handbook of Chemistry and Physics, 96th Edition, **2016***; ISBN 9781466571143.
172. Blasse, G.; Grabmaier, B. C. *Luminescent Material*; Wiley Interscience; New York, USA; **1994**; ISBN 13: 978-3-540-58019-5.
173. Patra, A.; Friend, C. S.; Kapoor, R.; Prasad, P. N. Upconversion in Er^{3+}:ZrO_2 Nanocrystals. *J. Phys. Chem. B* **2002**, *106*, 1909–1912, doi:10.1021/jp013576z.

174. Rajput, N. Methods of Preperation of Nanoparticles - A Review. *Int. J. Adv. Eng. Technol.* **2015**, *7*, 1806–1811, doi:10.1016/j.jare.2015.02.007.
175. Niederberger, M. Nonaqueous Sol – Gel Routes to Metal Oxide Nanoparticles. *Acc. Chem. Res.* **2007**, *40*, 793–800, doi:10.1021/ar600035e.
176. Swihart, M. T. Vapor-phase synthesis of nanoparticles. *Curr. Opin. Colloid Interface Sci.* **2003**, *8*, 127–133, doi: 10.1016/S1359-0294(03)00007-4.
177. Hench, L. L.; West, J. O. N. K. The Sol-Gel Process. *Chem. Rev.* **1990**, *90*, 33–72, doi:10.1021/cr00099a003.
178. Galusek, D.; Ghillanyova, K. *Ceramics Science and Technology Volume 2: Materials and Properties - Chapter: Ceramic Oxides*; **2010**; Vol. 2; ISBN 9783527631940.
179. Polman, A. Erbium implanted thin film photonic materials. *J. Appl. Phys.* **1997**, *82*, 1–39, doi:10.1063/1.366265.
180. Van den Hoven, G. N.; Snoeks, E.; Polman, A.; Van Dam, C.; Van Uffelen, J. W. M.; Smit, M. K. Upconversion in Er-implanted Al_2O_3 waveguides. *J. Appl. Phys.* **1996**, *79*, 1258, doi:10.1063/1.361020.
181. Maeda, N.; Wada, N.; Onoda, H.; Maegawa, A.; Kojima, K. Spectroscopic properties of Er^{3+} in sol–gel derived ZrO_2 films. *Thin Solid Films* **2003**, *445*, 382–386, doi:10.1016/S0040-6090(03)01171-4.
182. Macrae, C. F.; Bruno, I. J.; Chisholm, J. A.; Edgington, P. R.; McCabe, P.; Pidcock, E.; Rodriguez-Monge, L.; Taylor, R.; van de Streek, J.; Wood, P. A. Mercury CSD 2.0 – new features for the visualization and investigation of crystal structures. *J. Appl. Crystallogr.* **2008**, *41*, 466–470, doi:10.1107/S0021889807067908.
183. Morinaga, K.; Torikai, T.; Nakagawa, K.; Fujino, S. Fabrication of fine alfa-alumina powders by thermal decomposition of ammonium aluminum carbonate hydroxide (AACH). *Acta Mater.* **2000**, *48*, 4735–4741, doi:10.1016/S1359-6454(00)00265-2.
184. Krell, A.; Blank, P. The Influence of shaping method on the grain size dependence of strength in dense submicrometre alumina. *J. Eur. Ceram. Soc.* **1996**, *16*, 1189–1200, doi:10.1016/0955-2219(96)00044-1.
185. Krell, A.; Blank, P. Grain Size Dependence of Hardness in Dense Submicrometer Alumina. *J. Am. Ceram. Soc.* **1995**, *78*, 1118–1120, doi:10.1111/j.1151-2916.1995.tb08452.x.
186. Sharma, P. K.; Varadan, V. V.; Varadan, V. K. A critical role of pH in the colloidal synthesis and phase transformation of nano size α-Al_2O_3 with high surface area. *J. Eur. Ceram. Soc.* **2003**, *23*, 659–666, doi:10.1016/S0955-2219(02)00191-7.
187. Tanner, P. a.; Wong, K. L.; Liang, Y. Multiple phase production on doping Er^{3+} into α-Al_2O_3. *Chem. Phys. Lett.* **2004**, *399*, 15–19, doi:10.1016/j.cplett.2004.09.133.
188. Maciel, G. S.; Rakov, N.; Fokine, M.; Carvalho, I. C. S.; Pinheiro, C. B. Strong upconversion from $Er_3Al_5O_{12}$ ceramic powders prepared by low temperature direct combustion synthesis. *Appl. Phys. Lett.* **2006**, *89*, doi:10.1063/1.2338558.
189. Singh, V.; Rai, V. K.; Watanabe, S.; Gundu Rao, T. K.; Ledoux-Rak, I.; Kwak, H. Y. Infrared emissions, visible up-conversion, thermoluminescence and defect centres in $Er_3Al_5O_{12}$phosphor obtained by solution combustion reaction. *Appl. Phys. B Lasers Opt.* **2010**, *101*, 631–638, doi:10.1007/s00340-010-4199-z.
190. Al'myasheva, O. V.; Korytkova, E. N.; Maslov, A. V.; Gusarov, V. V.

Preparation of nanocrystalline alumina under hydrothermal conditions. *Inorg. Mater.* **2005**, *41*, 460–467, doi:10.1007/s10789-005-0152-7.
191. Yoldas, B. E. Transparent porous alumina. *Am. Ceram. Soc. Bull.* **1975**, *54*, 286–288.
192. Yoldas, B. Alumina sol preparation from alkoxides. *Am. Ceram. Soc. Bull.* **1975**, *3*, 8–9.
193. Ji, L.; Lin, J.; Tan, K. L.; Zeng, H. C. Synthesis of High-Surface-Area Alumina Using Aluminum Tri-sec-butoxide-2,4-Pentanedione-2-Propanol-Nitric Acid Precursors. *Chem. Mater.* **2000**, *12*, 931–939, doi:10.1021/cm990404u.
194. Wang, X. J.; Lei, M. K. Preparation and photoluminescence of Er^{3+}-doped Al_2O_3 films by sol–gel method. *Thin Solid Films* **2005**, *476*, 41–45, doi:10.1016/j.tsf.2004.08.169.
195. Wang, X. J.; Lei, M. K.; Yang, T.; Wang, H. Phase structure and photoluminescence Al_2O_3 powders prepared by the properties of Er^{3+}-doped sol-gel method. *Opt. Mater.* **2004**, *26*, 247–252, doi:10.1016/j.optmat.2004.01.012.
196. Chryssou, C. E.; Pitt, C. W. Er-Doped AlO_2 Thin Films By Plasma-Enhanced Chemical Vapor Deposition (PECVD) Exhibiting a 55-nm Optical Bandwidth. *IEEE J. Quantum Electron.* **1998**, *34*, 282–285.
197. Linsebigler, A. L.; Linsebigler, A. L.; Yates Jr, J. T.; Lu, G.; Lu, G.; Yates, J. T. Photocatalysis on TiO_2 Surfaces: Principles, Mechanisms, and Selected Results. *Chem. Rev.* **1995**, *95*, 735–758, doi:10.1021/cr00035a013.
198. Yin, Z. F.; Wu, L.; Yang, H. G.; Su, Y. H. Recent progress in biomedical applications of titanium dioxide. *Phys. Chem. Chem. Phys.* **2013**, *15*, 4844–58, doi:10.1039/c3cp43938k.
199. Sunada, K.; Watanabe, T.; Hashimoto, K. Studies on photokilling of bacteria on TiO_2 thin film. *J. Photochem. Photobiol. A Chem.* **2003**, *156*, 227–233, doi: 10.1016/S1010-6030(02)00434-3.
200. Johannsen, S. R.; Roesgaard, S.; Julsgaard, B.; Ferreira, R. A. S.; Chevallier, J.; Balling, P.; Ram, S. K.; Larsen, A. N. Influence of TiO_2 host crystallinity on Er^{3+} light emission. *Opt. Mater. Express* **2016**, *6*, 1664, doi:10.1364/OME.6.001664.
201. Bahtat, A.; Bouazaoui, M.; Bahtat, M. Fluorescence of Er^{3+} ions in TiO_2 planar waveguides prepared by a sol-gel process. *Opt. Commun.* **1994**, *111*, 55–60,doi: 10.1016/0030-4018(94)90138-4.
202. Zhang, W. F.; He, Y. L.; Zhang, M. S.; Yin, Z.; Chen, Q. Raman scattering study on anatase TiO_2 nanocrystals. *J. Phys. D. Appl. Phys.* **2000**, *33*, 912–916, doi:10.1088/0022-3727/33/8/305.
203. Bahtat, A.; Bouazaoui, M.; Bahtat, M.; Garapon, C.; Jacquier, B.; Mugnier, J. Up-conversion fluorescence spectroscopy in Er^{3+}: TiO_2 planar waveguides prepared by a sol-gel process. *J. Non-Cryst Solids* **1996**, *202*, 16–22, doi:http://dx.doi.org/10.1016/0022-3093(96)00172-X.
204. Johannsen, S. R.; Lauridsen, L. R.; Julsgaard, B.; Neuvonen, P. T.; Ram, S. K.; Larsen, A. N. Optimization of Er^{3+}-doped TiO_2 thin films for infrared light up-conversion. *Thin Solid Films* **2014**, *550*, 499–503, doi:10.1016/j.tsf.2013.10.123.
205. Fischer, S.; Goldschmidt, J. C.; Löper, P.; Bauer, G. H.; Brüggemann, R.; Krämer, K.; Biner, D.; Hermle, M.; Glunz, S. W. Enhancement of silicon solar cell efficiency by upconversion: Optical and electrical characterization. *Journal of Applied Physics*; **2010**; Vol. 108.

206. Trupke, T.; Green, M. A.; Würfel, P. Improving solar cell efficiencies by up-conversion of sub-band-gap light. *J. Appl. Phys.* **2002**, *92*, 4117–4122, doi:10.1063/1.1505677.
207. Zhang, Y.; Xing, Z.; Liu, X.; Li, Z.; Wu, X.; Jiang, J.; Li, M.; Zhu, Q.; Zhou, W. Ti^{3+} Self-Doped Blue TiO_2 (B) Single-Crystalline Nanorods for Efficient Solar-Driven Photocatalytic Performance. *ACS Appl. Mater. Interfaces* **2016**, *8*, 26851–26859, doi: 10.1021/acsami.6b09061.
208. Basse, L.; Hansen, J. L.; Jensen, P. B.; Julsgaard, B. Erbium diffusion in titanium dioxide. *AIP Adv.* **2017**, *7*, 045202, doi:10.1063/1.4979923.
209. Mignotte, C. Structural characterization for Er^{3+}-doped oxide materials potentially useful as optical devices. *Appl. Surf. Sci.* **2004**, *226*, 355–370, doi:10.1016/j.apsusc.2003.10.051.
210. Luo, W.; Fu, C.; Li, R.; Liu, Y.; Zhu, H.; Chen, X. Er^{3+}-doped anatase TiO_2 nanocrystals: Crystal-field levels, excited-state dynamics, upconversion, and defect luminescence. *Small* **2011**, *7*, 3046–3056, doi:10.1002/smll.201100838.
211. Zhang, H.; Banfield, J. F. Thermodynamic analysis of phase stability of nanocrystalline titania. *J. Mater. Chem.* **1998**, *8*, 2073–2076, doi:10.1039/a802619j.
212. Jeon, S.; Braun, P. V Hydrothermal Synthesis of Er-Doped Luminescent TiO_2 Nanoparticles. *Chem. Mater.* **2003**, 1256–1263, doi:10.1021/cm0207402.
213. Mignotte, C. EXAFS studies on erbium-doped TiO_2 and ZrO_2 sol-gel thin films. *J. Non. Cryst. Solids* **2001**, *291*, 56–77, doi:10.1016/S0022-3093(01)00805-5.
214. Knop, O.; Brisse, F.; Castelliz, L. Determination of the crystal structure of erbium titanate, $Er_2Ti_2O_7$, by x-ray and neutron diffraction. *Can. J. Chem.* **1965**, *43*, 2812–2826, doi:10.1139/v65-392.
215. Scolan, E.; Sanchez, C. Synthesis and Characterization of Surface-Protected Nanocrystalline Titania Particles. *Chem. Mater.* **1998**, *10*, 3217–3223, doi:10.1021/cm980322q.
216. Chemseddine, A.; Moritz, T. Nanostructuring Titania: Control over Nanocrystal Structure, Size, Shape, and Organization. *Eur. J. Inorg. Chem.* **1999**, *1999*, 235–245, doi:10.1002/(SICI)1099-0682(19990202)1999:2<235::AID-EJIC235>3.0.CO;2-N.
217. Ovenstone, J.; Yanagisawa, K. Effect of Hydrothermal Treatment of Amorphous Titania on the Phase Change from Anatase to Rutile during Calcination. *Chem. Mater.* **1999**, *11*, 2770–2774, doi:10.1021/cm990172z.
218. Yanagisawa, K.; Ovenstone, J. Crystallization of Anatase from Amorphous Titania Using the Hydrothermal Technique: Effects of Starting Material and Temperature. *J. Phys. Chem. B* **1999**, *103*, 7781–7787, doi:10.1021/jp990521c.
219. Cacciotti, I.; Bianco, A.; Pezzotti, G.; Gusmano, G. Synthesis, thermal behaviour and luminescence properties of rare earth-doped titania nanofibers. *Chem. Eng. J.* **2011**, *166*, 751–764, doi:10.1016/j.cej.2010.07.008.
220. Langlet, M. Sol–gel thin film deposition and characterization of a new optically active compound: $Er_2Ti_2O_7$. *Opt. Mater.* **2001**, *16*, 463–473, doi:10.1016/S0925-3467(01)00007-6.
221. Özgür, Ü.; Alivov, Y. I.; Liu, C.; Teke, A.; Reshchikov, M. A.; Doğan, S.; Avrutin, V.; Cho, S.-J.; Morkoç, H. A comprehensive review of ZnO

materials and devices. *J. Appl. Phys.* **2005**, *98*, doi:http://dx.doi.org/10.1063/1.1992666.
222. Nagao, M. Physisorption of water on zinc oxide surface. *J. Phys. Chem.* **1971**, *75*, 3822–3828, doi:10.1021/j100694a007.
223. Grabarek, Z.; Gergely, J. Zero-length crosslinking procedure with the use of active esters. *Anal. Biochem.* **1990**, *185*, 131–135, doi:10.1016/0003-2697(90)90267-D.
224. Horie, M.; Nishio, K.; Fujita, K.; Endoh, S.; Miyauchi, A.; Saito, Y.; Iwahashi, H.; Yamamoto, K.; Murayama, H.; Nakano, H.; Nanashima, N.; Niki, E.; Yoshida, Y. Protein adsorption of ultrafine metal oxide and its influence on cytotoxicity toward cultured cells. *Chem. Res. Toxicol.* **2009**, *22*, 543–553, doi:10.1021/tx800289z.
225. Yuan, Q.; Hein, S.; Misra, R. D. K. New generation of chitosan-encapsulated ZnO quantum dots loaded with drug: Synthesis, characterization and in vitro drug delivery response. *Acta Biomater.* **2010**, *6*, 2732–2739, doi:10.1016/j.actbio.2010.01.025.
226. Low, P. S.; Kularatne, S. A. Folate-targeted therapeutic and imaging agents for cancer. *Curr. Opin. Chem. Biol.* **2009,** *13*, 256–262, doi: 10.1016/j.cbpa.2009.03.022. Epub 2009 May 4.
227. Chakraborty, S.; Dhara, S.; Ravindran, T. R.; Pal, S. S.; Kamruddin, M.; Tyagi, A. K. Resonant exciton-phonon coupling in ZnO nanorods at room temperature. *AIP Adv.* **2011**, *1*, 032135, doi:10.1063/1.3628347.
228. John, R.; Rajakumari, R. Synthesis and Characterization of Rare Earth Ion Doped Nano ZnO. *Nano-Micro Lett.* **2012**, *4*, 65–72, doi:10.3786/nml.v4i2.p65-72.
229. Jayachandraiah, C.; Krishnaiah, G. Erbium induced raman studies and properties of Er-doped ZnO nanoparticles dielectric. *Adv. Mater. Lett.* **2015**, *6*, 743–748, doi:10.5185/amlett.2015.5801.
230. Elleuch, R.; Salhi, R.; Maalej, N.; Deschanvres, J. L.; Maalej, R. Structural and luminescence correlation of annealed Er-ZnO/Si thin films deposited by AACVD process. *Mater. Sci. Eng. B Solid-State Mater. Adv. Technol.* **2013**, *178*, 1124–1129, doi:10.1016/j.mseb.2013.07.005.
231. Ishii, M.; Komukai, Y. Theoretical prediction of local distortion in an ErO_6 cluster: Stabilization of a C4v structure by a rack and pinion effect. *Appl. Phys. Lett.* **2001**, *79*, 934–936, doi:10.1063/1.1392305.
232. Wang, X.; Kong, X.; Shan, G.; Yu, Y.; Sun, Y.; Feng, L.; Chao, K.; Lu, S.; Li, Y. Luminescence spectroscopy and visible upconversion properties of Er^{3+} in ZnO nanocrystals. *J. Phys. Chem. B* **2004**, *108*, 18408–18413, doi:10.1021/jp048021t.
233. Ishii, M.; Komuro, S.; Morikawa, T.; Aoyagi, Y. Local structure analysis of an optically active center in Er-doped ZnO thin film. *J. Appl. Phys.* **2001**, *89*, 3679–3684, doi:10.1063/1.1355284.
234. Choi, S. R.; Bansal, N. P. Mechanical behavior of zirconia/alumina composites. *Ceram. Int.* **2005**, *31*, 39–46, doi:10.1016/j.ceramint.2004.03.032.
235. Ai, D.; Kang, S. Synthesis of 3Y-ZrO2 nano-powders via a W/O emulsion. *Ceram. Int.* **2004**, *30*, 619–623, doi:10.1016/j.ceramint.2003.07.008.
236. Zhang, Y.; Chen, J.; Hu, L.; Liu, W. Pressureless-sintering behavior of nanocrystalline ZrO_2-Y_2O_3-Al_2O_3 system. *Mater. Lett.* **2006**, *60*, 2302–2305, doi:10.1016/j.matlet.2005.12.129.
237. Kelly, J. R.; Denry, I. Stabilized zirconia as a structural ceramic: An

overview. *Dent. Mater.* **2008**, *24*, 289–298, doi: 10.1016/j.dental.2007.05.005.
238. Holgado, J. P.; Pérez-Sánchez, M.; Yubero, F.; Espinós, J. P.; González-Elipe, a. R. Corrosion resistant ZrO_2 thin films prepared at room temperature by ion beam induced chemical vapour deposition. *Surf. Coatings Technol.* **2002**, *151–152*, 449–453, doi:10.1016/S0257-8972(01)01615-2.
239. Hajizadeh-Oghaz, M.; Shoja Razavi, R.; Ghasemi, A. Synthesis and characterization of ceria-yttria co-stabilized zirconia (CYSZ) nanoparticles by sol-gel process for thermal barrier coatings (TBCs) applications. *J. Sol-Gel Sci. Technol.* **2015**, *74*, 603–612, doi:10.1007/s10971-015-3639-y.
240. Lee, J. S.; Matsubara, T.; Sei, T.; Tsuchiya, T. Preparation and properties of Y_2O_3-doped ZrO_2 thin films by the sol–gel process. *J. Mater. Sci.* **1997**, *32*, 5249–5256, doi: 10.1023/A:1018650424335.
241. Hannink, R. H. J.; Kelly, P. M.; Muddle, B. C. Transformation Toughening in Zirconia-Containing Ceramics. *J. Am. Ceram. Soc.* **2004**, *83*, 461–487, doi:10.1111/j.1151-2916.2000.tb01221.x.
242. Vagkopoulou, T.; Koutayas, S. O.; Koidis, P.; Strub, J. R. Zirconia in dentistry: Part 1. Discovering the nature of an upcoming bioceramic. *Eur. J. Esthet. Dent.* **2009**, *4*, 130–151.
243. Garvie, R. C. The Occurrence of Metastable Tetragonal Zirconia as a Crystallite Size Effect. *J. Phys. Chem.* **1965**, *69*, 1238–1243, doi:10.1021/j100888a024.
244. MASCHIO, S.; BRUCKNER, S.; PEZZOTTI, G. Synthesis and Sintering of Zirconia-Erbia Tetragonal Solid Solutions. *J. Ceram. Soc. Japan* **1999**, *107*, 1111–1114, doi:10.2109/jcersj.107.1111.
245. Lee, J.-S.; Park, J.-I.; Choi, T.-W. Synthesis and characterization of CaO-stabilized ZrO_2 fine powders for oxygen ionic conductors. *J. Mater. Sci.* **1996**, *31*, 2833–2838, doi:10.1007/BF00355990.
246. Eliseeva, S. V.; Bünzli, J.-C. G. Lanthanide luminescence for functional materials and bio-sciences. *Chem. Soc. Rev.* **2010**, *39*, 189–227, doi:10.1039/B905604C.
247. Freris, I.; Riello, P.; Enrichi, F.; Cristofori, D.; Benedetti, A. Synthesis and optical properties of sub-micron sized rare earth-doped zirconia particles. *Opt. Mater.* **2011**, *33*, 1745–1752, doi:10.1016/j.optmat.2011.06.010.
248. Sh Atabaev, T.; Kurisu, M.; Konishi, K.; Hoa Hong, N. Concentration-dependent optical properties of erbium doped zirconia nanocrystals. *Am. J. Nanosci. Nanotechnol.* **2014**, *2*, 13–16, doi:10.11648/j.nano.20140201.13.
249. Yang, Z.; Luo, J.; Yang, S.; Wu, Q. Fabrication of ZrO_2:Er^{3+} Nanocrystals and the Researching of Emitting Mechanism. *Energy Procedia* **2012**, *17*, 305–310, doi:10.1016/j.egypro.2012.02.099.
250. Maiman, T. H. Stimulated Optical Radiation in Ruby. *Nature* **1960**, *187*, 493–494, doi:10.1038/187493a0.
251. Koester, C. J.; Snitzer, E. Amplification in a Fiber Laser. *Appl. Opt.* **1964**, *3*, 1182, doi:10.1364/AO.3.001182.
252. Kao, K. C.; Hockham, G. A. Dielectric-fibre surface waveguides for optical frequencies. *Proc. Inst. Electr. Eng.* **1966**, *113*, 1151–1158, doi:10.1049/piee.1966.0189.
253. Desurvire, E.; Simpson, J. R.; Becker, P. C. High-gain erbium-doped traveling-wave fiber amplifier. *Opt. Lett.* **1987**, *12*, 888, doi:10.1364/OL.12.000888.
254. Mears, R. J.; Reekie, L.; Jauncey, I. M.; Payne, D. N. Low-noise erbium-

doped fibre amplifier operating at 1.54μm. *Electron. Lett.* **1987**, *23*, 1026, doi:10.1049/el:19870719.
255. Payne, D. N.; Laming, R. I. Optical amplifiers-a telecommunications revolution. *International Electron Devices Meeting.* **1991**; pp. 3–4, doi: 10.1109/IEDM.1991.235436
256. Thyagarajan, K.; Ghatak, A. *Fiber Optic Essentials*; Elsevier, New York, USA, **2007**; ISBN 9780470152560.
257. Karmakar, B.; Kundu, P.; Chaudhuri, A. K.; Annapurna, K.; Kumar, A.; Dwivedi, R. N. Effect of hydroxyl content on the physical properties of calcium metaphosphate glasses. *Bull. Mater. Sci.* **1999**, *22*, 115–119, doi:10.1007/BF02745563.
258. Kasap, S. O. *Optoelectronics and Photonics: Principles and Practices*. Prentice Hall, 1st Ed. **2001**. ISBN-13: 978-0201610871.
259. Buck, J. A. *Fundamentals of Optical Fibers*; Wiley, Ed.; Second edi.; **2004**. ISBN: 978-0-471-22191-3.
260. Miya, T.; Terunuma, Y.; Hosaka, T.; Miyashita, T. Ultimate low-loss single-mode fibre at 1.55 microns. *Electron. Lett.* **1979**, *15*, 106–108, doi:10.1049/el:19790077.
261. Becker; Olsson; Simpson *Erbium doped fiber Amplifiers*; Elsevier, New York, USA, **2003**; ISBN 978-0-12-084590-3.
262. Lee, E. T. Y.; Taylor, E. R. M. Two-die assembly for the extrusion of glasses with dissimilar thermal properties for fibre optic preforms. *J. Mater. Process. Technol.* **2007**, *184*, 325–329, doi:10.1016/j.jmatprotec.2006.11.115.
263. Nagel, S.; MacChesney, J.; Walker, K. An overview of the modified chemical vapor deposition (MCVD) process and performance. *IEEE J. Quantum Electron.* **1982**, *18*, 459–476, doi:10.1109/JQE.1982.1071596.
264. Blankenship, M.; Deneka, C. The outside vapor deposition method of fabricating optical waveguide fibers. *IEEE J. Quantum Electron.* **1982**, *18*, 1418–1423, doi:10.1109/JQE.1982.1071426.
265. Cognolato, L. Chemical Vapour Deposition for Optical Fibre Technology. *Le J. Phys. IV* **1995**, *05*, C5-975-C5-987, doi:10.1051/jphyscol:19955115.
266. Dhar, A.; Pal, A.; Paula, M. C.; Ray, P.; Maiti, H. S.; Sen, R. The mechanism of rare earth incorporation in solution doping process. *Opt. Express* **2008**, *16*, 12835–12846, doi:10.1364/OE.16.012835.
267. Keiser, G.; Xiong, F.; Cui, Y.; Shum, P. P. Review of diverse optical fibers used in biomedical research and clinical practice. *J. Biomed. Opt.* **2014**, *19*, 080902, doi:10.1117/1.JBO.19.8.080902.
268. Friebele, E. J.; Baker, C.; Askins, C. G.; Fontana, J. P.; Hunt, M. P.; Peele, J. R.; Marcheschi, B. A.; Oh, E.; Kim, W.; Sanghera, J.; Zhang, J.; Pattnaik, R. K.; Merkle, L. D.; Dubinskii, M. Erbium nanoparticle doped fibers for efficient, resonantly-pumped Er-doped fiber lasers. *Proceedings Fiber Lasers XII: Technology, Systems, and Applications*, **2015**; Vol. 9344, pp. 934412–934418, doi: 10.1117/12.2079443.
269. Cheong, W. F.; Prahl, S. A.; Welch, A. J. A review of the optical properties of biological tissues. *IEEE J. Quantum Electron.* **1990**, *26*, 2166–2185, doi:10.1109/3.64354.
270. Jacques, S. L. Optical properties of biological tissues: a review. *Phys. Med. Biol.* **2013**, *58*, 37–61, doi:10.1088/0031-9155/58/11/R37.
271. Dorosz, D. Rare earth ions doped aluminosilicate and phosphate double clad optical fibres. *Bull. polish Acad. Sci. Tech. Sci.* **2008**, *56*, 103–111.
272. Desurvire, E. *Erbium-doped fiber amplifiers : principles and applications*;

Wiley, **1994**; ISBN 9780471589778.
273. Kasik, I.; Podrazky, O.; Mrazek, J.; Cajzl, J.; Aubrecht, J.; Probostova, J.; Peterka, P.; Honzatko, P.; Dhar, A. Erbium and Al_2O_3 nanocrystals-doped silica optical fibers. *Bull. Polish Acad. Sci. Tech. Sci.* **2014**, *62*, 641–646, doi:10.2478/bpasts-2014-0070.
274. Blanc, W.; Guillermier, C.; Dussardier, B. Composition of nanoparticles in optical fibers by Secondary Ion Mass Spectrometry. *Opt. Mater. Express* **2012**, *2*, 1504, doi:10.1364/OME.2.001504.
275. Hari Babu, B.; Ollier, N.; Savelli, I.; El Hamzaoui, H.; Pastouret, A.; Poumellec, B.; Bouazaoui, M.; Bigot, L.; Lancry, M. Study of Radiation Effects on Er^{3+}-Doped Nanoparticles Germano-Silica Fibers. *J. Light. Technol.* **2016**, *34*, 4981–4987, doi:10.1109/JLT.2016.2599173.
276. Savelii, I.; Bigot, L.; Capoen, B.; Gonnet, C.; Chanéac, C.; Burova, E.; Pastouret, A.; El-Hamzaoui, H.; Bouazaoui, M. Benefit of Rare-Earth "Smart Doping" and Material Nanostructuring for the Next Generation of Er-Doped Fibers. *Nanoscale Res. Lett.* **2017**, *12*, doi:10.1186/s11671-017-1947-6.
277. Blanc, W.; Dussardier, B.; Monnom, G.; Peretti, R.; Jurdyc, A.-M.; Jacquier, B.; Foret, M.; Roberts, A. Erbium emission properties in nanostructured fibers. *Appl. Opt.* **2009**, *48*, G119–G124, doi:10.1364/AO.48.00G119.
278. Blanc, W.; Dussardier, B.; Paul, M. C. Er doped oxide nanoparticles in silica based optical fibres. In *Glass Technology: European Journal of Glass Science and Technology Part A*; **2009**; Vol. 50, pp. 79–81. doi: 10.1504/IJNT.2012.045350.
279. Podrazky, O.; Kasik, I.; Pospisilova, M.; Matejec, V. Use of nanoparticles for preparation of rare-earth doped silica fibers. In *Physica Status Solidi C - Current Topics in Solid State Physics, Vol 6, No 10*; **2009**; Vol. 6, pp. 2228–2230 ISBN 1610-1634.
280. Augustyn, E.; Żelechower, M.; Stróż, D.; Chrapoński, J. The microstructure of erbium–ytterbium co-doped oxyfluoride glass–ceramic optical fibers. *Opt. Mater.* **2012**, *34*, 944–950, doi:10.1016/J.OPTMAT.2011.04.037.
281. Sauze, A. Le; Simonneau, C.; Pastouret, A.; Gicquel, D.; Bigot, L.; Choblet, S.; Jurdyc, A. M.; Jacquier, B. Nanoparticle Doping Process : towards a better control of erbium incorporation in MCVD fibers for optical amplifiers. *Opt. Soc. Am.* **2003**, 5–7, ISBN: 1-55752-752-0.
282. Baker, C. C.; Friebele, E. J.; Burdett, A. A.; Rhonehouse, D. L.; Fontana, J.; Kim, W.; Bowman, S. R.; Shaw, L. B.; Sanghera, J.; Zhang, J.; Pattnaik, R.; Dubinskii, M.; Ballato, J.; Kucera, C.; Vargas, A.; Hemming, A.; Simakov, N.; Haub, J. Nanoparticle doping for high power fiber lasers at eye-safer wavelengths. *Opt. Express* **2017**, *25*, 13903–13915, doi:10.1364/OE.25.013903.
283. Haque, P.; Parsons, A. J.; Barker, I. A.; Ahmed, I.; Irvine, D. J.; Walker, G. S.; Rudd, C. D. Interfacial properties of phosphate glass fibres/PLA composites: Effect of the end functionalities of oligomeric PLA coupling agents. *Compos. Sci. Technol.* **2010**, *70*, 1854–1860, doi:10.1016/J.COMPSCITECH.2010.06.012.
284. Abou Neel, E. A.; Ahmed, I.; Pratten, J.; Nazhat, S. N.; Knowles, J. C. Characterisation of antibacterial copper releasing degradable phosphate glass fibres. *Biomaterials* **2005**, *26*, 2247–2254, doi:10.1016/J.BIOMATERIALS.2004.07.024.
285. Qiu, T.; Li, L.; Schülzgen, A.; Temyanko, V. L.; Luo, T.; Jiang, S.; Mafi, A.;

Moloney, J. V.; Peyghambarian, N. Generation of 9.3-W multimode and 4-W single-mode output from 7-cm short fiber lasers. *IEEE Photonics Technol. Lett.* **2004**, *16*, 2592–2594, doi:10.1109/LPT.2004.836352.
286. Tammela, S.; Hotoleanu, M.; Janka, K.; Kiiveri, P.; Rajala, M.; Salomaa, a.; Valkonen, H.; Stenius, P. Potential of nanoparticle technologies for next generation erbium-doped fibers. *Opt. Fiber Commun. Conf. 2004. OFC 2004* **2004**, *2*, 4–6, doi: 10.1117/12.660405.
287. Bitar, M.; Salih, V.; Mudera, V.; Knowles, J. C.; Lewis, M. P. Soluble phosphate glasses: in vitro studies using human cells of hard and soft tissue origin. *Biomaterials* **2004**, *25*, 2283–92, doi: 10.1016/j.biomaterials.2003.08.054.
288. Zhang, H.; Ye, X. J.; Li, J. S. Preparation and biocompatibility evaluation of apatite/wollastonite-derived porous bioactive glass ceramic scaffolds. *Biomed. Mater.* **2009**, *4*, doi:10.1088/1748-6041/4/4/045007.
289. Vitale-Brovarone, C.; Di Nunzio, S.; Bretcanu, O.; Verné, E. Macroporous glass-ceramic materials with bioactive properties. *J. Mater. Sci. Mater. Med.* **2004**, *15*, 209–217, doi:10.1023/B:JMSM.0000015480.49061.e1.
290. Fu, Q.; Rahaman, M. N.; Bal, B. S.; Huang, W.; Day, D. E. Preparation and bioactive characteristics of a porous 13-93 glass, and fabrication into the articulating surface of a proximal tibia. *J. Biomed. Mater. Res. - Part A* **2007**, *82*, 222–229, doi:10.1002/jbm.a.31156.
291. Novajra, G.; Boetti, N. G.; Lousteau, J.; Fiorilli, S.; Milanese, D.; Vitale-Brovarone, C. Phosphate glass fibre scaffolds: Tailoring of the properties and enhancement of the bioactivity through mesoporous glass particles. *Mater. Sci. Eng. C* **2016**, *67*, 570–580, doi:10.1016/j.msec.2016.05.048.
292. Valappil, S. P.; Pickup, D. M.; Carroll, D. L.; Hope, C. K.; Pratten, J.; Newport, R. J.; Smith, M. E.; Wilson, M.; Knowles, J. C. Effect of silver content on the structure and antibacterial activity of silver-doped phosphate-based glasses. *Antimicrob. Agents Chemother.* **2007**, *51*, 4453–4461, doi:10.1128/AAC.00605-07.
293. Mishra, A.; Petit, L.; Pihl, M.; Andersson, M.; Salminen, T.; Rocherullé, J.; Massera, J. Thermal, structural and in vitro dissolution of antimicrobial copper-doped and slow resorbable iron-doped phosphate glasses. *J. Mater. Sci.* **2017**, *52*, 8957–8972, doi:10.1007/s10853-017-0805-3.
294. Valappil, S. P.; Ready, D.; Neel, E. A. A.; Pickup, D. M.; Chrzanowski, W.; O'Dell, L. A.; Newport, R. J.; Smith, M. E.; Wilson, M.; Knowles, J. C. Antimicrobial Gallium-Doped Phosphate-Based Glasses. *Adv. Funct. Mater.* **2008**, *18*, 732–741, doi:10.1002/adfm.200700931.
295. Brancaleon, L.; Moseley, H. Laser and non-laser light sources for photodynamic therapy. *Lasers Med. Sci.* **2002**, *17*, 173–186, doi:10.1007/s101030200027.
296. Garcez, A. S.; Fregnani, E. R.; Rodriguez, H. M.; Nunez, S. C.; Sabino, C. P.; Suzuki, H.; Ribeiro, M. S. The use of optical fiber in endodontic photodynamic therapy. Is it really relevant? *Lasers Med. Sci.* **2013**, *28*, 79–85, doi:10.1007/s10103-012-1073-8.
297. Wang, Z.; Chocat, N. Fiber-Optic Technologies in Laser-Based Therapeutics: Threads for a Cure. *Curr. Pharm. Biotechnol.* **2010**, *11*, 384–397, doi:10.2174/138920110791233271.
298. Bendsoe, N.; Bendsoe, N.; Axelsson, J.; Andersson-Engels, S.; Svanberg, S. Photodynamic therapy: superficial and interstitial illumination. *J. Biomed. Opt.* **2010**, *15*, 041502, doi:10.1117/1.3466579.

299. Jih, M. H.; Kimyai-Asadi, A. Fractional Photothermolysis: A Review and Update. *Semin. Cutan. Med. Surg.* **2008**, *27*, 63–71, doi:10.1016/j.sder.2008.01.002.
300. Boulnois, J.-L. Photophysical processes in recent medical laser developments: A review. *Lasers Med. Sci.* **1986**, *1*, 47–66, doi:10.1007/BF02030737.
301. Kim, T. Il; McCall, J. G.; Jung, Y. H.; Huang, X.; Siuda, E. R.; Li, Y.; Song, J.; Song, Y. M.; Pao, H. A.; Kim, R. H.; Lu, C.; Lee, S. D.; Song, I. S.; Shin, G.; Al-Hasani, R.; Kim, S.; Tan, M. P.; Huang, Y.; Omenetto, F. G.; Rogers, J. A.; Bruchas, M. R. Injectable, cellular-scale optoelectronics with applications for wireless optogenetics. *Science.* **2013**, *340*, 211–216, doi:10.1126/science.1232437.
302. Durduran, T.; Choe, R.; Baker, W. B.; Yodh, A. G. Diffuse optics for tissue monitoring and tomography. *Reports Prog. Phys.* **2010**, *73*, 076701, doi:10.1088/0034-4885/73/7/076701.
303. Pugliese, D.; Konstantaki, M.; Konidakis, I.; Ceci-Ginistrelli, E.; Boetti, N. G.; Milanese, D.; Pissadakis, S. Bioresorbable optical fiber Bragg gratings. *Opt. Lett.* **2018**, *43*, 671–674, doi:10.1364/OL.43.000671.
304. Yliniemi, S.; Albert, J.; Wang, Q.; Honkanen, S. UV-exposed Bragg gratings for laser applications in silver-sodium ion-exchanged phosphate glass waveguides. *Opt. Express* **2006**, *14*, 2898–2903, doi:10.1364/OE.14.002898.
305. Grobnic, D.; Mihailov, S. J.; Walker, R. B.; Smelser, C. W.; Lafond, C.; Croteau, A. Bragg gratings made with a femtosecond laser in heavily doped Er-Yb phosphate glass fiber. *IEEE Photonics Technol. Lett.* **2007**, *19*, 943–945, doi:10.1109/LPT.2007.898816.
306. Dennison, C. R.; Wild, P. M.; Wilson, D. R.; Gilbart, M. K. An in-fiber Bragg grating sensor for contact force and stress measurements in articular joints. *Meas. Sci. Technol.* **2010**, *21*, 115803, doi:10.1088/0957-0233/21/11/115803.
307. Arkwright, J. W.; Blenman, N. G.; Underhill, I. D.; Maunder, S. A.; Szczesniak, M. M.; Dinning, P. G.; Cook, I. J. In-vivo demonstration of a high resolution optical fiber manometry catheter for diagnosis of gastrointestinal motility disorders. *Opt. Express* **2009**, *17*, 4500, doi:10.1364/OE.17.004500.
308. Hao, J.; Jayachandran, M.; Ni, N.; Phua, J.; Liew, H.-M.; Aung, P. W. A.; Biswas, J.; Foo, S.-F.; Low, J.; Yap, L. K. P. An intelligent elderly healthcare monitoring system using fiber-based sensors. *J. Chinese Inst. Eng.* **2010**, *33*, 653–660, doi:10.1080/02533839.2010.9671654.
309. Hao, J.; Jayachandran, M.; Kng, P. L.; Foo, S. F.; Aung Aung, P. W.; Cai, Z. FBG-based smart bed system for healthcare applications. *Front. Optoelectron. China* **2010**, *3*, 78–83, doi:10.1007/s12200-009-0066-0.
310. Bertucci, A.; Manicardi, A.; Candiani, A.; Giannetti, S.; Cucinotta, A.; Spoto, G.; Konstantaki, M.; Pissadakis, S.; Selleri, S.; Corradini, R. Detection of unamplified genomic DNA by a PNA-based microstructured optical fiber (MOF) Bragg-grating optofluidic system. *Biosens. Bioelectron.* **2015**, *63*, 248–254, doi:10.1016/j.bios.2014.07.047.
311. Carvalho, L.; Alberto, N. J.; Gomes, P. S.; Nogueira, R. N.; Pinto, J. L.; Fernandes, M. H. In the trail of a new bio-sensor for measuring strain in bone: Osteoblastic biocompatibility. *Biosens. Bioelectron.* **2011**, *26*, 4046–4052, doi:10.1016/j.bios.2011.03.028.

312. Hey Tow, K.; Chow, D. M.; Vollrath, F.; Dicaire, I.; Gheysens, T.; Thévenaz, L. Towards a new generation of fibre optic chemical sensors based on spider silk threads. In; Chung, Y., Jin, W., Lee, B., Canning, J., Nakamura, K., Yuan, L., Eds.; International Society for Optics and Photonics, **2017**; Vol. 10323, p. 103231E.
313. Shan, D.; Zhang, C.; Kalaba, S.; Mehta, N.; Kim, G. B.; Liu, Z.; Yang, J. Flexible biodegradable citrate-based polymeric step-index optical fiber. *Biomaterials* **2017**, *143*, 142–148, doi:10.1016/j.biomaterials.2017.08.003.
314. Choi, M.; Humar, M.; Kim, S.; Yun, S.-H. Step-Index Optical Fiber Made of Biocompatible Hydrogels. *Adv. Mater.* **2015**, *27*, 4081–4086, doi:10.1002/adma.201501603.
315. Massera, J.; Ahmed, I.; Petit, L.; Aallos, V.; Hupa, L. Phosphate-based glass fiber vs. bulk glass: Change in fiber optical response to probe in vitro glass reactivity. *Mater. Sci. Eng. C* **2014**, *37*, 251–257, doi:10.1016/j.msec.2014.01.021.
316. Bae, B.-S.; Weinberg, M. C. Oxidation-reduction equilibrium in copper phosphate glass melted in air. *J. Am. Ceram. Soc.* **1991**, *74*, 3039–3045, doi:10.1111/j.1151-2916.1991.tb04299.x.
317. Parsons, A. J.; Burling, L. D.; Rudd, C. D.; Scotchford, C. A.; Walker, G. S. The effect of production regime and crucible materials on the thermal properties of sodium phosphate glasses produced from salts. *J. Biomed. Mater. Res. - Part B Appl. Biomater.* **2004**, *71*, 22–29, doi:10.1002/jbm.b.30061.
318. Massera, J.; Gaussiran, M.; Głuchowski, P.; Lastusaari, M.; Rodrigues, L. C. V; Hölsä, J.; Hupa, L. Effect of the glass melting condition on the processing of phosphate-based glass- ceramics with persistent luminescence properties. *Opt. Mater.* **2016**, *52*, 56–61, doi: 10.1016/j.optmat.2015.12.006.
319. Varshneya, A. K. *Fundamentals of inorganic glasses*; Elsevier, New York, USA, **2013**, ISBN 9780080571508.
320. Ehrmann, P. R.; Carlson, K.; Campbell, J. H.; Click, C. A.; Brow, R. K. Neodymium fluorescence quenching by hydroxyl groups in phosphate laser glasses. In *Journal of Non-Crystalline Solids*; **2004**; Vol. 349, pp. 105–114.
321. McCumber, D. E. Theory of phonon-terminated optical masers. *Phys. Rev.* **1964**, *134*, doi:10.1103/PhysRev.134.A299.
322. W. J. Miniscalco, R. S. Q. General procedure for the analysis of Er^{3+} cross sections. *Opt. Lett.* **1991**, *16*, 258–260, doi: 10.1364/OL.16.000258.
323. Martin, R. M.; Quimby, R. S. Experimental evidence of the validity of the McCumber theory relating emission and absorption for rare-earth glasses. *J. Opt. Soc. Am. B* **2006**, *23*, 1770, doi:10.1364/JOSAB.23.001770.
324. Digonnet, M. J. F.; Murphy-chutorian, E.; Falquier, D. G. Fundamental Limitations of the McCumber Relation Applied to Er-Doped Silica and Other Amorphous-Host Lasers. *J. quantum Electron.* **2002**, *38*, 1629–1637.
325. Kaminow, I. P.; Stulz, L. W. Loss in cleaved Ti-diffused $LiNbO_3$ waveguides. *Appl. Phys. Lett.* **1978**, *33*, 62–64, doi:10.1063/1.90191.
326. Kokubo, T.; Kushitani, H.; Sakka, S.; Kitsugi, T.; Yamamuro, T. Solutions able to reproducein vivo surface-structure changes in bioactive glass-ceramic A-W3. *J. Biomed. Mater. Res.* **1990**, *24*, 721–734, doi:10.1002/jbm.820240607.
327. Schwarz, J.; Tichá, H.; Tichý, L.; Mertens, R. Physical properties of PbO-ZnO-P_2O_5 glasses I. Infrared and Raman spectra. *J. Optoelectron. Adv. Mater.* **2004**, *6*, 737–746.

328. Sandhu, S.; Singh, D.; Kumar, S.; Thangaraj, R. Estimation of glass transition temperature of $Al_x(Ge_2Sb_2Te_5)_{1-x}$ glassy system. *J. Ovonic Res.* **2013**, *9*, 143–146.
329. Konidakis, I.; Varsamis, C. P. E.; Kamitsos, E. I.; Möncke, D.; Ehrt, D. Structure and properties of mixed strontium-manganese metaphosphate glasses. *J. Phys. Chem. C* **2010**, *114*, 9125–9138, doi:10.1021/jp101750t.
330. Shih, P. Y.; Shiu, H. M. Properties and structural investigations of UV-transmitting vitreous strontium zinc metaphosphate. *Mater. Chem. Phys.* **2007**, *106*, 222–226, doi:10.1016/j.matchemphys.2007.05.038.
331. Gao, H.; Tan, T.; Wang, D. Effect of composition on the release kinetics of phosphate controlled release glasses in aqueous medium. *J. Control. Release* **2004**, *96*, 21–28, doi:10.1016/j.jconrel.2003.12.030.
332. Moustafa, Y. M.; El-Egili, K. Infrared spectra of sodium phosphate glasses. *J. Non. Cryst. Solids* **1998**, *240*, 144–153, doi:10.1016/S0022-3093(98)00711-X.
333. Wilder, J. A.; Shelby, J. E. Property variation in alkali alkaline-earth metaphosphate glasses. *J. Am. Ceram. Soc.* **1984**, *67*, 438–444, doi:10.1111/j.1151-2916.1984.tb19732.x.
334. Abou Neel, E. A.; Chrzanowski, W.; Pickup, D. M.; O'Dell, L. A.; Mordan, N. J.; Newport, R. J.; Smith, M. E.; Knowles, J. C. Structure and properties of strontium-doped phosphate-based glasses. *J. R. Soc. Interface* **2009**, *6*, 435–446, doi:10.1098/rsif.2008.0348.
335. Bruni, S.; Cariati, F.; Narducci, D. Infrared specular reflection spectra of copper-zinc phosphate glasses. *Vib. Spectrosc.* **1994**, *7*, 169–173, doi:10.1016/0924-2031(94)85027-5.
336. Ilieva, D.; Jivov, B.; Bogachev, G.; Petkov, C.; Penkov, I.; Dimitriev, Y. Infrared and Raman spectra of Ga_2O_3-P_2O_5 glasses. *J. Non Cryst. Solids* **2001**, *283*, 195–202, doi:10.1016/S0022-3093(01)00361-1.
337. Meyer, K. Characterization of the structure of binary zinc ultraphosphate glasses by infrared and Raman spectroscopy. *J. Non. Cryst. Solids* **1997**, *209*, 227–239, doi:10.1016/S0022-3093(96)00563-7.
338. Velli, L. L.; Varsamis, C. P. E.; Kamitsos, E. I.; Möncke, D.; Ehrt, D. Structural investigation of metaphosphate glasses. *Phys. Chem. Glas.* **2005**, *46*, 178–181, doi: 10.1515/zna-2001-1114.
339. Walter, G.; Vogel, J.; Hoppe, U.; Hartmann, P. The structure of CaO–Na_2O–MgO–P_2O_5 invert glass. *J. Non. Cryst. Solids* **2001**, *296*, 212–223, doi:10.1016/S0022-3093(01)00912-7.
340. Lee, S.; Obata, A.; Kasuga, T. Ion release from SrO-CaO-TiO_2-P_2O_5 glasses in Tris buffer solution. *J. Ceram. Soc. Jpn* **2009**, *117*, 935 – 938, doi: 10.2109/jcersj2.117.935.
341. Karakassides, M. A.; Saranti, A.; Koutselas, I. Preparation and structural study of binary phosphate glasses with high calcium and/or magnesium content. *J. Non. Cryst. Solids* **2004**, *347*, 69–79, doi:10.1016/j.jnoncrysol.2004.08.111.
342. Kalampounias, A. G. Short-time vibrational dynamics of metaphosphate glasses. *J. Phys. Chem. Solids* **2012**, *73*, 148–153, doi:10.1016/j.jpcs.2011.11.014.
343. Segawa, H.; Akagi, N.; Yano, T.; Shibata, S. Properties and structures of TiO_2–ZnO–P_2O_5 glasses. *J. Ceram. Soc. Jpn.* **2010**, *118*, 278–282, doi: 10.2109/jcersj2.118.278.
344. Saddeek, Y. B.; Kaid, M. A.; Ebeid, M. R. FTIR and physical features of

Al_2O_3–La_2O_3–P_2O_5–PbO glasses. *J. Non. Cryst. Solids* **2014**, *387*, 30–35, doi:10.1016/j.jnoncrysol.2013.12.029.
345. Yan, Y.; Faber, A. J.; de Waal, H. Luminescence quenching by OH groups in highly Er-doped phosphate glasses. *J. Non Cryst. Solids* **1995**, *181*, 283–290, doi:10.1016/S0022-3093(94)00528-1.
346. Abualnaja, K. M.; Šiller, L.; Horrocks, B. R. Photoluminescence study of erbium-mixed alkylated silicon nanocrystals. **2015**, *9*, 234–244, doi: 10.1999/1307-6892/10000323.
347. Sontakke, A. D.; Biswas, K.; Tarafder, A.; Sen, R.; Annapurna, K. Broadband Er^{3+} emission in highly nonlinear bismuth modified zinc-borate glasses. *Opt. Mater. Express* **2011**, *1*, 344, doi:10.1364/OME.1.000344.
348. Zikmund, M.; Štepničková, L. Spectral study of chloro(tetrahydrofuran) titanium (III) complexes. *Chem. Pap.* **1969**, *23*, 850–855.
349. Cui S., Massera J., Lastusaari M., Hupa L., P. L. Novel oxyfluorophosphate glasses and glass-ceramics. *J. Non. Cryst. Solids* **2016**, *445*, 40–44, doi: 10.1016/j.jnoncrysol.2016.05.005.
350. Ebendorff-Heidepriem, H.; Seeber, W.; Ehrt, D. Spectroscopic properties of Nd^{3+} ions in phosphate-glasses. *J. Non Cryst. Solids* **1995**, *183*, 191–200, doi: 10.1016/0022-3093(94)00560-5.
351. Isshiki, H.; Polman, A.; Kimura, T. Fine structure in the Er-related emission spectrum from Er-Si-O matrices at room temperature under carrier mediated excitation. *Journal of Luminescence*; **2003**; Vol. 102–103, pp. 819–824, doi:10.1016/S0022-2313(02)00648-8.
352. Quimby, R. S.; Miniscalco, W. J.; Thompson, B. Clustering in erbium-doped silica glass fibers analyzed using 980 nm excited-state absorption. *J. Appl. Phys.* **1994**, *76*, 4472–4478, doi:10.1063/1.357278.
353. Reszczyńska, J.; Grzyb, T.; Sobczak, J. W.; Lisowski, W.; Gazda, M.; Ohtani, B.; Zaleska, A. Visible light activity of rare earth metal doped (Er^{3+}, Yb^{3+} or Er^{3+}/Yb^{3+}) titania photocatalysts. *Appl. Catal. B Environ.* **2015**, *163*, 40–49, doi:10.1016/j.apcatb.2014.07.010.
354. Bahtat, A.; Bouderbala, M.; Bahtat, M.; Bouazaoui, M.; Mugnier, J.; Druetta, M. Structural characterisation of Er^{3+} doped sol–gel TiO_2 planar optical waveguides. *Thin Solid Films* **1998**, *323*, 59–62, doi:10.1016/S0040-6090(97)01027-4.
355. Chen, X.-C.; Zhou, J.-P.; Wang, H.-Y.; Xu, P.-S.; Pan, G.-Q. *In situ* high temperature X-ray diffraction studies of ZnO thin film. *Chinese Phys. B* **2011**, *20*, 096102, doi:10.1088/1674-1056/20/9/096102.
356. Hubbard, C. R.; Snyder, R. L. RIR-measurement and use in quantitative XRD. *Powder Diffr.* **1988**, *3*, 74–77, doi:10.1017/S0885715600013257.
357. Li, J. G.; Wang, X. H.; Kamiyama, H.; Ishigaki, T.; Sekiguchi, T. RF plasma processing of Er-doped TiO2 luminescent nanoparticles. *Thin Solid Films* **2006**, *506–507*, 292–296, doi:10.1016/j.tsf.2005.08.093.
358. Zhao, J.-G.; Zhang, W.-Y.; Ma, Z.-W.; Xie, E.-Q.; Zhao, A.-K.; Liu, Z.-J. Structure and photoluminescence properties of Er^{3+}-doped TiO_2-SiO_2 powders prepared by sol—gel method. *Chinese Phys. B* **2011**, *20*, 087701, doi:10.1088/1674-1056/20/8/087701.
359. Ting, C. C.; Chen, S. Y.; Hsieh, W. F.; Lee, H. Y. Effects of yttrium codoping on photoluminescence of erbium-doped TiO_2 films. *J. Appl. Phys.* **2001**, *90*, 5564–5569, doi:10.1063/1.1413490.
360. Patra, A.; Friend, C. S.; Kapoor, R.; Prasad, P. N. Fluorescence upconversion properties of Er^{3+}-doped TiO_2 and $BaTiO_3$ nanocrystallites. *Chem. Mater.*

2003, *15*, 3650–3655, doi:10.1021/cm020897u.
361. Golding, P.; Jackson, S.; King, T.; Pollnau, M. Energy transfer processes in Er^{3+}-doped and Er^{3+},Pr^{3+}-codoped ZBLAN glasses. *Phys. Rev. B* **2000**, *62*, 856–864, doi:10.1103/PhysRevB.62.856.
362. Boivin, D. E.; Pastouret, A.; Burov, E.; Gonnet, C.; Cavani, O.; Lempereur, S.; Sillard, P.; Goldmann, C.; Saudry, E.; Chanéac, C.; Shlifer, A.; Ghera, U. Core-shell nanoparticle erbium-doped fibers for next generation amplifiers. *International Society for Optics and Photonics*, 2012; Vol. 8237, p. 82372, doi: 10.1117/12.907909.
363. Stöber, W.; Fink, A.; Bohn, E. Controlled growth of monodisperse silica spheres in the micron size range. *J. Colloid Interface Sci.* **1968**, *26*, 62–69, doi:10.1016/0021-9797(68)90272-5.
364. Yu, D. G.; An, J. H.; Bae, J. Y.; Kim, S.; Lee, Y. E.; Ahn, S. D.; Kang, S. Y.; Suh, K. S. Carboxylic acid functional group containing inorganic core/polymer shell hybrid composite particles prepared by two-step dispersion polymerization. *Colloids Surfaces A Physicochem. Eng. Asp.* **2004**, *245*, 29–34, doi:10.1016/j.colsurfa.2004.06.026.
365. Mani Rahulan, K.; Vinitha, G.; Devaraj Stephen, L.; Kanakam, C. C. Synthesis and optical limiting effects in ZrO_2 and ZrO_2@SiO_2 core–shell nanostructures. *Ceram. Int.* **2013**, *39*, 5281–5286, doi:10.1016/j.ceramint.2012.12.029.
366. Mura, E.; Lousteau, J.; Milanese, D.; Abrate, S.; Sglavo, V. M. Phosphate glasses for optical fibers: Synthesis, characterization and mechanical properties. *J. Non. Cryst. Solids* **2013**, *362*, 147–151, doi:10.1016/j.jnoncrysol.2012.11.029.
367. Ceci-Ginistrelli, E.; Smith, C.; Pugliese, D.; Lousteau, J.; Boetti, N. G.; Clarkson, W. A.; Poletti, F.; Milanese, D. Nd-doped phosphate glass cane laser: from materials fabrication to power scaling tests. *J. Alloys Compd.* **2017**, *722*, 599–605, doi:10.1016/j.jallcom.2017.06.159.
368. Martin, R. A.; Knight, J. C. Silica-clad neodymium-doped lanthanum phosphate fibers and fiber lasers. *IEEE Photonics Technol. Lett.* **2006**, *18*, 574–576, doi:10.1109/LPT.2005.863999.
369. Said Mahraz, Z. A.; Sahar, M. R.; Ghoshal, S. K.; Reza Dousti, M. Concentration dependent luminescence quenching of Er^{3+}-doped zinc boro-tellurite glass. *J. Lumin.* **2013**, *144*, 139–145, doi:10.1016/j.jlumin.2013.06.050.
370. Stambouli, W.; Elhouichet, H.; Ferid, M. Study of thermal, structural and optical properties of tellurite glass with different TiO_2 composition. *J. Mol. Struct.* **2012**, *1028*, 39–43, doi:10.1016/j.molstruc.2012.06.027.
371. Choi, M.; Choi, J. W.; Kim, S.; Nizamoglu, S.; Hahn, S. K.; Yun, S. H. Light-guiding hydrogels for cell-based sensing and optogenetic synthesis in vivo. *Nat. Photonics* **2013**, doi:10.1038/nphoton.2013.278.
372. Dupuis, A.; Guo, N.; Gao, Y.; Godbout, N.; Lacroix, S.; Dubois, C.; Skorobogatiy, M. Prospective for biodegradable microstructured optical fibers. *Opt. Lett.* **2007**, doi:10.1364/OL.32.000109.
373. Parker, S. T.; Domachuk, P.; Amsden, J.; Bressner, J.; Lewis, J. A.; Kaplan, D. L.; Omenetto, F. C. Biocompatible silk printed optical waveguides. *Adv. Mater.* **2009**, doi:10.1002/adma.200801580.
374. Lopez-Iscoa, P.; Salminen T.; Hakkarainen T.; Petit L.; Janner D.; Boetti N.G.; Lastusaari M.; Pugliese D.; Paturi P.; Milanese D. Effect of partial crystallization on the structural and luminescence properties of Er^{3+}-doped

phosphate glasses. *Materials*. **2017,** vol. 10, pp. 473, doi:10.3390/ma10050473.
375. Hockicko, P.; Kudelcik, J.; Munoz, F.; Munoz-Senovilla, L. Structural and Electrical Properties of $LiPO_3$ Glasses. *J. Phys. Chem. B*, **2015**, doi:10.15598/aeee.v13i2.1250.
376. de Aza, P. N.; Guitián, F.; Santos, C.; de Aza, S.; Cuscó, R.; Artús, L. Vibrational Properties of Calcium Phosphate Compounds. 2. Comparison between Hydroxyapatite and β-Tricalcium Phosphate. *Chem. Mater.* **1997**, *9*, 916–922, doi:10.1021/cm9604266.
377. Antonakos, A.; Liarokapis, E.; Leventouri, T. Micro-Raman and FTIR studies of synthetic and natural apatites. *Biomaterials* **2007**, doi:10.1016/j.biomaterials.2007.02.028.

List of acronyms and symbols

ATR-FTIR Attenuated Total Reflectance Mode FTIR
BO Bridging Oxygen
CVD Chemical Vapor Deposition
CTE Coefficient of Thermal Expansion
DSC Differential Scanning Calorimetry
DTA Differential Thermal Analysis
ESA Excited State Absorption
FBG Fiber Bragg Grating(S)
FTIR Fourier Transform Infrared Spectroscopy
FWHM Full Width Half Maximum
GC Glass Ceramic
ICDD International Center Diffraction Database
IR Infrared
JCPDS Joint Committee on Powder Diffraction Standards
LASER Light Amplification by Stimulated Emission Process Of Radiation
LED Light Emitting Diode
LIDAR Light Detection and Ranging
MCVD Modified Chemical Vapor Deposition
NA Numerical Aperture
NIR Near Infrared
NP Nanoparticle
NBO Non-Bridging Oxygen
OSA Optical Spectrum Analyzer
OVD Outside Vapor Deposition
PCVD Plasma Chemical Vapor Deposition
PECVD Plasma-Enhanced Chemical Vapor Deposition
PDT Photodynamic Therapy
RE Rare-Earth
SM Single Mode
SBF Simulated Body Fluid
XRD X-Ray Diffraction
TIR Total Internal Reflection
UV Ultra-Violet
UV-VIS Ultra-Violet Visible
VAD Vapor Phase Axial Deposition
VIS Visible

$\boldsymbol{\alpha_{dB}}$ Optical Attenuation
$\boldsymbol{\alpha}$ Absorption coefficient
$\boldsymbol{I}$ Beam intensity
$\boldsymbol{n}$ Refractive Index
$\boldsymbol{N}$ Concentration of one element (cm^{-3})
$\boldsymbol{N_0}$ Critical concentration for self-quenching (cm^{-3})
$\boldsymbol{T_g}$ Glass transition temperature
$\boldsymbol{T_d}$ Glass softening temperature
$\boldsymbol{T_x}$ Glass crystallization temperature
$\boldsymbol{\theta_c}$ Critical angle for total internal reflection
$\boldsymbol{\rho}$ Density
$\boldsymbol{\sigma_a}$ Absorption cross-section
$\boldsymbol{\sigma_e}$ Emission cross-section
$\boldsymbol{\lambda}$ Wavelength
$\boldsymbol{\tau}$ Fluorescence lifetime

List of publications and conferences during PhD

Publications in International Peer-Reviewed Journals

Lopez-Iscoa P.; Ojha N.; Mishra A.; Pugliese D.; Gumenyuk R.; Boetti N. G.; Janner D.; Troles J.; Boussard-Plédel C.; Massera J.; Petit L.; Milanese D.; *"Design, processing and characterization of an optical core - bioactive clad phosphate fiber for biomedical applications"*; Submitted to the Journal of Materials Science and Engineering C: Materials for Biological Applications. **2019**.

Lopez-Iscoa, P.; Ojha, N.; Aryal, U.; Pugliese, D.; Boetti, N.G.; Milanese, D.; Petit, L.; *"Spectroscopic properties of Er^{3+}-doped particles-containing phosphate glasses prepared using direct doping method"*; Materials. Vol. 12 (1), pp. 129, **2019**, doi: 10.3390/ma12010129.

Dmitrieva I.; Lopez-Iscoa P.; Milanese D.; Petit L.; *"Ternary borosilicates as potential cladding glasses for semiconductor core optical fibers"*; Int. J. Appl. Glass Sci. pp. 1–6, **2018**, doi: 10.1111/ijag.12874.

Lopez-Iscoa P.; Pugliese D.; Boetti N.G.; Janner D.; Baldi G.; Petit L.; Milanese D.; *"Design, synthesis and structure-property relationships of Er^{3+}-doped TiO_2 luminescent particles synthesized by sol-gel";* Nanomaterials. vol. 8(1), pp. 20, **2018**, doi: 10.3390/nano8010020.

Lopez-Iscoa P.; Salminen T.; Hakkarainen T.; Petit L.; Janner D.; Boetti N.G.; Lastusaari M.; Pugliese D.; Paturi P.; Milanese D.; *"Effect of partial crystallization on the structural and luminescence properties of Er^{3+}-doped phosphate glasses"*; Materials. vol. 10, pp. 473, **2017**, doi:10.3390/ma10050473.

Lopez-Iscoa P.; Petit L.; Massera J.; Janner D.; Boetti N.G.; Pugliese D.; Fiorilli S.; Novara C.; Giorgis F.; Milanese D.; *"Effect of the addition of Al_2O_3, TiO_2 and ZnO on the thermal, structural and luminescence properties of Er3+-doped phosphate glasses"*; J. Non. Cryst. Solids, vol. 460, pp. 161–168, **2017**, doi:10.1016/j.jnoncrysol.2017.01.030.

Conference paper

Petit L.; Nguyen H.; Hongisto M.; Salminen T.; Hakkarainen T.; Lopez-Iscoa P.: Pugliese D.; Boetti N.G.; Milanese D.; *"Novel Er^{3+} doped phosphate glass-ceramics for photonics"*; 19th Int. Conf. Transparent Opt. Networks, Girona, Spain, **2017**, doi:10.1109/ICTON.2017.8024877.

International Conferences

Oral presentation: Lopez-Iscoa P.; Mishra A.; Ojha N.; Pugliese D.; Gumenyuk R.; Boetti N. G.; Janner D.; Massera J.; Troles J.; Bureau B.; Boussard-Plédel C.; Petit L.; Milanese D. (Presenter); *"Fabrication and characterization of a multi-mode Er^{3+}-doped phosphate fiber for biomedical applications"*; European Optical Society Biennial Meeting (EOSAM), 8 - 12 October **2018**, Delft, Netherlands.

Oral presentation: Lopez-Iscoa P.; Mishra A.; Ojha N.; Pugliese D.; Gumenyuk R.; Boetti N. G.; Janner D.; Massera J.; Bureau B.; Boussard-Plédel C.; Petit L.; Milanese D.; *"Fabrication and characterization of single-mode and multi-mode Er^{3+}-doped phosphate fibers for biomedical applications"*; Photoluminescence in Rare Earths (PRE'17), 30 November - 2 December **2017**, Rome, Italy.

Poster: Lopez-Iscoa P.; Pugliese D.; Boetti N. G.; Janner D.; Petit L.; Milanese D.; *"Fabrication and characterization of erbium doped bioactive glasses, glass ceramics and optical fibers"*; Photoluminescence in Rare Earths (PRE'17), 30 November - 2 December **2017**, Rome, Italy.

Oral presentation: Lopez-Iscoa P.; Petit L.; Massera J.; Janner D.; Boetti N. G.; Pugliese D.; Milanese D.; *"Synthesis and characterization of innovative Er^{3+}-doped nanoparticles containing phosphate glasses and glass ceramics"*; The 2nd International Conference on Phosphate Materials, 24 - 28 July **2017**, Oxford, UK.

Oral presentation: Lopez-Iscoa P.; Petit L.; Massera J.; Milanese D.; Janner D.; Boetti N. G.; Pugliese D.; Novara C.; Fiorilli S.; *"Effect of partial crystallization on the thermal, structural and luminescence properties of Er^{3+}-doped phosphate glasses"*; The EMN Meeting on Photonics **2016**, 19 - 23 September 2016, Barcelona, Spain.

Oral presentation: Lopez-Iscoa P.; Ferraris M.; Salvo M.; Milanese D.; Petit L.; Massera J.; Baldi G.; *"Synthesis and Characterization of Er^{3+}-doped Al_2O_3, TiO_2 and TiO_2@SiO_2 Core-Shell Structure Nanoparticles and Their Incorporation into Phosphate Glasses"*; 18th Italian National Conference on Photonic Technologies, 6 - 8 June **2016**, Rome, Italy.

Poster: Lopez-Iscoa P.; Petit L.; Massera J.; Milanese D. (Presenter); Baldi G.; Ferraris M.; Salvo M.; *"Design, synthesis and characterization of innovative glasses with Er^{3+}-doped nanoparticles"*; Glass and Optical Materials Division (GOMD 2016), 22 - 26 May **2016**, Madison, USA.